Forschungszentrum Jülich

Institut für Schicht- und Ionentechnik

# *Multi-Layer Josephson Tunnel Junctions*

*Norbert Thyssen*

Jül-3696

# *Multi-Layer Josephson Tunnel Junctions*

*Norbert Thyssen*

**Berichte des Forschungszentrums Jülich ; 3656**
ISSN 0944-2952
Institut für Schicht- und Ionentechnik Jül-3656
D 29 (Diss. Universität Erlangen-Nürnberg, 1999)

Zu beziehen durch: Forschungszentrum Jülich GmbH · Zentralbibliothek
D-52425 Jülich · Bundesrepublik Deutschland
☎ 02461/61-6102 · Telefax: 02461/61-6103 · e-mail: zb-publikation@fz-juelich.de

# Multi-Layer Josephson Tunnel Junctions

*Abstract:*

The most important active element in superconducting circuits are Josephson junctions. Their high frequency properties motivated many different projects to implement Josephson junctions in circuits for active and passive devices. The limiting points for applications in the low temperature superconducting field are broad line width and small power of a single Josephson junctions. The present work presents experimental and theoretical investigations on vertical stacked Josephson junctions in linear or annular geometry. Presenting results of up to *28* stacked elements is the state of the art of preparing stacked Low-$T_c$ Josephson Tunnel Junctions. Stacks of up to 10 junctions show a parameter spread of less than 5% due to the developed preparation procedures.

Magnetic flux quanta in Josephson junctions, called fluxons, in many cases behave as solitons. Recent experiments and modeling of fluxon dynamics in annular Josephson junctions show the influence of an external magnetic field on a single moving fluxon. The resulting dynamics are strongly analogous to the motion of a particle in a washboard potential. Experiment, theoretical model and numerical simulations are in good agreement.

Experiments on fluxons in two-fold stacks show the dynamic and static properties of this configuration. The critical current dependence on the external magnetic field displays different possible values, due to the voltage states of the junctions. First experimental hints on Cherenkov radiation by resonant structures in the current-voltage (*I-V*) characteristic is found with stacks prepared during this work.

The flux-flow dynamics in *N*-layered Nb/Al-$AlO_x$/Nb Josephson tunnel junctions is investigated experimentally and by numerical simulations. Collective flow of Josephson vortices is displayed in the magnetic field dependent *I-V* characteristics as cavity-like resonances. Numerical calculations with a finite difference method, using the coupled sine-Gordon equation explain these structures, accounted by the calculated characteristic frequencies. Voltage-locked flux-flow motion in the inner junctions is found. The difference to the outer junctions is explained by the film thickness which leads to higher fluxon numbers in those junctions. Numerical data and experiments show very good overall agreement. First experimental results on radiation emission of stacked junctions are shown.

First results about sub-micrometer junction preparation and high quality junctions in X-band coupling circuits show the broad field of application for the developed preparation machine and procedures.

# Contents

# 1. Introduction

This work is dealing with low-$T_c$ superconductor multi-layer Josephson tunnel junctions, which are often called Josephson stacks. Josephson stacks rise an interest due to their importance for understanding the basic properties of anisotropic superconducting materials, and also have promising potential for applications.

As an object for basic research, superconductivity is very important. The macroscopic manifestation of its quantum mechanical properties remains an interesting field. The possible use of mesoscopic long Josephson junctions for investigation of macroscopic quantum tunneling and quantum coherence[1.9] is an example. Understanding the d-wave symmetry of superconducting condensate in the high-$T_c$ cuprates is another present effort[1.10].

One of the major fields in Josephson physics is nonlinear dynamics of extended Josephson junctions. The penetration of magnetic field in these structures in form of soliton-like waves (also called Josephson fluxons, Josephson vortices or sine-Gordon kinks) and their dynamics is the topic related to this work. Josephson fluxons moving in an annular Josephson junction[1.11] represent relativistic particles moving in a ring of about *0.1*mm in diameter. The possibilities of comparing theoretical predictions with experiments are very good for these systems. In general, the interest in soliton dynamics is widely spread over other fields like fiber optics, magnetic materials, liquid crystals and plasma physics.

Devices like cables, current limitters, filters, magnets, engines, oscillators, mixers, sensors, logic, and others are all examples from the wide field of applications of superconductivity[1.1,2,3]. Josephson junctions, which offer tunable emission of high frequency radiation up to the THz range, can also be of great use as heterodynes in receivers[1.4]. On the other hand, the quantum-mechanically exact voltage response of such devices to external irradiation by a high frequency signal is already commercialized in the voltage standard[1.5,6,7].

The most popular example of superconducting applications are high-sensitive magnetometers (**S**uperconducting **QU**antum **I**nterference **D**evice → SQUID). They show a sensitivity of less than $10^{-10}$G/(Hz)$^{1/2}$ bandwidth. Such devices are used in material science, geology, geophysics, biophysics and medicine. In combination with special pick-up loops, SQUIDs resolve flux densities of less than $10^{-5}$ of the magnetic flux quantum $\Phi_0$. Measurements of heart signals, human brain activity or non destructive material evaluation are examples of the SQUID uses[1.1]. Very fast logic, like the superconductive **R**apid **S**ingle **F**lux **Q**uantum devices (RSFQ)[1.8], also contain a potential for the market. RSFQ circuits offer the advantage of very high frequencies up to some *100*GHz and low power dissipation. Until now, these

devices did not pass from basic demonstrations to real market, and one reason for that is the lack of reliable and cheap cooling technique required for their operation.

The dynamic properties of Josephson junctions are interesting also for another reason. The emission of high frequency radiation from Josephson junctions is closely related to fluxon dynamics[1.2,3,12,13]. A better understanding of this dynamics can help to improve the devices used for applications. Josephson **F**lux-**F**low **O**scillators (FFO) are suitable as radiation source in the frequency range between *100* - *700*GHz[1.14] with a maximum output power in the order of μW, narrow linewidth and a continuous frequency and power tunability. The basis of this radiation emission is the unidirectional flow of Josephson fluxons along the junction[1.15,16,17]. Here the propagation velocity of fluxons reaches several percentage of the light speed in vacuum. The use of FFOs in integrated receivers for sub-millimeter band, which incorporate an SIS mixer and a local FFO on the same chip[1.18], is particularly interesting for space applications. With a low power consumption, small size and weight, these devices possess big advantages over standard microwave technology. The crucial point for broader applications is the limitation of output power and linewidth of a single FFO. An approach to overcome this limitation is to force several Josephson junctions in a state of coherent radiation emission. Two proposals are presently under investigation.

First, various configurations of planar arrays of small Josephson junctions have been tested and demonstrated a power of up to *0.85*mW[1.19]. The disadvantage of this approach is its large size and problems in power and frequency adjustment. Another very promising and probably more feasible idea is the vertical stacking of many ($N$) Josephson junctions. In this way the mutual inductive coupling, determined by the thickness of the intermediate superconducting electrodes, can be higher by several orders of magnitude. Besides the expected increase of output power proportional to $N^2$ (for a not impedance-matched load, and $N$ as number of stacked junctions), the decrease of the linewidth by $\frac{1}{N}$ should bring crucial advantages. It has already been shown that stacked junctions can be used in an integrated receiver layout[1.18] using a simple replacement of a single junction by a stack.

The basic interest in the Josephson fluxon dynamics in multi-layer systems and its possible use in applications were the main motivations for this work. In addition, the discovery of the intrinsic Josephson effect in high-$T_c$ $Bi_2Sr_2Ca_1Cu_2O_8$ single crystals[1.20,21] naturally invited a comparison of these materials with the well controlled low-$T_c$ $Nb/(Al\text{-}AlO_x/Nb)_N$ multilayers (*Fig.1.1(a)-(b)*). Although the parameter ranges are very different (see *Fig.1.1*), their theoretical description is presently based on the same model of inductively coupled sine-Gordon equations[1.22]. Starting from the simplest *2*-fold stacks, this thesis work lead to

fabricating samples with up to $N=28$ stacked Josephson junctions. Experiments and numerical simulations had been carried out and showed a good agreement. This allowed to conclude positively about applicability of the above mentioned model to complex multilayer structures.

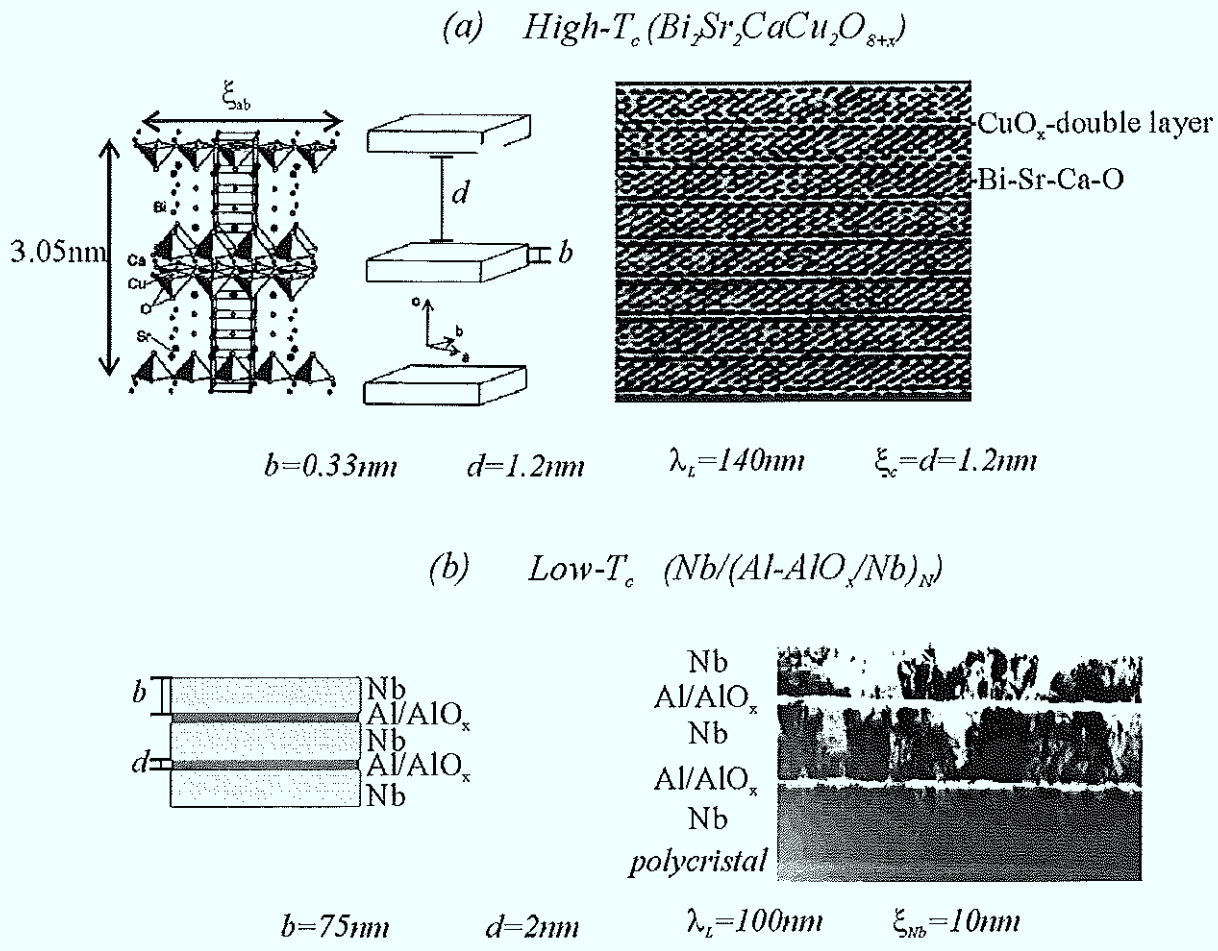


*Fig.1.1: Stacked Josephson junctions*
*(a) natural $Bi_2Sr_2CaCu_2O_{8+x}$ stack, (b) artificial $Nb/Al\text{-}AlO_x/Nb$ stack*

First, an introduction in the theoretical background will be given. For more detailed theoretical considerations the references[1,2,3,12,13] were found to be very useful. **Chapter 2** starts from the background of superconductivity, Josephson effect and SIS junctions. It includes the basic theoretical model for a single junction and some original experimental results. The preparation procedures for different layouts is explained in detail in **Chapter 3**. Introducing the theory of stacked junction systems in **Chapter 4**, **Chapter 5** presents the experimental investigations on two-fold stacks. The work with multi-layer Josephson junctions is the focus of **Chapter 6**. Here is discussed the comparison between numerical simulations and experimental results, and radiation measurements are presented at *80-*

*120*GHz. Several satellite projects are described in **Chapter 7**. Final conclusions in **Chapter 8** and the appendix in **Chapter 10** complete this thesis.

# 2. Background

## 2.1. Superconductivity and weak links

Nearly *90* years ago H. Kamerling-Onnes discovered the superconducting property of mercury at very low temperature in the Leiden laboratory[2.1]. The property of disappearing resistance below the measurable limits (today $R<10^{-24}\Omega$cm) was found for many other elements, alloys and intermetallic compounds. An important complement of this new state was given by the discovery of ideal diamagnetism[2.2] of superconductors. The so-called Meissner-Ochsenfeld effect is a consequence of the phase transition of a sample changing into the superconducting state, when cooling below the critical temperature $T_c$. During the first years superconductivity remained a low temperature effect, where liquid helium ($T=4.2$K) was used for cooling. The research activities were further increased by two important events. First, there was the theoretical prediction of the Josephson-effects in 1962[2.3] followed by its experimental evidence[2.4]. And second, there was the discovery of superconductors with high critical temperature, like $LaBaCuO_4$ at *40*K, in *1987* by J. Bednorz and K.A. Müller[2.5]. Now the superconductivity can be realized at liquid nitrogen temperatures ($T=77$K) and transition temperatures became possible of up to *130*K for $HgBa_2Ca_2Cu_3O_8$.

A profound description and comprehension of superconductivity is based on theoretical models, started from the phenomenological London theory in 1935[2.6]. It describes a two-fluid model of electrons in normal and superconducting reservoirs. The density of electrons inside these two fluids pretends the normal or superconducting character. This approach was broadened by the still phenomenological Ginzburg-Landau theory[2.7] in 1935, which for the first time took into account the quantum effects and described the coherent behavior of all superconducting electrons. Also the complement by Abrikosov[2.8] in 1957 did not change the fact that this theory was not able to explain the microscopic origin for superconductivity. A better description started with a suggestion of Cooper in 1956, who defined superconductivity as a pairing state of two electrons with opposite spin and momentum, the Cooper-pair. In the Bardeen-Cooper-Schrieffer (BCS) theory[2.9,10,11] an interaction between electrons via crystal phonons explained an attractive potential between them, which causes Cooper-pairs. These electron pairs have a vanishing total angular momentum and spin, and can be described as one particle. Their distribution function follows the Bose statistic and all pairs condense in the same ground state, which is superfluid. An energetic interaction of a single pair with the

crystal is not possible. The observed dissipation free current is characterized by Cooper pairs of an elementary charge of *2e*.

A static model to explain an electron-electron interaction was assuming a lattice of atomic residues with two negative charges, neglecting all other electrons. A negative charge attracts the surrounding positive ones and polarize the lattice, as shown in *Fig.2.1(a)*[1.12]. Each of this two electrons senses the polarization of the other one and experiences an attraction in this direction. This first description of an attractive interaction of two electrons in a lattice of atomic residues. A mechanical analog is shown in *Fig.2.1(b)-(c)*[1.12]. The elastic deformable lattice of atomic residues is represented by an elastic membrane. Two spheres represent the negative charges and the deformation on account of their weight corresponds to the polarization. When both spheres group together in a single trough, the system decreases its potential energy in the gravitational field. Again we see the attractive interaction, but we did not take into account that in reality the electrons have considerable velocities. Nevertheless we can understand a possible attraction between electrons that depends on the time in which the lattice of atomic residues can undertake a displacement. Qualitatively this shows a dependence of the interaction on the natural frequency of the lattice.

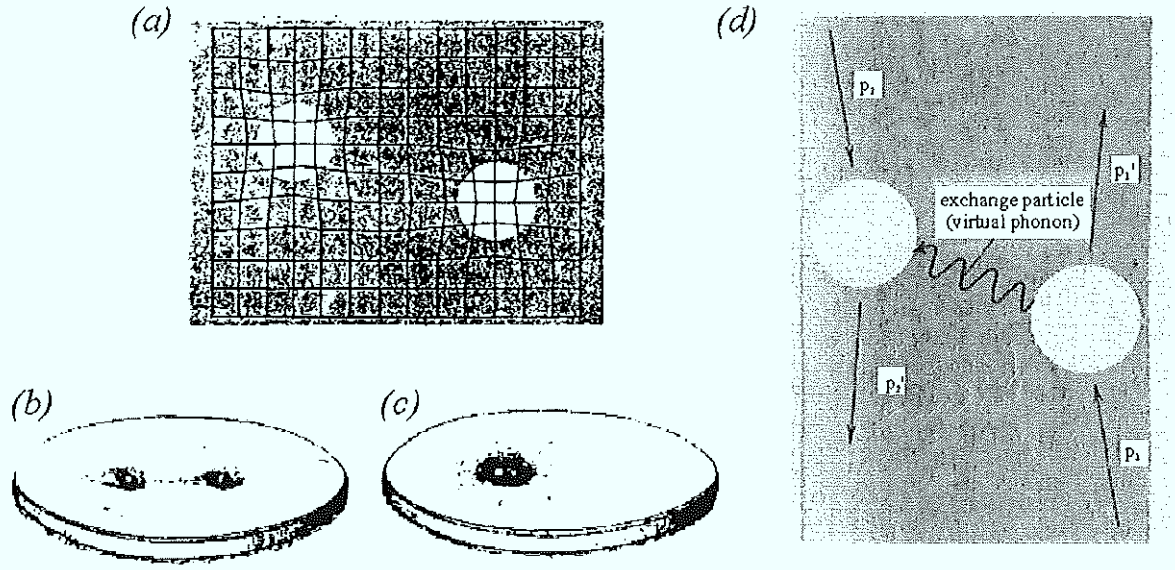


*Fig.2.1*[1.12]*: (a) Polarization of a lattice of atomic residues by two electrons; (b),(c) the attraction of spheres on an elastic membrane {configuration (b) is unstable and goes over to (c)}; (d) electron-electron interaction via virtual phonons*

From this heuristic model we can understand an approach from modern physics. Here the electron-electron interaction is described by the exchange of virtual phonons. These phonons

are called virtual and they exist only during the exchange from one electron to the other. They do not have the possibility to pass away from the electrons into the lattice as real phonons. In a superconductor the electron-electron interaction can overcome the repulsion of the electrons by electrostatic forces and we achieve the pair correlation. The extension of such Cooper pairs is in the range of *100* to *1000*nm for a pure superconductor, which is much larger than the distance of two conducting electrons that amounts to a few *0.1*nm. The resulting overlap of the Cooper pairs shows a particular rigid correlation that is described as condensation in one common state.
Due to this condensation of the Cooper pairs, regarded as Bose particles, in the same ground state, a superconductor can be described with an effective macroscopic wave function

$$\Psi(\vec{r},t) = \sqrt{N(\vec{r},t)} \cdot e^{i \cdot \varphi(\vec{r},t)} . \qquad \{2.1\}$$

$N(\vec{r},t)$ is the density of Cooper pairs and $\varphi(\vec{r},t)$ is a common phase factor. If two bulk superconductors are coupled via a weak link, we reach the condition for the Josephson-effects[2,3]. For two identical isolated bulk superconductors ($S_1$ and $S_2$) the amplitude of the wave function ($\Psi_i$) has to be equal, just their phases are arbitrary different.

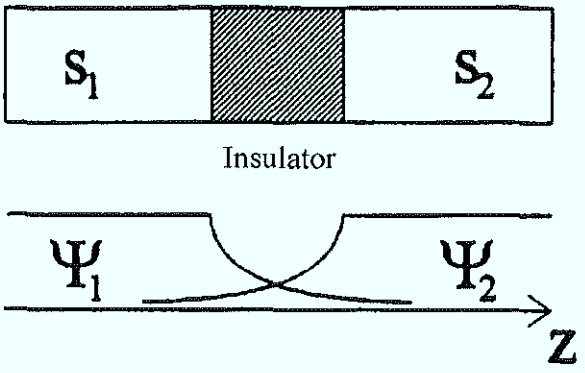


*Fig. 2.2: Overlap of the two wave functions for a weak link (demonstrated by an insulator) between two superconductors*

Connected via a weak link their phases have an overlapping region (*Fig2.2*) and, as a result, they are mutually dependent. Such weak links can be realized in many ways and the crucial parameter is the coherence length $\xi$ of the superconductor, which is in the order of a few nanometers for low-$T_c$ systems. *Fig.2.3(a)* shows examples for weak links like superconductor-insulator-superconductor junctions (SIS), superconductor-normal metal-superconductor junctions (SNS), microbridges, and point contacts. In high-$T_c$ materials the coherence length is much shorter and a broken crystal structure in such films already creates

weak links. Examples are bicrystal, edge-type, ramp-type, and e-beam written junctions (*Fig.2.3(b)*).

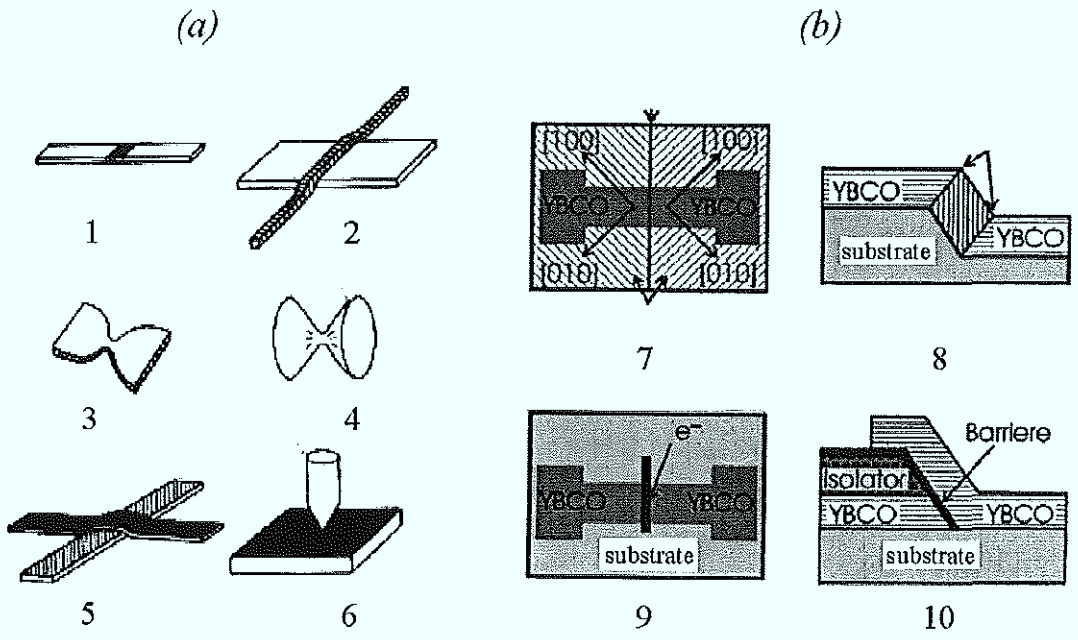


*Fig.2.3: (a) Low-$T_c$ weak links: 1: phase slip, 2: proximity effect, 3: two-dim. microbridge, 4: three-dim. microbridge, 5: SIS/SNS tunnel junction, 6: point contact;*
*(b) high-$T_c$ weak links: 7: bicrystal, 8: step edge, 9: e-beam written, 10: ramp type*

For superconducting weak links the quantum mechanical tunneling problem was solved by Josephson[2,3]. In the following, we concentrate on the SIS Josephson tunnel junction which can be realized using the niobium-aluminum technology.

### 2.2. Josephson effects in SIS junctions

For an SIS-junction, Josephson derived two different effects[2,3], based on the description of superconductors with a macroscopic wave function:
The **dc Josephson effect** describes a current without energy dissipation, passing through a weak link. The exchange of Cooper pairs between the two superconducting electrodes takes place due to the overlap of the wave functions. This Cooper pair tunneling current is limited by a maximum value and periodical dependence on the phase difference $\phi$ between the wave functions. The local superconducting tunnel current density at zero voltage is found to be

$$j(\vec{r},t) = j_C \sin(\phi(\vec{r},t)) , \qquad \{2.2a\}$$

or for the current $$I(t) = I_c \sin(\phi(t)) \,, \qquad \{2.2b\}$$

where $j_c$ is the maximum supercurrent density and $\phi = \varphi_2 - \varphi_1$ is the phase difference. The quantum mechanical problem of Cooper pair tunneling, expressed in the equation {2.2}, was simultaneously derived by Feynman[2.12] and Larkin[2.13]. While Feynman solved the problem in the Schrödinger picture, Larkin used the Ginzburg-Landau approach.
The second effect is the **ac Josephson effect** which follows directly from the principles of quantum mechanics. For currents above the critical value $I_c$, , the junction switches into a voltage state. The system can also be forced to remain in this state by an external current or voltage bias. The Schrödinger equation for one side is given as

$$i\hbar \frac{\partial \Psi}{\partial t} = \hat{H}\Psi \,. \qquad \{2.3\}$$

For the stationary state it is $\hat{H}\Psi_1 = E\Psi_1$ , with $\Psi_1 = |\Psi_1| e^{i\varphi(t)}$ . $\{2.4\}$

So it follows $$-\hbar \frac{\partial \varphi}{\partial t} = E \,. \qquad \{2.5\}$$

Both sides of the weak link are related by the voltage V

$$E_1 - E_2 = 2\mathrm{eV} \,, \qquad \{2.6\}$$

because the elementary carrier charge is *2e*. We end up with the second Josephson equation that is

$$V(\vec{r},t) = \frac{\hbar}{2e} \frac{\partial \varphi(\vec{r},t)}{\partial t} \,. \qquad \{2.7\}$$

After the integration and substitution in {2.2b}, we obtain the Josephson ac current for non-zero voltages as

$$I = I_c \sin\left(\phi(0) + \frac{2e}{\hbar} Vt\right). \qquad \{2.8\}$$

For the exact and complete derivation I refer again to the basic books on this topic[1.2,3,12,13]. In equation {2.7} the local voltage and the rate of phase change between the electrodes are proportional to each other with the magnetic flux quantum being the proportionality constant

$$\Phi_0 = \frac{h}{2e} = 2.07 \cdot 10^{-15}\,\mathrm{Wb} \,. \qquad \{2.9\}$$

The oscillation frequency of the phase difference per applied voltage unit is given directly as

$$\frac{\frac{\partial \varphi}{\partial t}}{2\pi V} = \frac{2e}{\hbar} = 483.6\,\mathrm{GHz/mV} \,. \qquad \{2.10\}$$

The first experimental observation of this ac Josephson effect was done by Yanson, Svitsunov and Dmitrenko in 1964[2.14] who measured directly the radiation frequency, emitted by a Josephson junction. Let us discuss in detail the finite-voltage state of an SIS junction.

The quasiparticle distribution in the superconducting state can be presented using the semiconductor energy band model (*Fig.2.4)*. Cooling the system under the critical temperature creates Cooper pairs which energetically are located on the Fermi level. The position of the Fermi level between the two bands is in a forbidden energy area, the energy gap ($2\Delta_i$) which is displayed schematically in *Fig.2.4*. For temperatures above zero there are quasiparticles excited above the gap.

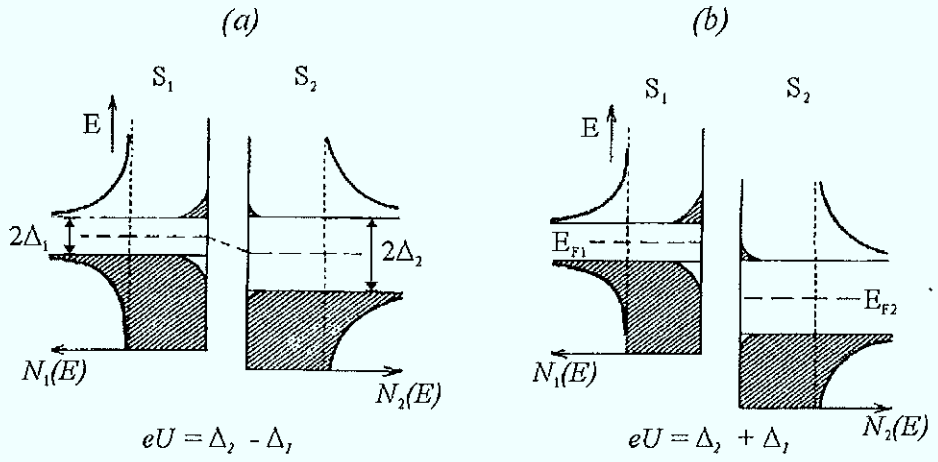


*Fig.2.4[1.12]: Energy band model for a weak link of two different superconductors ($S_1$ and $S_2$)*

For an SIS-junction, two superconductors are connected by a tunnel barrier and a tunneling current is possible. If a voltage is applied to this structure (*Fig.2.4(a)*), the resulting total current flow is different from zero. Above the voltage corresponding to the energy of the sum of the gaps ($V > \frac{\Delta_1 + \Delta_2}{e}$) (*Fig.2.4(b)*), quasiparticles tunnel from one side of the tunnel barrier to the other.

To clarify the different tunneling regimes in SIS junctions, it is useful to follow a standard measured current-voltage (*I-V*) characteristic of a typical Nb-Al/$AlO_x$-Nb junction as it is shown in *Fig.2.5*. This characteristic is usually measured in the current biased scheme. Here we assume $\Delta_1=\Delta_2=\Delta$.

*(a)→(b):* Starting from zero current, the zero voltage current branch corresponds to the tunneling of Cooper pairs, as described by the dc Josephson equation {2.2}.

*(b)→(c):* Reaching the critical value $I_c$ , the lossless current transport breaks down and the system jumps into a voltage state that corresponds to the double gap energy $2\Delta$. This gap

energy is the breakup energy for the Cooper pairs. The resulting voltage is $V_{gap} = \frac{2}{e}\Delta \approx 2.8\text{mV}$ in experiment(*Fig.2.5*).

*(c)→(d):* The tunneling current is dominated by quasiparticles (charge = ±*e*) now. Due to the overlap of the peaks in the densities of states for the two superconductors. The "knee" region *(d)* can be explained in detail by the proximity effect, which appears due to the presence of not oxidized aluminum near the barrier. The real configuration of the junction has to be described by an SNIS model and its microscopic treatment can be found in the references[2,15,16].The aluminum thickness can be minimized to have a less pronounced proximity effect, if necesarry.

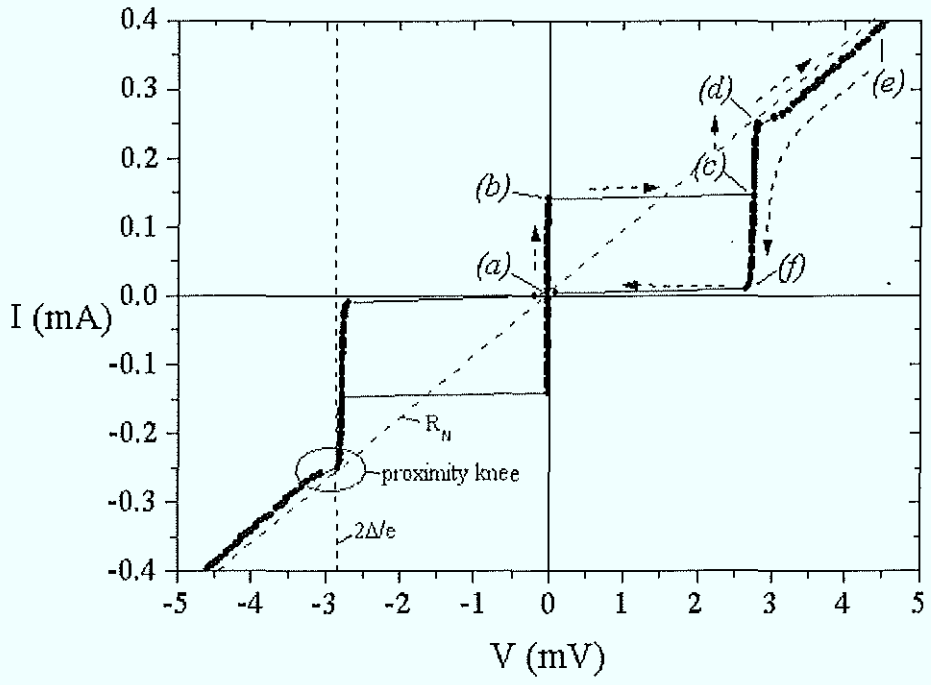


*Fig.2.5: A standard measured I-V curve for an Nb/Al-ALO$_x$ /Nb Josephson tunnel junction [sample: window1.1.4/2.1]*

*(d)→(e):* Further increase of the current merely displays Ohms law at $V>2\Delta/e$. The slope gives the usual resistance $R_N$ of the junction.

*(e)→(f):* While decreasing the current we observe a hysteretic behavior. The tunneling current remains to be carried by quasiparticles. For *0* temperature the current should decrease to zero before the zero voltage state would be achieved again.

*(f)→(a):* For temperatures above zero, a sub-gap quasiparticle current is observed due to the temperature induced excitation of quasiparticles. The displayed branch is often called the

McCumber branch[2.17] and corresponds to a uniform rotation of $\phi$. The similar cycle, as described above, can also be realized with the opposite bias. A more complete analytical treatment for the relevant tunneling processes can be found in reference[2.18].
Using the gauge invariance of $\phi$ it is possible to calculate the effect of an external magnetic field applied in plane to the junction area[1,2](*Fig.2.6*). The two-dimensional expression for the gradient of $\phi$ can be given by

$$\nabla\phi = \left(\frac{2ed'\mu_0}{\hbar}\right)\cdot\left(\vec{H}\times\vec{n}\right), \qquad \{2.11\}$$

where

$$d' = d + \lambda_L \coth\left(\frac{b_1}{\lambda_L}\right) + \lambda_L \coth\left(\frac{b_2}{\lambda_L}\right) \qquad \{2.12\}$$

is the magnetic thickness of the junction, which is the associated penetration of the magnetic filed in the superconductor to a depth of $\lambda_L$ with $d$ as the thickness of the insulating layer, $b_1$ and $b_2$ as the thickness of the superconducting films, and $\vec{n}$ as the unit vector, normal to the junction plane. Equation {2.11} gives the relation of $\phi$ to a magnetic field, whereas equation {2.7} relates $\phi$ to electric fields.

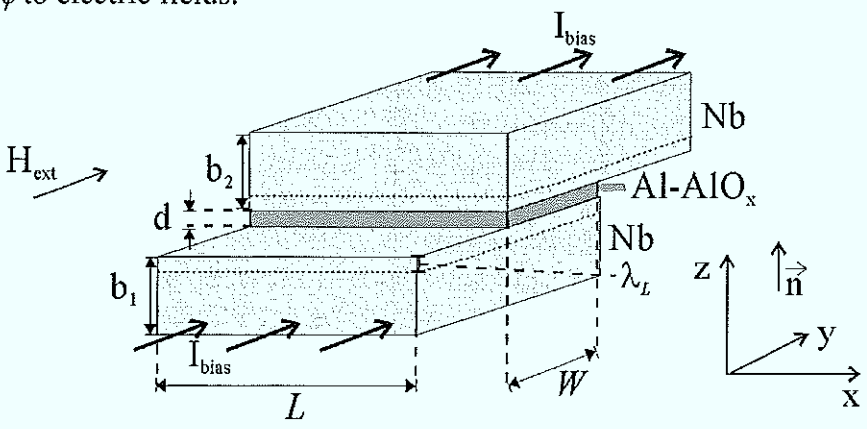


*Fig.2.6: View graph of a Josephson tunnel junction*

### 2.3 Electrodynamics of Josephson junctions

In order to formulate the electrodynamics of a Josephson junction, it is possible to start from the third Maxwell equation

$$\nabla\times\vec{H} = \vec{j} + \frac{\partial\vec{D}}{\partial t}. \qquad \{2.13\}$$

If we choose the junction area parallel to the *x-y plane* (*Fig.2.6*), we should concentrate on the *z-component* of the vector product which is than

$$\frac{\partial H_y}{\partial x} - \frac{\partial H_x}{\partial y} = j_z + \varepsilon_0 \varepsilon_r \frac{\partial E_z}{\partial t} \,. \qquad \{2.14\}$$

The total current density across the barrier in *z-direction* has to be given by equation {2.2} with two additional terms

$$j_z = j_c \sin\phi + \sigma V + \sigma_i V \cos\phi \,, \qquad \{2.15a\}$$

where $j_c \sin\phi$ gives the Josephson current density of the Cooper pairs, $\sigma V$ stands for the quasiparticle current density, and $\sigma_i V \cos\phi$ is a current density contribution due to interference of the previous two. For most cases the latter term can be neglected, and[1.2]

$$j_z = j_c \sin\phi + \sigma V \,. \qquad \{2.15b\}$$

For the SIS junction the electric field can be given as

$$E_z = V / d \,. \qquad \{2.16\}$$

If we use in addition the dc Josephson equation {2.2} and the gauge invariance {2.11} we end up with the wave equation for the phase difference $\phi$ in the form

$$\frac{\hbar}{2e\mu_0 d}\left(\frac{\partial^2\phi}{\partial x^2} + \frac{\partial^2\phi}{\partial y^2}\right) - \frac{\hbar}{2e}\frac{\varepsilon_0\varepsilon_r}{b.}\frac{\partial^2\phi}{\partial t^2} = j_c \sin(\phi) + \frac{\hbar\sigma}{2e}\frac{\partial\phi}{\partial t} \,. \qquad \{2.17\}$$

Introducing the characteristic length

$$\lambda_J = \sqrt{\frac{\hbar}{2e}\frac{1}{\mu_0 j_c d'}} \qquad \{2.18\}$$

as ***Josephson penetration length***, the characteristic frequency

$$\omega_p = \sqrt{\frac{2e}{\hbar} j_c \frac{d}{\varepsilon\varepsilon_r}} \qquad \{2.19\}$$

as ***plasma frequency***, the relaxation rate

$$\omega_c = \frac{2e}{\hbar}\frac{j_c}{\sigma} \qquad \{2.20\}$$

as the ***characteristic frequency***, we can write equation {2.17} in the form

$$\boxed{\phi_{xx} + \phi_{yy} - \frac{1}{\left(\lambda_J \omega_p\right)^2}\phi_{tt} = \frac{1}{\lambda_J^2}\sin(\phi) + \frac{1}{\lambda_J^2 \omega_c}\phi_t} \,. \qquad \{2.21\}$$

The resulting non-linear partial differential equation is called ***perturbed sine-Gordon equation*** and is describing the electrodynamics of an extended *2*-dimensional Josephson junction. The maximum propagation velocity of an electromagnetic wave in this system is called the ***Swihart velocity***[2.19] and is given as

$$\bar{c} = \lambda_J \omega_p = \frac{1}{\sqrt{\mu_0 d' C^*}} . \qquad \{2.22\}$$

Here $$C^* = \frac{\varepsilon\varepsilon_r}{d} \qquad \{2.23\}$$

is the specific capacitance per unit area. For convenience the equation {2.21} is often used in normalized units, with the time normalization to the inverse plasma frequency $\frac{1}{\omega_p}$ and the coordinates normalization to the Josephson penetration length $\lambda_J$. Equation {2.21} in normalized units looks like

$$\phi_{x'x'} + \phi_{y'y'} - \phi_{t't'} = \sin(\phi) + \alpha\phi_{t'} . \qquad \{2.24\}$$

The damping coefficient $\alpha$ is a characteristic parameter for the system and can be written as

$$\alpha = \frac{\sigma}{\sqrt{\frac{2e}{\hbar} j_c C^*}} . \qquad \{2.25\}$$

The used model neglects the high frequency quasiparticle currents in the superconducting electrodes. These currents lead to an additional damping term $\beta$ in the sine-Gordon equation[2.20,21,22]. For not very low temperatures the $\alpha$ term is dominant and, for simplicity, the $\beta$ term is usually neglected.

Till now we used the two-dimensional model for the description. In reality, experimentally investigated junctions in most cases can be considered as quasi-one-dimensional, because the width $W$ of the junction is usually chosen smaller than $\lambda_J$. In this case the equation {2.24} can be simplified by assuming a constant phase difference $\phi$ in *y-direction*. For the overlap geometry (*Fig.2.6*) the bias current is approximately constant and is accounted by the normalized term

$$\gamma = j/j_c , \qquad \{2.26\}$$

where $j_c$ is the critical current density. Thus, the final form of the one-dimensional perturbed sine-Gordon equation is

$$\boxed{\phi_{x'x'} - \phi_{t't'} = \sin(\phi) + \alpha\phi_{t'} + \gamma} . \qquad \{2.27\}$$

### 2.3.1. Long Josephson junctions

Equation {2.27} is completed by the boundary conditions that depend on the junction geometry. We will consider now a straight overlap Josephson junction as shown in *Fig.2.7(b)*.

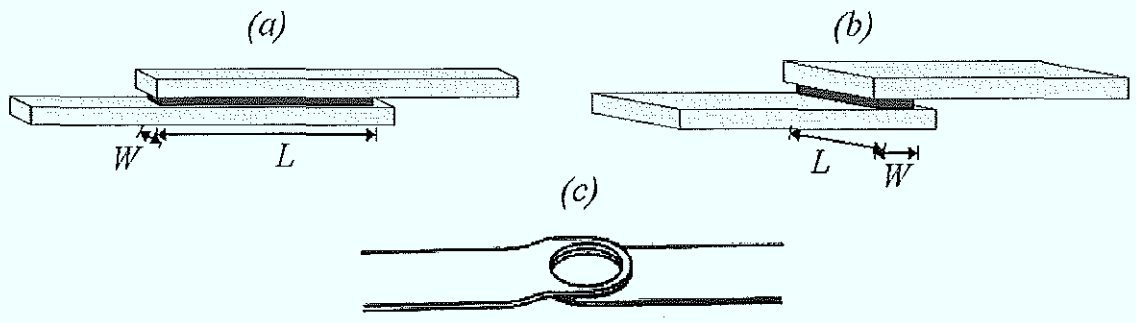


*Fig.2.7: Long Josephson junctions: (a) inline, (b) overlap, and (c) annular*

For a magnetic field in y-direction the boundary conditions can be given in the form

$$\phi_{x'}(0,t) = \phi_{x'}(L,t) = \eta \ , \qquad \{2.28\}$$

with

$$\eta = \frac{H_y}{\lambda_J j_c} \qquad \{2.29\}$$

as normalized external magnetic field component. At this point all electromagnetic quantities can be derived from the phase $\phi$. The given values in equation {2.27} can experimentally be interpreted in the following way:

$\phi_{xx'}$ represents the spatial change of the current,

$\phi_{tt}$ represents the change by time of the voltage,

and $\phi_{x'}$ can be interpreted as magnetic field component.

M. Cirillo et al.[2.23] developed a complex mechanical analog described by {2.27}. An easier way to imagine this system is a row of coupled pendula. This is less exact but more straight forward. The phase is represented by the angle of the pendulum, and so a change in phase is represented by an angle shift between neighboring pendula. This picture will become clearer discussing the solutions of the sine-Gordon equation.

Exact analytical solutions for the nonlinear partial differential equation {2.27} are not known. Two approaches are used to solve the equation. The first way are numerical simulations and the other uses some analytical perturbation method, for which are needed the analytical solutions of the unperturbed sine-Gordon equation

$$\phi_{x'x'} - \phi_{t't'} = \sin(\phi) \ . \qquad \{2.30\}$$

These solutions can be subdivided in three different classes:

**(1) The soliton solutions:**

The phase difference is given as

$$\phi(x,t) = 4\arctan\left[\exp\left(\pm\frac{x-ut-x_0}{\sqrt{1-u^2}}\right)\right]. \qquad \{2.31\}$$

Here (+) stands for a soliton and (-) for an antisoliton, which represents a $+2\pi$ ($-2\pi$) change of the phase difference $\phi$ around the soliton's center at $x=x_0$. The combination of a nonlinear dispersion relation and additional nonlinearities render solitonic solutions. A soliton represents a stable solitary wave propagating with the velocity $u$. Its energy is localized at $x_0$. The phase and its first spatial derivative for two different velocities are shown in *Fig.2.8.*

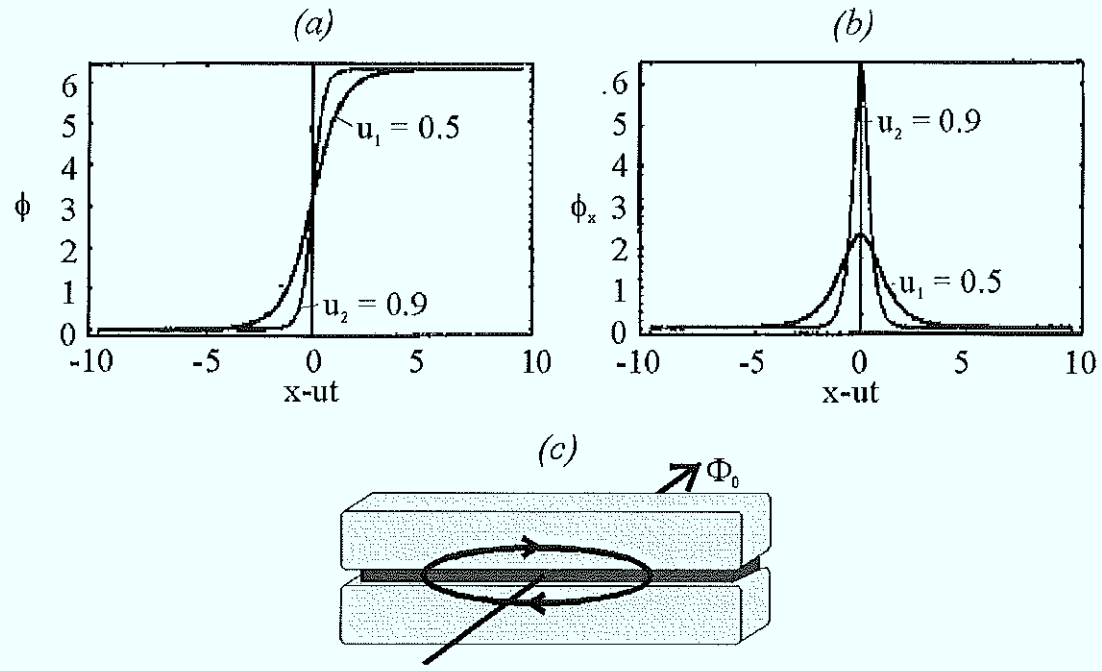


*Fig.2.8: The soliton solution: (a) phase $\phi$, (b) phase derivative $\phi_x$, and (c) penetrated Josephson fluxon in a tunnel junction*

In the case of long overlap Josephson junctions $\phi_x$ represents a magnetic field component. Thus the soliton solution corresponds to a localized magnetic flux and it is often called ***Josephson fluxon (antifluxon)***. Other frequently used expressions are: ***$2\pi$-kink, vortex, soliton***. All expressions describe the same phenomenon of a $2\pi$ shift in the phase difference $\phi$ inside a length scale of about $2\lambda_J$. The properties of this kind of solutions for nonlinear

systems were investigated by Zabusky and Kruskal[2.24]. For multi-soliton solutions in systems of finite length the more general traveling wave solution by Kulik[2.25] can be used. It is possible to understand it as a traveling fluxon chain in the junction. The energy of a fluxon in normalized units is given by

$$E_{fluxon}=8\Gamma(u)\,, \qquad \{2.32\}$$

where

$$\Gamma(u)=\frac{1}{\sqrt{1-u^2}} \qquad \{2.33\}$$

is the Lorentz factor. The spatial extension is determined by the factor: $\sqrt{1-u^2}$ . For higher velocity of the soliton one can see its Lorentz-contraction (*Fig.2.8(b)*).

**(2) <u>Plasma oscillations</u>:**

This kind of solution describes small-amplitude oscillations of the phase difference $\phi$ around an equilibrium state $\phi_0$. In long Josephson tunnel junctions these oscillations can built standing waves, which characterize resonant states of the junction.

**(3) <u>Breathers</u>:**

In general breathers are unstable with respect to the perturbation terms and therefore they decay after some transient time. The breather can be interpreted as a bound state of a soliton-antisoliton pair. Due to the decay (annihilation of soliton and antisoliton) of this solution it is not taken into account for time averaged measurements and in this work I will not refer to it any more.

All solutions had also been investigated very instructively, using the mentioned mechanical analog by M. Cirillo et al [2.23].

The relativistic invariance of the system is very important. As shown in *Fig.2.8*, for higher velocities the kink shows a contraction on the *x-scale* which is often refered to as the relativistic contraction of solitons. This property follows directly from the invariance of the sine-Gordon equation under the Lorentz transformation. Investigations with **L**ow **T**emperature **S**canning **E**lectron **M**icroscopy (LTSEM) have shown an impressive evidence for the Lorentz contraction of a single soliton in an annular Josephson junction[2.26].

Approximate solutions for the perturbed sine-Gordon equation can be calculated with two different approaches. For strong perturbations the multimode theory[2.27] is used. In this case all three analytic solutions of the unperturbed system become unstable[2.28,29] and the soliton solution starts to have more and more an electromagnetic wave character. Resonant states of

the system can be explained by cavity resonances and for small normalized junction length $L/\lambda_J << 1$ sometimes it is enough to consider one mode. The single mode theory was derived by Takana[2.30] and Kulik[2.31]. For normalized length of the junction $L/\lambda_J >> 1$ the number of regarded modes for the spatial Fourier components is increasing.
For small perturbations, the soliton solution stays stable with some modifications[2.28,29]. An approximation of the solution is done using a perturbation theory. Mc Laughlin and Scott[2.27] developed such an approach, treating the energy dissipating terms and the bias current as small perturbations. In this way the soliton solution for the system is given by

$$\phi(x,t,u,x_0) = 4\arctan\left[\exp\left(\frac{x - X(t)}{\sqrt{1-u(t)^2}}\right)\right], \qquad \{2.34\}$$

with the perturbation $X(t) = x_0 + \int_0^t u(\tau)d\tau$. Such solitons behave like relativistic particles with an energy of $E(\phi) = 8\left(1-u^2\right)^{-1/2}$. The investigated SIS junctions with typically $\alpha \leq 0.05$ are well described by the perturbed sine-Gordon equation with small perturbations.

### 2.3.2 Zero Field Steps (ZFS)

The bias current across the junction acts on a Josephson fluxon inside a long junction with the Lorentz force caused by the interaction of the penetrated magnetic field inside the fluxon and the passing current. Fluxons and antifluxons are driven in the opposite directions due to the inverse polarity of their magnetic flux. This motion generates a voltage across the junction which is proportional to the number of moving fluxons and their velocity. One stable regime for zero external magnetic field is the reflection of a fluxon as antifluxon and vice versa at the junction boundaries. In the *I-V* characteristic this state is displayed by resonant steps, the **Z**ero **F**ield **S**teps (ZFSs)[2.32,33,34,35]. Each of them accounts for a constant number of simultaneously moving fluxons (antifluxons) inside the junction. With increasing the bias current, the fluxon velocity reaches asymptotically a maximum value. This characterizes the compensation point between the energy dissipation of the moving fluxon and the enrgy supply by the bias current[2.36]. From the perturbation theory the soliton velocity $u$ can be calculated by solving the equation[2.37,38]

$$\frac{4}{\pi}u\gamma(u)\left(\alpha + \frac{\beta}{3}\gamma^2(u)\right) = 0\ . \qquad \{2.35\}$$

The asymptotic voltage of the ZFSs can be given by

$$V_{ZFS} = n\frac{\Phi_0}{L}\bar{c} \ , \qquad \{2.36\}$$

with $\bar{c}$ as Swihart velocity[2.19] characterizing the maximum soliton velocity. Various possible fluxon-antifluxon configurations are illustrated in *Fig.2.9.*

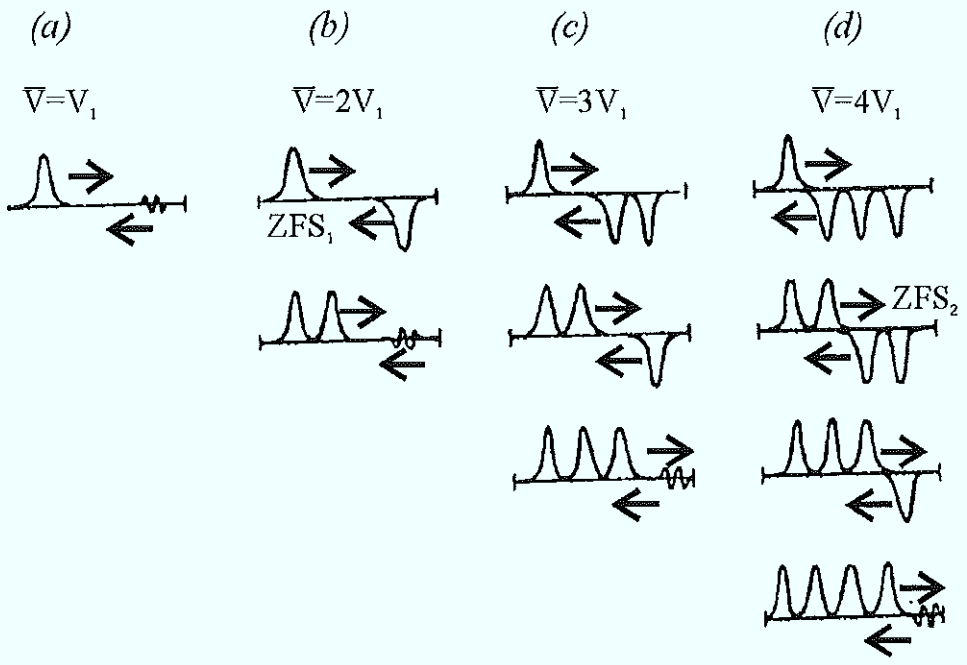


*Fig.2.9*[1.2]*: Fluxon configurations in a long Josephson junction*

The marked (ZFS) states in *(b)* and *(d)* represent the ZFSs. We have to distinguish reflections and annihilations in this figure. For annihilations the energy of the fluxon is partly reflected back as plasma or breather oscillation[2.37]. Measured fine structures on ZFSs can be explained by an interaction of the linear plasma waves with the fluxons[2.38].

### 2.3.3 Fiske steps (FS)

When applying an external field in the plane of the junction, the reflection of solitons becomes energetically adverse. The external field adds energy to fluxons reflected at one boundary, but subtracts energy on the opposite side. Sufficiently large external fields prevent the fluxon reflection and an unidirectional fluxon motion is the consequence. Fluxons are nucleated at one end and annihilate at the opposite end of the junction. The energy supply by an external field[2.36] to a junction extending from $-L/2$ to $L/2$ on the $x$-axis, is $\Delta H_1\left(\pm\frac{L}{2}\right)=\pm\frac{\pi}{2}\eta$ .

Thus, magnetic field absorbs the fluxon energy at $x = +L/2$ and contributes with increasing it at $x = -L/2$.
If the energy of this plasma packet is high enough, it can trigger the creation of a fluxon at the opposite boundary[2.39,40]. This process explains the appearance of Fiske steps (FS)[2.41] in long junctions. In the *I-V* curve these steps appear for non-zero external fields. Their voltage is given by

$$V_{FS} = n\frac{\Phi_0}{2L}\bar{c} \ . \qquad \{2.37\}$$

Let us note here that Fiske steps in short junctions are well described by the linear single-mode theory, derived by Kulik[2.25].
At low fields the dynamics of long junctions are very complicated and manifested by a **D**isplaced **L**inear **S**lope (DLS)[2.42,43], which appear on the *I-V* curve. The displaced linear slope does not have a pronounced resonant shape and its voltage can be tuned smoothly with the magnetic field in a limited range. Numerical simulations and radiation emission measurements[2.44] recently explained the DLS as intrinsically chaotic dynamic fluxon states.

### 2.3.4. Flux-flow regime (FF)

For high fields the voltage is determined by the unidirectional fluxon motion. When the fluxons reach the Swihart velocity, they generate the flux-flow voltage[2.45]

$$V_{FF} = dH\bar{c} \ . \qquad \{2.38\}$$

This regime is called the flux-flow regime (FF) and is interesting for applications in **F**lux-**F**low **O**scillators (FFO). The frequency of the emitted radiation can be tuned by the external magnetic field. Long Josephson junctions working in this regime have been already successfully implemented as local oscillators for integrated receivers[2.46,47].

ZFSs, FSs and the FF regime are displayed in the experimental *I-V* characteristic. *Fig.2.10(a)* shows the *I-V* curves for zero magnetic field, obtained by choosing different current offsets on the McCumber branch. *Fig.2.10(b)* shows the traces of *I-V* curves obtained by continuously varying the external magnetic field.

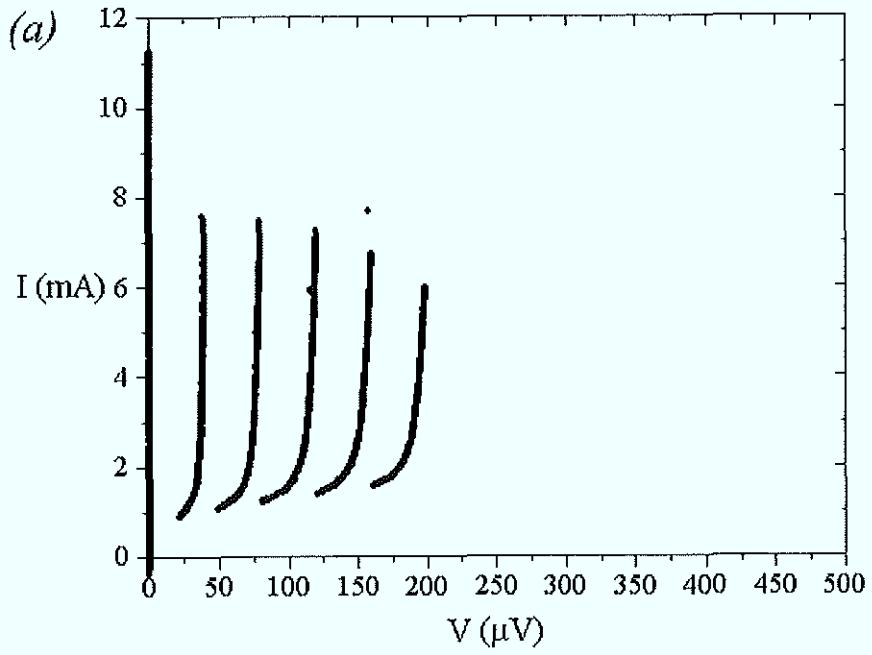


*Fig.2.10(a): I-V characteristics of an overlap junction without external magnetic field [sample: window1.1.4/2.2, (350×20μm²)]*

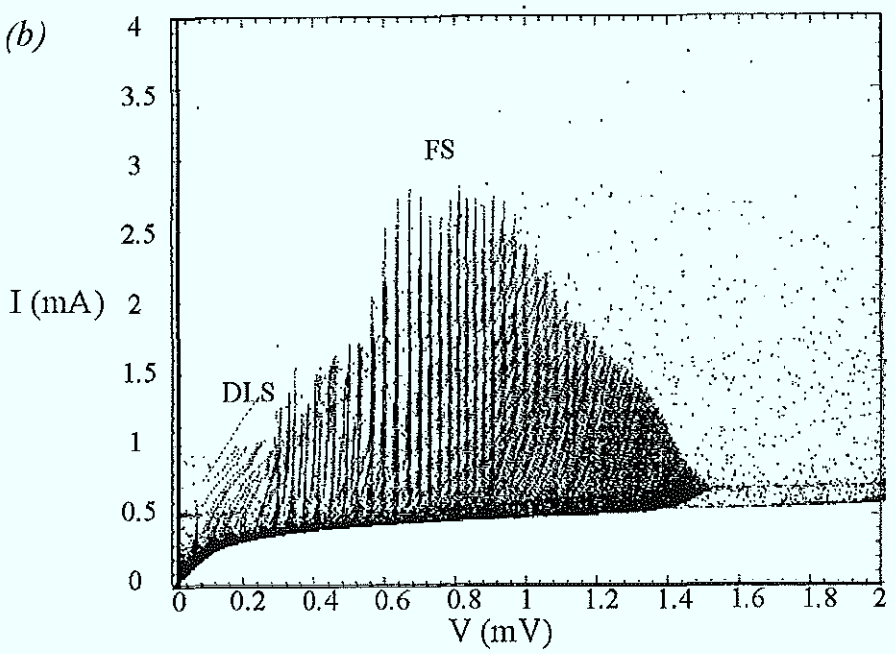


*Fig.2.10(b): I-V characteristics of an overlap junction with continuously sweeped external magnetic field; [sample: window1.1.6/3.3, (200×10μm²)]*

### 2.4. Modulation of $I_c$ by an external magnetic field

Another effect of the external magnetic field is the modulation of the maximum Cooper pair tunneling current. The external field evokes a screening Cooper pair current, as demonstrated in *Fig.2.11(a)*. Across the junction, the critical current density is much smaller than inside the electrodes and so the dissipation free current is protruding into the junction. Mathematically, the momentum of a Cooper pair is calculated as

$$\hbar \nabla f = 2m_e \vec{v}_s + \frac{2e}{c}\vec{A} \,, \qquad \{2.39\}$$

where $m_e$ is the electron mass, $\vec{v}_s$ is the pair velocity and $\vec{A}$ is the vector potential of the external field.
Integrating along the path *(a)→(b)→(c)→(d)→(a)* (*Fig.2.11(b)*), for a one-dimensional Josephson junction one ends up with the Ferrell-Prange equation[2.43]

$$\frac{\partial^2 \phi}{\partial x^2} = \frac{1}{\lambda_J^2}\sin\phi \,. \qquad \{2.40\}$$

It represents a time independent version of the unperturbed sine-Gordon equation which has the soliton solution in the form $\phi_0(x) = 4\arctan\left[\exp\left(x/\lambda_J\right)\right]$. For weak fields the Gibbs free energy of a fluxon is given by

$$G_0 = W_0 - \frac{\Phi_0 H_0}{4\pi} \,, \qquad \{2.41\}$$

with

$$W_0 = \frac{4\Phi_0 j_c}{\pi c}\lambda_J \,. \qquad \{2.42\}$$

The state of $G_0 > 0$ is energetically unfavorable, and the energy $G_0$ remains negative for $H < H_0$, where

$$H_0 = \frac{2\Phi_0}{\pi^2 \lambda_J d'} \,. \qquad \{2.43\}$$

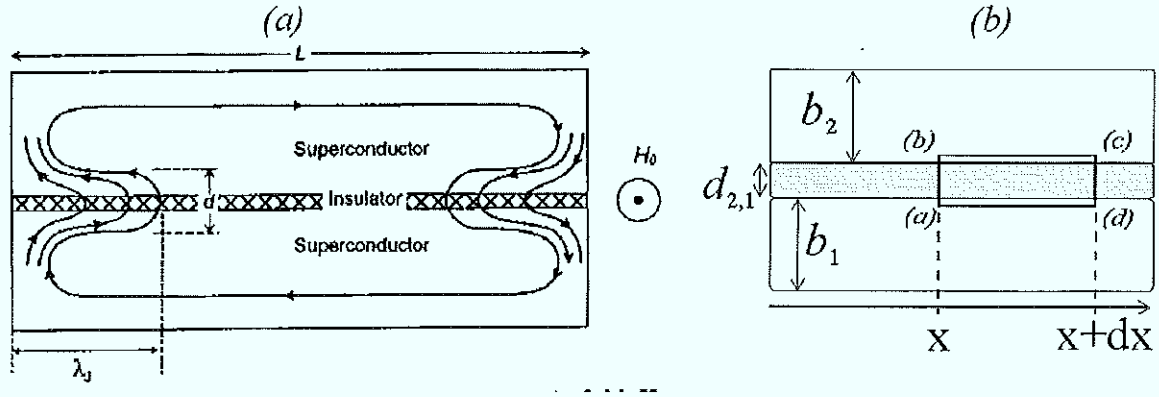


*Fig.2.11*[2.48]*: (a) Screening current for an external magnetic field and (b) integration path*

$H_0$ is usually noted as thermodynamic critical field of a long Josephson junction. However a fluxon can penetrate through the junction boundary only at[1,2,3]

$$H \geq H_{c1} = \frac{\Phi_0}{\pi \lambda_J d} > H_0 \,. \qquad \{2.44\}$$

### 2.4.1. Small Josephson junctions

First we will discuss small Josephson junctions, where the junction length $L$ is much smaller than the Josephson penetration depth $\lambda_J$ ($L << \lambda_J$). The external field and phase difference are related as given by equation {2.11}. Assuming $H=H_y=const.$ in the interior of the junction, integrating {2.11}, and inserting the result in the dc Josephson equation {2.2} one obtains

$$j = j_c \sin\left(\phi(0) + \frac{2ed\mu_0}{\hbar} H_y x\right). \qquad \{2.45\}$$

The result is a spatial modulation of the Josephson current density by the external field. Integration of {2.45} along the junction[1,13] gives the total maximum current

$$I_c(\zeta) = I_c(0)\left|\frac{\sin\left(\pi \zeta/\Phi_0\right)}{\pi \zeta/\Phi_0}\right|, \qquad \{2.46\}$$

where $\zeta = H_y L d$ represents the total magnetic flux generated by the external field. For external flux $\zeta$ equal to an integer number of $\Phi_0$ the resulting critical current is zero. A sequence of selected field values is shown in *Fig.2.12*. The vertical arrows indicate the critical current density.

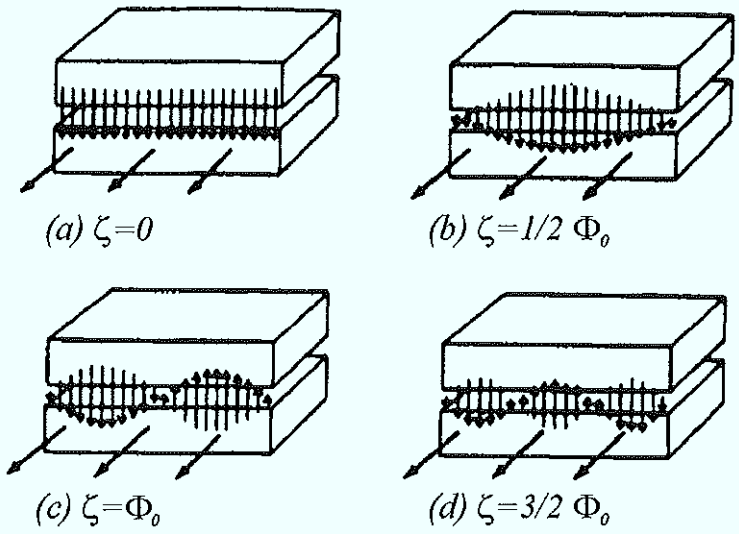


*Fig.2.12[1,3]: Modulation of $j_c$ for different $\zeta$*

Assuming an external magnetic flux of $\zeta={}^{1}/_{2}\Phi_0$ and fixing the phase difference $\phi(0)=0$, the resulting $j$ at the edges of the junction is zero, while at the junction center $j=j_c$. The resulting total current is reduced. For external flux of $\zeta=1\Phi_0$ the phase modulation along the junction is changing over $2\pi$ and the resulting critical current is zero. This situation is repeated for $\zeta = n\Phi_0$, where $n$ is an integer. For intermediate flux values non vanishing total $j_c$ appears with maxima at $\zeta={}^{n}/_{2}\Phi_0$. These maxima decrease in amplitude with increasing $n$. *Fig.2.13* shows a typical $I_c(H)$ pattern measured in experiment.

Interesting is the analogy of this behavior to the diffraction of light at a single small slit. Therefore in small junctions it is common to call $I_c(H)$ as Fraunhofer pattern.

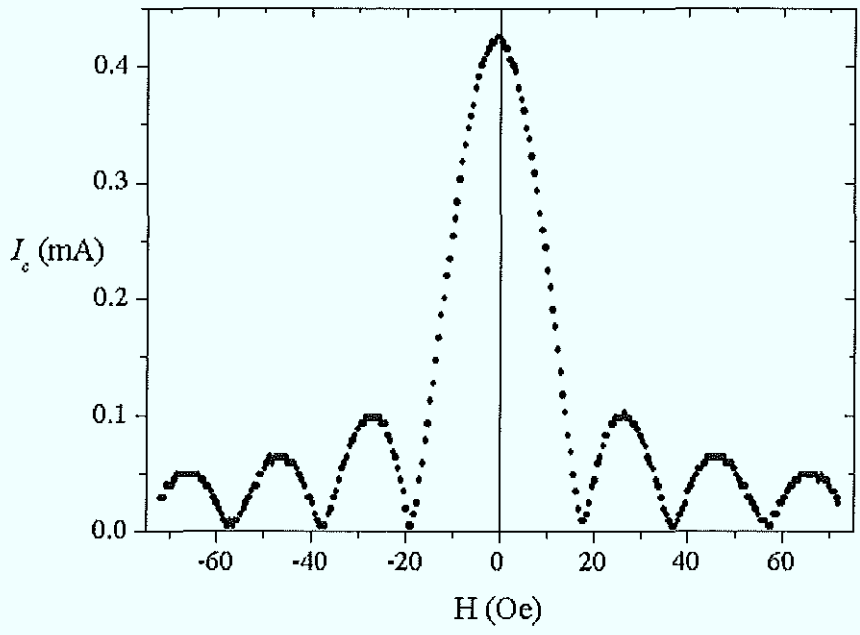


*Fig.2.13: $I_c(H)$ pattern for a small junction (10x10μm²) [sample: window1.1.6/3.8]*

### 2.4.2. Long Josephson junctions

One-dimensional long Josephson junctions have a length of $L/\lambda_J>>1$ and, quiet often, an inhomogeneous current density along the junction. As shown in *Fig.2.7*, the two typical geometries are inline and overlap junctions. While for inline geometry the real current flow is mainly concentrated at the ends, for the overlap geometry it is more or less homogeneous. The current flow near the ends is assumed to be higher due to self-field effects[1,12]. Due to the preparation procedure the top and bottom electrodes form the so called idle part, representing

an SIS sandwich, surrounding the junction. Former investigations about the influence of this idle region[2.49,50] on junction properties have shown an increase of the inline character for larger idle. Due to the possible nucleation of Josephson vortices in long junctions, the flux configuration is not strictly determined by the external field as for small junctions. The fluxons can move inside the junction and, as a result, different system states can be observed for the same external field value. The system state depends on the antecedent of the measured value. *Fig.2.14* shows a typical $I_c(H)$ pattern measured for a long overlap junction.

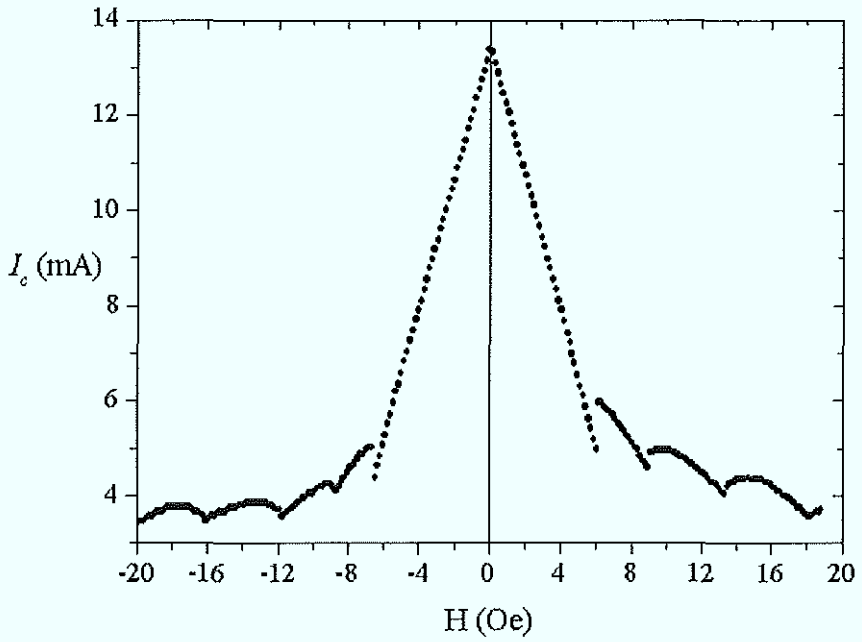


*Fig.2.14: $I_c(H)$ pattern for a long overlap junction (350×20μm²) [sample: window1.1.6/2.2]*

### 2.4.3. Annular junctions

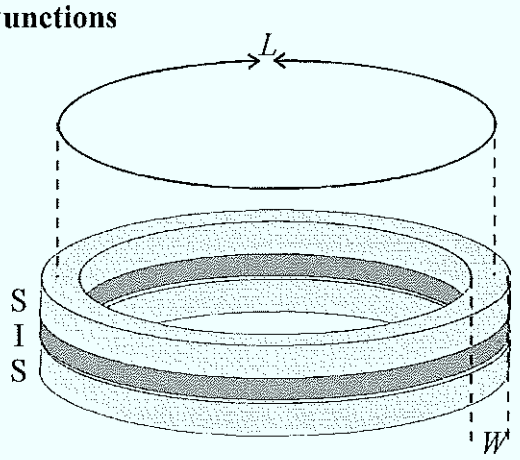


*Fig.2.15: Annular junction geometry*

The annular junction is a long Josephson junction closed in the form of a ring, as shown in *Fig.2.15*. In this geometry fluxon reflections at the boundaries do not occur. Annular junctions account for periodic boundary conditions.
The model is again given by equation {2.27} with the boundary conditions

$$\phi(0,t) = \phi(L,t) - 2\pi N_f \text{ and } \phi_x(0,t) = \phi_x(L,t)\,, \qquad \{2.47\}$$

where $N_f$ gives the number of fluxons trapped inside the junction. The external magnetic field can be included as a spatially-dependent current term of the sine-Gordon equation, as proposed by Grønbech-Jensen et al.[2.51]:

$$\phi_{x'x'} - \phi_{t't'} = \sin(\phi) + \alpha\phi_{t'} + \gamma - h\sin\left(\frac{2\pi x}{L}\right). \qquad \{2.48\}$$

Here $h \propto H_{ext}$ is normalized by some sample specific factor[2.51,52].
Annular junctions show fluxon steps that correspond to the nucleation of soliton-antisoliton pairs. The resulting voltage is twice larger than the corresponding step voltage of a single moving fluxon. *Fig.2.16* shows the fluxon steps and the critical current modulation for a typical annular junction.

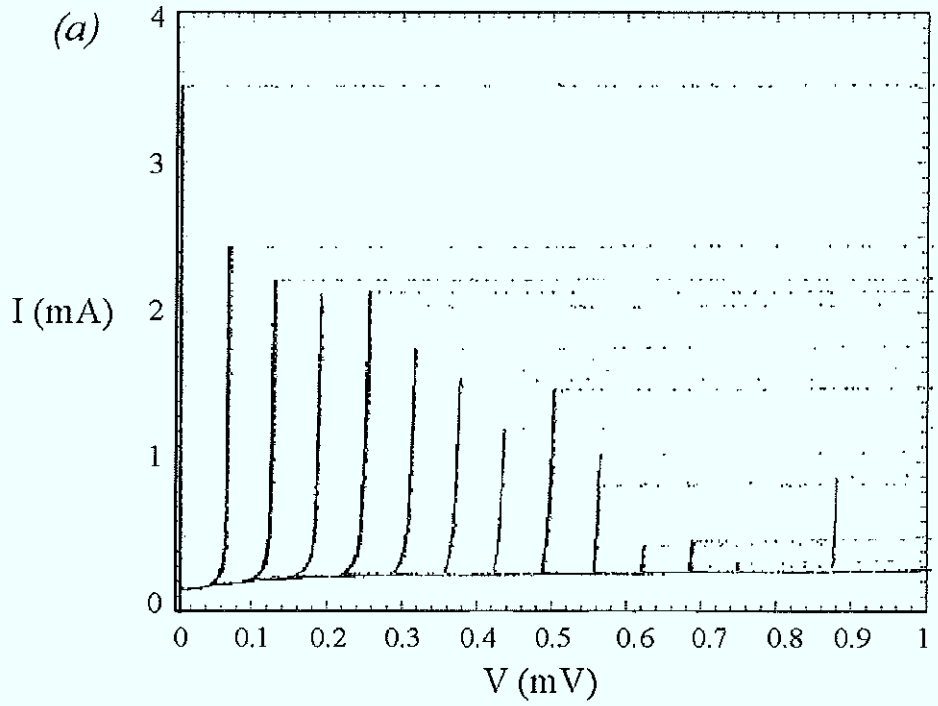


*Fig.2.16(a): fluxon-antifluxon steps for an annular junction (W=10μm; diameter D=185μm) [sample: annstac1.1.17/8.3]*

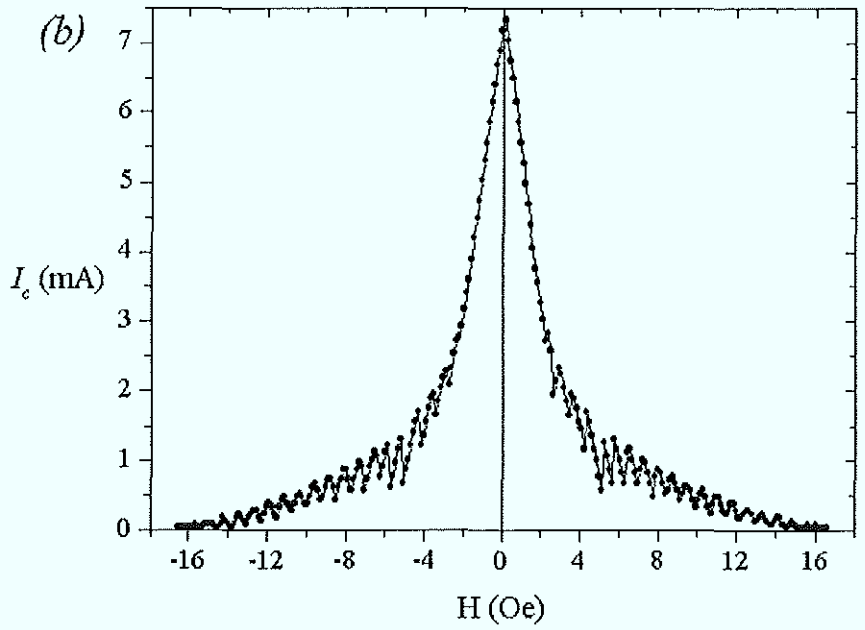


*Fig.2.16(b): $I_c(H)$ pattern with no trapped fluxons for an annular junction (W=10μm; diameter D=185μm) [sample: annstac1.1.17/8.3]*

## 2.5 A single trapped fluxon in a Josephson junction ring

We performed measurements[2.53] of individual fluxons trapped in annular junctions. Here the number of fluxons is conserved due to the magnetic flux quantization in a superconducting ring, and the bias current acts as a driving force for the fluxon, which circulates in one direction.

The introduced sine-Gordon model {2.48}, and the boundary conditions {2.47}, include the field-induced potential for the round motion of a fluxon. An experimental *I-V* characteristics (*Fig.2.17(a)*) shows the fluxon steps for different number of trapped fluxons, measured during different cooling cycles. The magnetic flux in the ring was trapped applying a small dc bias current while cooling the sample below the critical temperature of niobium.

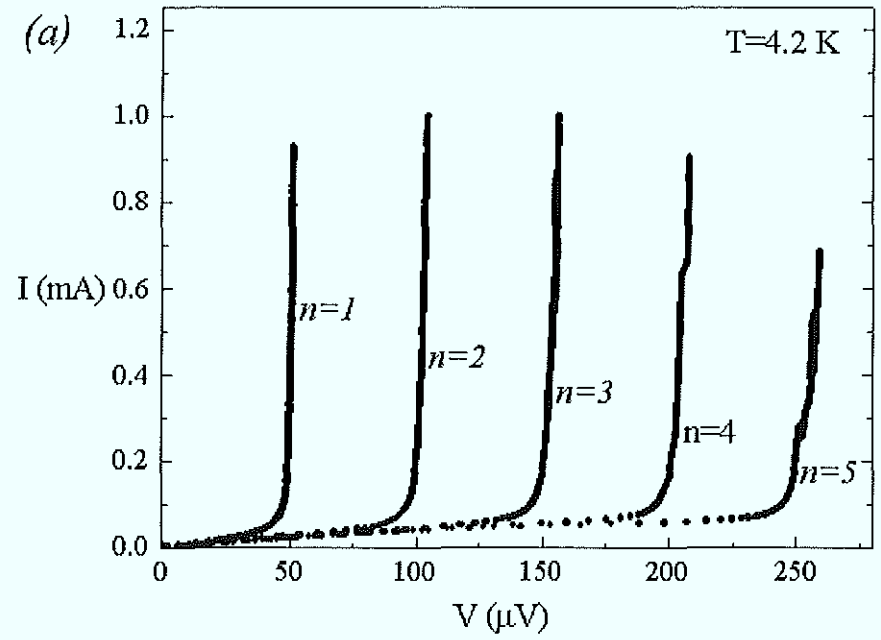


*Fig.2.17(a) Fluxon steps for n fluxons in a ring,*
*(W=10μm; D=142μm) [sample: annstac1.1.6/2.3]*[2.53]

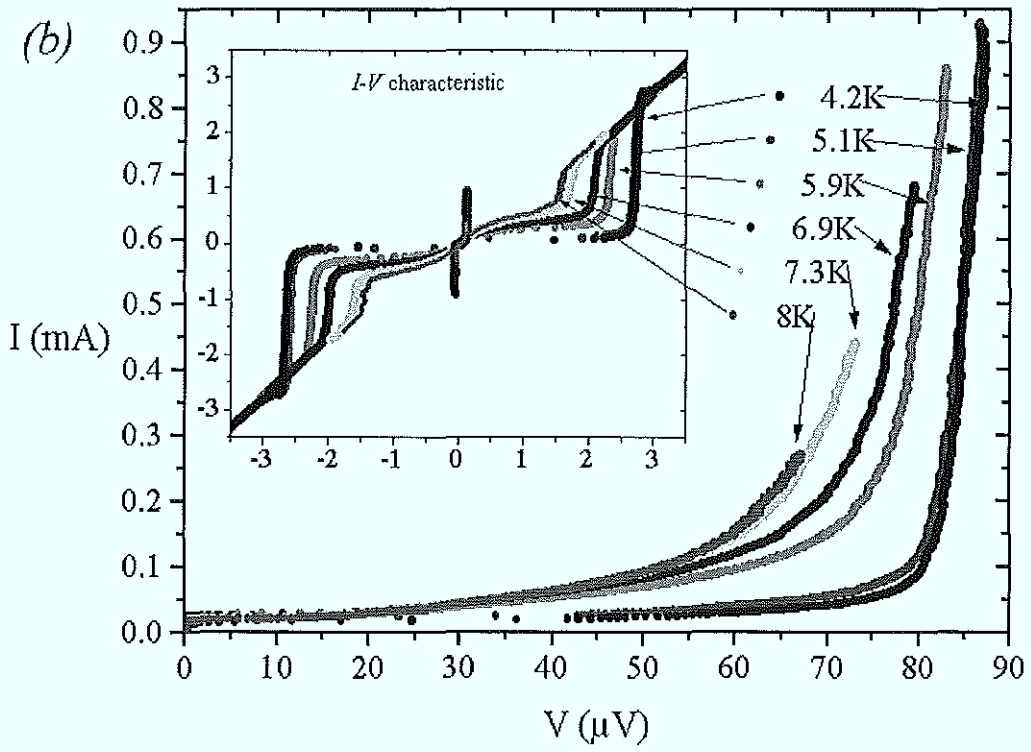


*Fig.2.17(b): Temperature dependence for the single-fluxon step (W=10μm; D=142μm)*
*[sample: annstac1.1.12/8.2]*

We measured the dc voltage which is proportional to the average velocity of the fluxon, and the steepness of the measured fluxon step is determined by the losses which occur during the fluxon motion. These losses are increasing for higher temperatures, which causes the low-bias velocity decrease. The asymptotic voltage of the step is decreasing with increasing temperature due to the increasing London penetration depth $\lambda_L$ at high temperatures, as $\bar{c} \propto \lambda_L^{-1/2}$. The relation between the normalized fluxon velocity $u$ and voltage $V$ is

$$u = \frac{VL}{\Phi_0 \bar{c}} . \qquad \{2.49\}$$

When the external magnetic field is applied, the fluxon as a particle can be compared with a driven and damped pendulum[2.54]. *Fig.2.18* shows the analog between these two systems. The ratio between the critical current $I_c$ without trapped fluxon, and the pinning current $I_{cr}$ of a fluxon step in zero external field is the measure for the homogeneity of the junction. Our samples typically show a factor of *300* which reflects their high homogeneity.

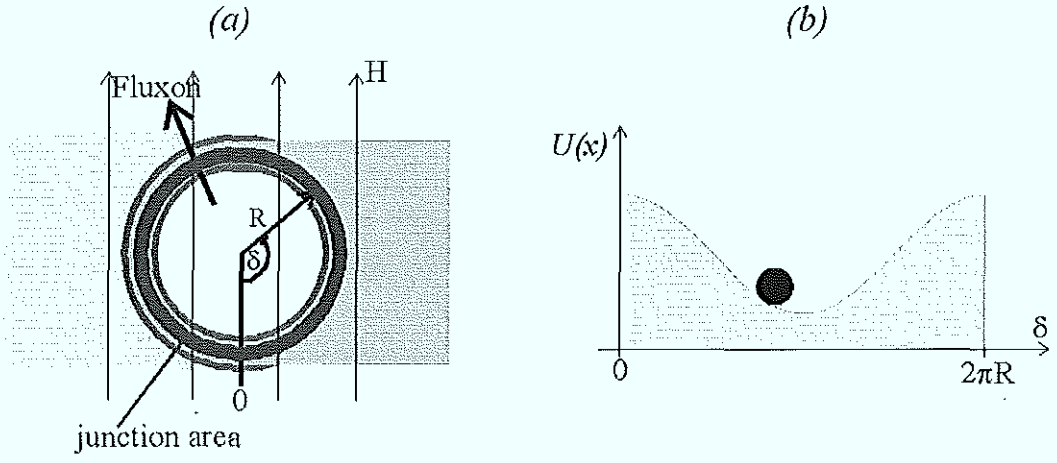


*Fig.2.18: (a) A fluxon in an annular junction, and (b) a particle in a cos-like potential*

The magnetic field induces a cos-like potential for the fluxon trapped in the junction, and the *I-V* characteristic can be explained by fluxon pinning and trapping by the field induced potential (*Fig.2.19*). The potential minimum is located in the region of the ring where the fluxon is directed along the field, as shown in *Fig.2.18(a)*.

A bias current tilts the potential shown in *Fig.2.18(b)*. At small bias current the soliton is trapped and the driving force has to overcome the pinning force. This pinning current of the fluxon is noted as $I_{cr}$. Once moving, the fluxon generates dc voltage. It shows the inertial behavior and, while decreasing the bias current $I$, its underdamped motion continues. Finally the fluxon is trapped again by the pinning potential at $I_{tr}$ which is called threshold current. The

hysteresis of this system, determined by the effective Stewart-McCumber parameter[2.54,55], depends on the external magnetic field $H$ and the length of the junction $L$. The pinning force is given by the amplitude of the external magnetic field $H$.

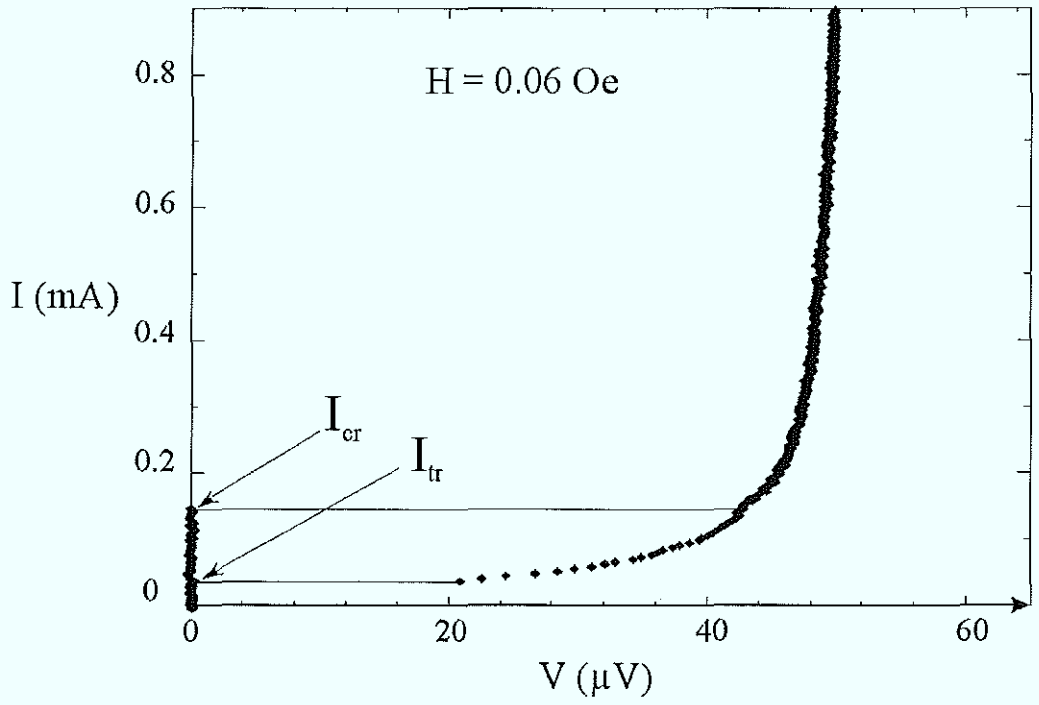


*Fig.2.19[2.53]: Hysteresis of the single fluxon step at $H_{ext}$=0.06 Oe (W=10μm; D=142μm), [sample: annstac1.1.6/2.3]*

Using a simple approach for the non-relativistic limit ($u^2 \ll 1$) the equation of motion for the fluxon as a particle is[2.54]

$$\xi_{tt} + \alpha\xi_t + \frac{\pi}{4}\gamma = \frac{\pi}{4}\gamma_{cr}\sin\left(\frac{2\pi\xi}{L}\right), \qquad \{2.50\}$$

where $\xi$ stands for the fluxon coordinate. Here $\gamma_{cr} = \frac{1}{\cosh\left(\frac{\pi^2}{l}\right)}$. The analog of the McCumber parameter for such a system is[2.55; 2.17] $\beta_c' = \frac{\pi^2 h}{2L\alpha^2}\frac{1}{\cosh\left(\frac{\pi^2}{L}\right)}$. $\qquad \{2.51\}$

For a given $\alpha$, the parameter $\beta_c'$ is proportional to $h$ and for $\beta_c > 1$ hysteresis should appear. Calculating the critical trajectory for the particle, $\gamma_{th}$ and $\gamma_{cr}$ can be calculated analytically. The final expression for the critical[2.54] and the threshold current[2.56] are

$$\gamma_{cr} = h\frac{1}{\cosh\left(\frac{\pi^2}{L}\right)}, \quad \text{and} \quad \gamma_{tr} = \frac{4\alpha}{\pi^2}(2+\theta)\left(\arcsin\sqrt{\frac{\theta}{2+\theta}} + \frac{\sqrt{2\theta}}{2+\theta}\right), \qquad \{2.52\}$$

with $\theta = \gamma_{cr}\frac{L}{4}$. The very impressive agreement between model and measurements is shown in *Fig.2.20*[2.56,57].

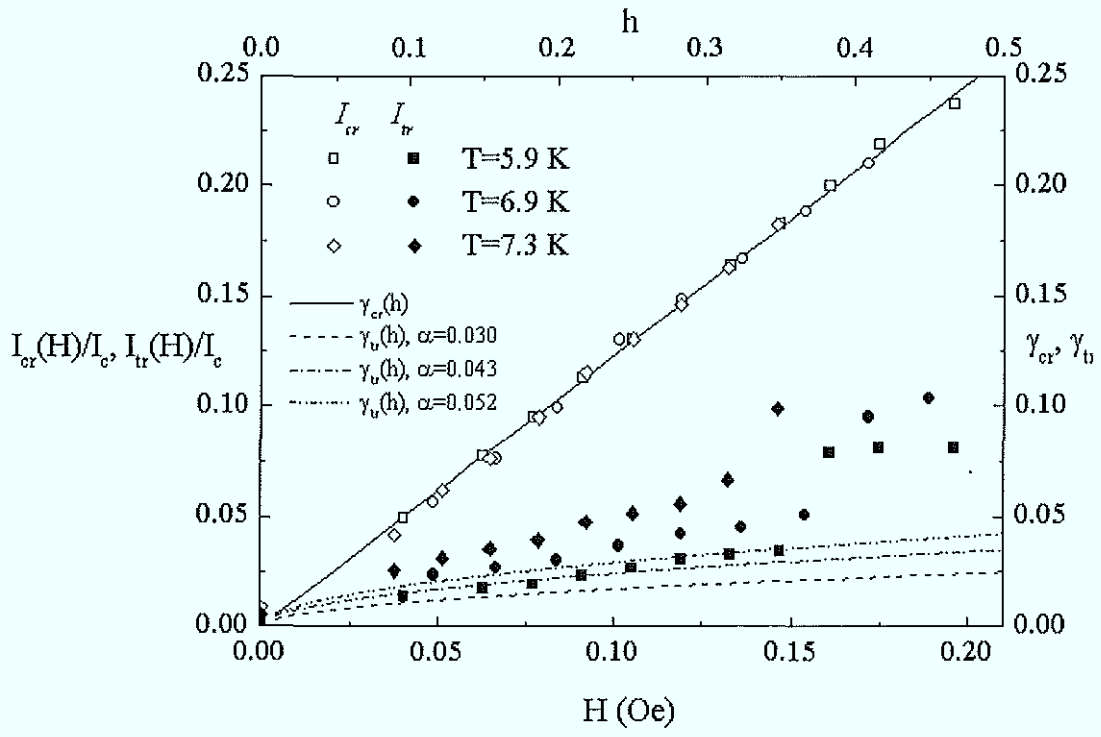


*Fig.2.20*[2.53]*: Measured and calculated values for $I_{cr}$ and $I_{tr}$ ($W=10\mu m$; $D=142\mu m$), [sample: annstac1.1.6/2.3]*

The trapping current depends on the losses experienced by the fluxon. At different temperatures, we determined $\alpha$ and $\beta$ by fitting the *I-V* curve with the standard procedure for the $V^{-2}$ versus $I^{-2}$ diagram[2.58]. This approach relies on the soliton force-velocity relation[2.27]

$$\frac{1}{\gamma^2} = \left(\frac{\pi}{4\alpha}\right)^2\left(\frac{1}{u^2} - 1\right)\left(1 + \frac{\beta}{3\alpha\left(1-u^2\right)}\right)^2. \qquad \{2.53\}$$

As discussed above, the $\beta$ loss term is just relevant for very low temperatures and high soliton velocities. At low velocities, it can be approximated by an effective $\alpha_{eff} \approx \alpha + \beta/3$. The obtained effective values are: $\alpha_{eff}(T=5.9K) \approx 0.03$; $\alpha_{eff}(T=6.9K) \approx 0.043$; and $\alpha_{eff}(T=7.3K) \approx 0.052$. We found an increasing discrepancy between model and experiment at higher temperatures. This

can be explained by thermal noise that is not included in the used models. Estimating additional losses by *30%* higher $\alpha$ values improves the agreement. Also, we observed abrupt deviation of measurements from analytical prediction for high magnetic fields. Here the treatment of a fluxon as a quasi-particle that moves in the external potential in the presence of dissipation is no more correct. Now the fluxon interacts strongly with the field induced potential and spends a large part of its energy in the excitation of plasma waves.
The fluxon is predicted to emit small amplitude plasma waves with a wave number $k$, the frequency $\omega = \sqrt{1+k^2}$ depends on the spatial period $l$ and the fluxon velocity $u$[2.59]. This radiation should lead to a series of resonances for $\omega = 2\pi n v / l$, with integer number $n$. In the *I-V* characteristic these resonances are predicted to appear as voltage steps [2.54] at the fluxon velocities

$$u_n = \sqrt{\left(1-\frac{L}{na}\right)^2 + \left(\frac{L}{2\pi n}\right)^2}\,, \qquad \{2.54\}$$

with $n$ being a positive integer. According to reference [2.27] the amplitude of the emitted waves has its maximum near the radiation threshold $u_{thr} = \left(1+(2\pi/a)^2\right)^{-1/2}$. In our system

$$L = l = a\,. \qquad \{2.55\}$$

A comparison of experimental and numerical data is shown in *Fig.2.21.*

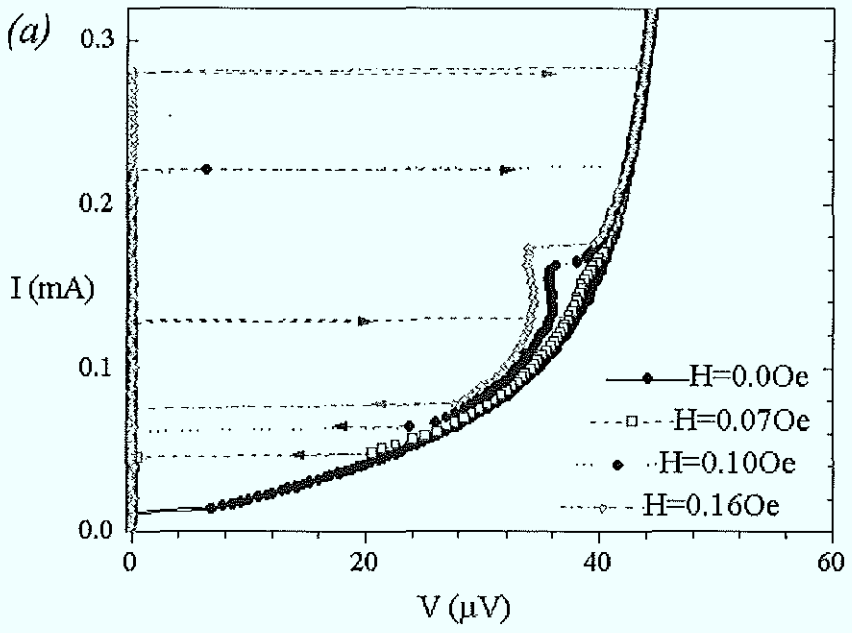


*Fig.2.21(a)*[2.53]*: Resonant fine structure on the fluxon step*[2.60]*; experiment [sample: annstac1.1.6/2.3]*

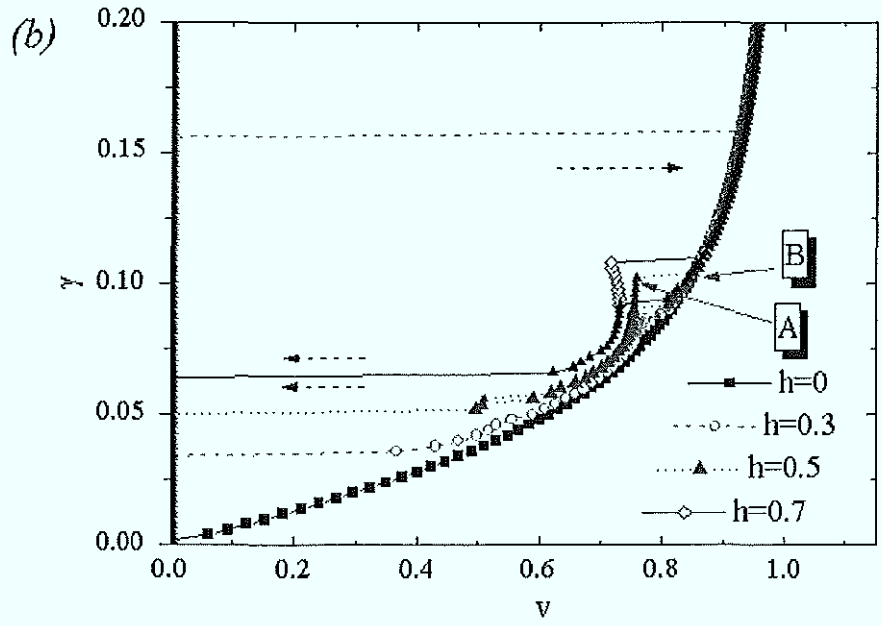


*Fig.2.21(b)[2.53]: Resonant fine structure on the fluxon step[2.60]; numerical simulation*

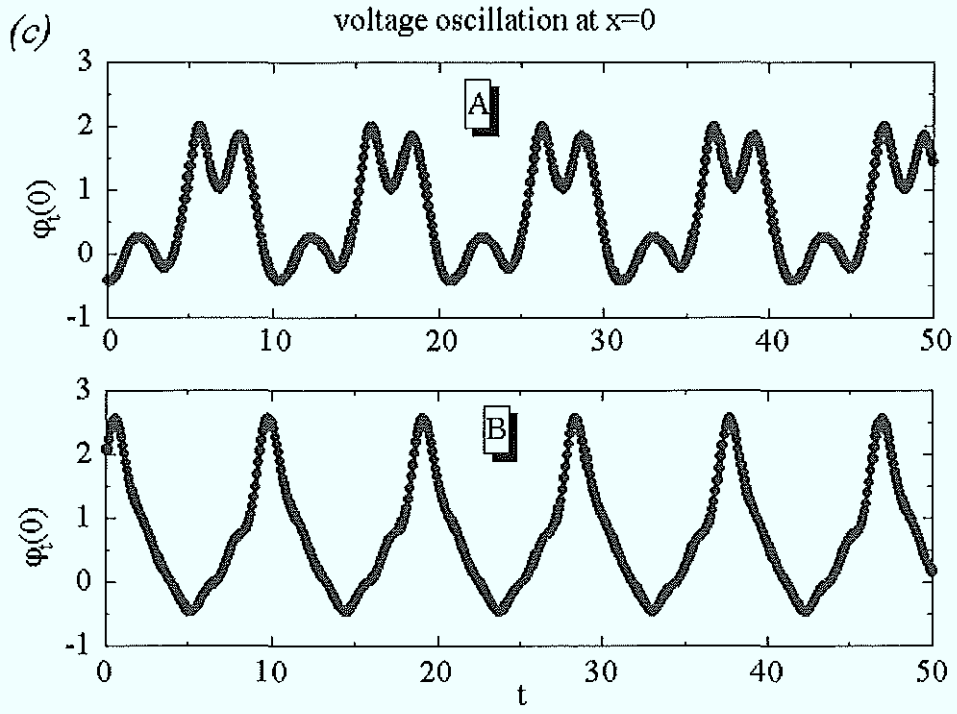


*Fig.2.21(c)[2.53]: Resonant fine structure on the fluxon step[2.60]; voltage oscillations at x=0 calculated analytically*

It also shows the ac voltage oscillations at $x=0$ that cause the additional resonant voltage step at fluxon velocity given by {2.54}.

It is possible to observe this resonance in another way. We have fixed the bias current at different values on the fluxon step and measured the voltage as a function of the external field. These measurements display the fine structure resonance in the lower bias range. In *Fig.2.22* are shown the results for two samples with different diameters. Both graphs can be subdivided in three different regions of bias current. For low bias current the external field slows down the fluxon velocity. At a certain point the field is strong enough to trap the fluxon and the voltage jumps to zero. In the intermediate bias current range [*40-60*μA in *Fig.2.22(a)* and *35-60*μA in *Fig.2.22(b)*], the voltage jumps between two values. For the smaller ring of *90*μm in diameter *(a)*, the distance between these two states is *20*μV. The similar behavior is observed for the junction of *185*μm in diameter *(b)*. Here the voltage jump is smaller (*5*μV) due to the increased length of the ring in agreement with {2.54}.

For high bias current the fluxon motion is deeply in the relativistic regime and a slight increase of the fluxon velocity is observed for higher fields. Here trapping does not occur because the junction switches into a rotating (high voltage) state.

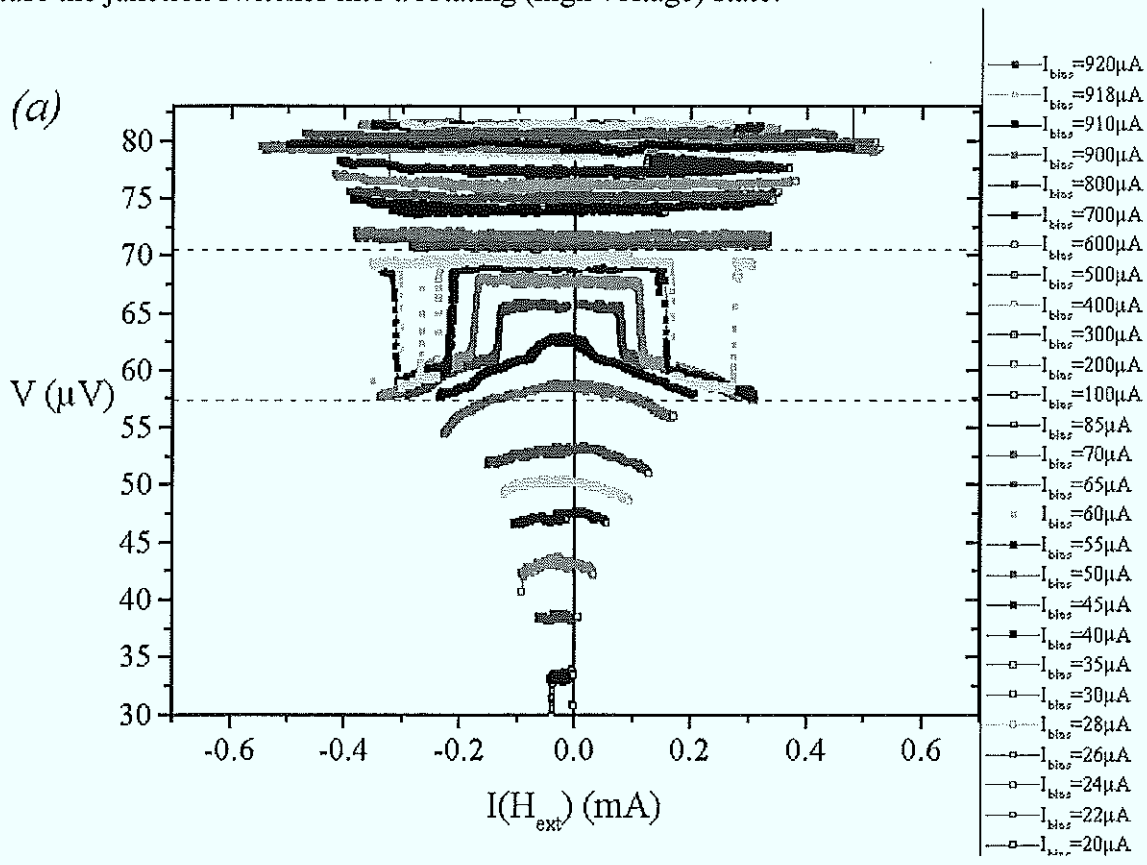


*Fig.2.22(a): Tuning of the soliton voltage by external field at fixed bias current junction diameter 90*μm*; [sample: annstac1.1.12/8.2]*

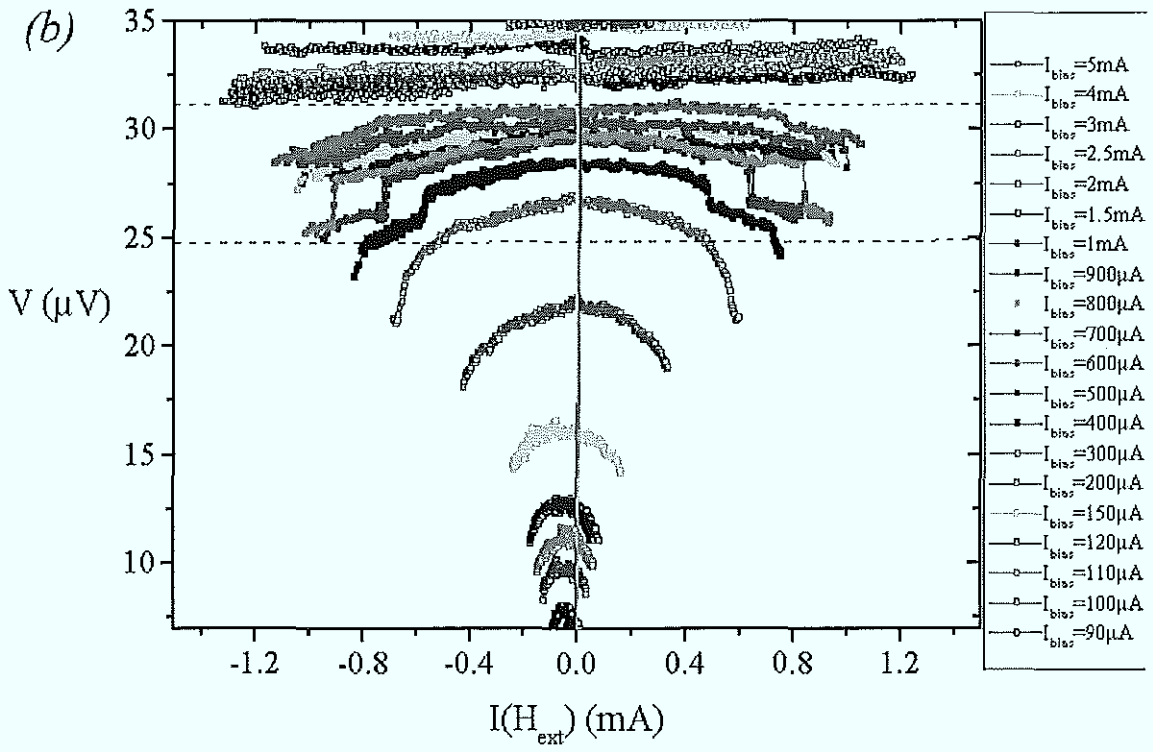


*Fig.2.22(b): Tuning of the soliton voltage by external field at fixed bias current junction diameter 185*μm*; [sample: annstac1.1.12/8.3]*

Equal measurements had been carried out by N. Martucciello et al.[2.61]. They observed a similar tuning of the fluxon velocity but no resonant state. The explanation are different junction length (very large), in this case $u_{\text{th}} \rightarrow 1$ in {2.54}, because other parameters were chosen similar to those described here.

## 2.6. Imaging of fluxons in annular junctions

Beside measuring *I-V* characteristics and $I_c(H)$ patterns, a spatially resolved imaging of the fluxons proved to be a powerful experimental method for investigations of their properties. The main method here is the **L**ow **T**emperature **S**canning **E**lectron **M**icroscopy (LTSEM)[2.62]. Using a high energy electron beam (carrying a negligible current) as active[2.63] or passive[2.64,65] probe, a few microns large area is heated locally. As active probe the beam can be used to change the fluxon state of the junction, for example trapping individual fluxons in annular junctions. Here the e-beam of high power destroys the former junction state. As

passive probe the low power e-beam is creating a small perturbation that is measured as a function of the beam coordinates. By LTSEM the fluxon's Lorentz contraction[2.26] was observed for the first time. In addition investigations had been carried out for various multi-soliton modes in long junctions[2.65,66,67,68] and complex patterns in two dimensional systems[2.69]. A detailed overview about the LTSEM techniques is given in reference[2.62]. Some of our annular junctions had been investigated[2.68,70]. The work contained trapping of fluxons in the ring and the study of their dynamics, dependent on an external magnetic field which produces the pinning potential for fluxons. It was possible to resolve collisions between moving and pinned fluxons. Examples are shown in *Fig.2.23* and *Fig.2.24.*

The bright areas in *Fig.2.23* indicate the collision sites between moving and trapped fluxons. In *(a)* one fluxon is moving and one is trapped, while *(b)* shows the situation with two trapped and two moving fluxons. Shown is the voltage image of the annular junction.

In *Fig2.24* the bright areas indicate a dc Josephson current flow from the bottom to the top electrode. In *(a)* the e-beam induced change of the maximum critical current is shown, while *(b)* shows the sketch of the measured pinned fluxon configuration. On the top there are three fluxons and on the bottom we can see two antifluxons. The inserted arrows show the fluxon and the circles indicate the Josephson current flow.

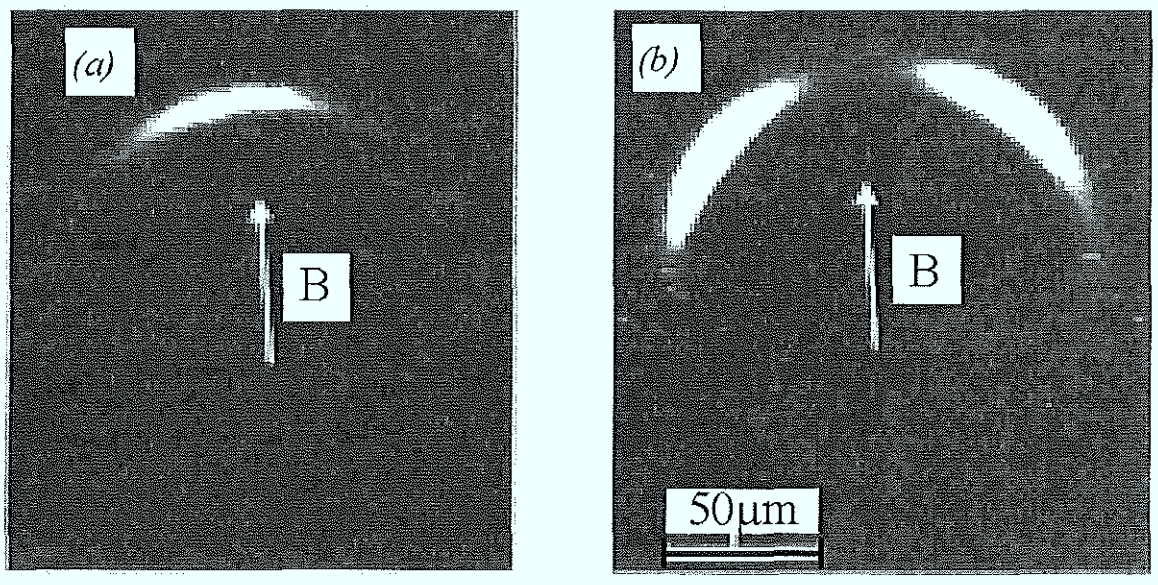


*Fig.2.23[2.70]: LTSEM voltage images of an annular junction; [sample: annstac1.1.2/3.3]*
*(a) two trapped fluxons and one of them is pinned B=0.05*mT*;*
*(b) four trapped fluxons and two of them are pinned, B=0.07*mT

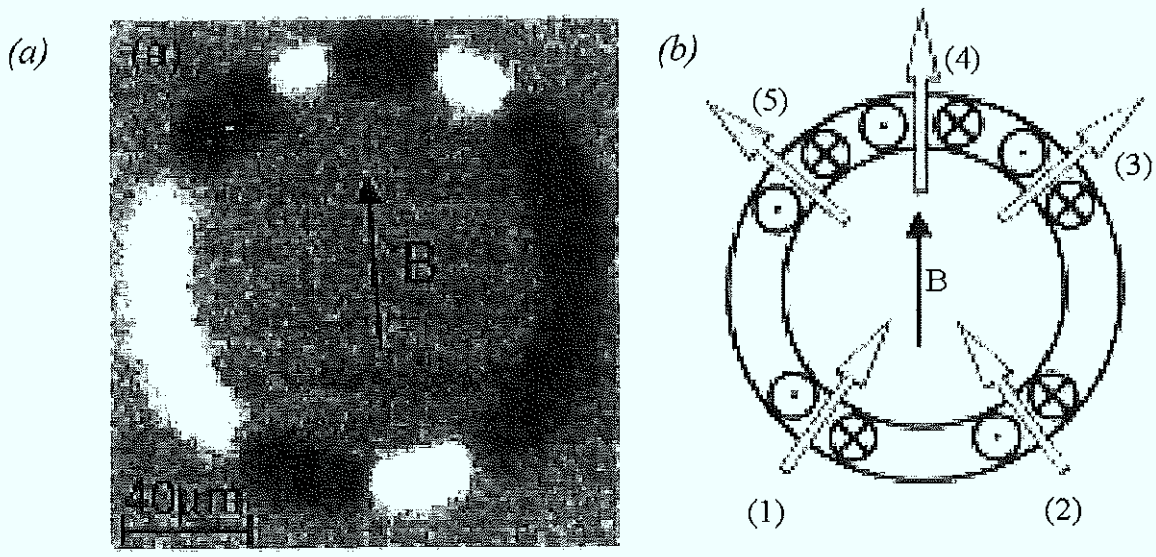


*Fig.2.24*[2.70]*: E-beam induced change of the maximum critical current of an annular junction*
*(a) measured image;(b) sketch of pinned fluxons B=0.19*mT
*[sample: annstac1.1.2/3.3]*

# 3. Sample Preparation

All samples prepared within this thesis are SIS-type Josephson-junctions. Niobium served here as superconductor and thermally oxidized aluminum served as barrier material[3.1]. Different modifications of the standard Selective-Niobium-Anodization-Process (**SNAP**)[3.2] had been developed. The insulation of the junctions is realized by anodic oxidation in combination with evaporated SiO. As substrates were used thermally oxidized silicon wafers with a diameter of *2* inch and a resulting oxide thickness of *1*µm. For the anodic oxidation process it is necessary to use substrates with resistance between *0.1-10*kOhm×cm or higher, but their crystal orientation is not crucial. Structure dimensions down to *2*µm were realized with standard photolithography tools. Sub-micron structures were defined with an electron beam writer.

An important aim of this work was the development of a reproducible technology for high quality stacked Josephson junctions with a minimized spread in parameters. Clean experiments required a spread of less than *5*%.. In spite that this request was a great challenge in the beginning of the project, it has been successfully achieved in the final stage of this work. Without being to modest, let us state that the achieved minimum parameter spread and the number of stacked SIS junctions (up to *28*) by now remain unrepeated anywhere in the world and are, in fact the present state of the art for this field.

## 3.1. Methods and Tools

### 3.1.1. Deposition system for the Nb-(Al/$AlO_x$-Nb)$_N$ multilayer

*Fig.3.1(a): Automatic multi-layer deposition machine*

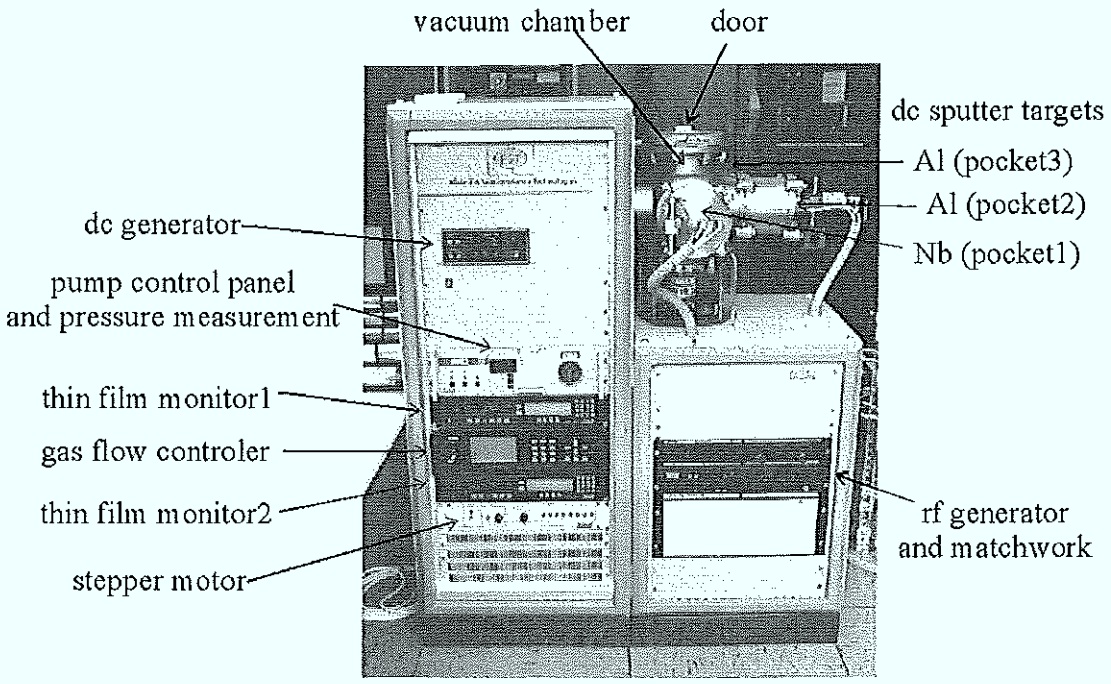


*Fig.3.1(b): Devices of the sputter machine*

To achieve a reproducible multi-layer deposition, an automatic system was designed and realized in collaboration with the company **P**lasma & **S**emiconductor **T**echnology (PST Filderstadt, Germany). As base a vacuum system from Pfeiffer (Aßlar, Germany) was chosen. A stainless steel vacuum chamber with *6* KF160 connectors is pumped with a two station pumping combination. The prepump is an oil filled rotary pump. A turbomolecular pump with high rotation frequency serves to achieve a background pressure of around $5\times10^{-7}$mbar. Three dc magnetrons with shutter are placed in the horizontal plane. The fourth connection serves as pump truncate. Different sample sizes can be fixed mechanically on a copper cube ($5.5\times5.5\times5.5$cm$^3$). This cube works also as temperature stabilizer due to its high thermal capacitance. The sample plane is oriented in parallel to the targets and turned to the different positions by a stepper motor. An rf generator is connected with the sample plate in order to use Ar backsputtering as cleaning process. Cold water (*10*°C) and warm water (*60*°C) can be chosen to control the temperature. A four channel gas flow controller regulates the pressure and gas content for Ar and $O_2$ . As processing unit, two thin film monitors are connected with all devices. The generators, gas controller, valves and pumps are driven using remote control. The analog and digital outputs and inputs are combined to stabilize the process using feed back signals. In addition, an RS232 port of each thin film monitor is connected to a personal computer (PC). Although the windows interface to be used is flawed, the PC can be used to measure the flow chart. An important factor is the reliability of the thin film monitors, which

do not malfunction is in the case of a breakdown of the PC program. The deposited niobium films have a critical temperature of about *8.8*K as shown in *Fig.3.2*. The resistance ratio $R(300K)/R(10K)$ is about *1.7*. This measured $T_c$ is close to the literature value of *9.2*K for niobium. The gap voltage of standard Nb/Al-$AlO_x$/Nb junctions is between *2.6* and *2.7*mV and was independent of the film thickness down to *30*nm. For thinner films it decreases strongly.

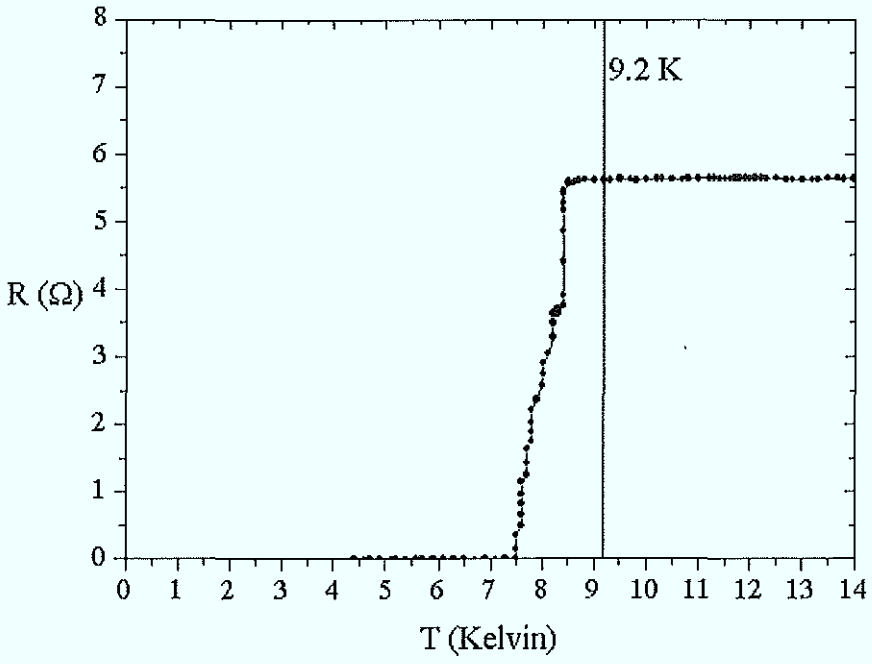


*Fig.3.2: Resistive transition curve of a sputtered 100*nm *thick Nb film*

### 3.1.2. Etching procedures

Two different etching processes were used: isotropic chemical wet etching in HF acid (*40*g $NH_4F$ + *60*ml $H_2O$ + *15*ml HF ⇒ *48*% HF) and anisotropic dry ion etching.

To create a ditch structure on the wafer, the samples with defined photoresist mask were placed into the acid inside an ultrasonic bath. Each *25*s the ultrasound was switched on for *5*s to bolster the homogeneous etching across the wafer. A typical etching rate was *67*nm/min at *20*°C. The photoresist was not attacked and the result is a photoresist overhang at the ditch edges as shown in *Fig.3.3*.

For a material deposition with lift-off, this feature was very useful and it demonstrated sufficient flat surface for the following processes.

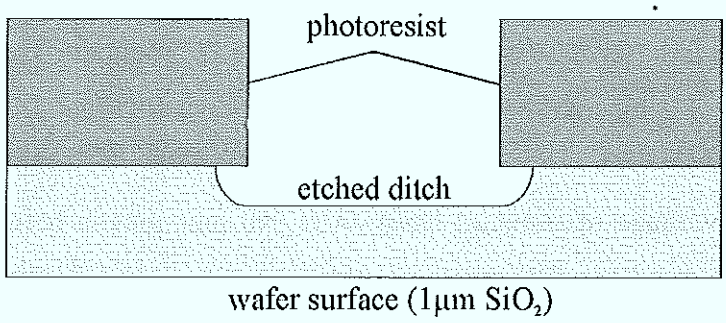


*Fig.3.3: Resulting overhang at the edges after wet etching of the oxidized wafer surface*

Two dry etching processes were applied. With an rf plasma etcher, as shown in *Fig.3.4*, the deposited Nb and Al films can be etched in non-isotropic etching. The sample plate was temperature controllable between *-10*°C to *40*°C. The Ar, $CF_4$, and $SF_6$ ions from the plasma gas were accelerated towards the sample surface by a dc potential. For Nb we used a **R**eactive **I**on **E**tching (RIE) with $SF_6$. The gas pressure was *0.02*mbar and an applied rf power of *50*Watt was matched by the electronics to a *-180*V dc potential. The resulting etching rate was *100*nm/min. Due to the low power of *50*Watt the thermal charge for this process was very moderate. A reactive ion etching for Al films was not possible in this machine. Therefore backsputtering with Ar ions was used. A pressure of *0.01*mbar with a gas mixture of Ar:$CF_4$ = *2:1* was fixed. The rf power of *250*Watt was matched to a dc potential of *-600*V. This process was rather slow and it took *2*min. to etch *6*nm Al/$AlO_x$, of which *2*nm were oxidized. As a consequence of the time and the high power, the sample is heated and for thicker Al films the etching was subdivided in two steps, introducing a cooling break.

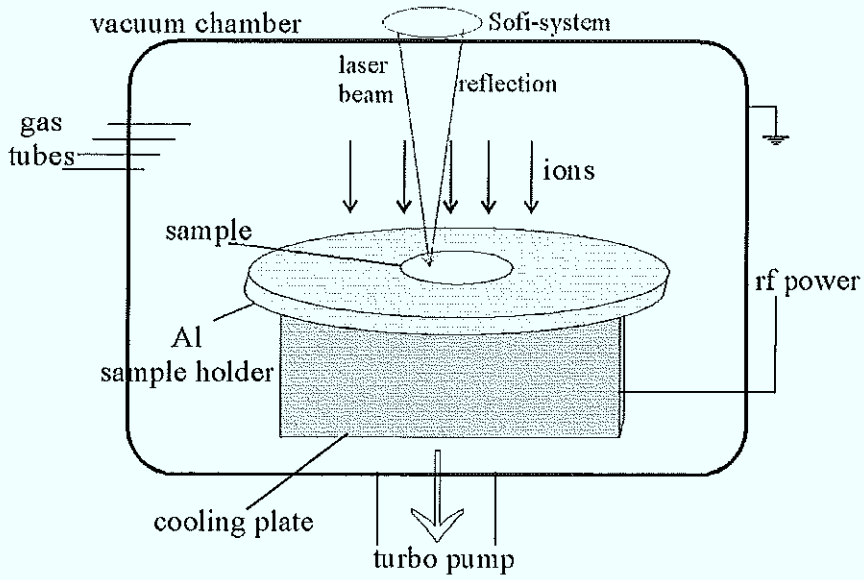


*Fig.3.4: Plasma etching system (RIE)*

The etching system was built as cluster tool and a robot is loading and unloading the samples. This process makes it difficult to achieve a good thermal contact between the sample and the cold plate, so the cooling periods have to be introduced adequately (after *1.5*min etching time, *3-4*min break).

For organic materials such as photoresist, PMMA or Polyimide, an $O_2$ plasma was used. Here the applied power differed between *200*Watt and *300*Watt. The resulting dc potentials were between *-500*V and *-580*V. Due to different resist post-bakeing procedures, the etching rate varied a lot. For all processes, a laser system (SOFI) offered the possibility to distinguish between surfaces with different reflection coefficients. For the organic materials the interference dependence on the film thickness was used. The typical etching flanks were vertical and perpendicular to the sample surface.

### 3.1.3. Insulation methods

As mentioned above a selective anodization process was used in this work[3.2]. Therefore, all areas that should be insulated, are electrically connected to the positive output of a dc current supply with a maximum current of *5*mA. The junction area and contact pads are covered by photoresist. The negative output of the power supply is connected to a gold covered plate. Sample and gold plate are immersed in an anodic solution, which consist of *78*g ammonium pentaborat, *560*ml ethylene glycol and *380*ml $H_2O$. Applying a dc current, the sample is anodized by implanting oxygen from the solution inside the Nb films. This process can be controlled by the increasing voltage between sample and gold plate. The needed current depends strongly on the oxidizing area and has to be adjusted during the process. To create a closed anodic oxide it is recommended to use voltage increase rates around *1*V/s. In this way a stable and pin-hole free oxidized surface is created. As a control characteristic the time derivative of the voltage is plotted simultaneously. In this characteristics the different anodization rates for Nb and Al films can be seen[3.3]. An example for an etched Al-$AlO_x$ barrier film with an underlying Nb film is shown in *Fig.3.5*

The maximum anodization voltage for a photoresist covered sample is *60*V. For higher voltages the resist burns and becomes unremovable. Our standard anodization voltage is *40-50*V, but tests show that already *15*V form a sufficient electrical insulator film. In the profile we can see the highest rate for the oxidized Al, after that the Al layer is anodized with rates around *4*(arb.units). A broad range of *3*V corresponds to the transition to the Nb layer. The

smooth slope can be explained by the surface roughness of the Nb layer which defines the measured average voltage. The anodization rate for Nb (*0.87*nm/V) and for Al (*0.9*nm/V) allow a fast estimation of the sputtered film thickness. The expansion coefficient for the anodization of Nb into $Nb_2O_5$ is about *2.3* and can be used to calculate the resulting insulator thickness. According to the maximum voltage limit, the reachable insulator thickness is limited to *100*nm.

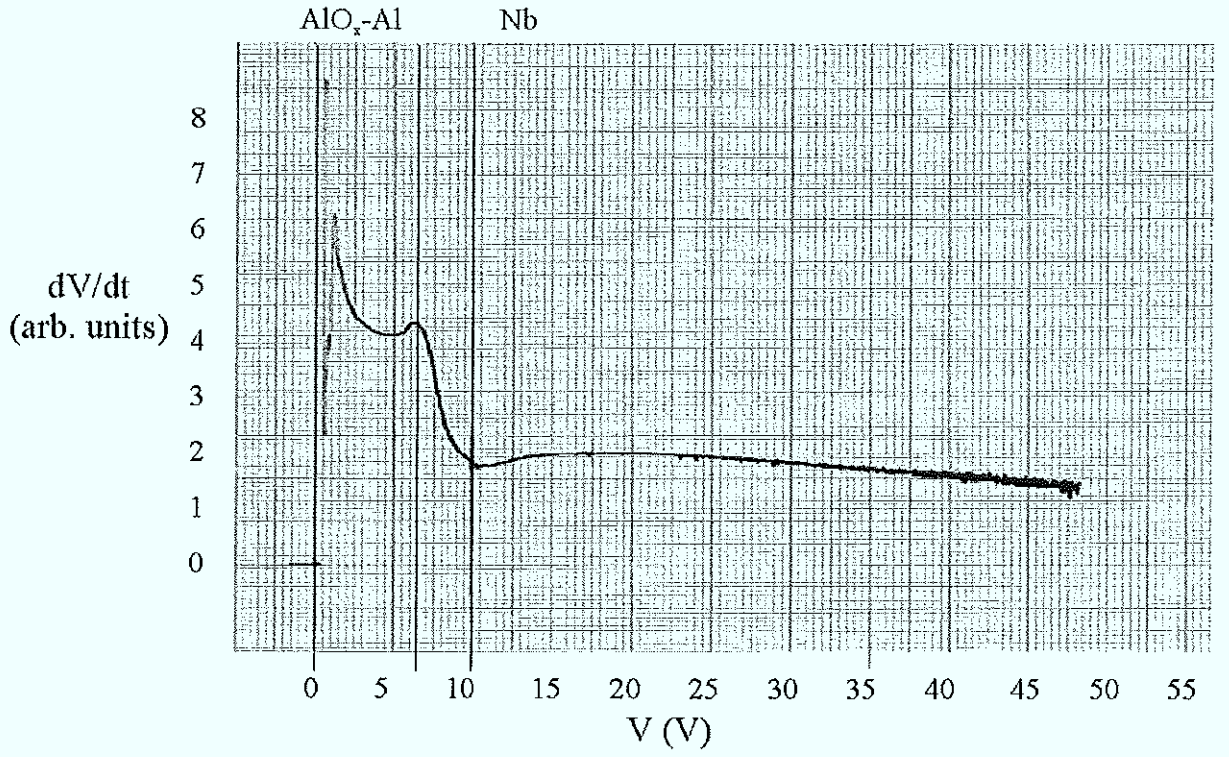


*Fig.3.5: Time derivative of the voltage for an $AlO_x$ -Al - Nb film (anodization profile)*

A second insulation process is the evaporation of an insulator, that is structured by lift-off. We use SiO, deposited by thermal evaporation. This machine has an oscillating crystal film growth control. To clean the sample surface an ion gun is integrated and Ar ions are used. For evaporation processes, the thickness of the insulator is not strongly limited and thicknesses of up to *1*µm are possible. The disadvantage of the method are growing pin holes that cause shorts. Our general approach was a combination of the anodization and evaporation methods. A pin-hole free anodic oxide prevents shorts and an additional evaporated SiO layer increases the insulator thickness.

### 3.1.4. Lithography

The photolithography process was executed in the clean room (classification *100*). A standard sample cleaning consists of three steps. First they were placed in acetone which is rinsed by water. Than the samples are dried by nitrogen gas flow and placed for about *30*s in isopropyl alcohol (propanol). After drying them again with nitrogen gas, the samples are placed on a hot plate at *90*°C to evaporate eventual rests of the liquids. A photoresist (AZ 5214E from Hoechst) is spinned on the sample with rotation speed between *3000* and *4000* revolutions per minute which defines a film thickness of about *1.2-1.4*µm. Than the sample is placed on the hot plate for *5* minutes at *90*°C. To create thicker resist films, this procedure was repeated once more or even twice more with decreasing the rotation velocity from *4000* ($1^{st}$ film) to *3000* ($2^{nd}$ film). The photoresist exposition (light of *365*nm wave length) is done in two different ways. For positive resist it consists of one exposure step of *4.5-5*s, using the structured mask, followed by the development in AZ 400K developer (AZ400K:$H_2O$ = *1:4* for around *45-55*s. The negative resist process requires a prebacking at *115*°C after the first exposing of *2.5*s using the structuring mask. A final exposure of *10*s without any structuring mask is added before developing for around *20-30*s. The main difference between positive and negative resists are the resulting edges. As shown in *Fig.3.6* the positive process produces ramptype flanks and, therefore, it was mainly used for a following etching process. The negative lithographic process produces overhanging flanks which are recommended for a following film deposition and lift-off[3,4]. For twice spinned resist films the structuring exposure times are also increased for a factor of *2* which sometimes results in lightly shorter development times.

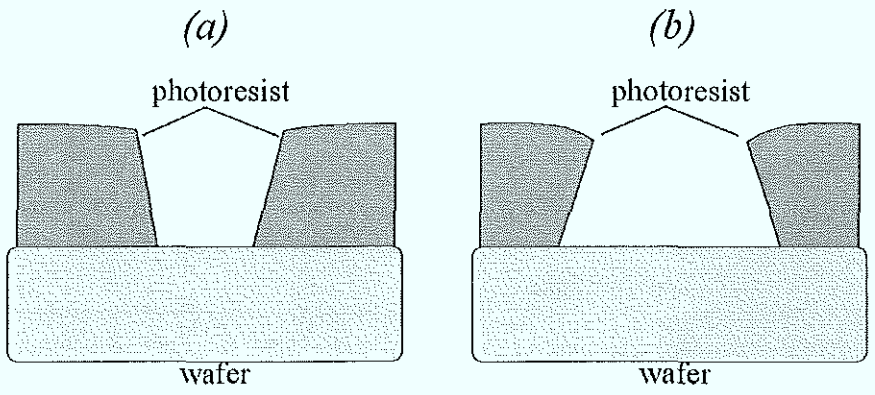


*Fig.3.6: Flanks of photoresist after (a) positive and (b) negative lithography*

Similar procedures were used for the electron beam lithography. Replacing the photoresist by PMMA and the light exposure by the e-beam, the positive process works as described above. For a better spatial resolution we used a thin PMMA film in the range of *200-400*nm. It is also possible to crosslink the PMMA with higher electron dose. This makes it unresolvable in acetone. In this way the cross-linked PMMA areas can be defined very exactly as an organic insulator. This procedure is used for the preparation of sub-micron wide Josephson junctions, where the standard processes can not satisfy the requirements.

## 3.2. Layouts and specific preparation procedures

### 3.2.1. The dummy junction

The preparation of stacked Josephson junctions evokes several specific requirements. One of the most difficult is the minimization of the parameter spread between stacked Josephson barriers. A spread of less than *5%* in $j_c$ is not easy to attain even in the case of a reliable single-barrier array technology. Small variations in the thermal oxidation process or in the morphology of the Nb/Al interface can drastically influence the homogeneity of the tunnel barriers and subsequently the current densities.

First preparations of three fold stacks showed a rather large difference between the critical currents of stacked junctions (*Fig.3.7).*

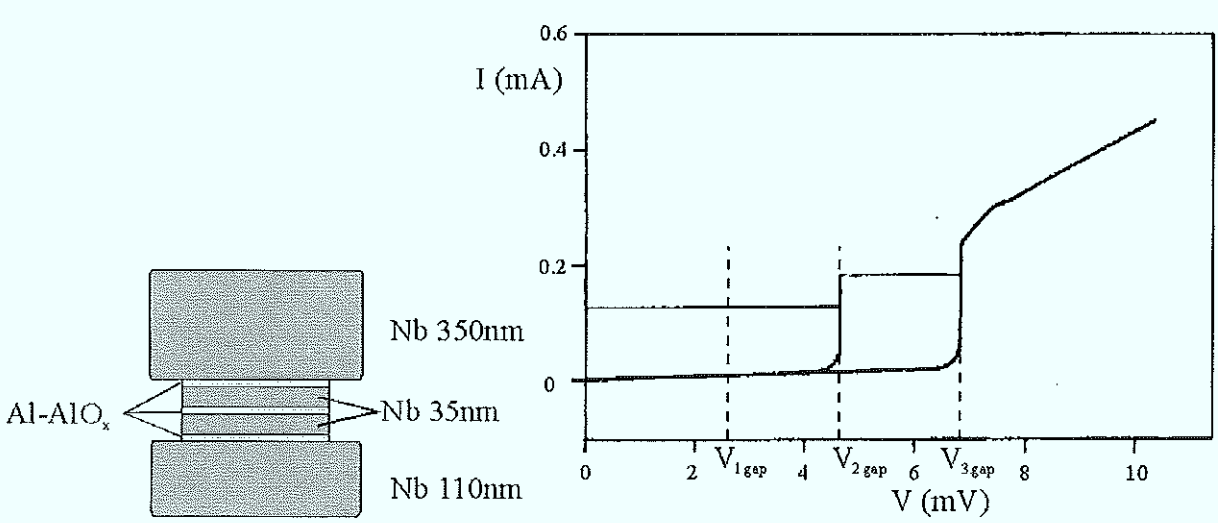


*Fig.3.7: I-V curve for a 3-fold stack prepared in the standard way; $\Delta I_c$=40%*

*[sample: H. Kohlstedt]*

We noticed, that one of the junctions always differs from the other junctions in critical current by about *40%*. While two junctions in *Fig.3.7* show a difference of less than *2%* in $I_c$ , the third one has a much higher critical current. The systematic appearance of this property lead us to the search of its cause during the preparation procedure. An examination of the surface roughness in the fabrication of stacked Nb/Al-$AlO_x$/Nb tunnel junctions was carried out[3.5]. We figured out that the ratio between the thickness of middle electrodes and base electrode play the crucial role for the spread. For the sample shown in *Fig.3.7* the base Nb electrode is *100*nm and the intermediate Nb layer thickness is *30*nm. From the theory of kinetic roughning it is known that the surface roughness increases with film thickness[3.6,7]. We measured the surface roughness using x-ray specular reflectivity at a photon energy of *8.048*keV. This method allows to achieve a resolution of about *0.1*nm[3.8,9]. The important advantage of this method over **S**canning **T**unneling **M**icroscopy (STM)[3.10] and **A**tomic **F**orce **M**icroscopy (AFM)[3.11] is the possibility to measure also the roughness of internal interfaces[3.12]. Another advantage is the determination of the mean square surface roughness with high precision.

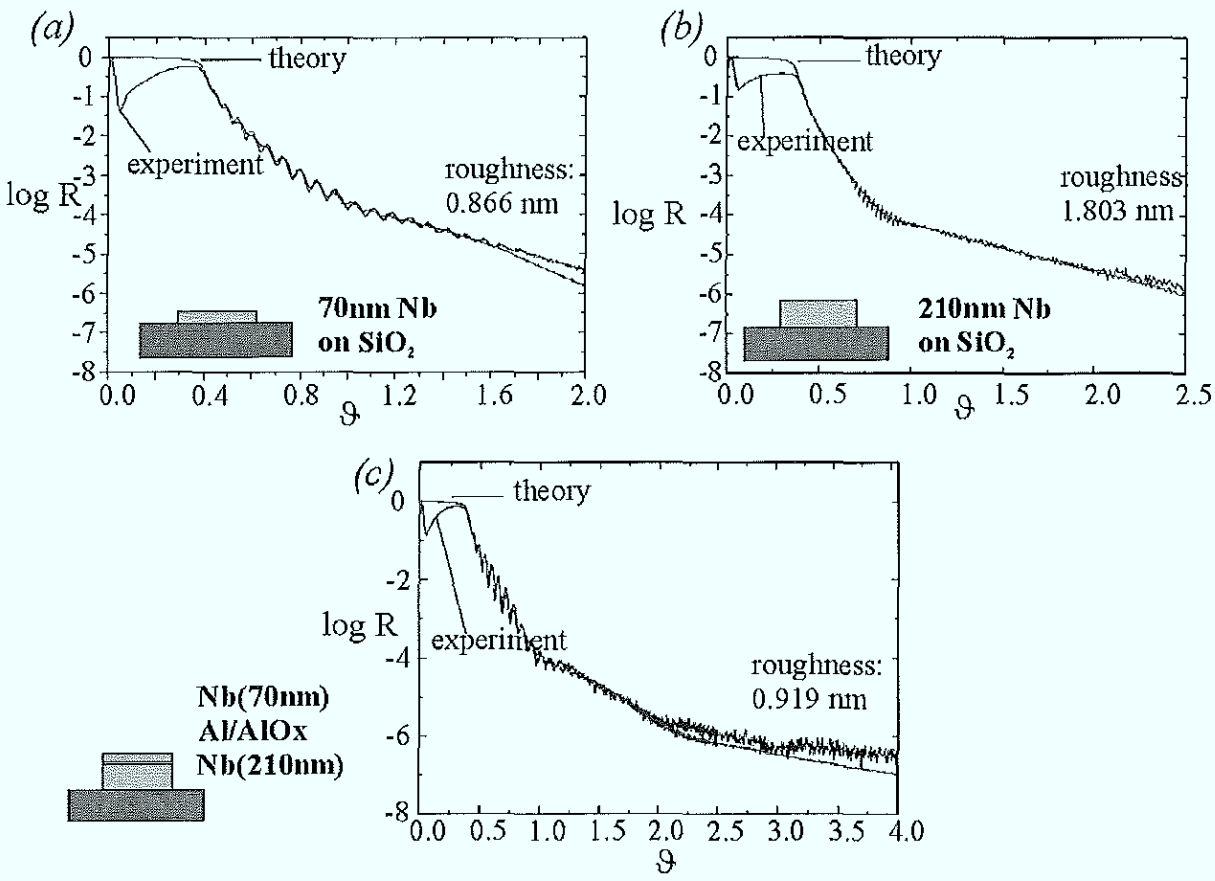


*Fig.3.8: Surface roughness for a 70*nm *(a) and 210*nm *(b) thick Nb film*
*(c) surface roughness for a standard trilayer*

In *Fig.3.8(a),(b)* the results for a *70*nm and a *210*nm thick niobium film on a standard substrate are shown. These plots show the logarithm of the reflection coefficient (log*R*) versus the scattering angle $\vartheta$. To determine the roughness of the measured surface the experimental data are fitted with the theoretical model[3.8,9], and the best fit defines the roughness parameter. The roughness of the substrate is *0.3*nm, for *70*nm Nb it was determined to *0.9*nm and for *210*nm Nb it is *1.8*nm. The roughness on top of a standard tunnel junction with *210*nm base Nb electrode, an Al-$AlO_x$ tunnel barrier, and a *70*nm thick top Nb electrode is found again to be as small as *0.9*nm (*Fig.3.8(c)*). This roughness is approximately the same as that of the single *70*nm Nb film. Thus, the Al barrier layer planarizes the surface of the underlying niobium base electrode for subsequent Nb film growth. These results confirm the planarization effect of Al-$AlO_x$ on Nb which was observed by **H**igh **R**esolution **T**ransmission **E**lectron **M**icroscopy (HRTEM)[3.13]. In spite of the junction preparation with equal oxidation parameters, the junction made on top of the thicker base electrode has larger critical current density. The conclusion here is that the Nb thickness due to the surface roughness determines the critical current density. To decrease the spread in a stack, it is possible to change the oxidation parameters for the first junction and to end up with smaller spread in $j_c$. A more elegant solution is the use of a dummy junction as an underlayer for the whole stack. In this case one replaces the Nb base electrode by a trilayer structure.

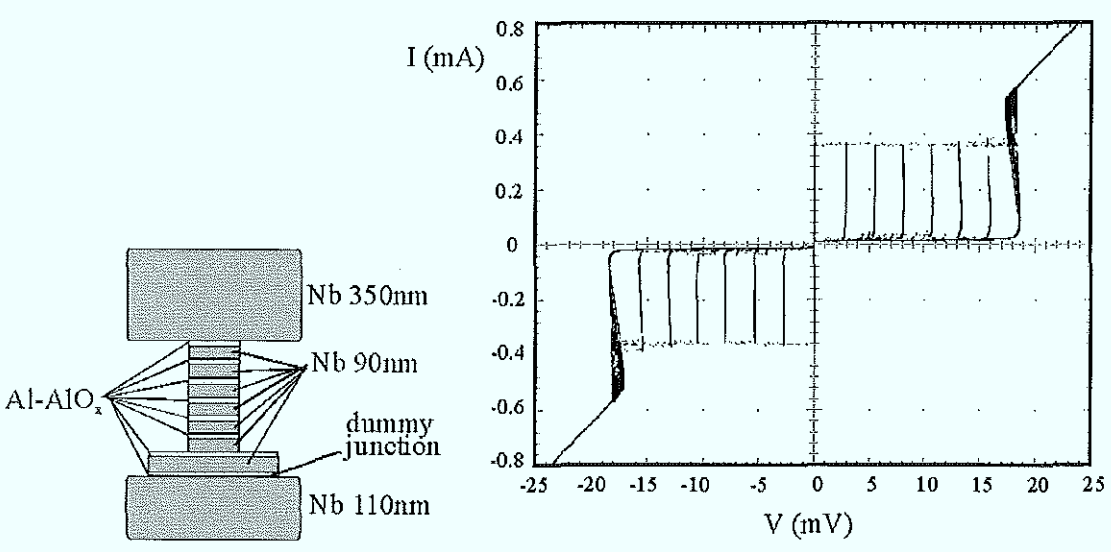


*Fig.3.9: 7-fold Josephson junction stack with $\Delta I_c$<5%*

*[sample: window1.7.1/1.8] (10×10μm²)*

A dummy junction can have very large dimensions and works as a superconducting dc short. The advantages of this technology are an arbitrary thick base electrode and minimized spread

in the critical currents of the following stacked barriers. Important is, that all junctions are formed on Nb layers of equal thickness. *Fig.3.9* shows an example of 7 stacked junctions prepared with dummy junction. We find now a spread in $I_c$ of less than *5%* !
The method of using dummy layers is patented in Germany and can be found under the patent number ***DE 196 15 632 A1***. The patent is shared by *50%* by Herman Kohlstedt and Norbert Thyssen.

### 3.2.2. "Window" layout

The most simple layout used in this work are window-type junctions (*Fig.3.10*). It consists of three masks: the ground layer, the junction area definition layer, and the Nb wiring as top layer. In one preparation run were prepared *4* chips, each with *6* long and *2* short junctions. Using this layout for single-barrier junctions, we performed investigations on the influence of a window part (idle area) on the properties of long Josephson junctions[2.49,50]. Due to the simplicity of the layout it was also used for the preparation of stacked junctions. The standard preparation procedure for single-layer junctions is shown in *Fig.3.11(a)*.
*(i)* The ground layer area is freed from photoresist by negative lithography. After that the Nb/Al-$ALO_x$/Nb trilayer is sputtered and the resist lift-off[3.4] in acetone defines the ground layer.
*(ii)* The second mask step defines the junction areas by covering them with the photoresist. Also, the contact pads stay covered and the resulting large area junctions work as shorts. The original SNAP process[3.2] is done with the anodic oxidation of the free surfaces. Before anodization we add a RIE step to etch the top Nb layer of the sputtered trilayer. The advantage of that is a free choice of the top Nb film thickness. As mentioned before, the anodic process is limited to *60*V for photoresist covered samples. This means the limit of the top anodizable Nb thickness of *54*nm.
*(iii)* The junction sides are insulated by anodic oxidation of the open base electrode area. Here it is important that the layout provides electrical connections between all parts of the sample which have to be anodized.
*(iv)* In the last step a negative lithography frees the surfaces for the top Nb film. The deposited Nb layer is defined by a lift-off.
A crystal dicing saw is used to separate the different chips and to disconnect the shorts between the ground layers.

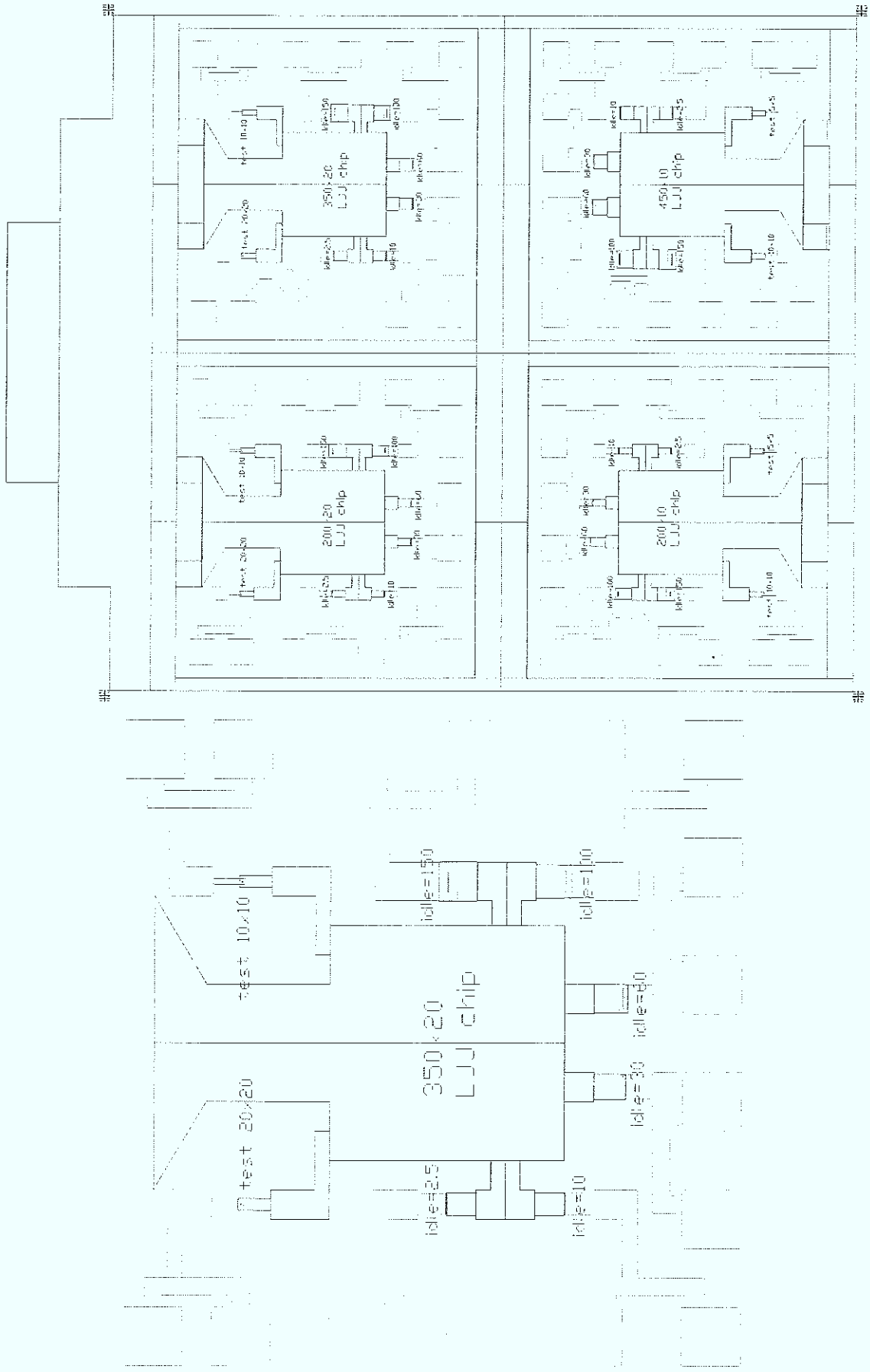


*Fig.3.10: Window junction layout*

For the preparation of stacked junctions just three points are changed in the above described process (*Fig.3.11(b)*). Instead of a single trilayer, a multilayer is deposited. The number of Al-$AlO_x$ layers is $N+1$ for $N$ stacked junctions, where this additional barrier layer represents the dummy junction. The etching is also done in multiple steps. Nb and Al-$AlO_x$ layers are etched down to the last junction defining Al-$AlO_x$ film. After the anodic oxidation an evaporation of SiO is added. This step is important for radiation measurements and homogeneous action of the external magnetic field on the stack. Without this SiO insulation the edges of upper junctions of the stack would be covered by the top Nb electrode. This is made rather thick (*600*nm) in order to cover large altitude differences on the wafer.

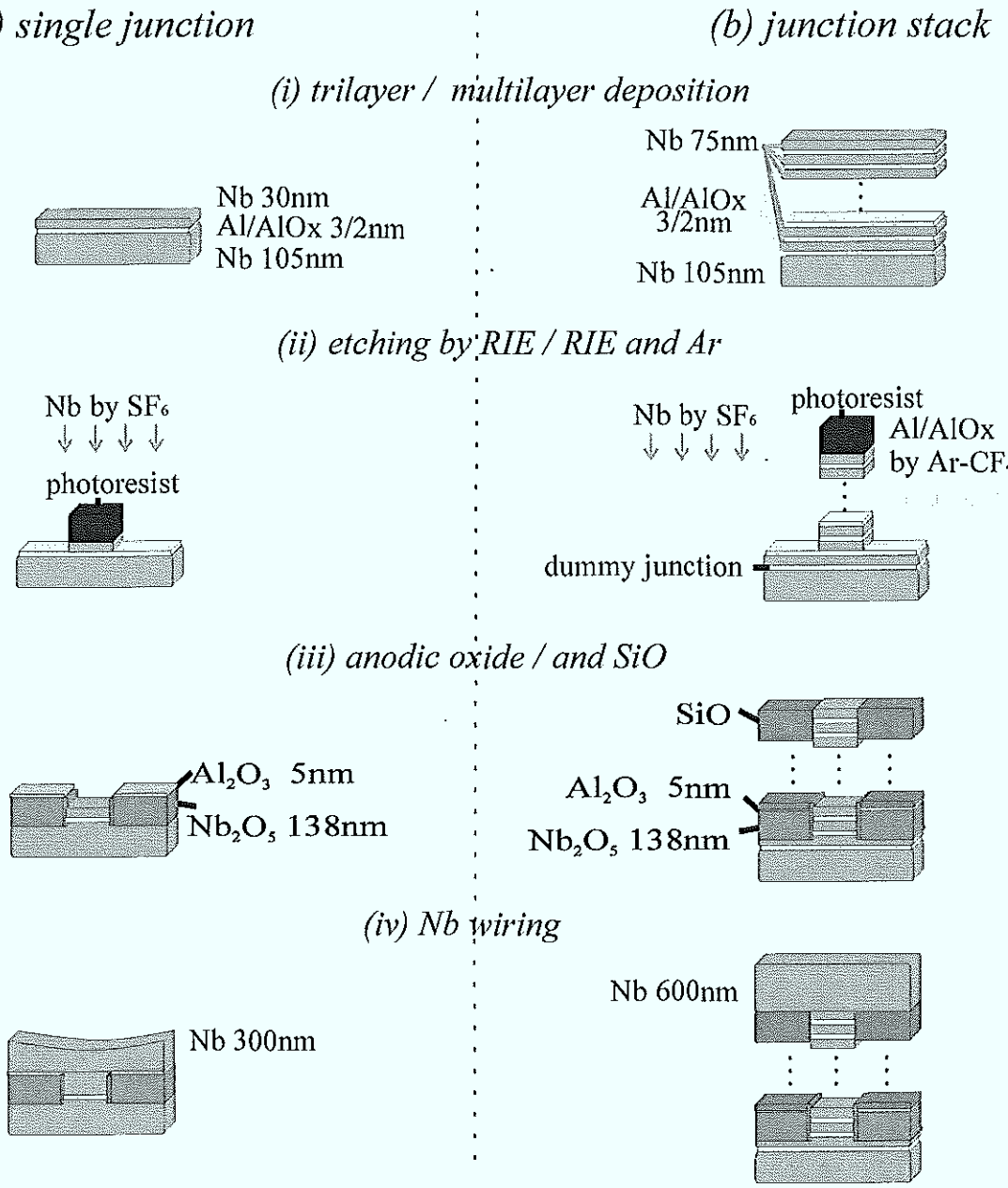


*Fig.3.11: Preparation process for window junctions;*
*(a) single-barrier junction, (b) junction stack*

### 3.2.3. "Annular" layout

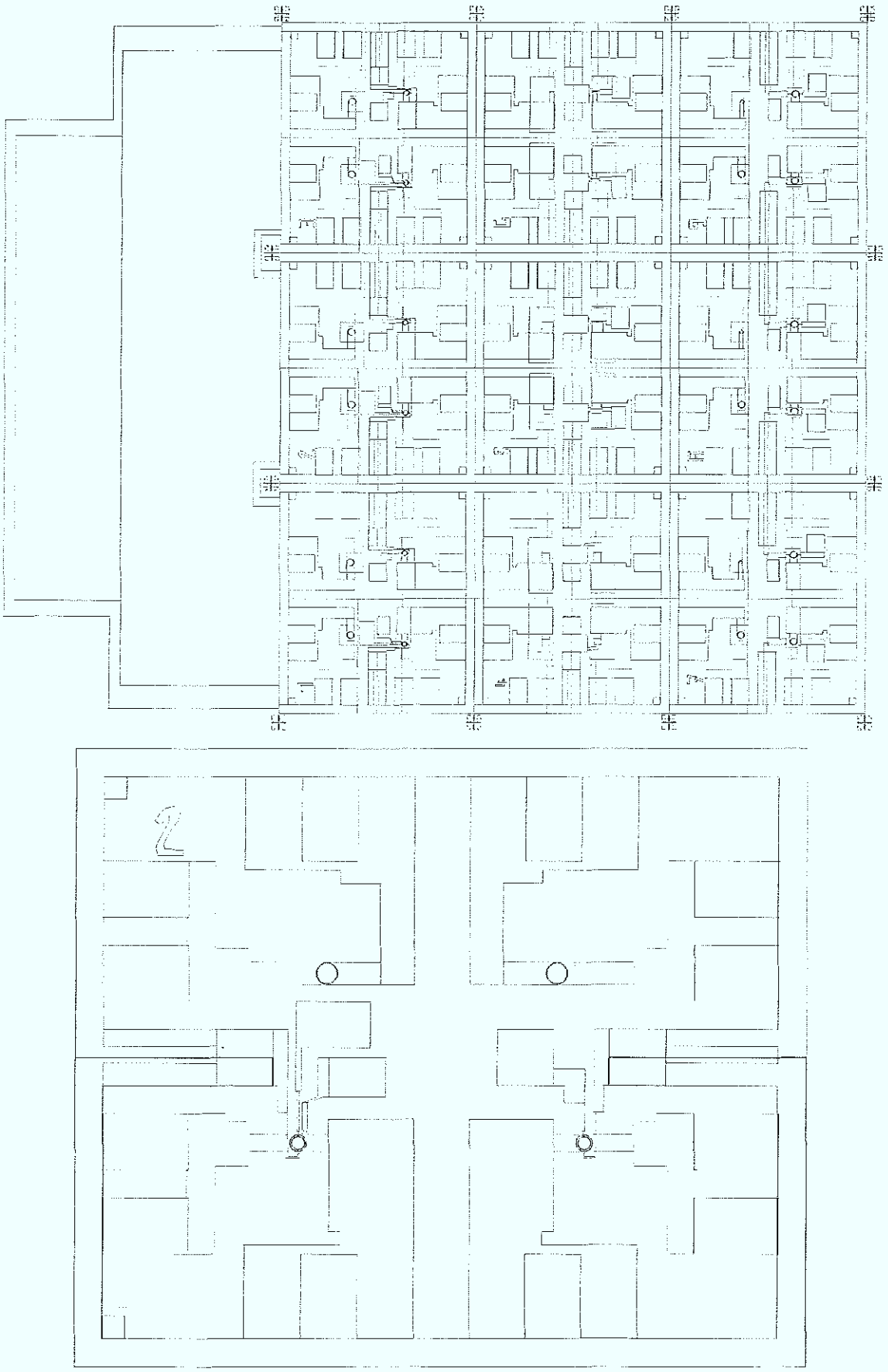

*Fig.3.12: Annular junction layout*

The possibility to investigate the dynamics of trapped Josephson solitons under periodic boundary conditions is realized in the annular junction layout. This layout is shown in *Fig.3.12*. It was used to prepare single-layer junctions and stacked junction samples (*Fig.3.11*).

This layout includes an additional (optional) layer mask for the definition of electrical contacts to the middle (inner) Nb electrodes in stacked junctions. As shown above there are annular and straight overlap junctions on the mask. In the case of stacks with an access to the middle electrode, the multilayers are not sputtered in situ like described before. Each junction of the stack is sputtered as single trilayer and its area is defined by Nb etching and anodic oxidation, as it is described above. Here the base electrodes of these single junction processes represent the electrical contact to the middle (inner) Nb electrodes, but the total intermediate Nb thickness is defined as the sum of two sputtered films. A first part is placed as top Nb film of the underlying junction, and the second part is added as base electrode of the overlaying one. For a useful coupling between two neighboring junctions this total thickness of the intermediate Nb electrode is chosen in the range of *(90±45)*nm. Therefore it is important to avoid steep flanks with large altitudes as base for a following single junction process. This demonstrates the need of a planarization procedure. We use a self-planarization by imbedding the bottom junction in the wafer surface. A wet etching process, as described in **chapter 3.1.2**, serves to prepare the needed ditches in the $SiO_2$. The complete preparation process is shown in *Fig.3.13*.

First, the base electrode is lithographically defined. Then a wet etching process with HF acid is done. The resulting ditch depth is chosen equal to the total thickness of the first trilayer. A following deposition of the trilayer with lift-off in acetone defines the base electrode. Nb etching and anodic oxidation are done before the middle electrode mask is used. Than the second trilayer is deposited and the electrical access to the middle electrode is defined by lift-off. The following etching and anodization is done equal to the previous junction with the same mask. Finally the top Nb layer is deposited and defined by lift-off.

*(i) wet etching (200nm ditches)*

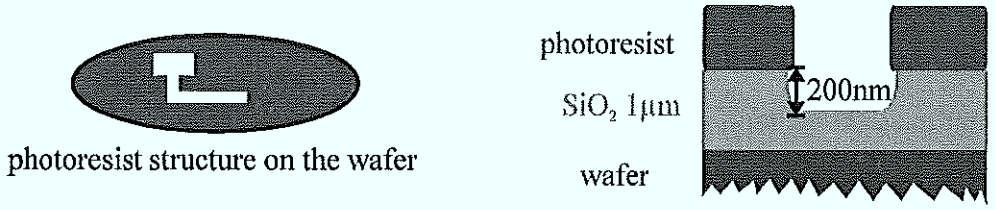


*(ii) imbedded base junction*

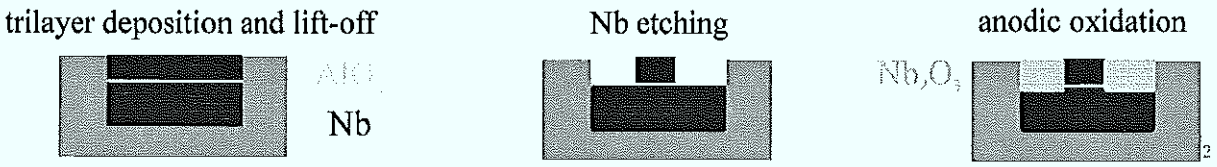


*(iii) access and top junction*

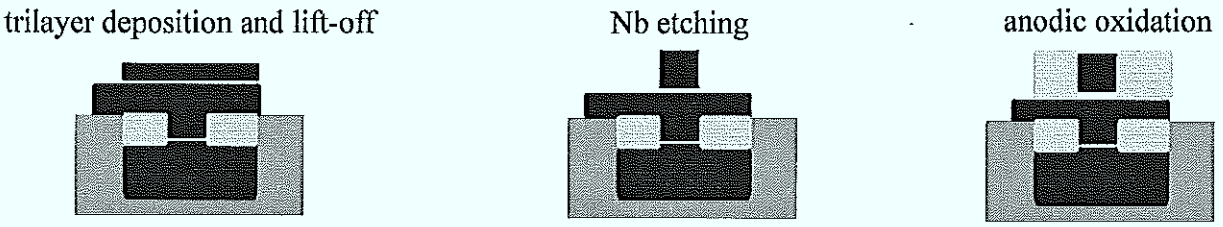


*(iv) Nb wiring*

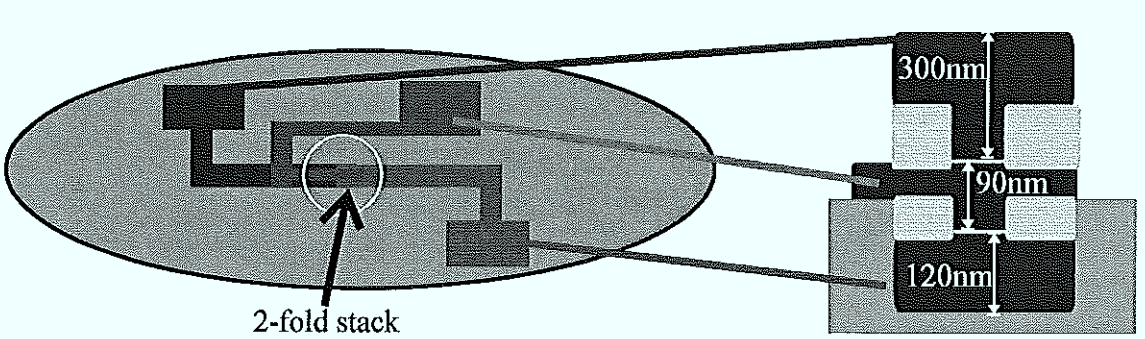


*Fig.3.13: Preparation process for 2-fold stacks with access to the intermediate electrode*

The self-planarization effect due to the combination of $SiO_2$ etching, lift-off, Nb etching and anodic oxidation worked well for this layout. The surface profiles for the first trilayer process are shown in *Fig.3.14*.

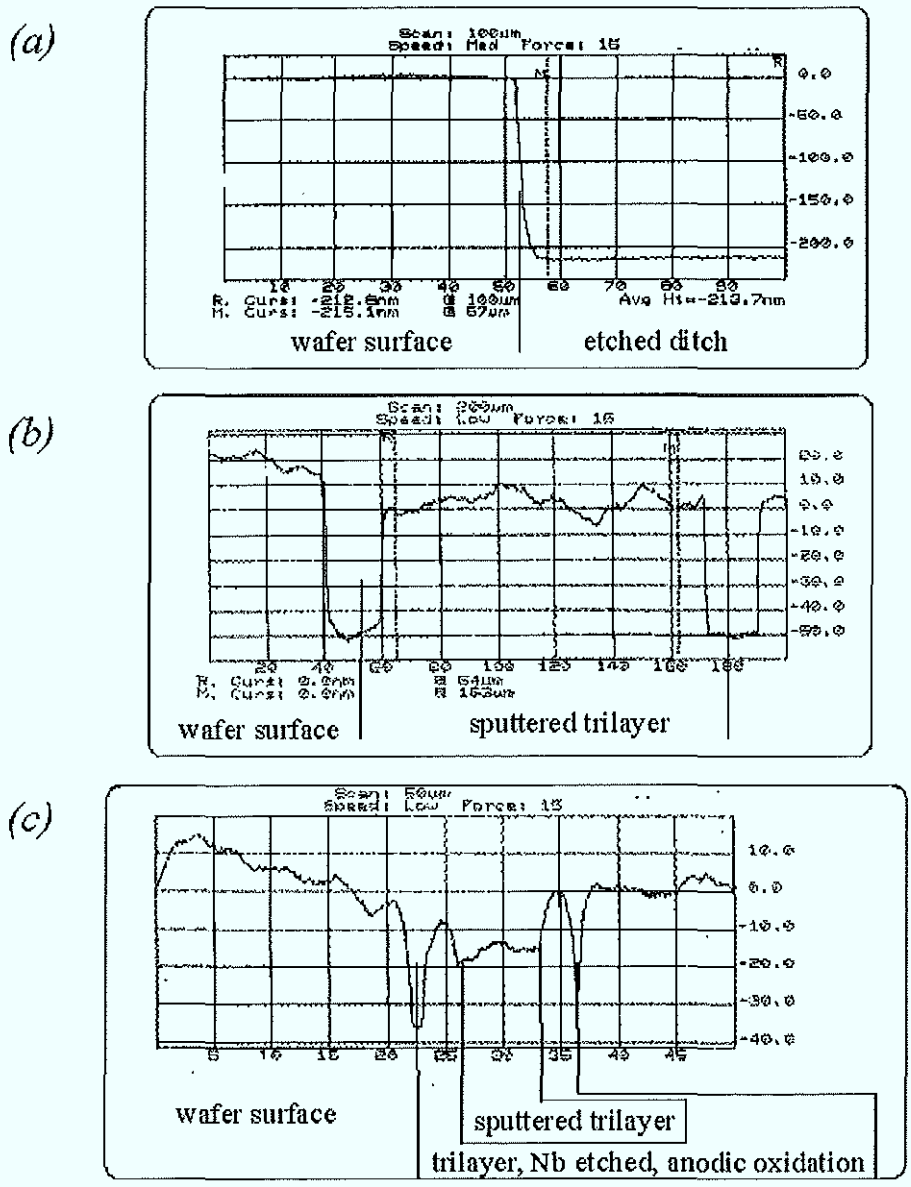


*Fig.3.14: Surface profile of an annstac process for the bottom junction*
*(a) etched ditch by HF acid; (b) first trilayer inside the ditch; (c) after etching and anodization; in picture (c) "sputtered trilayer" is representing the junction area of the bottom junction*

Another possibility for the planarization is evaporation of insulating materials. However, the thickness of the ground electrode leads to problems at the edges. The idea is to use the etching photomask for the lift-off process of evaporated SiO. A material deposition at the photoresist

flanks leads to high peaks at this points (*Fig.3.15*). With a thin Nb electrode as the base of the second trilayer, this approach often leads to pinholes.

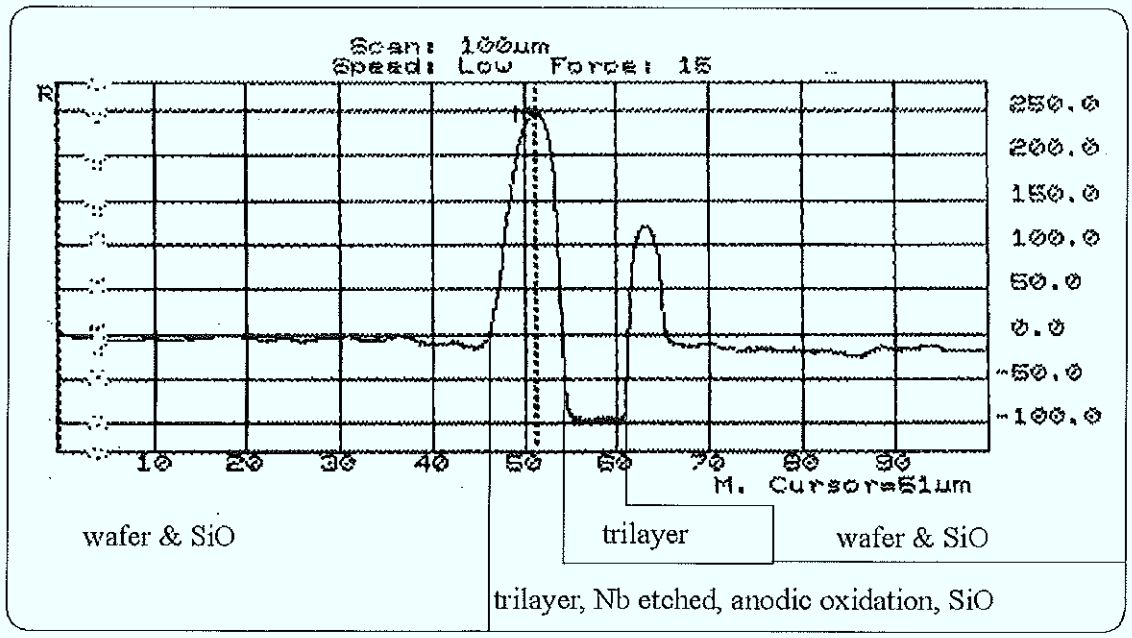


*Fig.3.15: Surface profile after SiO evaporation*

### 3.2.4. "Finchip" layout

For the radiation emission measurements it is necessary to couple a Josephson junction stack to a high frequency receiver. We used an on-chip finline antenna that was inserted in a slit of a wave guide. The emitted radiation couples to the room-temperature receiver with a band of *80-120*GHz.. The large impedance mismatch between the junction and the wave guide is partially compensated with the antenna. The ground and top electrodes of the Josephson stack form the antenna structure and allow to use our standard process for preparation. The layout is shown in *Fig.3.16*. This layout contains several small test junctions in the down part of the masks. These junctions have dimensions from $1\times1\mu m^2$ to $5\times5\mu m^2$.

This multilayer junction process (*Fig.3.11(b)*) uses a variation of the preparation procedure. Due to small window area around the junction a problem can occur during etching. For small structure surfaces the etching rate is much slower which prevents a correct definition of the junction area. The required change in the preparation procedure is demonstrated in *Fig.3.17*. It mainly contains a different definition of the ground layer. Instead of defining this by a lift-off process, an etching step is used.

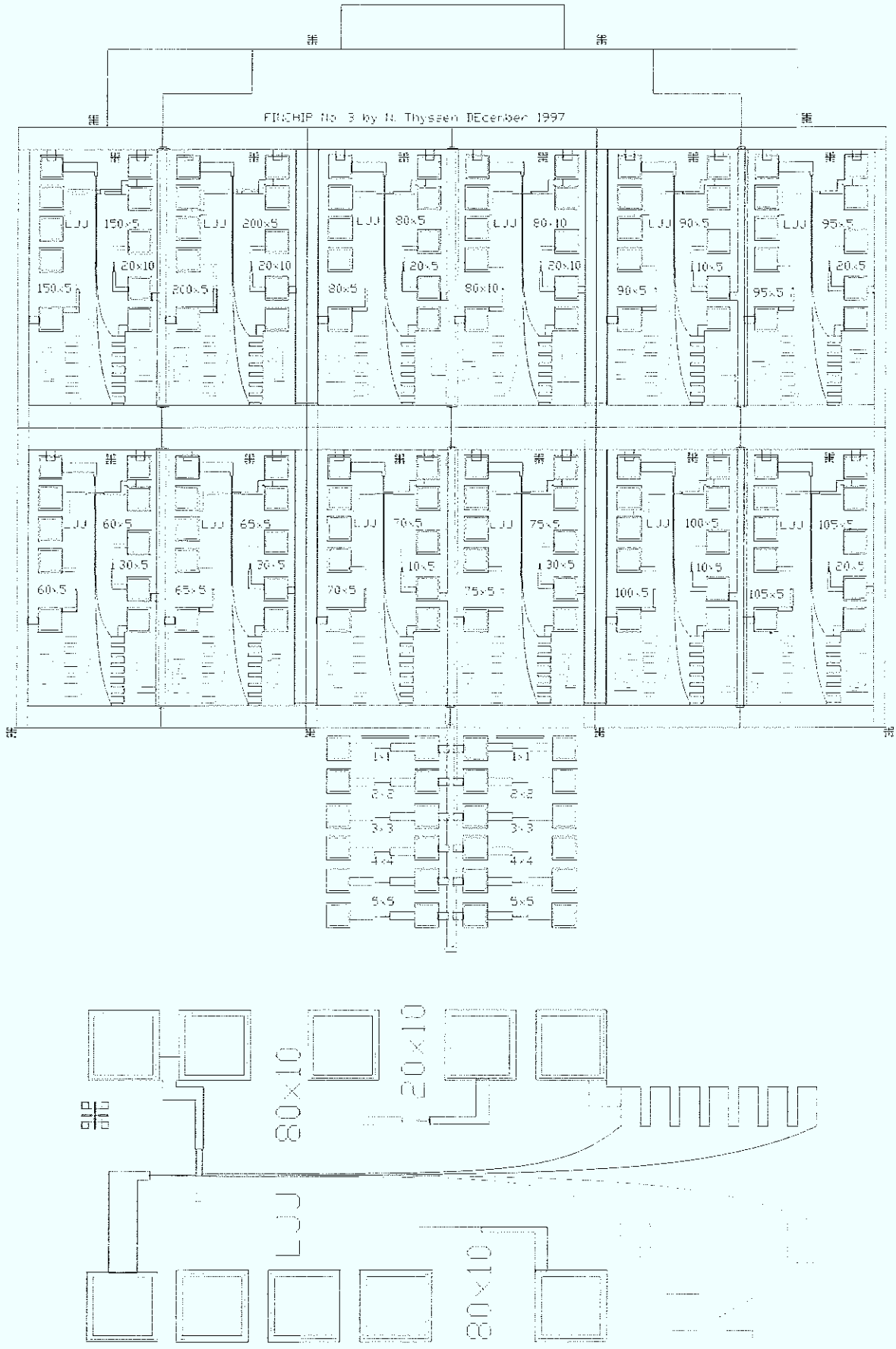


*Fig.3.16: Finchip junction layout*

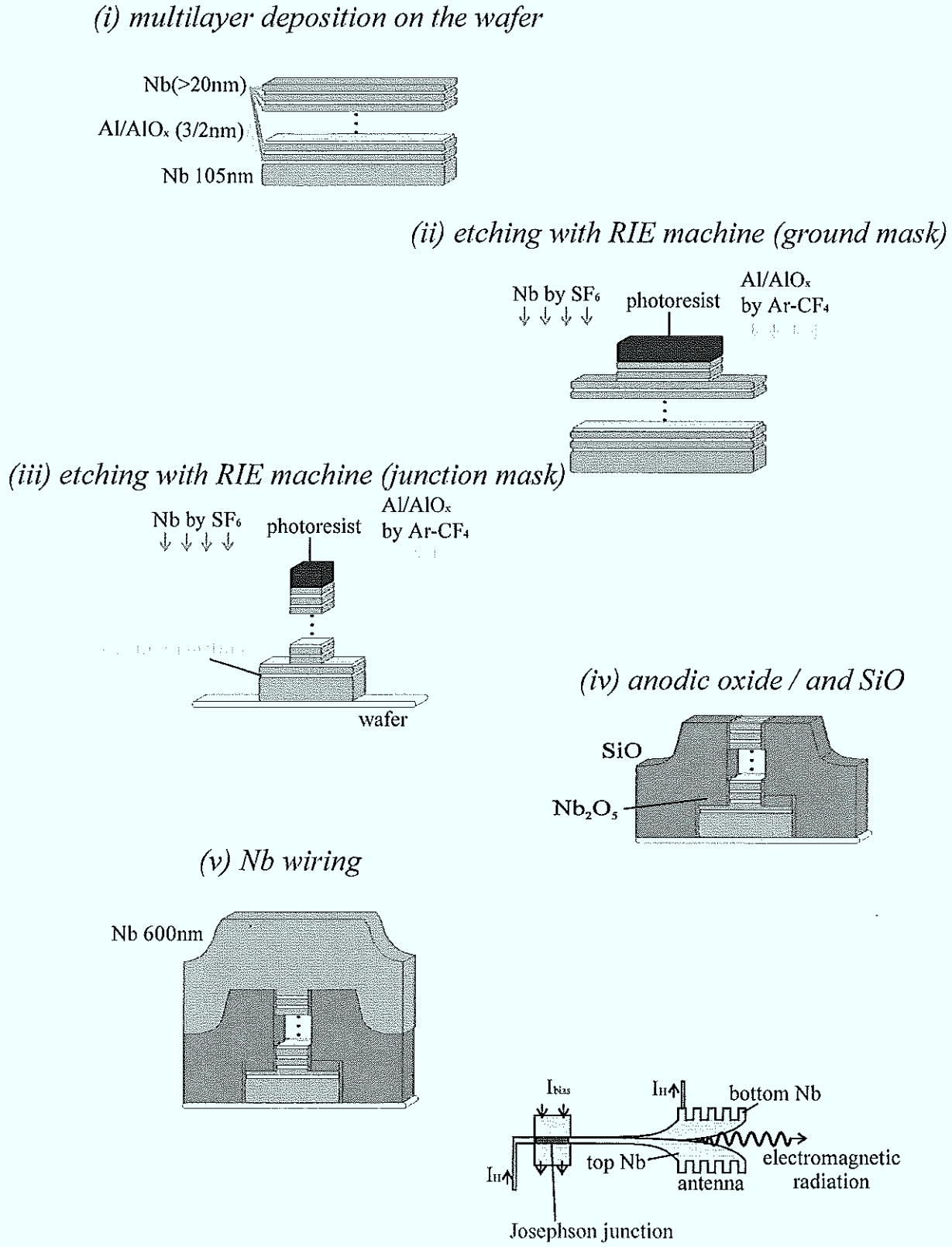


*Fig.3.17: Preparation process for N-fold stacks with finline antenna*

After depositing the multi-layer on the wafer *(i)*, the top Nb/Al-$AlO_x$/Nb/Al-$AlO_x$ layers are etched to define the ground electrode structure *(ii)*. Than the two different altitude levels are

etched simultaneously with a photoresist mask that covers the junction area *(iii)*. In the contrast to the standard multilayer process, here the wafer surface is not etched. Therefore, deep ditches on the wafer are avoided and the deposition of following films is done on a smoother surface. The following steps are the same as in the standard process (*Fig.3.11(b)*). For intermediate Nb thicknesses of less than *30*nm during the step *(ii)* the lower Nb/Al-$AlO_x$ layer are also etched. In this case an anodization voltage of *50-60*V is used to define the two bottom junctions.

# 4. Theoretical model for multi-layer Josephson junctions

In this chapter I present the theoretical model for coupled junctions in vertical stacks. Starting point is again the sine-Gordon equation for a single junction. The first theoretical work on two inductively coupled Josephson junctions was done by Mineev et al.[4.1]. Their perturbation approach for small coupling limit has been further explored by Kivshar and Malomed[4.2] and Grønbech-Jensen[4.3,4]. In the following we present the model derived by Sakai, Bodin and Pedersen[1.22], which is including an arbitrary coupling between the junctions. We will use this model in **chapter 7** to compare obtained experimental results with theory. The main discussion here will be focused on straight long overlap junction geometry and extended to other geometries in the specific points. A sketch of the junction geometry is shown in *Fig.4.1.*

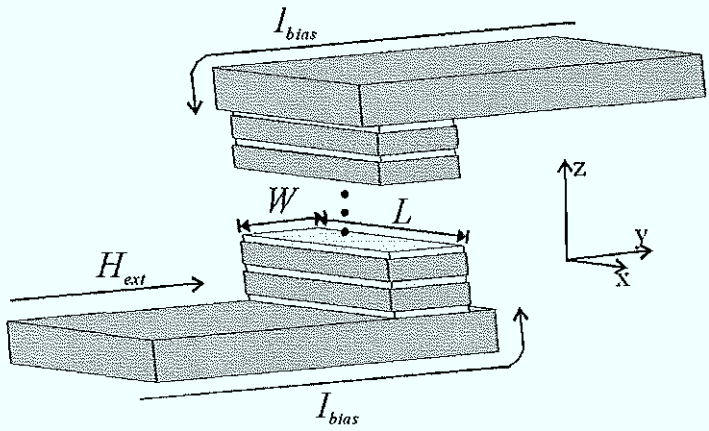


*Fig.4.1: Overlap Josephson junction stack*

The simplest stacked structure is a two-fold stack. We will denote the superconducting electrodes by the index $i=0,1,2$ , starting with the bottom layer. Assuming magnetic coupling, the electrodynamics of the whole system is described by coupled sine-Gordon equations. One starts with the gauge invariant phase difference between two layers $i$ and $i-1$,

$$\phi_{i,i-1}(x) = \varphi_i - \varphi_{i-1} + \frac{2e}{\hbar}\int \vec{A}_{i,i-1} d\vec{l}, \qquad \{4.1\}$$

with a vector potential $\vec{A}_{i,i-1}$ that determines the enclosed flux between the two layers in the way that

$$\oint \vec{A}_{i,i-1} d\vec{l} = \Phi = \int B_{i,i-1} dS. \qquad \{4.2\}$$

Considering the finite thickness of the superconducting layers, we have to take into account that the current flow on the opposite surfaces of the same superconducting electrode is given by the gradient of the phase and the vector potential as

$$j_i^{u,l} = -\frac{1}{2e\mu_0\lambda_{L_i}^2}\left(\nabla\varphi_i + 2e\vec{A}_{i,i-1}\right), \qquad \{4.3\}$$

with index *u* defining the upper surface and index *l* defining the lower surface of the electrode. The spatial variation of the phase difference can be derived from equation {4.1}. Differentiation with respect to *x* and replacing the magnetic flux density {4.2} and the phase gradient {4.3} will end up in

$$\frac{\partial\tilde{\varphi}_{i,i-1}}{\partial x} = \frac{2e}{\hbar}d_{i,i-1}B_{i,i-1} - \frac{2e\mu_0\lambda_{L_i}^2}{\hbar}j_i^l + \frac{2e\mu_0\lambda_{L_{i-1}}^2}{\hbar}j_{i-1}^u . \qquad \{4.4\}$$

At this moment it is necessary to calculate the surface currents in the superconducting electrode that are determined by the penetration of magnetic field more exactly (*Fig.4.2(a)*). Following the notation, the current density $j_{i-1}^u$ is in the upper surface of the superconducting electrode *i-1*. In the same notation $j_{i-1}^l$ defines the current at the lower surface of layer *i-1*. The magnetic flux penetration inside the superconducting layer *i* in *y-direction* can be given as

$$\partial_{zz}B = \lambda_J^{-2}B . \qquad \{4.5\}$$

On the other hand the magnetic flux density in the insulating layers can be regarded using the London equation

$$\nabla\times\vec{H} = \vec{j}. \qquad \{4.6\}$$

In this way we obtain the surface current density by

$$j_i^l = \frac{1}{\mu_0\lambda_{L_i}}\frac{B_{i,i-1}\cosh\left(\frac{t_i}{\lambda_{L_i}}\right) - B_{i+1,i}}{\sinh\left(\frac{t_i}{\lambda_{L_i}}\right)}, \qquad \{4.7\}$$

and

$$j_i^u = \frac{1}{\mu_0\lambda_{L_{i-1}}}\frac{B_{i+1,i}\cosh\left(\frac{t_i}{\lambda_{L_i}}\right) - B_{i,i-1}}{\sinh\left(\frac{t_i}{\lambda_{L_i}}\right)} . \qquad \{4.8\}$$

Now we can obtain a relation between the phase derivative and the magnetic flux density using equations {4.4, 4.7, and 4.8}

$$-\frac{\hbar}{2e}\frac{\partial\tilde{\varphi}_{i,i-1}}{\partial x} = d'_{i,i-1}B_{i,i-1} + s_iB_{i+1,i} + s_{i-1}B_{i-1,i-2}, \qquad \{4.9\}$$

where the effective magnetic thickness of the junction between the superconducting layers *i* and *i-1* is given as:

$$d'_{i,i-1} = d_{i,i-1} + \lambda_{L_i}\coth\left(\frac{b_i}{\lambda_{L_i}}\right) + \lambda_{L_{i-1}}\coth\left(\frac{b_{i-1}}{\lambda_{L_{i-1}}}\right), \qquad \{4.10\}$$

and the parameter $s_i$ is describing the coupling between two neighboring junctions. The coupling is determined by the ratio of the thickness of the superconducting electrode $t_i$ and its London penetration depth $\lambda_{L_i}$

$$s_i = -\frac{\lambda_{L_i}}{\sinh\left(\frac{b_i}{\lambda_{L_i}}\right)}. \qquad \{4.11\}$$

For two stacked junctions, for example, we can now write equation {4.9} in matrix form like:

$$-\frac{\hbar}{2e}\frac{\partial}{\partial x}\begin{pmatrix}\phi_{0,1}\\ \phi_{1,0}\end{pmatrix}=\begin{pmatrix}s_0 & d'_{1,0} & s_1 & 0\\ 0 & s_1 & d'_{2,1} & s_2\end{pmatrix}\begin{pmatrix}B_{0,-1}\\ B_{1,0}\\ B_{2,1}\\ B_{3,2}\end{pmatrix}, \qquad \{4.12\}$$

where $B_{0,-1}$ and $B_{3,2}$ are standing for the external magnetic density outside the stack. For a homogeneous field these values have to be given by $B_{0,-1}=B_{3,2}=B_{ext}$. The case of $N$ stacked junctions results in the matrix equation

$$-\frac{\hbar}{2e}\frac{\partial}{\partial x}\begin{pmatrix}\phi_{1,0}\\ \phi_{2,1}\\ \vdots\\ \phi_{i,i-1}\\ \vdots\\ \phi_{N,N-1}\end{pmatrix}=\begin{pmatrix}s_0 & d'_{1,0} & s_1 & 0 & \cdots & & & \cdots & 0\\ 0 & s_1 & d'_{2,1} & s_2 & \cdots & & & \ddots & \vdots\\ \vdots & \ddots & \ddots & \ddots & & & & & \\ \cdots & 0 & s_{i-1} & d'_{i,i-1} & s_i & 0 & \cdots & & \\ & & \ddots & \ddots & \ddots & \ddots & \ddots & & \\ \vdots & \iddots & & & \cdots & 0 & s_{N-2} & d'_{N-1,N-2} & s_{N-1}\\ 0 & \cdots & & & & \cdots & 0 & s_{N-1} & d'_{N,N-1}\end{pmatrix}\begin{pmatrix}B_{0,1}\\ B_{1,0}\\ \vdots\\ B_{i,i-1}\\ \vdots\\ B_{N,N-1}\\ B_{N+1,N}\end{pmatrix}, \qquad \{4.13\}$$

where, again, the external magnetic flux values $B_{0,-1}$ and $B_{N+1,N}$ are equal to the external magnetic flux $B_{ext}$.

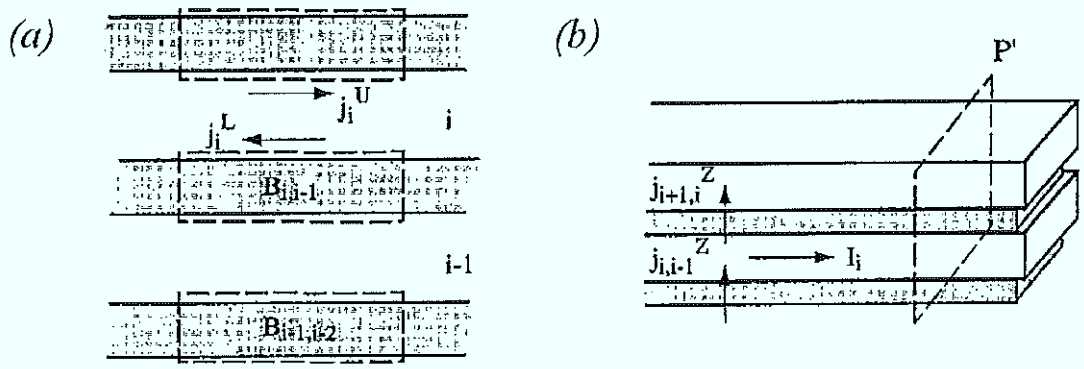


*Fig.4.2: Integration path P'*

To calculate the magnetic density in one layer we integrate along the closed path $P_i'$ as shown in *Fig.4.2(b)*. The contribution of all currents to the magnetic flux density is calculated using the London equation {4.6}. The magnetic flux in one junction can be written as

$$B_{i,i-1} = \frac{\mu_0}{W} \sum_{k=i}^{N} I_k B_{ext} \,. \qquad \{4.14\}$$

The latter expressions can be introduced in the matrix form {4.12}. For the usual Josephson junction model the total current is the sum of a capacitive, a resistive and a Josephson current across the insulating barriers. Therefore we introduce capacitance $C_{i,i-1}$ per unit area, the conductivity $G_{i,i-1}$ per unit area ,and the maximum dc Josephson current density $j_{i,i-1}$ and write the total current as

$$j^z_{i,i-1} = \frac{\hbar}{2e} C_{i,i-1} \frac{\partial^2 \phi_{i,i-1}}{\partial x^2} + \frac{\hbar}{2e} G_{i,i-1} \frac{\partial \phi_{i,i-1}}{\partial x} + j_{i,i-1} \sin \phi_{i,i-1} \qquad \{4.15\}$$

Now it is possible to replace

$$-\frac{1}{W}\frac{\partial I_i}{\partial x} = j^z_{i,i-1} - j^z_{i+1,i} \quad \text{for} \quad 1 \le i \le N-1 \quad \text{, and} \quad -\frac{1}{W}\frac{\partial I_N}{\partial x} = j^z_{N,N-1} \,.$$

The final general system of equations for the $N$-fold stack looks like

$$-\frac{\hbar}{2e\mu_0}\frac{\partial^2}{\partial x^2}\begin{pmatrix} \phi_{1,0} \\ \phi_{2,1} \\ \vdots \\ \phi_{i,i-1} \\ \vdots \\ \vdots \\ \phi_{N,N-1} \end{pmatrix} = \begin{pmatrix} d'_{1,0} & s_1 & 0 & & & \cdots & 0 \\ s_1 & d'_{2,1} & s_2 & \ddots & & & \vdots \\ 0 & & \ddots & & & & \\ & 0 & s_{i-1} & d'_{i,i-1} & s_i & 0 & \\ & & & & \ddots & & 0 \\ \vdots & & & \ddots & & & s_{N-1} \\ 0 & \cdots & & & 0 & s_{N-1} & d'_{N,N-1} \end{pmatrix} \begin{pmatrix} j^z_{1,0} \\ j^z_{2,1} \\ \vdots \\ j^z_{i,i-1} \\ \vdots \\ j^z_{N-1,N-2} \\ j^z_{N,N-1} \end{pmatrix} . \qquad \{4.16\}$$

If we now remember the definition of the total current in equation {4.15}, this matrix equation represents the coupled system of sine-Gordon equations for $N$ stacked junctions without bias current. A bias current term can be added in the right hand side of {4.16} in the form of

$$-I_B \begin{pmatrix} d'_{1,0} + s_1 \\ d'_{2,1} + s_1 + s_2 \\ \vdots \\ d'_{N-1,N-2} + s_{N-2} + s_{N-1} \\ d'_{N,N-1} + s_{N-1} \end{pmatrix}, \qquad \{4.17\}$$

for the **overlap geometry**, as regarded till now. The external magnetic field is included in the boundary conditions. For the overlap case these are given as

$$-\frac{\hbar}{2e}\frac{\partial}{\partial x}\begin{pmatrix}\phi_{1,0}\\ \vdots\\ \phi_{i,i-1}\\ \vdots\\ \phi_{N,N-1}\end{pmatrix}_{\substack{x=0\\ x=L}} = B_{ext}\begin{pmatrix}s_0+d'_{1,0}+s_1\\ \vdots\\ s_{i-1}+d'_{i,i-1}+s_i\\ \vdots\\ s_{N-1}+d'_{N,N-1}+s_N\end{pmatrix}. \qquad \{4.18\}$$

For **annular junctions** the boundary conditions are periodic and given by

$$\frac{\partial}{\partial x}\begin{pmatrix}\phi_{1,0}\\ \vdots\\ \phi_{i,i-1}\\ \vdots\\ \phi_{N,N-1}\end{pmatrix}_{x=0} = \frac{\partial}{\partial x}\begin{pmatrix}\phi_{1,0}\\ \vdots\\ \phi_{i,i-1}\\ \vdots\\ \phi_{N,N-1}\end{pmatrix}_{x=L}, and \begin{pmatrix}\phi_{1,0}\\ \vdots\\ \phi_{i,i-1}\\ \vdots\\ \phi_{N,N-1}\end{pmatrix}_{x=0} = \begin{pmatrix}\phi_{1,0}\\ \vdots\\ \phi_{i,i-1}\\ \vdots\\ \phi_{N,N-1}\end{pmatrix}_{x=L} - 2\pi\begin{pmatrix}F^{1,0}\\ \vdots\\ F^{i,i-1}\\ \vdots\\ F^{N,N-1}\end{pmatrix}, \{4.19\}$$

where $F^{i,i-1}$ is the number of fluxons in the junction $(i,i-1)$. The external field adds a spatially dependent current term in the right hand side of equation {4.16} (see **chapter 2.5**).

With this system of coupled sine-Gordon equations, it is possible to perform numerical simulations and compare results with experimental data. This thesis work presents first experimental results on multi-layer stacks in Nb technology and compares them with theory. In **chapter 5** I concentrate on two fold stacks. Than, in **chapter 6** I present results for stacked systems with large number of junctions.

## 5. Two stacked Josephson junctions

The electrodynamics for a two fold stack is described by two coupled sine Gordon equations. It is possible to simplify the expressions in case of equal parameters for all junctions. The important parameters are the thickness of superconducting electrodes, critical currents and resistances. Using equation {4.16} for $N=2$ and inserting the expression for the current density, the system of equations is

$$-\frac{\hbar}{2e\mu_0}\frac{\partial^2}{\partial x^2}\begin{pmatrix}\phi_{1,0}\\ \phi_{2,1}\end{pmatrix}=\begin{pmatrix}d'_{1,0} & s_1\\ s_2 & d'_{2,1}\end{pmatrix}\begin{pmatrix}\frac{\hbar C_1}{2e}\frac{\partial^2\phi_{1,0}}{\partial t^2}+\frac{\hbar G_1}{2e}\frac{\partial\phi_{1,0}}{\partial t}+j_1\sin\phi_{1,0}\\ \frac{\hbar C_2}{2e}\frac{\partial^2\phi_{2,1}}{\partial t^2}+\frac{\hbar G_2}{2e}\frac{\partial\phi_{2,1}}{\partial t}+j_2\sin\phi_{1,0}\end{pmatrix}-I_{bias}\begin{pmatrix}d'_{1,0}+s_1\\ d'_{2,1}+s_2\end{pmatrix}, \quad \{5.1\}$$

with the magnetic thicknesses $d'_{i,i-1}=d_{i,i-1}+\lambda_{L_i}\coth\left(\frac{b_i}{\lambda_{L_i}}\right)+\lambda_{L_{i-1}}\coth\left(\frac{b_{i-1}}{\lambda_{L_{i-1}}}\right)$, {5.2}

and the coupling parameter $s_i=-\frac{\lambda_{L_i}}{\sinh\left(\frac{b_i}{\lambda_{L_i}}\right)}$. {5.3}

For numerical simulations it is convenient to use normalized units, as introduced for single junctions. Time scale is normalized to the inverse plasma frequency and spatial coordinate is normalized to the Josephson penetration depth. For equal parameters $G_1=G_2$, $j_1=j_2$, $C_1=C_2$, $d_{1,0}=d_{2,1}$ and $s_1=s_2$ ,we end up with two equations in the form

$$\begin{aligned}\frac{1}{1-S^2}\phi_{1_{xx}}-\phi_{1_{tt}}&=\sin\phi_1+\alpha\phi_{1_{tt}}+\gamma_1+\frac{S}{1-S^2}\phi_{2_{xx}}\\ \frac{1}{1-S^2}\phi_{2_{xx}}-\phi_{2_{tt}}&=\sin\phi_2+\alpha\phi_{2_{tt}}+\gamma_2+\frac{S}{1-S^2}\phi_{1_{xx}}\end{aligned}, \quad \{5.4\}$$

with a normalized coupling parameter $S$

$$S=-\left[\left(\frac{d}{\lambda_L}+\coth\frac{b_1}{\lambda_L}+\coth\frac{b_2}{\lambda_L}\right)\sinh\frac{b_1}{\lambda_L}\right]^{-1}, \quad \{5.5\}$$

that vanishes for large thickness of the superconducting electrode between the junctions $b_1 >> \lambda_L$ . Typical experimental values for $S$ are in the interval from *-0.2* to *-0.9*. For a fluxon solution in one junction the coupling term changes the length scale. In addition, a fluxon in one junction creates a magnetic "image" in the second junction.

## 5.1 Mutual phase locking

First calculations had been done for equal parameter for both junctions. For equal junctions the penetration of fluxons is taking place simultaneously in both junctions[5.1]. The small-amplitude linear wave solutions for a coupled system are subdivided in $N$ distinct branches of dispersion relation for an $N$-fold stack[5.2,3]. For a two-fold stack, this means a splitting in two different modes, the so called *in-phase* ($\phi_1=\phi_2$) and *out-of-phase* ($\phi_1=-\phi_2$) mode[5.3]. The modes shown in *Fig.5.1* are a consequence of this plasma wave dispersion relation split.

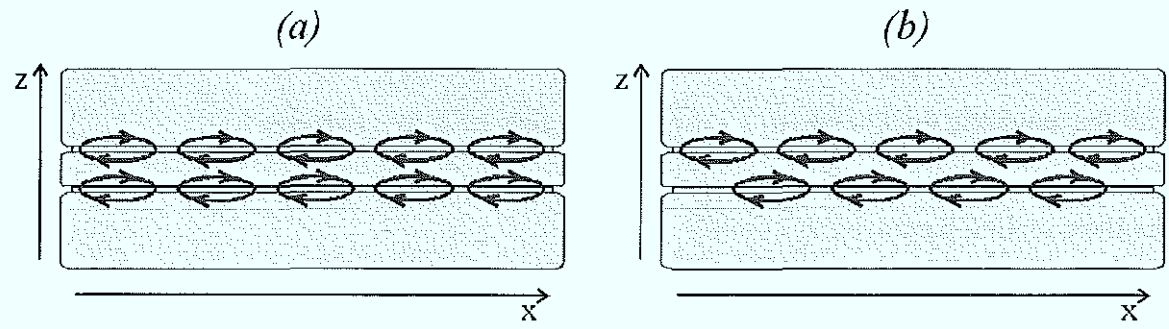


*Fig. 5.1: (a) In-phase and (b) out-of-phase mode for a two-fold stack*

For the *in-phase* mode, the moving fluxons of equal polarity form a bound state with identical phase differences in both junctions. This state was predicted by numerical simulations[1.22] and proved to be stable by analytical calculations[5.4]. For the *out-of-phase* mode the flûxon positions are shifted between the junctions, and the resulting total voltage across the system is changed. This is important for the radiation emission in this mode. Radiation emission investigation showed the possibility of the Josephson frequency doubling due to half-period shift of the fluxon chains in two junctions[1.18]. The characteristic velocity of the *in-phase* mode is

$$\bar{c}_+ = \frac{\bar{c}}{\sqrt{1+S}} ,$$

and for the *out-of-phase* mode

$$\bar{c}_- = \frac{\bar{c}}{\sqrt{1-S}} . \qquad \{5.6\}$$

In experiments, the two different velocities are measured as two coexisting Fiske steps for one field value (*Fig.5.2*). The voltage spacing between the resonance at different field values is given by $\Delta V_\pm = \frac{\Phi_0}{2L}\bar{c}_\pm$ . This spacing allows to calculate the coupling constant between the

junctions. Variation of the coupling by changing the thickness of the intermediate electrode has been investigated in detail[5.3] and good agreement between theory and experiment was found.

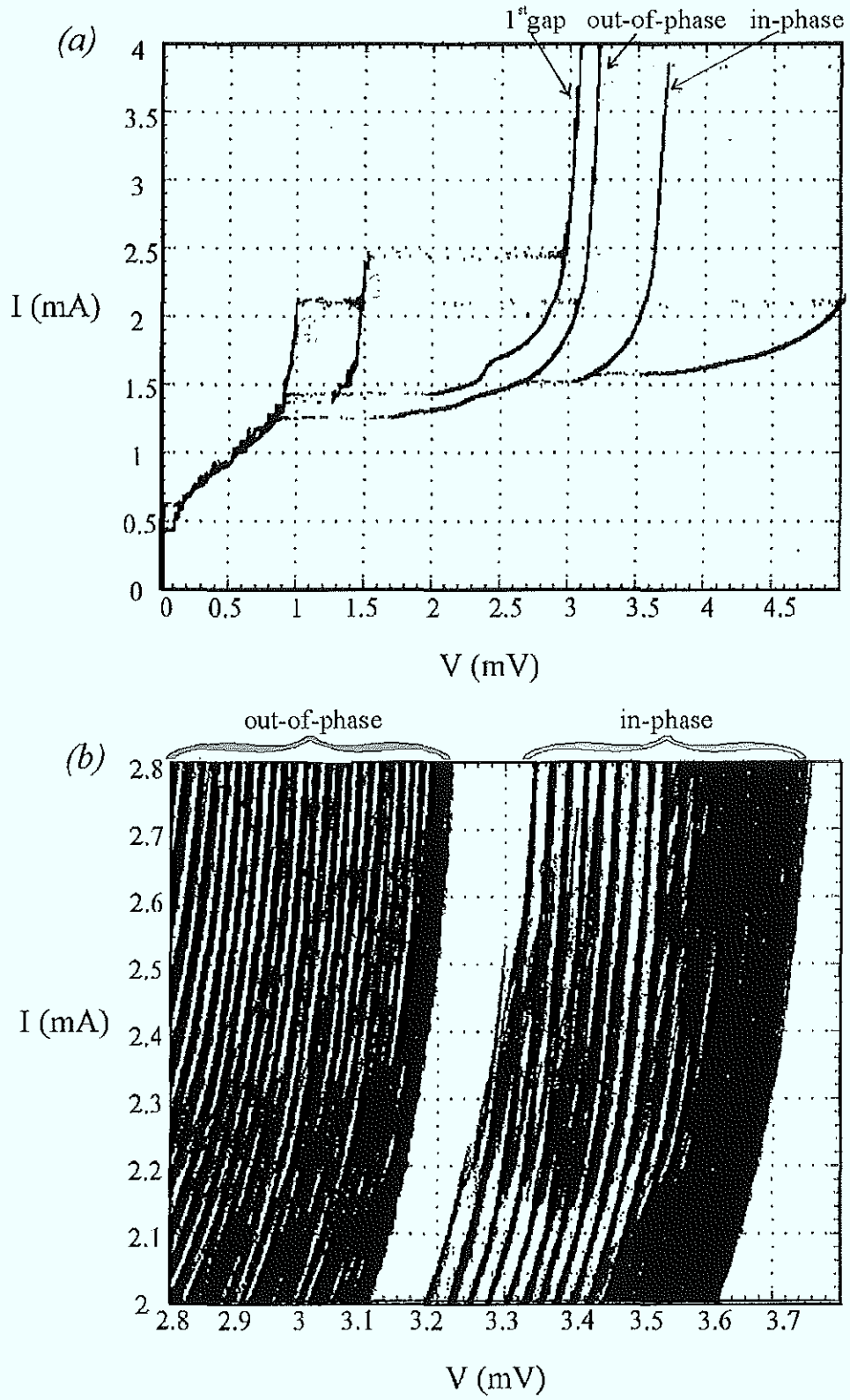


*Fig.5.2: Stored I-Vs for a 2-fold stack with continuously changed magnetic field;*
*(a) H=8.2Oe, and (b) Fiske step spacing; [sample: window01.2.1/2.4], (350×20μm²)*

For high magnetic fields the only stable solution in statics is the *out-of-phase* triangular fluxon arrangement. Its formation was studied in detail by Song et al.[5.5]. Systematic numerical studies of the stability of the states versus fluxon velocity were carried out[5.6,7]. In case of a parameter spread between the junctions, locked states for the fluxon chains may exist in a limited velocity range. These locked states are destroyed via delocking transition[5.8] accompanied by flux-flow drag[5.9]. In experiment the transition between the *out-of-phase* and *in-phase* states was observed as a change in the spectrum of fluxon generated radiation[1.18]. The velocity range for a stable state with identical solitary fluxons in both junctions was analytically calculated for the fluxon velocity between $\bar{c}_-$ and $\bar{c}_+$ [5.4]. For strongly coupled stacks, Monaco et al.[5.10] found an experimental indication for stable zero-field modes with $u = \bar{c}_+$. In the situation with one fluxon in the first and one antifluxon in the second junction the coherent state with limiting velocity $u = \bar{c}_-$ was experimentally reported by Carapella et al.[5.11].

## 5.2. Internal and external magnetic coupling

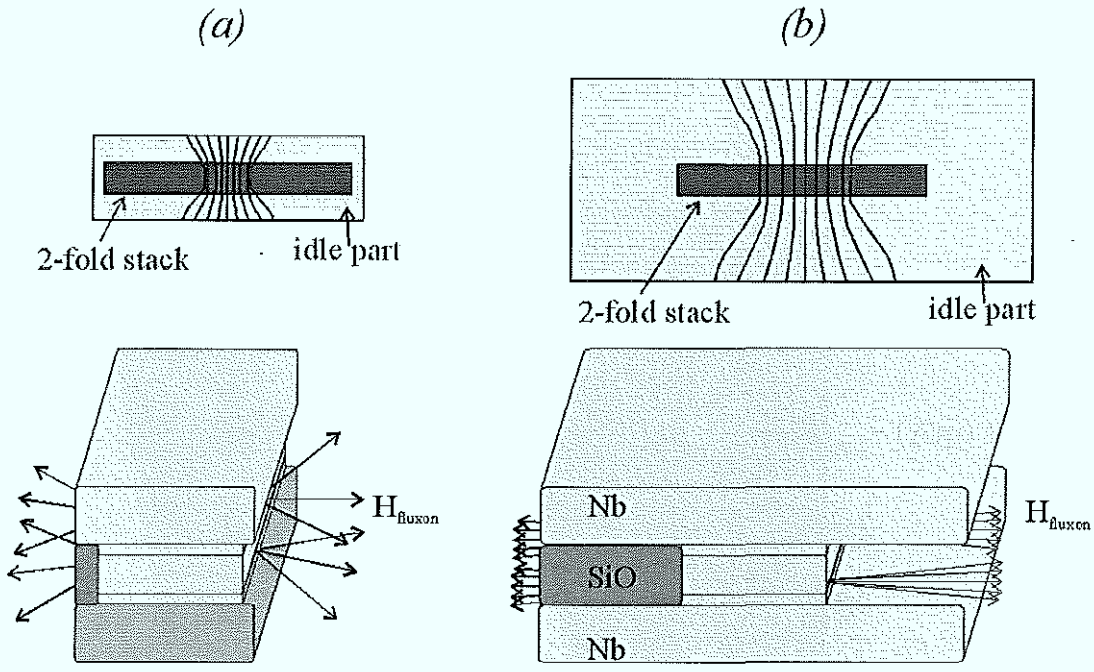


*Fig.5.3: Flux focusing for 2-fold stacks of window type junctions*

The possibility to measure directly the dependence of the two characteristic velocities on the coupling parameter was shown with good agreement[5.3] between experiment and theory.

Grønbech-Jensen et al.[5.12] have discussed an alternative mechanism of magnetic coupling between junctions in a stack, namely due to their magnetic interaction outside the junction. We investigated a series of samples of the so-called window geometry, with intention to test experimentally the effect of this alternative coupling mechanism. The spread of the magnetic field inside the idle part in window geometry can be expected to increase the external magnetic coupling between the junctions. Former investigations of the influence of the idle part on single junction properties[2.49,50] indicated the magnetic flux focusing effect. For different idle sizes, this effect should have a significant influence on the external coupling as is schematically shown in *Fig.5.3*.

The expansion of the magnetic field of the Josephson fluxon outside the junction causes this external coupling. According to Grønbech-Jensen and Samuelsen[5.12], the external coupling energy is

$$\Delta_0 = \frac{G}{4\pi}\frac{d'\lambda_J}{Wb}, \qquad \{5.7\}$$

where $d'$ is the magnetic thickness, $W$ is the junction width and $b$ is the thickness of the intermediate electrode. The geometrical prefactor $G$ is estimated to be *16* for the stacked system. On the other hand, the normalized internal coupling energy is

$$\Delta_1 = e^{-\frac{S}{\lambda_L}}. \qquad \{5.8\}$$

Both interactions are included in the dynamic field equations. Following the calculations of Grønbech-Jensen and Samuelsen[5.12] both internal and external coupling should contribute into the splitting velocities.

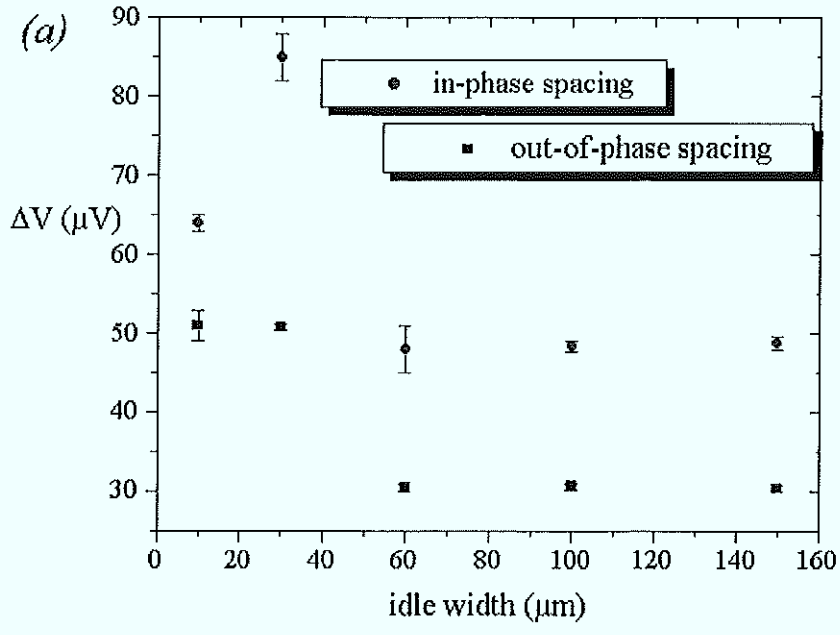

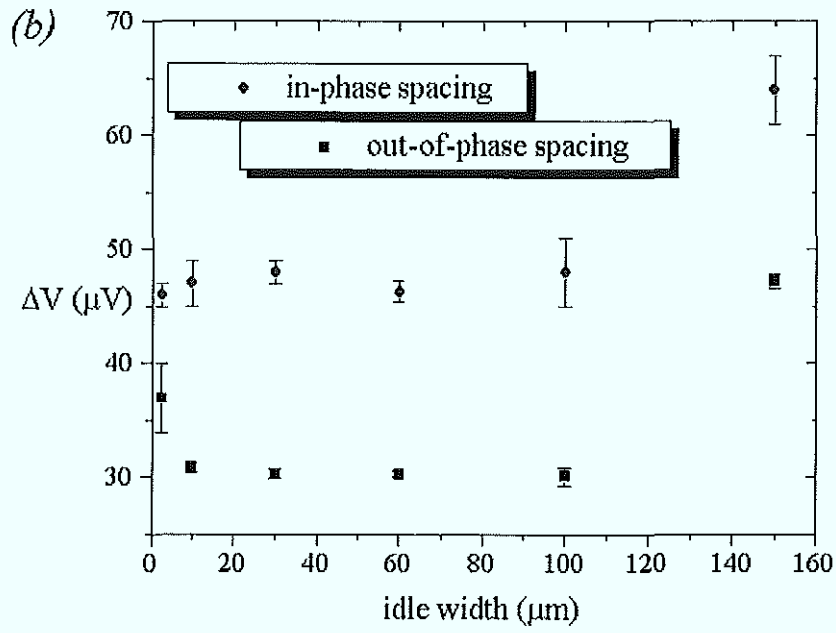


*Fig.5.4.: Voltage spacing for the in-phase and out-of-phase steps for junctions with different window sizes. Nb middle electrode thickness is 90nm: (a) [sample: window01.2.1/chip3], 200×10*μm², *(b) [sample: window01.2.1/chip2], 350×20*μm² *samples*

To produce samples with the same internal but different external coupling, I used different dimensions for the idle part in the same preparation run. The differences in the Fiske step voltage spacings are expected to show changes in the total coupling. The data for the voltage spacing with different idle part sizes are summarized in the *Fig.5.4.*

One can see that the results are rather scattered. In general, we can not interpret the full set of data in some specific way. Nevertheless, both samples show smaller difference between *in-phase* and *out-of-phase* spacing for the smallest idle size. It is possible that the external coupling is already giving its full contribution with idle dimensions of *5*μm and therefore there is no noticeable change in the measured dimension range. To check this argumentation new samples had been prepared [window01.2.2-4, see appendix]. The internal coupling was decreased by choosing a thicker intermediate Nb electrode of *100*nm and *120*nm. For these samples the splitting was not observed at all, probably due to a larger spread in $j_c$ of about *15%* which results from technological problems. Due to the time limitation of this thesis work and the main aim to prepare and investigate multi-layer Josephson junctions this particular work remains not completed. For the final answer on the external coupling problem more experiments are needed.

### 5.3. Magnetic field patterns

During my three month visit at the University of Salerno (Italy), I systematically investigated the magnetic field patterns of two-fold stacks prepared in Jülich. Annular, limear long and small overlap samples were measured, biasing both junctions in series. Other samples with access to the intermediate electrode were also studied. The *I-V* characteristics and magnetic field patterns show significant changes in comparison to single-layer junctions. These experiments have been compared with numerical simulations.

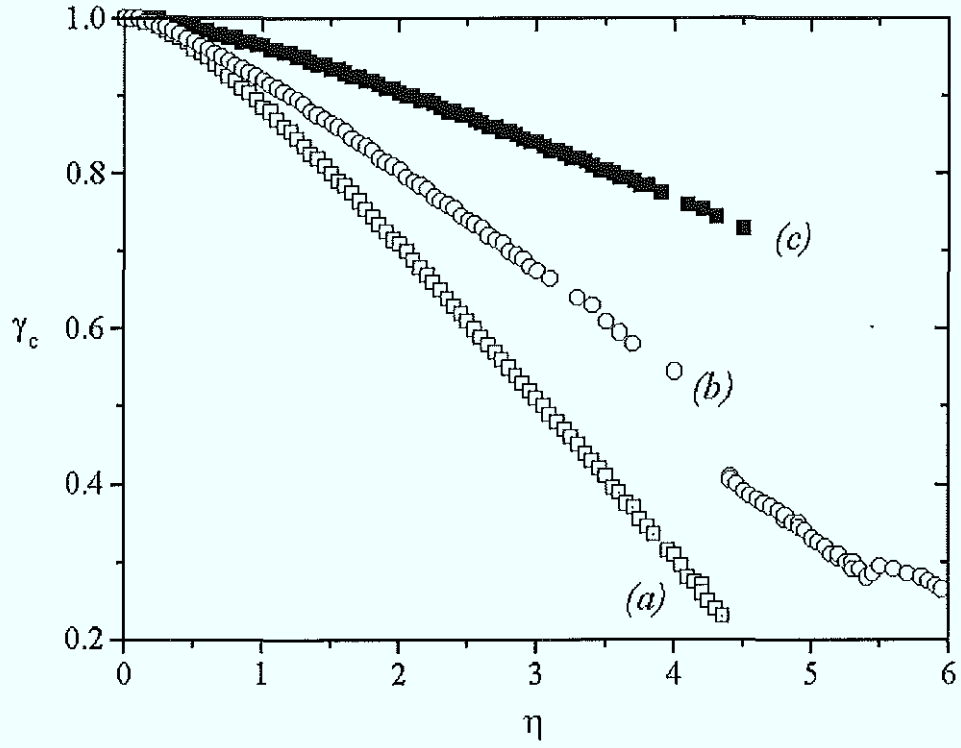


*Fig.5.5: Numerical simulation of the $I_c(H)$ pattern for an annular two-fold stack, using equation {5.10}; L=12, $\alpha$=0.05, $\eta$=3.0*

The interaction between the junctions depends strongly on the spatial non-uniformity of the local magnetic field. As shown in **chapter 2.5** in the annular junction geometry the external magnetic field induces the term which accounts well for the experimentally observed behavior of single junctions[5.13; 2.53,68]. In the model we consider the critical current density as the only varying parameter between the junctions in the stack. The equations can be written in the form

$$\begin{aligned}\phi_{1_{tt}} - \phi_{1_{xx}} &= \gamma - \sin\phi_1 - \alpha\phi_{1_t} - S\phi_{2_{xx}} - \eta k^2 \sin(kx) \\ \phi_{2_{tt}} - \phi_{2_{xx}} &= \gamma - \frac{1}{\Delta j}\sin\phi_2 - \alpha\phi_{2_t} - S\phi_{1_{xx}} - k_n \eta k^2 \sin(kx)\end{aligned} \quad \{5.9\}$$

We assume periodic boundary conditions, the bias current is represented by $\gamma$ and the external field by $\eta$. The factor $k_n$ defines the ratio between the effective external field acting on either junction and can be calculated using the different thickness of the superconducting layers. The geometrical factor $k$ is given for an annular junction by $k=2\pi/L,'$ with $L \triangleq L/\lambda_J$ as normalized circumference. A numerical result of the $I_c(H)$ pattern for equal critical current densities is presented in *Fig.5.5*. The parameters for simulation are taken from experiment.

Three patterns which appear in this calculation can be interpreted in the following way.

Pattern number *(a)*, the lower branch, displays a switching of at least one of the two junctions from the zero voltage state of both junctions. This branch should be measured at the zero voltage critical current.

The middle branch *(b)* displays a critical current of the junction number 1, while junction 2 remains in a non-zero voltage state. This branch should be measured at the first gap voltage.

The highest branch *(c)* now displays the situation opposite to *(b)*. Here the junction number 2 is at the gap voltage state and junction number 1 switches from zero voltage. Also this branch should be measured at the first gap voltage with exchanged roles of the participating junctions.

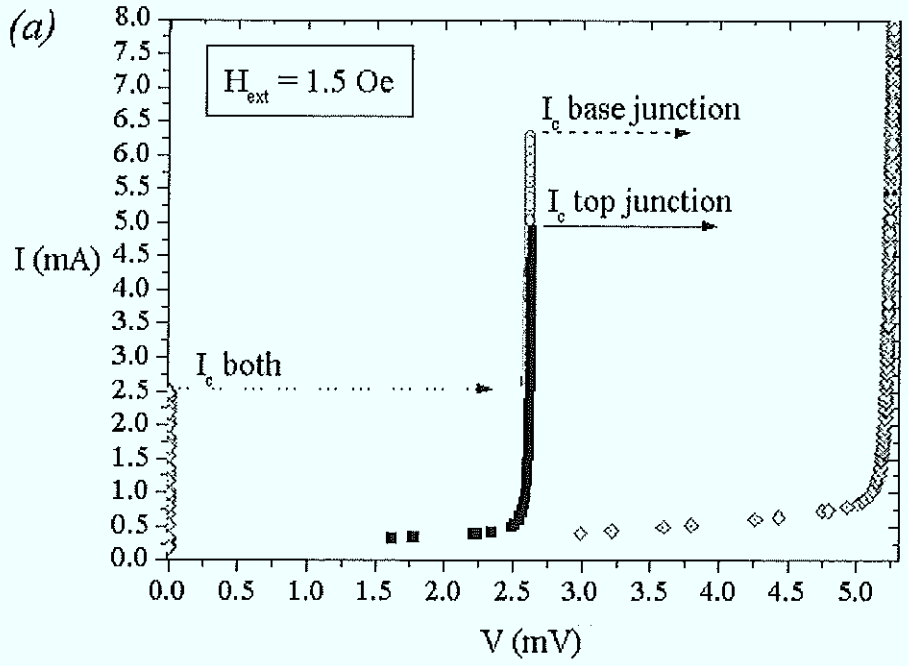


*Fig.5.6(a): I-V characteristic with $H_{ext}$=10*Oe

*[sample: annstac1.1.6/3.3], (diameter. 122*μm*; width 10*μm*)*

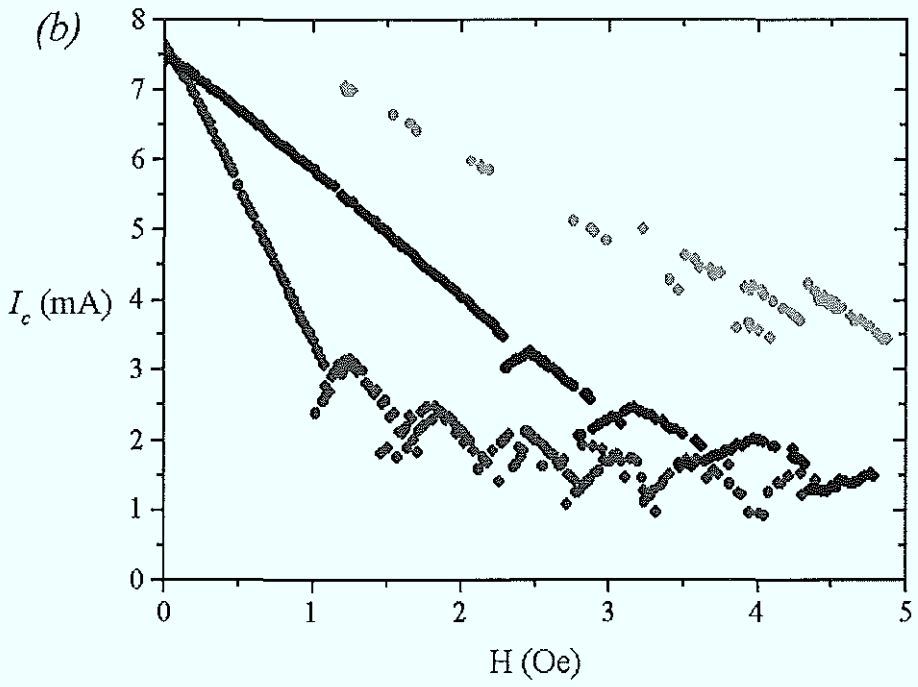


*Fig.5.6(b): $I_c(H)$ pattern for an annular 2-fold stack*
*[sample: annstac1.1.6/3.3], (diameter. 122μm; width 10μm)*

The measurements with long straight and annular junctions show the three characteristic critical current values. In *Fig.5.6* the *I-V* characteristic and the $I_c(H)$ pattern for an annular sample are shown.

This phenomenon was already reported experimentally earlier[5.10,14,15]. To understand this behavior better, we focused our attention on a single junction of the stack. The calculation of the phase derivative for an annular geometry was done for a small magnetic field ($\eta=3$). We determined the zero voltage state and the finite voltage state of the junction. The resulting phase derivatives are presented in *Fig.5.7*.

The lower amplitude curves are corresponds to the zero voltage state and the higher amplitude displays the finite voltage state of the junction. At zero voltage state the junction is in a Meissner-like state and a screening supercurrent prevents the field from entering the barrier completely. On the contrary, when the junction is in the dynamic state, the external field can freely enter the barrier and modulate the phase. A less perturbed state occurs when the first junction is static, and a more perturbed state is when the first junction has switched to a dynamic state.

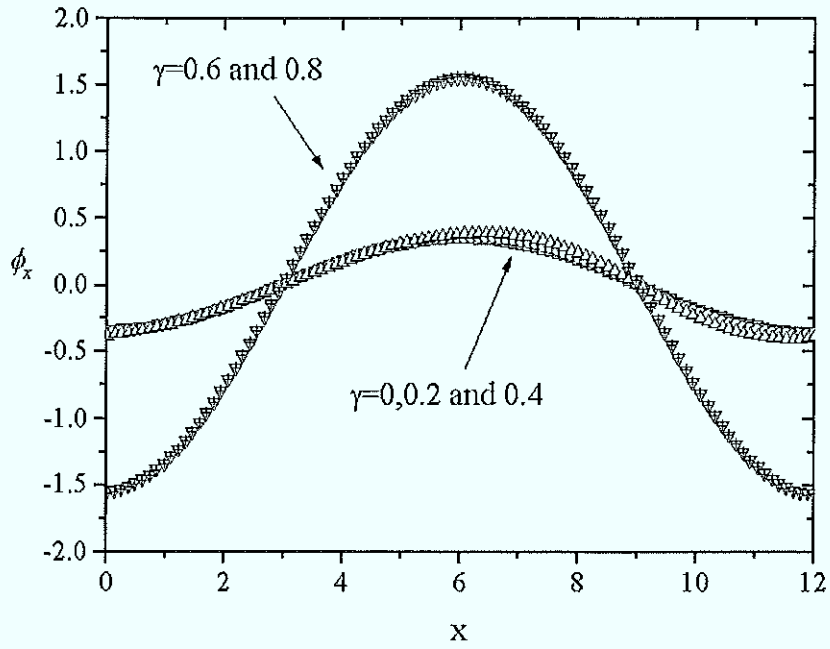


*Fig.5.7: Numerical calculated spatial phase derivative along an annular junction for different bias γ, L=12, α=0.05, η=3.0*

Using the access to the intermediate electrode for a linear two-fold stack, it was possible to separate directly the measured critical current values for both junctions. We biased the single junctions separately to receive the *I-V* characteristic and $I_c(H)$ pattern. From the separate measured *I-V* characteristics (*Fig.5.8*) the different gap voltages of the two junctions can be used to distinguish the two values measured at the first gap voltage, as shown in *Fig.5.6.*

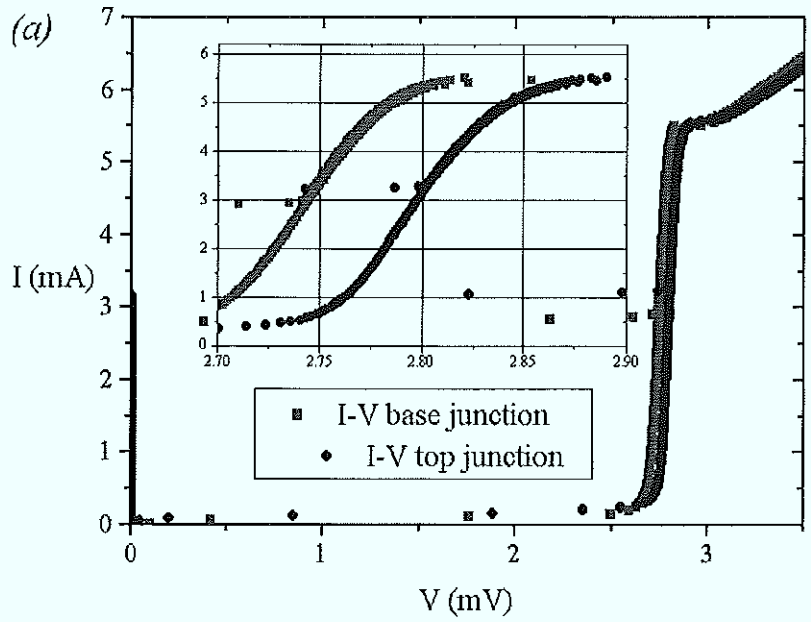

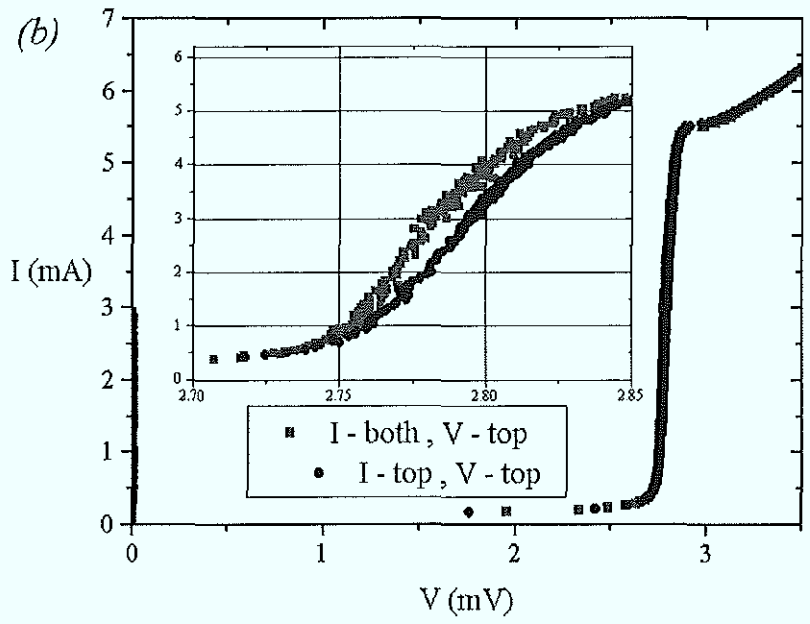


*Fig.5.8: I-V curves of individual junctions in a 2-fold stack; [sample: amstac1.2.16/4.4] (200×10μm²)*
*(a) separately biased, (b) biased in series*

The difference between *Fig.5.8(a)* and *(b)* is due to the bias current distribution. In fact, the symmetric overlap biasing was realized only for one of the junctions, while for the second one the biasing was asymmetric as demonstrated in *Fig.5.9*.

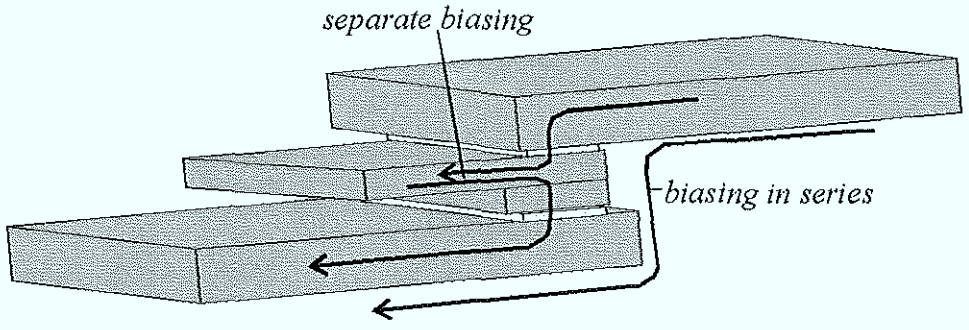


*Fig.5.9: Bias current scheme for the separate measurements*

The $I_c(H)$ measurements for various biasing schemes differ from each other, as shown in (*Fig.5.10*). The pattern with the highest critical currents for larger field values is observed only for biasing the junctions in series.

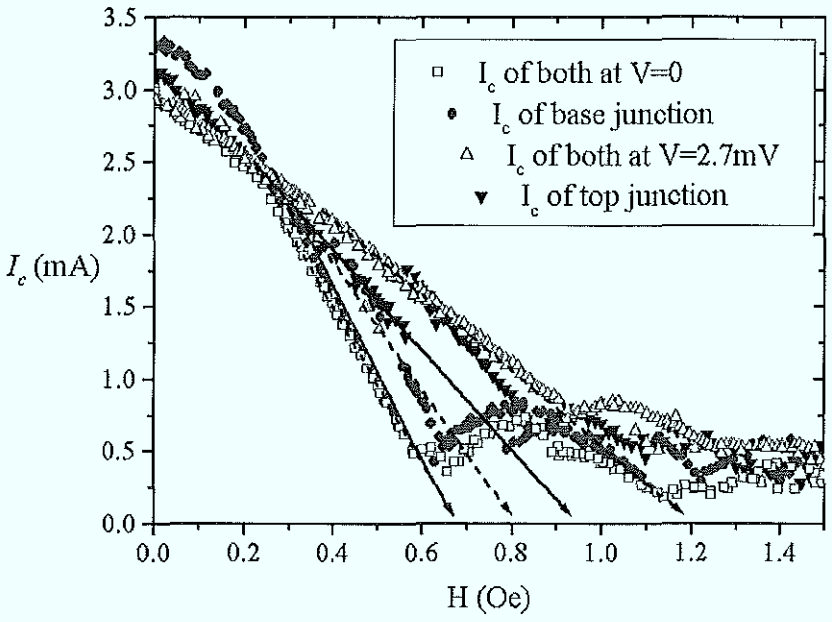


*Fig.5.10: $I_c(H)$ for current bias in series and separate biased junctions [sample: annstac1.2.16/4.4], (200×10μm²)*

In measurements of $I_c(H)$ curves we followed also another measurement procedure. Fixing the bias current below the critical value, the magnetic field was increased up to the moment of the voltage jump. Then the field is set to zero again and the bias too. For a next point of the pattern we fixed another bias current value. In this way one can measure "hidden" branches of the *Ic(H)* curve corresponding to the fluxon-free state as shown in *Fig.5.11*.

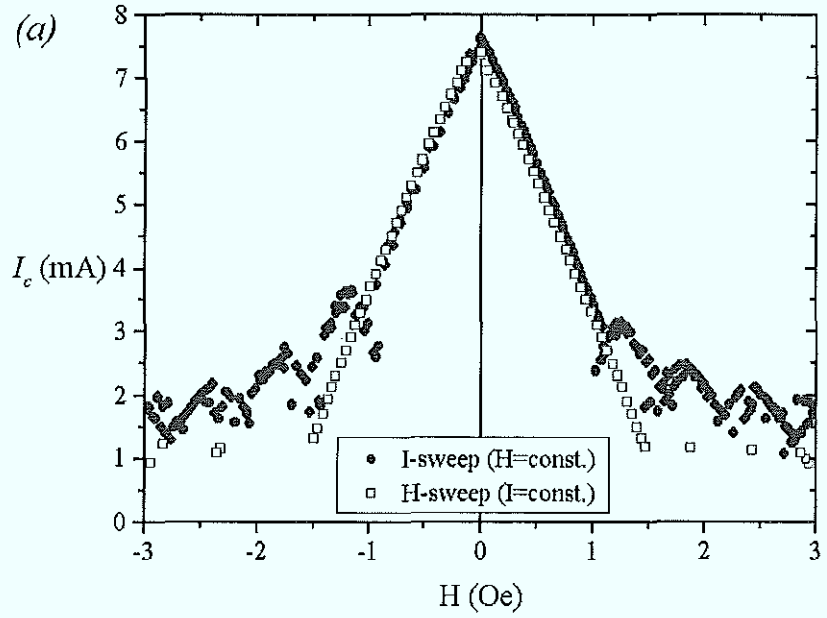


*Fig.5.11(a): $I_c(H)$ at V=0 for I-sweep and H-sweep, [sample: annstac1.2.6/3.3], (diameter 122μm, width 10μm)*

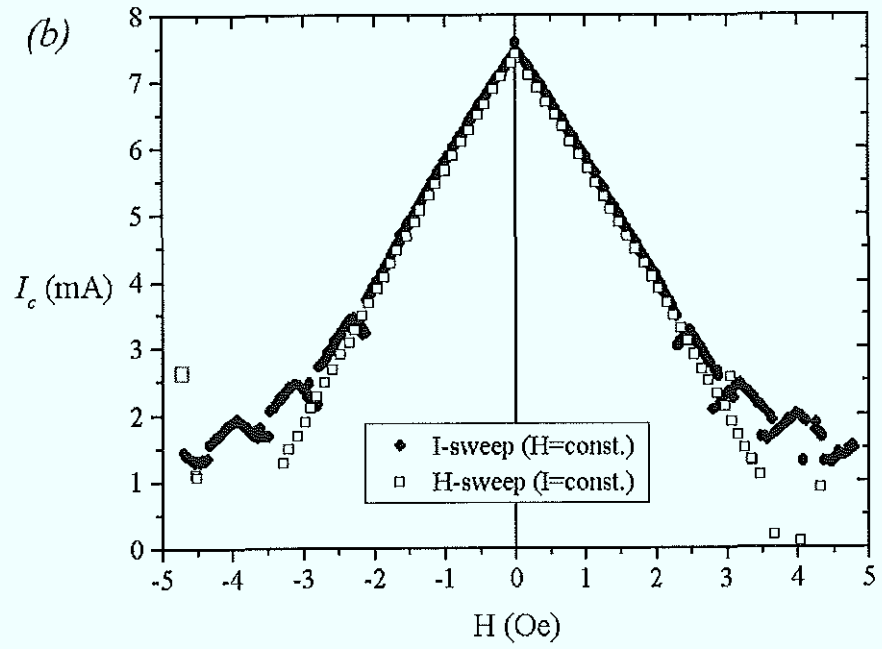


*Fig.5.11(b): $I_c(H)$ at V=2.7*mV *for I-sweep and H-sweep; [sample: annstac1.2.6/3.3]*

The measurements confirm three different critical current values (νυσ *Fig.5.12*) for a two fold stack. As in the numerical prediction, the critical current of one junction strongly depends on the static or dynamic state of its neighbor junction.

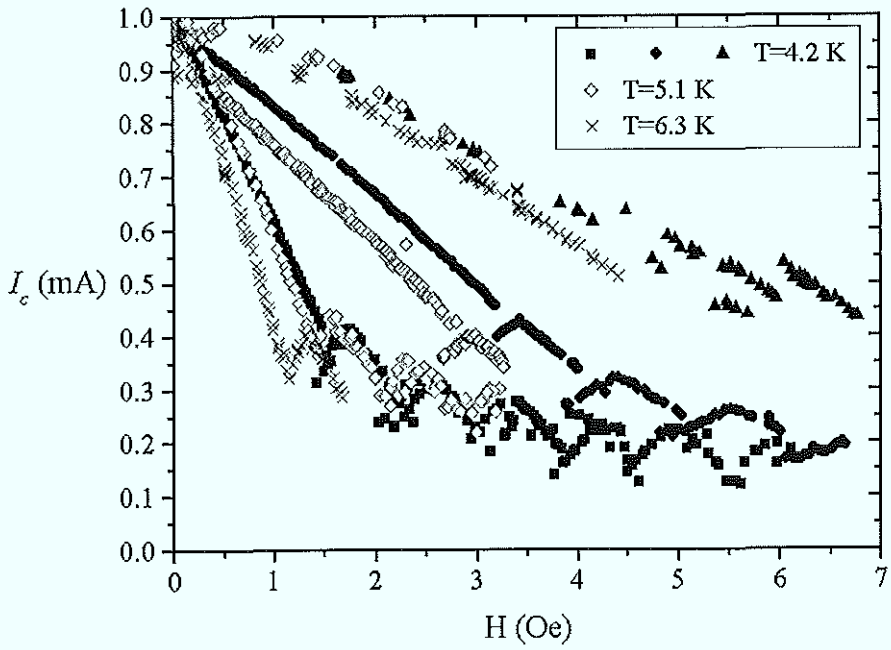


*Fig.5.12: $I_c(H)$ pattern at T=4.2*K, *T=5.0*K, *and T=5.8*K; *[sample: annstac1.2.6/3.3]*

It has been shown analytically[5.15] that a high-voltage dynamic state of one junction in a stack cancels any influence of its outer electrode on the second junction. The high voltage state can also be characterized in the pendulum model as a whirling state. If one of the junctions is in the whirling state, the other junction behaves identically to a single junction with one thin electrode given by the thin intermediate Nb layer. The measurements do not show any anomaly in the temperature dependence, as shown in *Fig.5.12.*

In addition, we observed the influence of the junction idle part ("window") dimension on the magnetic field dependence. The expected increase of the inline character for larger idle dimensions[2.50] and the flux focusing effect are observed clearly for the critical current value at zero voltage. The measured values at the first gap voltage (upper slope) show nearly no change for different idle dimensions (*Fig.5.13*). As mentioned before the upper slopes display the single junction behavior with thin electrode. For this condition the effect of the idle part is compensated by the penetration of magnetic flux inside the second junction. The two junctions had been prepared in-situ without an access to the intermediate electrode. In this measurements the third slope of $I_c(H)$ can not be resolved.

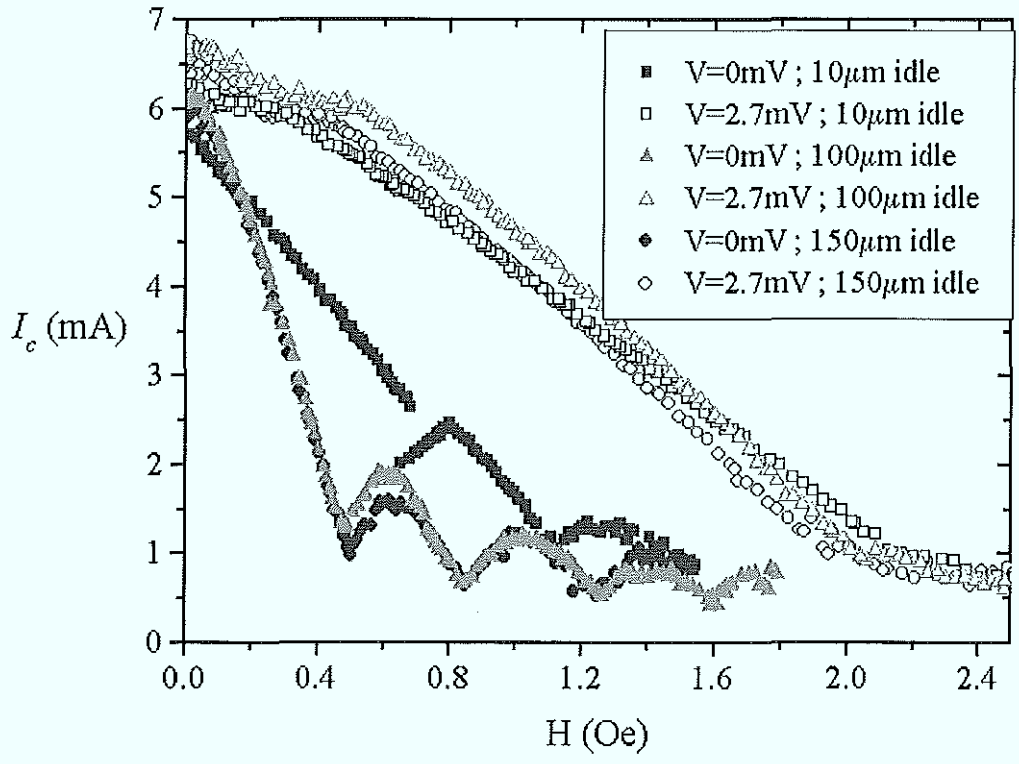


*Fig.5.13: $I_c(H)$ pattern for different idle area; [sample: window01.2.3/3.3], (200×10μm²)*

### 5.4. Cherenkov Radiation

Another interesting case is the presence of a single fluxon in one junction of a 2-fold stack[5.16]. The idea of Cherenkov radiation, generated by a moving fluxon in a Josephson junction, was discussed already some time ago[4.2; 5.17,18]. Recently experimental investigations were carried out and here I want to present the results obtained with two-fold annular junctions, prepared during my work. The measurements and calculations were performed by Edward Goldobin and Andreas Wallraff. Cherenkov radiation is a very general phenomenon and it can be generated, when the velocity of a particle (soliton) $v = u\bar{c}$ is equal to the phase velocity of linear electromagnetic waves $\omega/k$. For a single junction this is not possible, because the asymptotic maximum velocity for the soliton, taken as a particle with its own mass and velocity, is the Swihart velocity $\bar{c}$. This velocity is at the same time the minimum velocity for linear electromagnetic waves. Also, for the symmetric (one soliton in each junction) or antisymmetric (soliton in one and antisoliton in the other junction) states in *2*-fold stacks do not lead to the generation of Cherenkov radiation. However, Cherenkov radiation may occur in the asymmetric mode with just one fluxon in the whole stack. Due to the conservation of the trapped flux in a superconducting ring the annular junction geometry offers the advantage here because it conserves the number of fluxons. To verify the state with just one trapped fluxon we use the $I_c(H)$ pattern at zero voltage and at the first gap voltage. The coupling parameter and the velocities for the investigated system are measured using the asymptotic voltages for the *in-phase* and the *out-of-phase* Fiske steps, as described in **chapter 5.2**. The resulting coupling parameter for the intermediate electrode of *90*nm is about $S \approx -0.55$ at *4.2*K. The mean diameter of the fabricated stack was *132*μm with the width of *10*μm. Calculating the Josephson penetration depth we estimate the normalized diameter to be around *7*. Numerical simulations[5.16] show the range of possible fluxon velocities that are larger than the velocity $\bar{c}_-$. Following the argumentation above, for this situation Cherenkov radiation may exist and be manifested as an oscillating wake behind the moving soliton. The simulations[5.16] show this wake for velocities $v \geq \bar{c}_-$, as demonstrated in *Fig.5.14*.

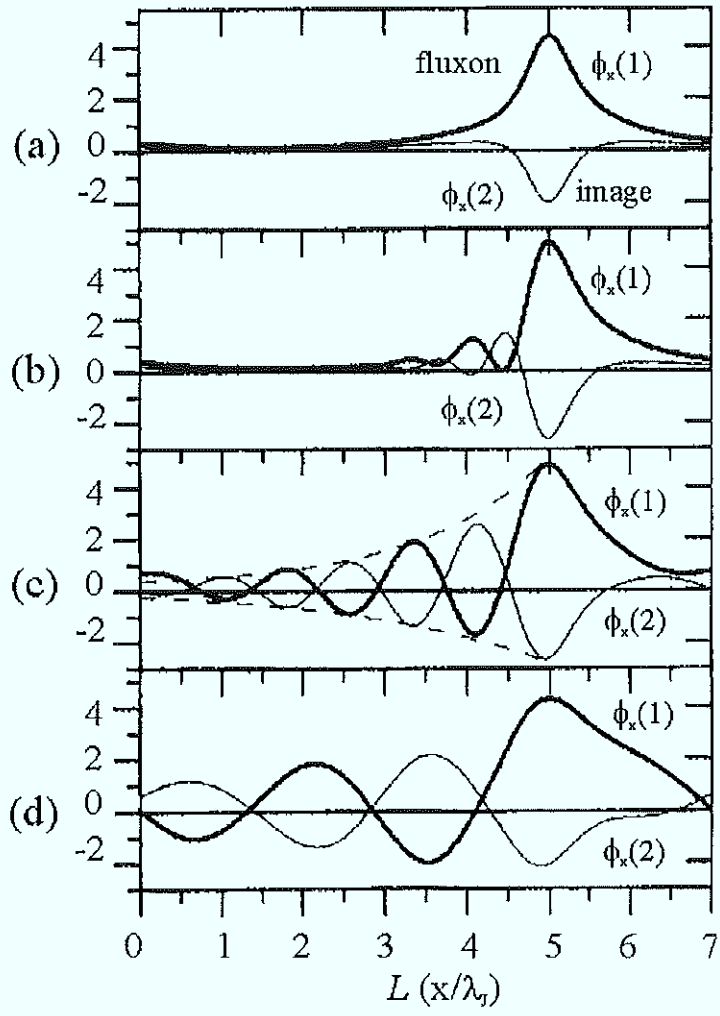


*Fig.5.14*[5.16]*: Phase derivative for junction (1) and (2) with one fluxon in (1)*
*(a) - (d) correspond to the bias current positions marked in Fig.5.15(b)*

With increasing soliton velocity the wavelength of the radiation increases while the amplitude and length of the wake quickly grow. If the wake is long enough that an integer number of this oscillations fits in the ring, an interaction between the moving soliton and this wake is possible. This interaction is manifested by new resonant states in the *I-V* curve. Such resonant steps are found in the investigated samples in good agreement between simulations and experiment (*Fig.5.15*).

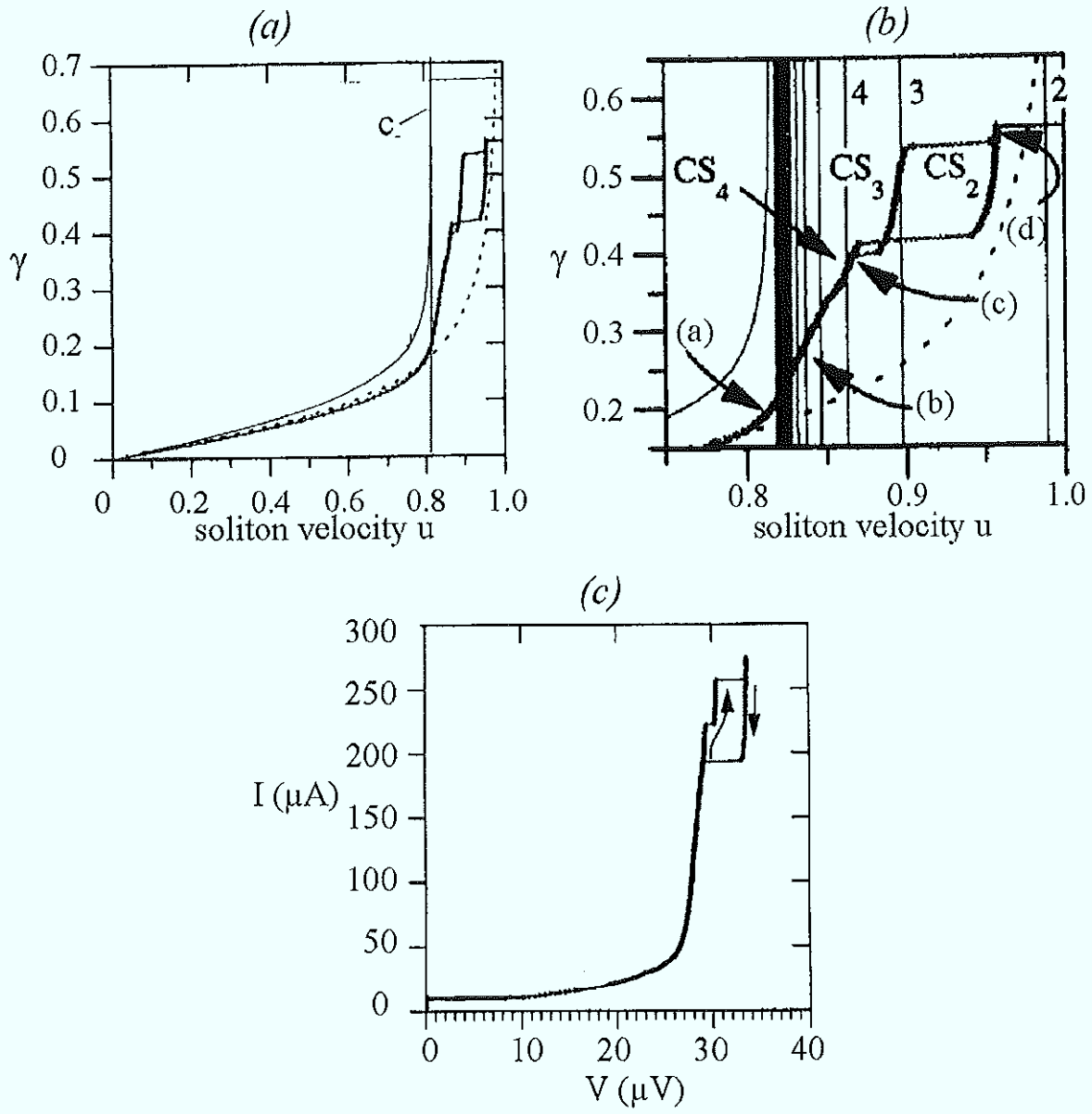


*Fig.5.15*[5.16]*: Cherenkov resonance in the I-V characteristic,(a) and (b) numeric simulation; (c) experiment*

An unusual broad band non-Josephson radiation emission from BSCCO samples recently observed by Hechtfischer et al.[5.19] can also be interpreted as possible result of Cherenkov radiation. Currently further work in this direction is in progress.

# 6. Multi-layer Josephson tunnel junctions

First experimental investigations of three-fold stacks[6.1,2] showed complicated features of the measured *I-V* curves. The intrinsic Josephson effect in BSCCO and similar structures[6.3,4] increased the interest in modeling of multi-stacked systems. The possibility to check theoretical predictions with an experimentally reliable and well controlled system of low $T_c$ junctions turned out to be an important and challenging task. The previous work about two-fold stacks shows two significant states, the *in-phase* and the *out-of-phase* modes. For a multi-layer stack, it is possible to imagine various mixed states between these modes. This, in fact, for *N*-layer stack leads into the splitting of the dispersion relation in *N* different branches[5.2,3]. Since a long junction can be considered as one-dimensional resonator, for multi-stacked junctions the dimension perpendicular to the layers represents an additional degree of freedom.

For a large number of stacked junctions, the presented dc measurements are always done by biasing the whole stack in series. Therefore, the displayed voltage is the sum of the single junction voltages and the bias current flows through all junctions in the stack.

## 6.1. Kleiner modes in *N*-fold stacks

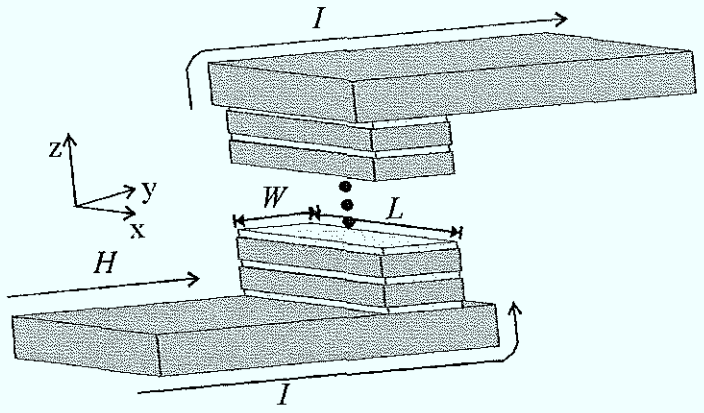


*Fig.6.1: Scheme of an N-fold stack*

According to Kleiner's model [6.3], Josephson junction stacks form a two dimensional resonator in the cross-sectional plane perpendicular to the tunnel barriers. In other words, the coherent vortex motion in a stack is promoted by two dimensional resonances that are the two dimensional analog of Fiske resonances in single junctions. Kleiner showed analytically and

with numeric simulations that these resonances are manifested as voltage steps in the *I-V* characteristic at voltages of

$$V_{n_x,n_z} = \frac{\Phi_0}{2L\sqrt{\varepsilon\mu_0}} n_x \sqrt{\frac{d}{d' + 2s\cos\frac{n_z\pi}{N+1}}} \,. \qquad \{6.1\}$$

Here $n_x$ is the resonance number in a layer plane and $n_z$ is the vertical resonance number. $L$ is the junction length, $d$ the tunnel barrier thickness and $d'$ the magnetic thickness. The coupling parameter is $s = {}^{-\lambda_L}\!/_{\sinh(b/\lambda_L)}$. The resonances in *z-direction* can be understood as standing waves of the electrical field component as demonstrated in *Fig.6.2.*

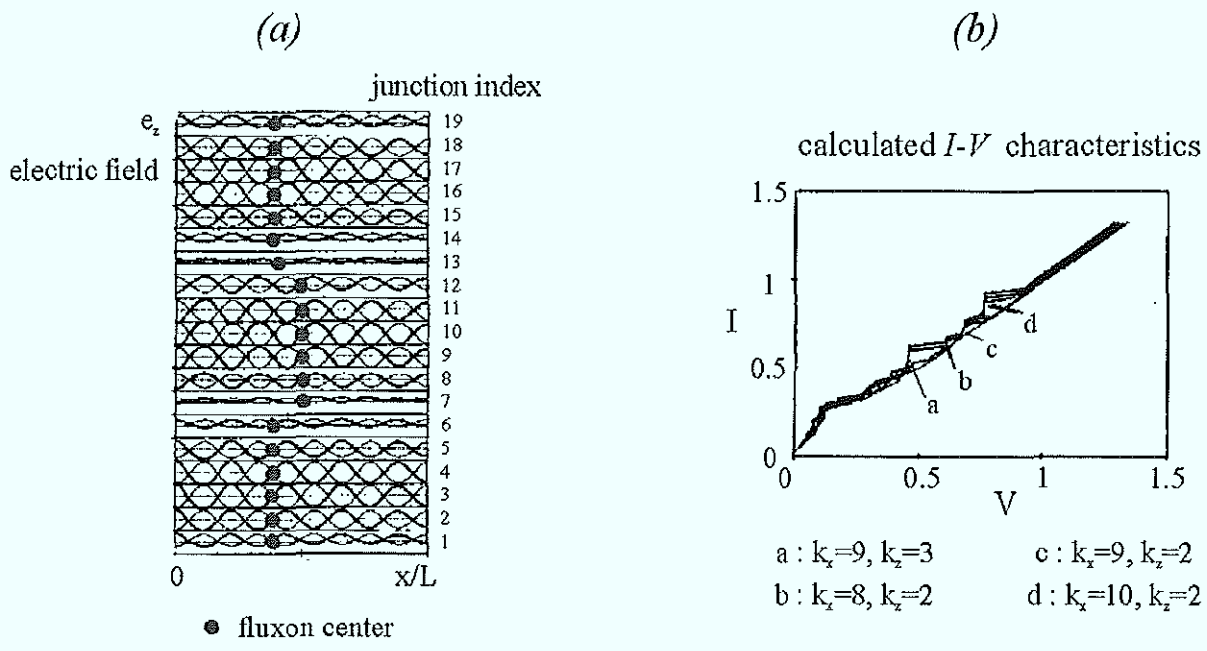


*Fig.6.2*[6.3]*: Kleiner modes for a 19-fold stack; (a) fluxon configuration, and (b) I-V characteristics*

In this picture the dots mark the centers of fluxons. The resonance shown in *Fig.6.2(a)* is characterized by three domains of *in-phase* flux motion. The expected resonance voltages can be calculated and compared with an experiment. Some calculated examples[6.3] of Kleiner steps are given in the *I-V* curve in *Fig.6.2(b)*. If we use the parameters for our typical *7*-fold Nb stack in formula {6.1} (the intermediate thickness is *78*nm, the London penetration depth is *90*nm), the calculated voltage steps for a junction of *200*μm length are plotted in *Fig.6.3.* The *x-axis* is defined as *z* resonance number. The plotted voltages are given according to the resonance number $n_x=1$.

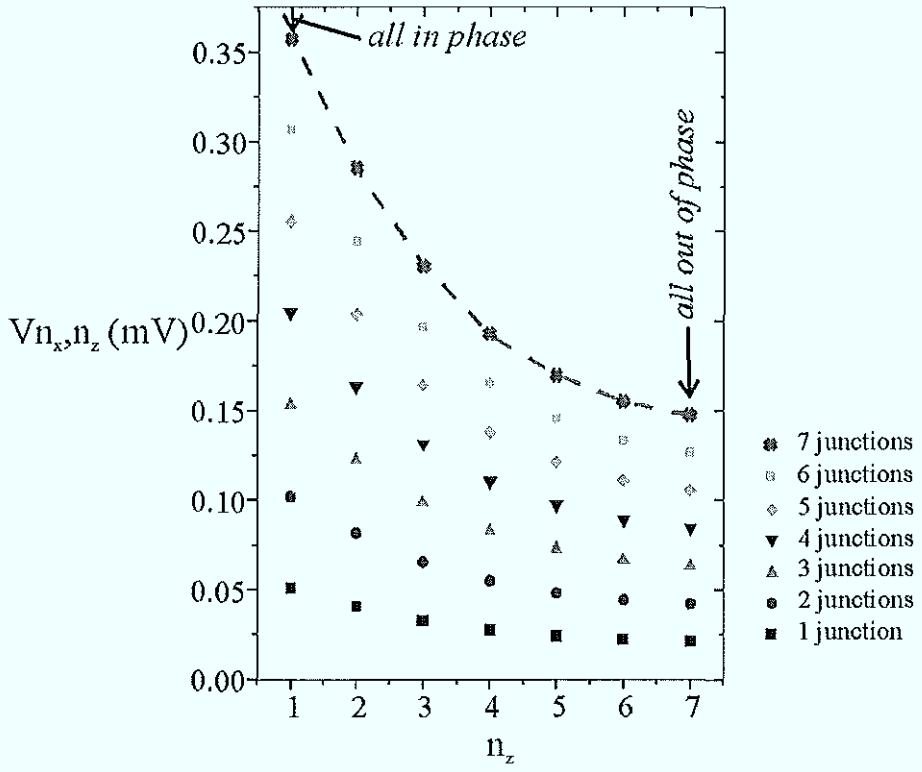


*Fig.6.3: Kleiner mode voltages for a Nb-based 7-fold stack, $n_x$=1*

The indicated junction number is refering to the number of equivalent junctions participating in this voltage resonance. The demonstrated resonances (*Fig.6.3*) apply to a symmetric stack. In reality, the bottom and the top electrodes usually have to be chosen thicker than the inner electrodes and they influence significantly the properties of the outer junctions in the stack.

### 6.2. Dc measurements at zero field

Measurements of 7-fold stacks with intermediate Nb electrode thickness of around 78nm are shown in *Fig.6.4.*

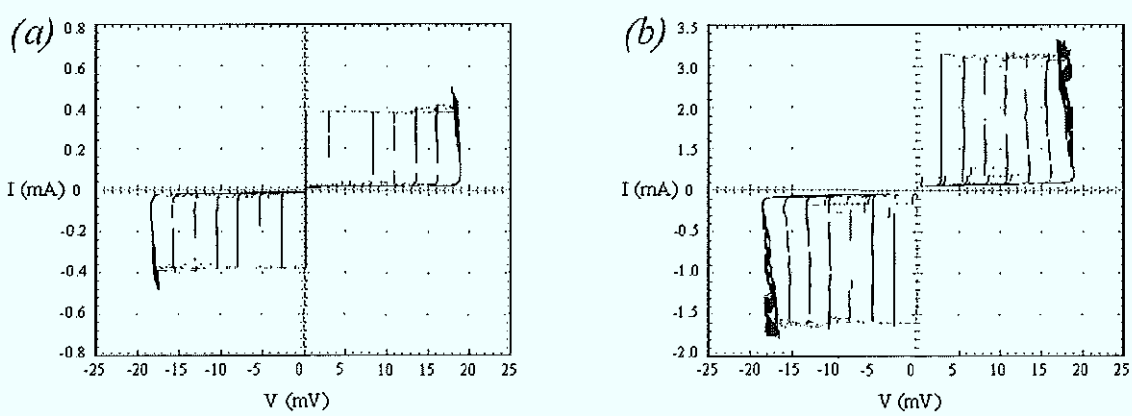

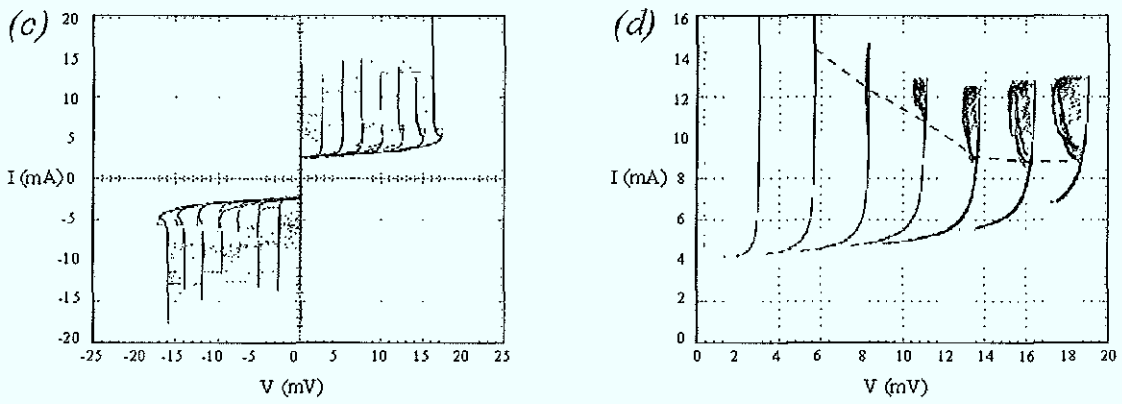


*Fig.6.4: I-V curve of 7-fold stacks with $\Delta I_c$<5%*
*(a) 10×10μm² junction; [sample: window01.7.1/1.8] (b) 20×20μm² junction; [sample: window01.7.1/1.1], and (c),(d) 350×20μm² junction; [sample: window01.7.1/2.2]*

Seven single-junction gap structures are resolved which is the evidence for seven tunnel junctions. For small junctions of *10×10*μm² *(a)* we define the spread in critical current as less than *5%*. Equal properties are shown for a *20×20*μm² *(b)* junction area. We observe a back bending of *I-V* curves at the gap region for higher voltages and note that it is much more pronounced for the long junctions *350×20*μm² *(c),(d)*. This effect is caused by heating in the intermediate electrodes due to the injection of quasiparticles. The passivation of the stack side walls by anodic oxidation thermally decouples the intermediate layers from the environment. The remaining heat flow is through the outer electrodes. If an inner junction switches into a gap state, the injected quasiparticles heat the inner electrodes. The importance of the thermal coupling at the side walls is the strong dependence of the heating on the junction size. In addition, the back bending occurs at smaller and smaller bias current with increasing the gap number (higher voltages), as indicated by the dashed line in *Fig.6.4(d)*. The individual critical currents in the long junction stack are suppressed due to this heating and, also, due to trapped flux in the superconducting electrodes near the junction. The top electrode covers an altitude differences of more than *1*μm for these samples. With a thickness of *600*nm, the edges near the junction form a thin Nb film, where flux is trapped easily. In the following sample preparations the critical current density was decreased, and the resulting lower current injection minimized the heating. This effect is shown for a *9*-fold stack in *Fig.6.5*. In addition, better planarization by evaporating SiO helped to avoid flux trapping in the top film.

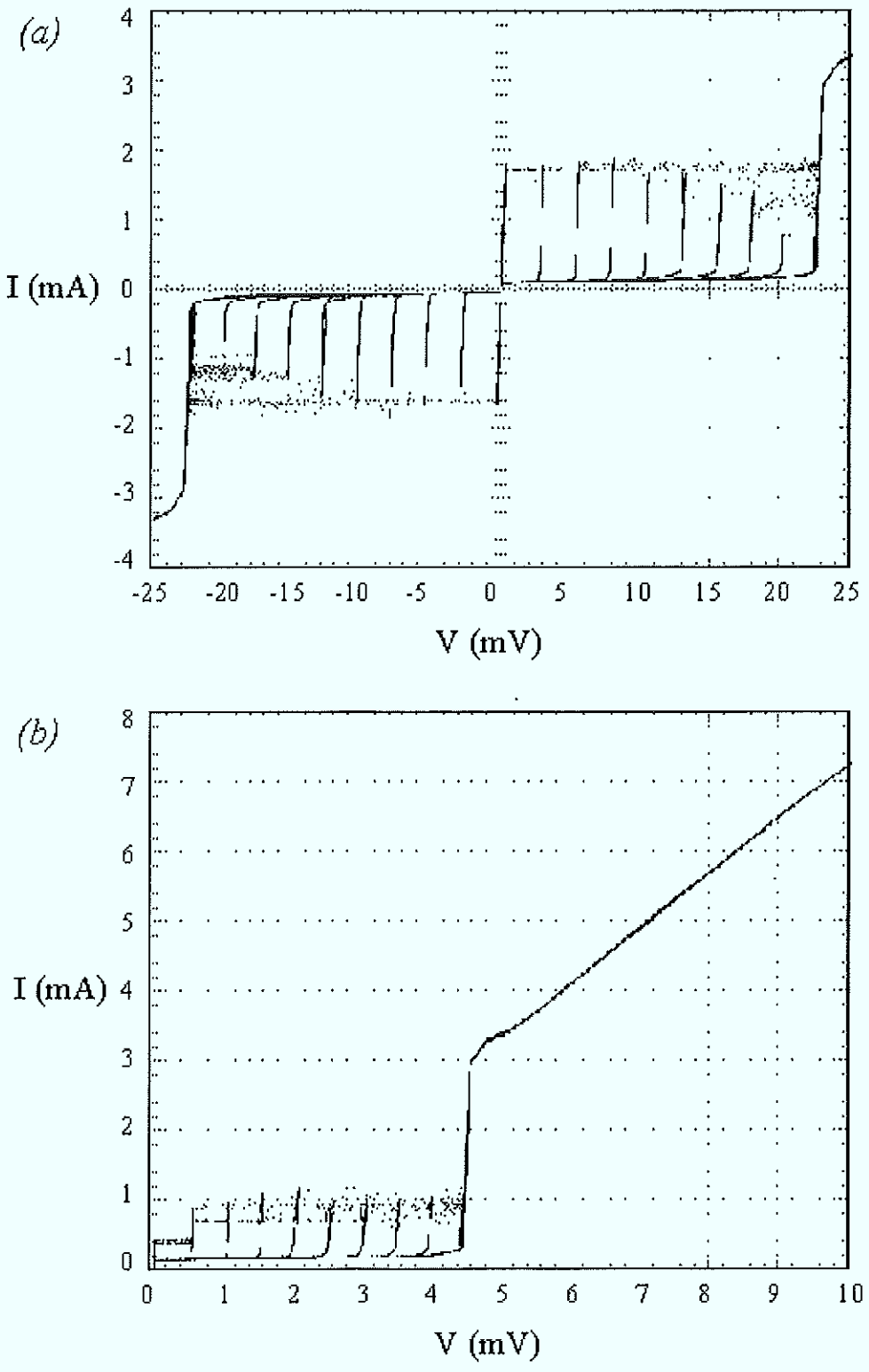


*Fig.6.5: I-V curve for 9-fold stacks with lower critical current density; [sample: winfin9.1/3.2], (200×10μm²)*

For higher gap number in *Fig.6.5* we still observe the suppression of the critical current. But the backbending effect disappeared for these samples. When increasing the bias current along

the resistive branch we do not see spread changes in its slope. This is another evidence of low parameter spread for the stack. The stacked long junctions do not show regular ZFSs. Some irregular high voltage ZFSs were measured for small junction stacks, as shown in *Fig.6.6*. The origin of these voltage steps is up to now not clear and they seem to have rather irregular background.

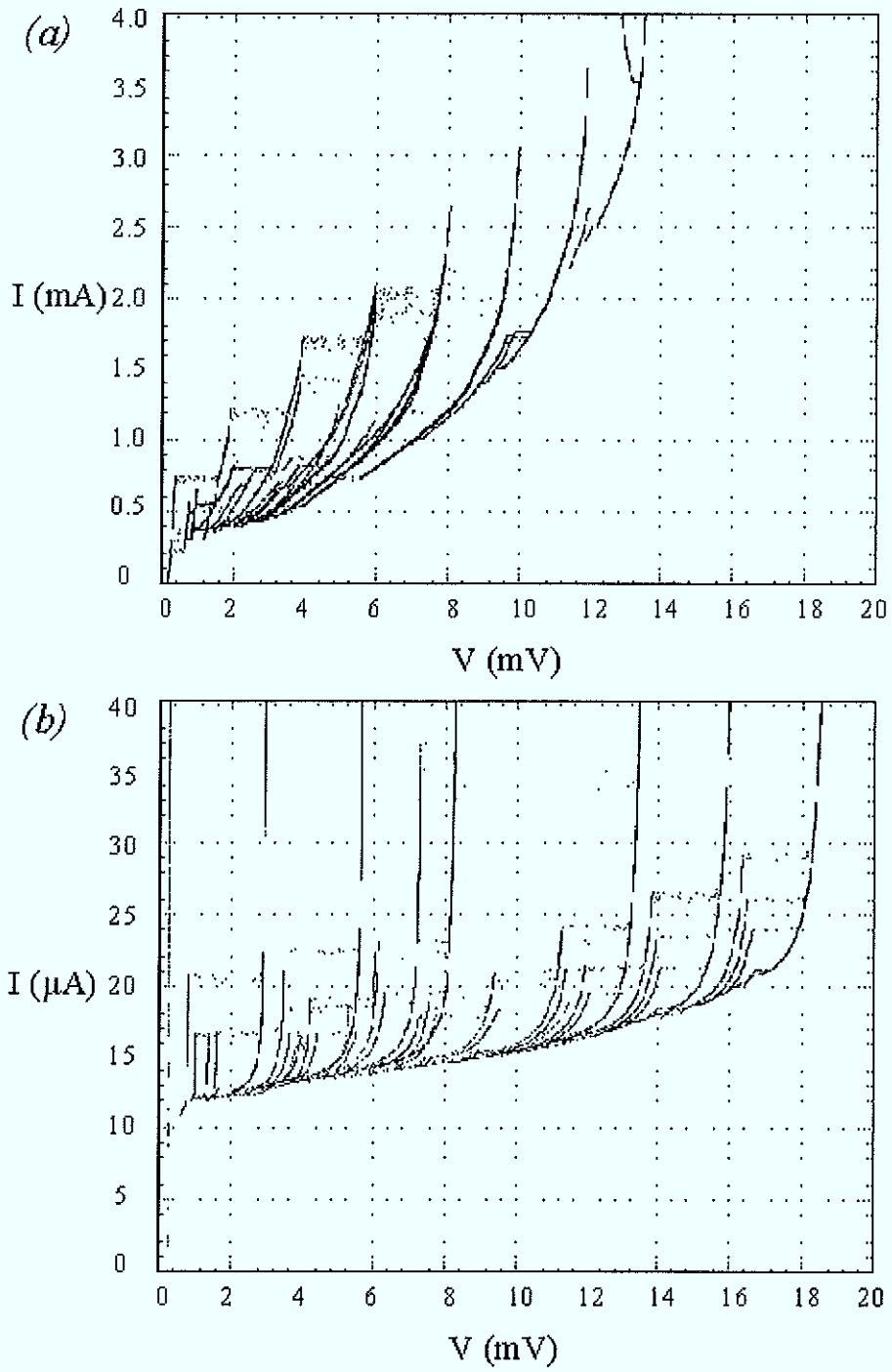


*Fig.6.6: Zero field resonances for 7-junction stacks*

*(a) [sample: window01.7.1/2.2], (350×20μm²)*

*(b) [sample: window01.7.1/1.8], (10×10μm²)*

### 6.3. Dc measurements with external magnetic field

To observe the flux-flow states, we applied an external magnetic field in plane of the junction and perpendicular to its larger dimension (see *Fig.6.1*). For the discussed *7*-fold stacks, we observe simultaneously the flux-flow behavior at different gap voltages. *Fig.6.7* shows the storage of many bias current sweeps for a continuous magnetic field sweep.

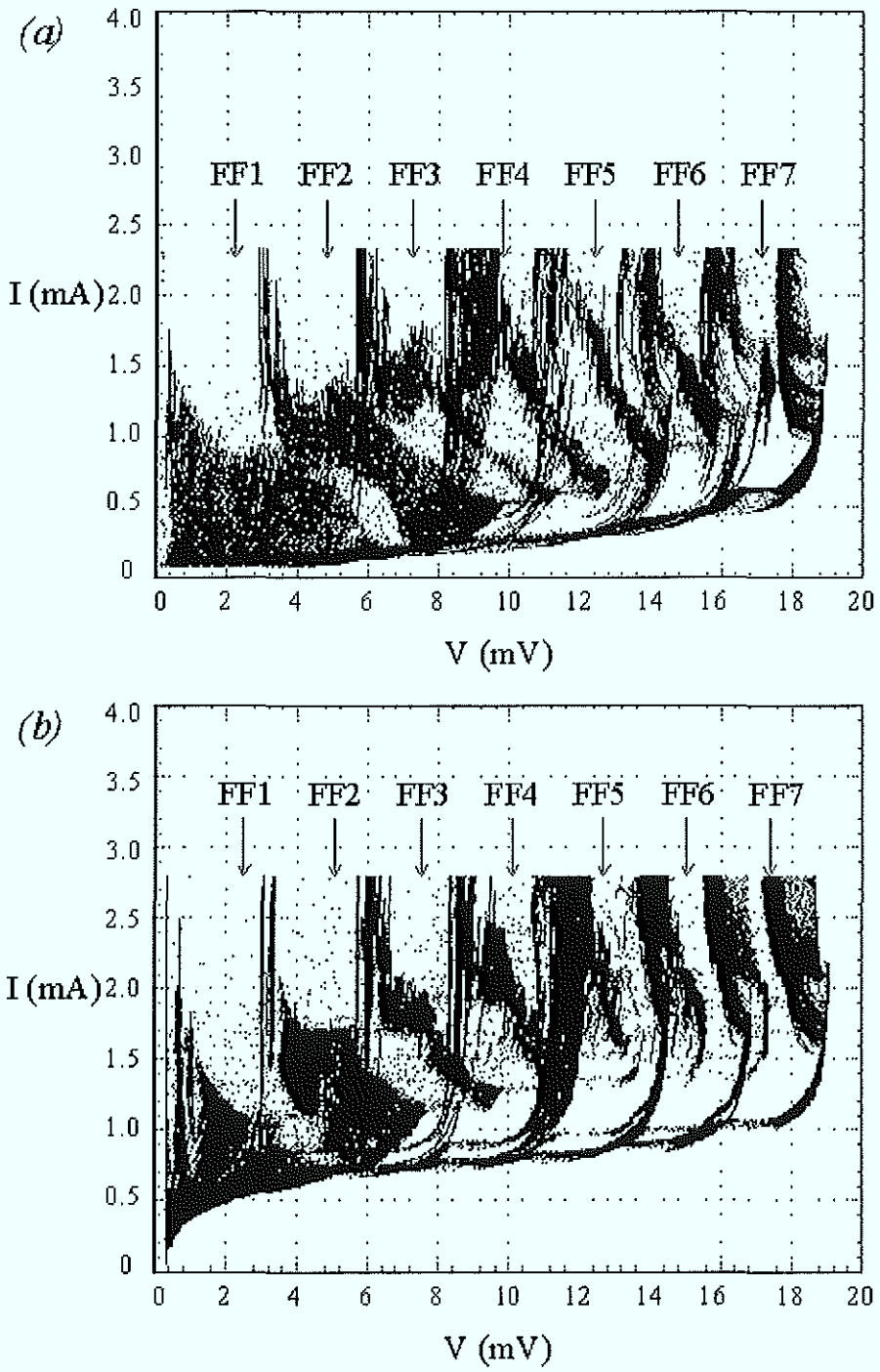


*Fig.6.7(a)(b): I-V characteristics for 7-fold long junction stacks with continuos H-sweep*
*(a) [sample: window01.7.1/4.3], (450×10μm²) and (b) [sample: window01.7.1/1.14], (200×20μm²)*

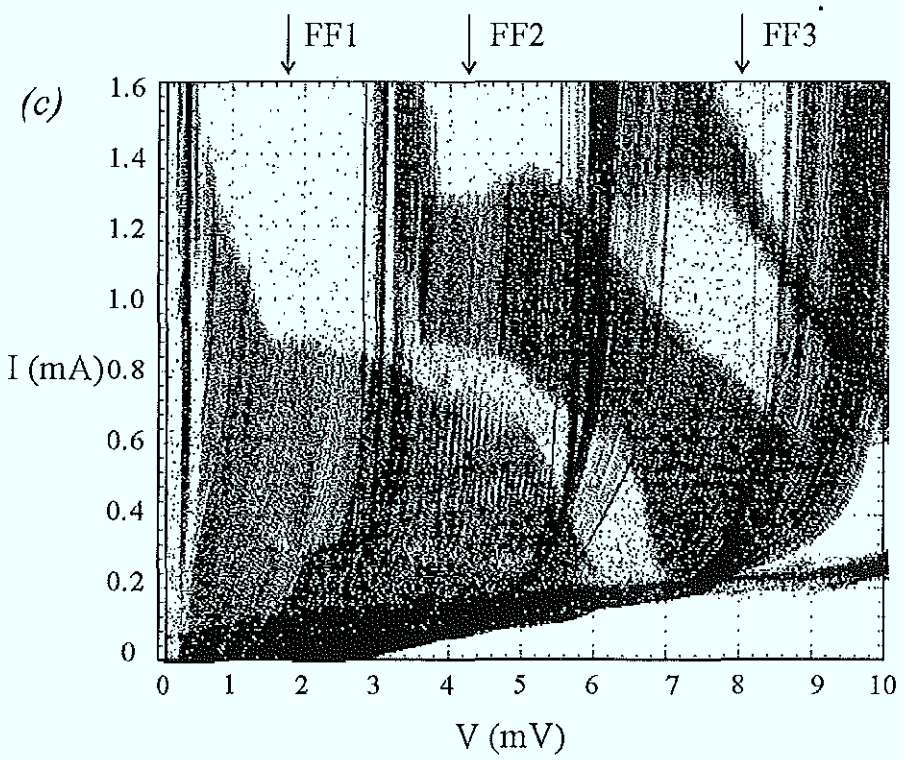


*Fig.6.7(c): I-V characteristics for 7-fold long junction stacks with continuos H-sweep [sample: window01.7.1/4.3], (450×10μm²)*

We distinguish different groups of flux-flow branches (FF1; FF2; ...; FFN) according to their offset gap voltage. Starting from zero voltage, all junctions are supposed to participate in the measured voltage. By studying in detail the FF1 branch (*Fig.6.8*) we can subdivide the stored curves in three groups.

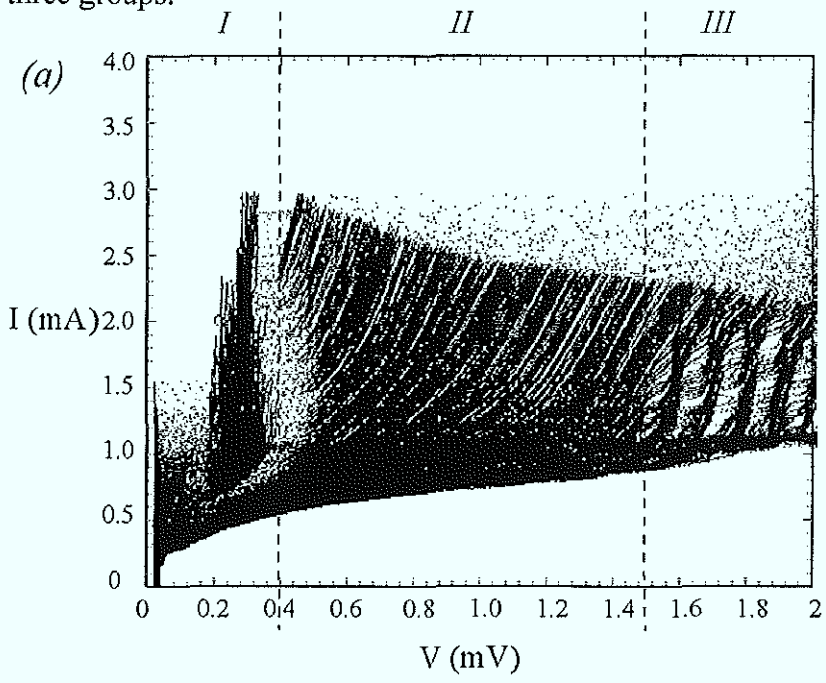


*Fig.6.8(a): I-V curve of 7-fold stacks with sweeped magnetic field [sample: window01.7.1/2.3], (350×20μm²)*

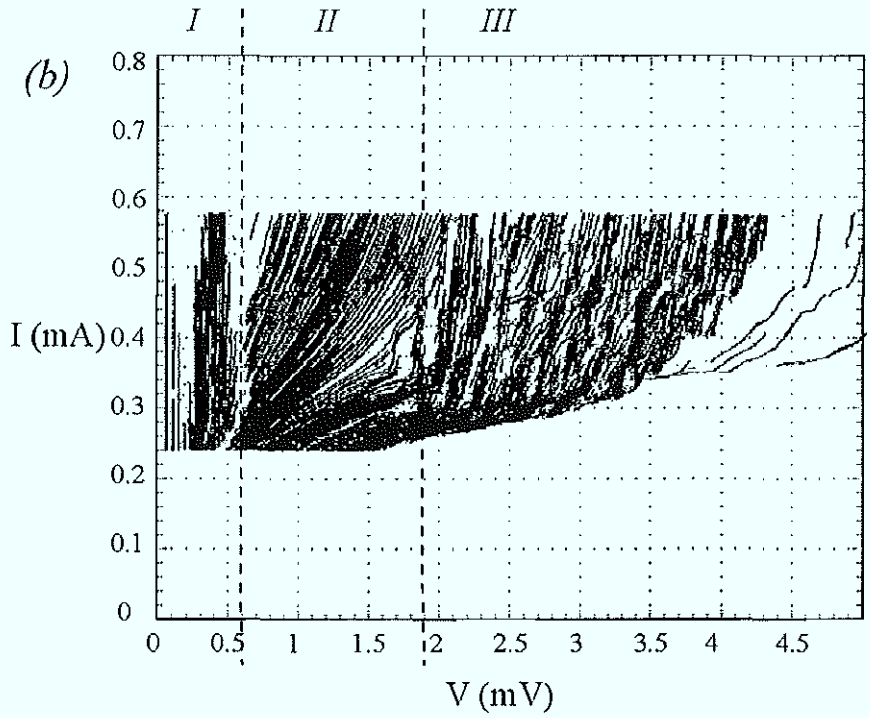


*Fig.6.8(b): I-V curve of 7-fold stacks with sweeped magnetic field [sample: window01.7.1/3.3], (200×10μm²)*

In the lower voltage range (*I*) resonant steps occur that resemble the Fiske steps of a single junction, though the former are not equally spaced. A comparison between these steps with the Fiske steps of a single-barrier junction with equal dimensions and critical current density is shown in *Fig.6.9*.

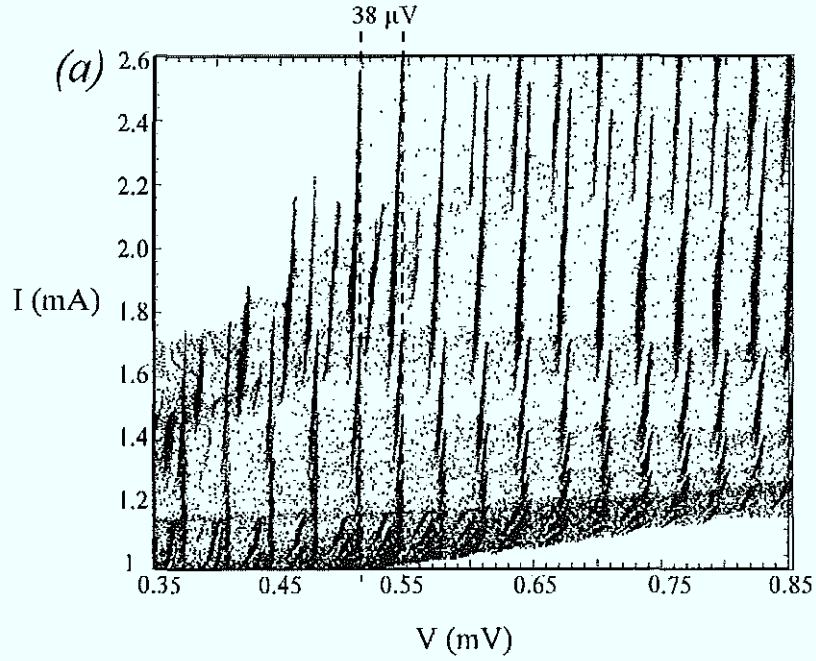


*Fig.6.9(a): Fiske steps, single junction; [sample: window01.1.4/1.2], (200×20μm²),*

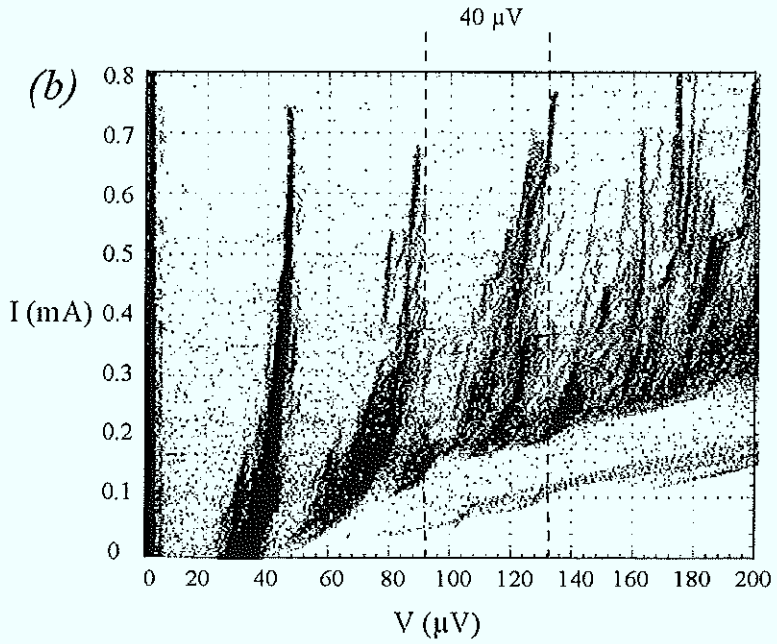


*Fig.6.9(b): Fiske steps, 7-fold stack; [sample: window01.7.1/1.3], (200×20μm²)*

The registered voltage spacing of *38*μV for a single junction is rather close to the typical spacing of *40*μV for the stacked system. Still the stacked system does not show clear well-separated single resonant steps. Different steps are grouped together and demonstrate high complexity of the dynamics. The expected Kleiner voltages are by a factor of *2-3* larger than the measured voltages inside each group. In general, slightly different Fiske-like steps of individual junctions in the stack may form these step groups. For higher order resonances their structure smears out, as seen in the figure.

In the intermediate voltage range (*II*) a smooth flux-flow behavior is measured up to large voltages. In contrast to the single-junction case the flux-flow branch amplitude does not decrease to zero at the single Nb gap voltage of *1.4*μV, which is a clear sign for a collective regime of several junctions. The high voltage region (*III*) shows some resonant steps. Their spacing is very large in comparison with the low-voltage Fiske steps and different values can be resolved. Since the individual junction voltages are not known and can be different from each other, the comparison with Kleiner mode voltages is hard to make without detailed numerical simulations.

### 6.4. Numerical simulations

The numerical simulations were done by A.V. Ustinov in collaboration with S. Sakai from the ETL in Japan. The system of equations for multi-stacked junctions and parameters were already described in **chapter 4**. It is solved by a finite difference method, and the external magnetic field is implemented in the boundary conditions in the form

$$-\frac{\partial \phi_i}{\partial x}\bigg|_{x=0,L} = \frac{2\pi\mu_0 H}{\Phi_0}\left(s_{i-1} + d_i' + s_i\right) = \frac{2\pi\mu_0 H}{\Phi_0}\left(d_i + \lambda_{i-1}\tanh\left(\frac{b_{i-1}}{2\lambda_{i-1}}\right) + \lambda_i \tanh\left(\frac{b_i}{2\lambda_i}\right)\right), \qquad \{6.2\}$$

for $i$ as number of the superconducting layer ($i=0,1,2,3,...,7$). It was possible to use a real time simulation program on a personal computer, that was developed by Ustinov and Sakai, with a real time graphics by Hechtfischer and Kleiner. No normalization has been used so that the parameters were given in true physical units. Therefore the matrix in equation {4.16} has to be transformed to its inverse matrix $F$ and the resulting system of equations can be written in the form

$$\frac{\Phi_0 C_{i,i-1}}{2\pi}\frac{\partial^2 \phi_{i,i-1}}{\partial t^2} + \frac{\Phi_0}{2\pi R_{i,i-1}}\frac{\partial \phi_{i,i-1}}{\partial t} = j - j_{c_{i,i-1}}\sin\left(\phi_{i,i-1}\right) + \frac{\Phi_0}{2\pi\mu_0}\sum_{i=1}^{N} F_{i,i-1}\frac{\partial^2 \phi_{j,i-1}}{\partial x^2}, \qquad \{6.3\}$$

with $i=0,1,...,7$. Inside the program code the matrix element $F_{i,i-1}$ is calculated in analytical forms for $N<6$, but for arbitrary $N$ the subroutine LSGRR in the numerical library IMSL[6.5] is applied. The used finite difference procedure is a natural extension of the one that was utilized for simulating fluxon dynamics in single-barrier long Josephson junctions. To avoid spurious oscillations, the second derivative with respect to $x$ in equation {6.3} was replaced by a finite difference form using five spatial points instead of three points like before[6.6]. To satisfy the boundary conditions at every time step, virtual points outside the two edges had been introduced. In order to receive detailed $I$-$V$ curves long time simulations had been carried out on a CRAY computer system at ETL, Japan. In this way the voltage contribution of each junction can be extracted and the sum is directly comparable with the experimental results. On the other hand, the real time demonstration of the phase derivative with a controllable sweep of the bias current on a PC served to find stable *in-phase* modes. Beside the simulations of the 7-fold stack, with relatively weak coupling, simulations for *10*-fold stacks with strong coupling had been performed[6.7].

## 6.5. Comparison of experiment with numerical simulations: 7-fold stacks with weak coupling

Numerical calculations were done for the measured sample with a length of *350*μm and a width of *20*μm[6.7]. The layer thicknesses are *185*nm for the bottom electrode, *600*nm for the top electrode and *78*nm for the intermediate Nb electrodes between the *7* junctions. For all layers the London penetration depth is taken as *100*nm. The critical current density is $j_c$=*380*A/cm². The used quasiparticle conductance is $G=6\times10^{4}\Omega^{-1}\text{cm}^{-2}$ and the capacitance is $C=8.85\mu\text{F/cm}^2$. A typical time for the bias current ramp during the calculation of one *I-V* curve is about *200*ns in the units of equation {6.3}. *Fig.6.10* shows the calculated *I-V* characteristics for the sum of dc-voltages of the *7*-fold stack. The magnetic field values differs between *8*Oe and *12*Oe in steps of *0.2*Oe. Separated resonant voltage steps are observed.

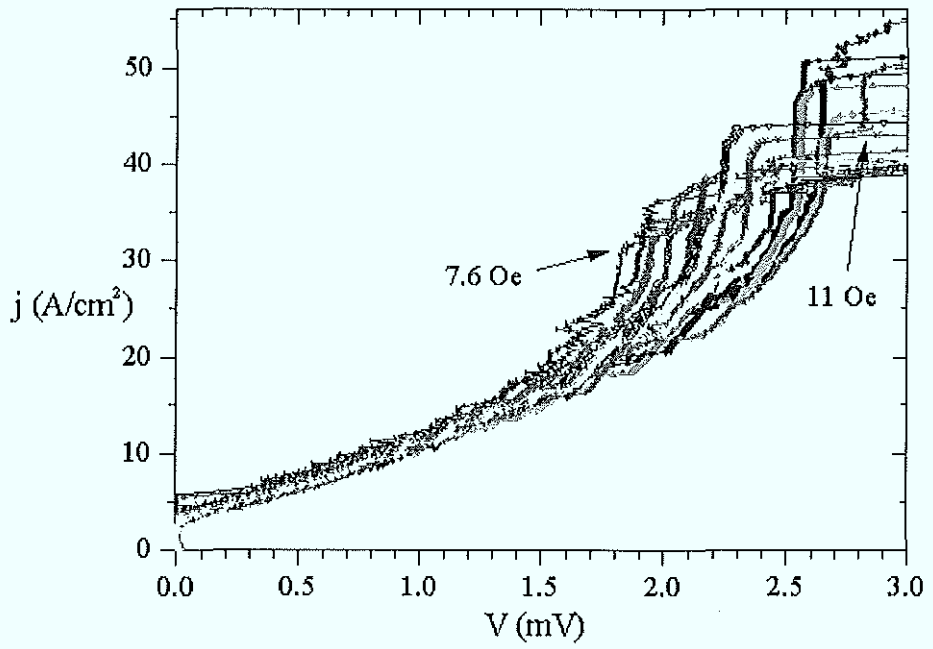


*Fig.6.10: Numerical simulated I-V curve with varied H for the 7-fold stack (350×20μm²)*

The displayed spacing between these resonances is *100*μV, which is rather close to the experimental results of *110*μV resonance spacing in the flux-flow region *III* (see *Fig.6.11*). Measurements and simulations use the same field values and the resonances appear in a very similar voltage range which demonstrates an impressive agreement.

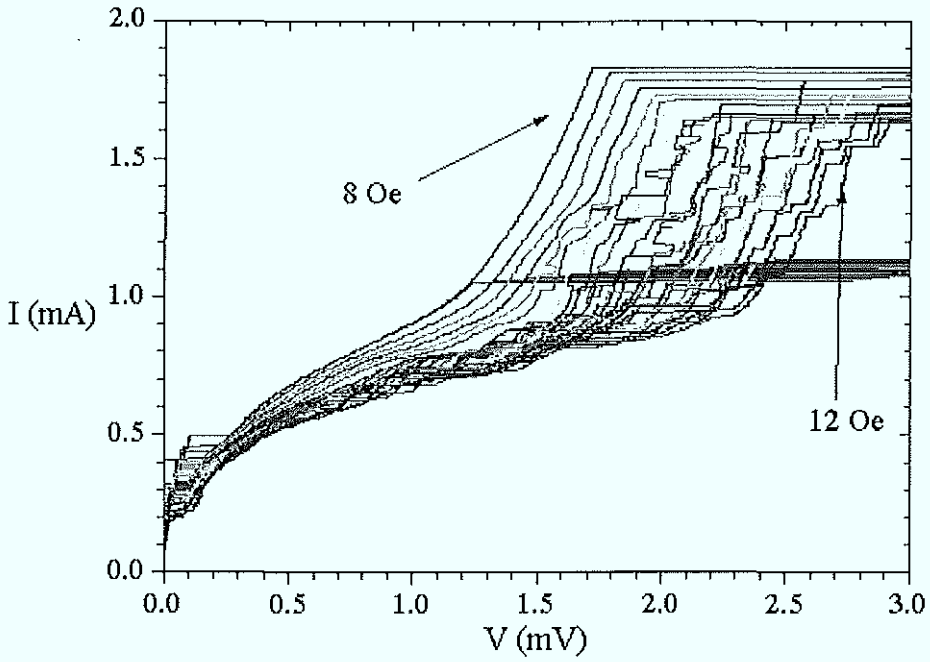


*Fig.6.11: Experimental I-V curve with varied H for the 7-fold stack; [sample: window01.7.1/2.3], (350×20μm²)*

The numerical simulations allow to distinguish between the individual voltages of the junctions. The single junction voltages and the resulting sum are shown as an example in *Fig.6.12.*

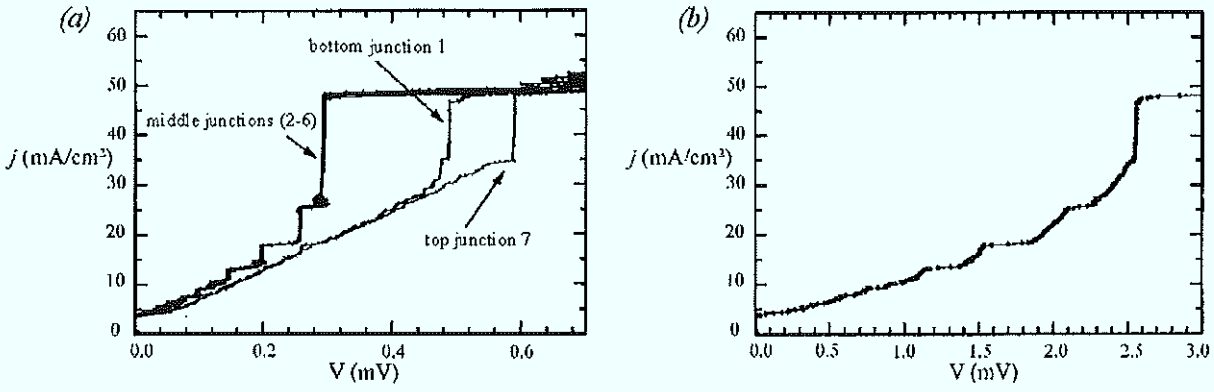


*Fig.6.12: (a) Individual junction and (b) total stack voltages versus the bias current for H=10.4*Oe

For a low bias current density all individual voltage branches display a smooth flux flow. In the bias range of *30-50*A/cm² sharp resonant steps are registered for all junctions. The inner junctions numbered (*2-6)* show the same voltage state and just the bottom (*1*) and the top junction (*7*) show larger voltages. This is the consequence of the thicker Nb electrodes as bottom and top layer. The voltage of junction *7* is by nearly a factor *2* larger than the one for

all inner junctions. A detailed analysis of the junction phases was also carried out. Snapshots of the supercurrent distribution $sin\phi_i(x)$ for all junctions are shown in *Fig.6.13* with the horizontal axis being the spatial coordinate of the junction.

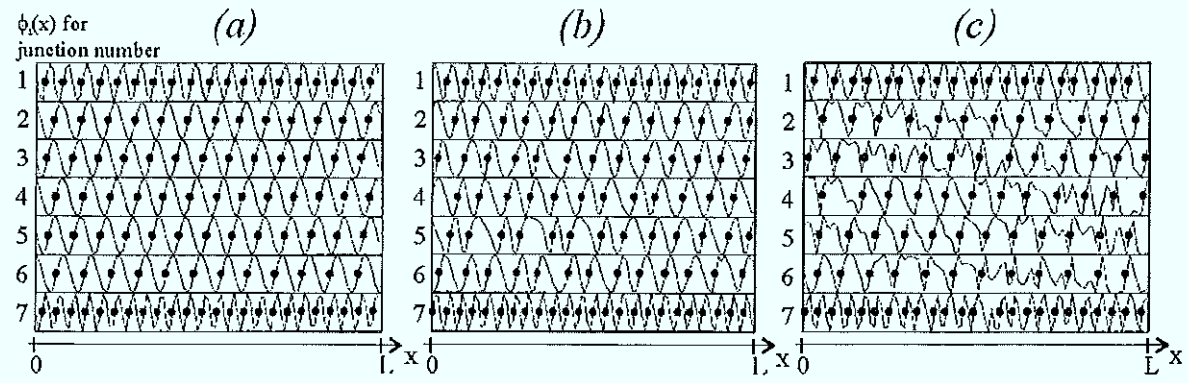


*Fig.6.13: Snapshots of the flux flow state in 7-fold stack*
*(a) j=0A/cm², (b) j=13A/cm², and (c) j=37A/cm²*

For the inner junctions *(2-6)* there are *12* fluxons in each junction that form a triangular lattice (checkered pattern). The center of mass for each fluxon is signed by the dots and indicates the phase differences $\phi_i$ equal to $\pi+2\pi m$ with an integer number $m$. The bottom junction *(1)* contains *20* and the top junction *(7) 24* fluxons. With increasing the bias current this fluxon configuration moves as a whole and generates a dc-voltage. Two additional snapshots for different bias current densities are also demonstrated. Using the number of fluxons $N_i$, the dc-voltages $V_i$ and the junction length $L$, the fluxon velocities $u_i$ can be calculated using the equation

$$u_i = \frac{L}{\Phi_0 N_i} V_i \,. \qquad \{6.4\}$$

These velocities for the different junctions are in the range $(4.05\pm0.06)\times10^6$m/s. This value is very close to the smallest Kleiner mode velocity[5.2,3] in such a *7*-fold stacks of $\bar{c}_7 = 4.16\times10^6$m/s. A comparison of the dc-voltages from *Fig.6.10* for the inner junctions *(2-6)*, that lock simultaneously to several resonant steps, with expected Fiske steps was done. To calculate the Fiske steps for an individual junction the smallest wave velocity $\bar{c}_7 = 4.16\times10^6$m/s is assumed which gives the Fiske step spacing

$$\Delta V_{FS} = \frac{\Phi_0}{2L}\bar{c}_7 \approx 12.3\mu V \,. \qquad \{6.5\}$$

The simulated values of *147*μV, *198*μV, *258*μV, and *295*μV in *Fig.6.13* turn out to be very close to integer multiples of the single junction Fiske step spacing. In *Fig.6.14* a fit between the theoretically expected slope $m = {}^{V_{Fs}}/_{\Delta V_{Fs}}$ and the numerically calculated steps is given for two different magnetic field values.

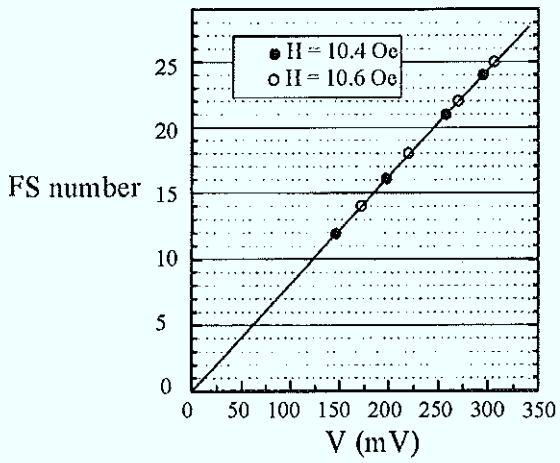


*Fig.6.14: Comparison between the theoretical expected slope* $m = {}^{V_{Fs}}/_{\Delta V_{Fs}}$ *and numerically calculated steps*

Due to the excellent fit it can be concluded, that for this broad band velocity range, the flux-flow dynamics in the inner junctions is characterized by cavity resonances of the lowest Kleiner mode $\bar{c}_7 = 4.16 \times 10^6$m/s. Another illustration of this dynamic mode can be done by comparing two voltage patterns for two different bias current density values, taken at arbitrary chosen time. In *Fig.6.15* the spatial distribution of the instantaneous voltages $V_i(x) \propto \phi_i(x)$ for the different junctions is shown as a function of coordinate.

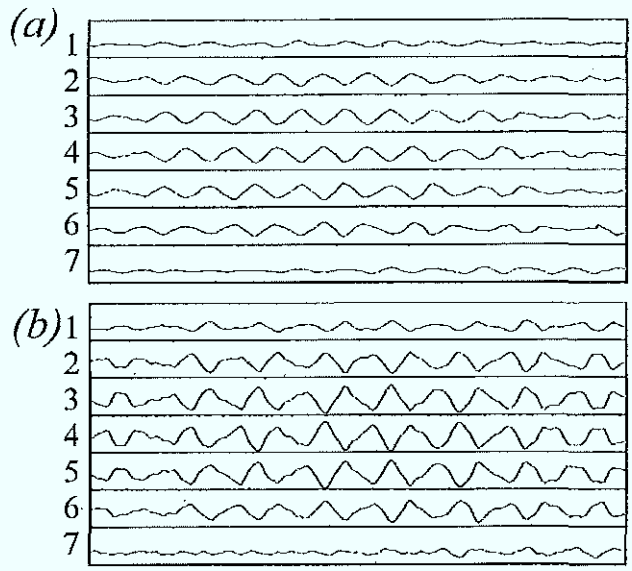


*Fig.6.15: Simulated dynamic states, instantaneous voltages*

The neighboring junctions always show *out-of-phase* oscillations. This checkered pattern is characteristic for the lowest velocity mode as mentioned above. The out of phase oscillations of the inner junctions lead to a very small sum voltage across the whole stack. In *Fig.6.18* the voltage at the boundary *x=0* for junction number five is shown together with the sum voltage of all junctions.

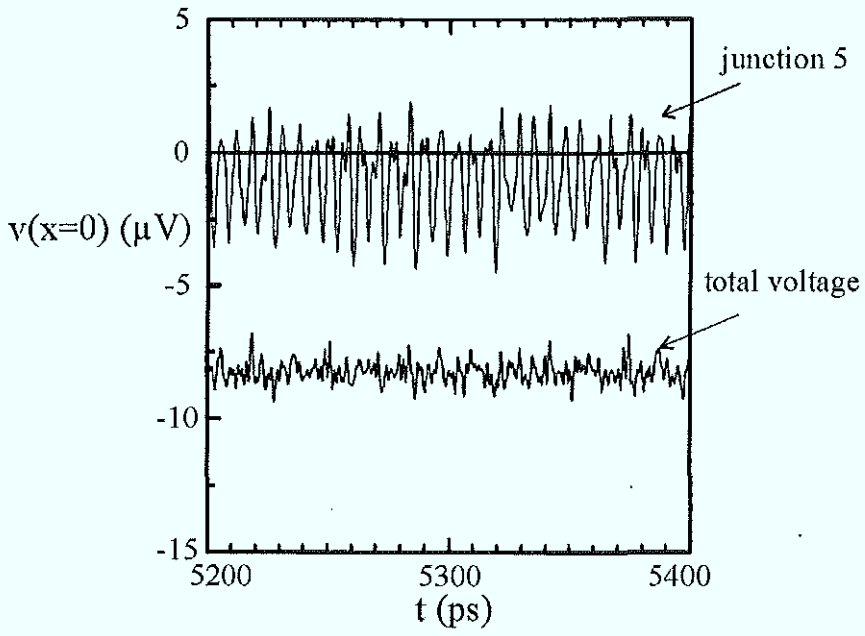


*Fig.6.16: Ac voltages at the boundary x=0*

The resulting amplitude of the ac voltage on the stack is smaller than the individual junction voltage oscillation amplitude. As a conclusion, the investigated 7-fold stack displays the *out-of-phase* state but does not show any coherent *in-phase* mode that is required for a useful oscillator. On the other hand, the excellent fit between experimental data and the numerical simulations is important. Although the chosen parameters resulted in the *out-of-phase* mode, the model delivers realistic results and can be used to find possible parameter range for stable *in-phase* dynamics.

## 6.6. Comparison of experiment with numerical simulations: *10*-fold stacks with strong coupling

By changing the parameters in numerical simulations it turned out to be possible to find coherent *in-phase* flux motion for all inner junctions[(6.7a)]. The most crucial parameter is the coupling, which was increased but still remained within the experimental reachable range. Instead of *70-90*nm intermediate Nb thickness, it was reduced to *20*nm Nb thickness.

For reasons of simplicity, the first preparation were done with an old set of photomasks for the finline layout. The junction length is *400*µm and the width *5* or *10*µm. For *10*-fold stacks the critical current spread easily increases due to the preparation procedure (see **chapter 3.**). Only one sample showed sufficiently equal junction properties for possible investigations of the *in-phase* mode. The illustrative *I-V* curves are shown in *Fig.6.17.*

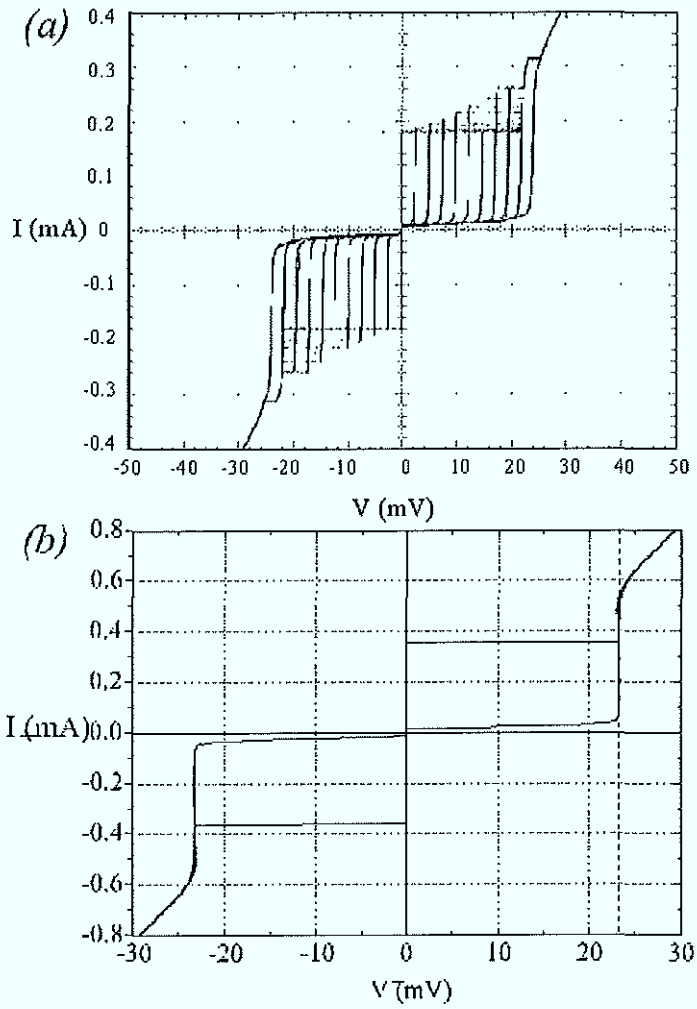


*Fig.6.17: I-V characteristics for 10-fold stacks with 20*nm *thick inner Nb layers,*

*(a) large $\Delta I_c$; [sample: winfin10.5/2.1], (20×20*µm²*),*

*(b) current locking for small spread in $I_c$ ; [sample: winfin10.5/2.1], (20×20*µm²*),*

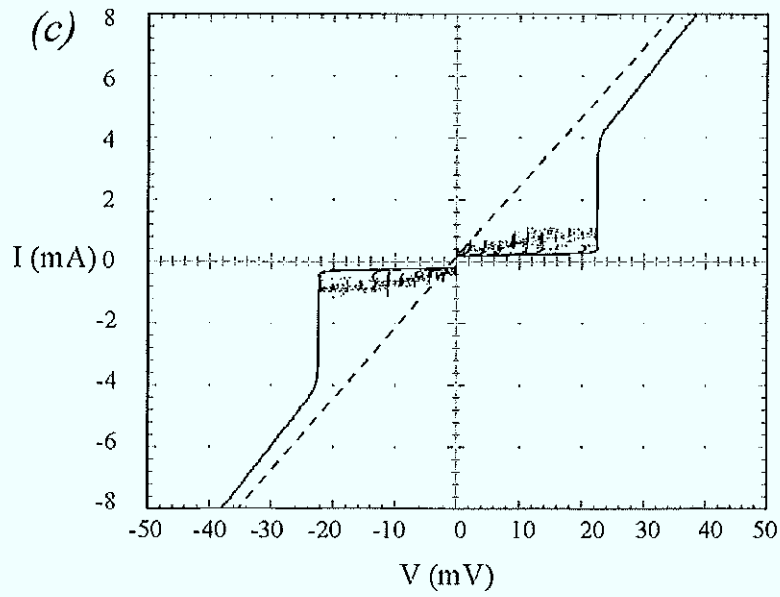


*Fig.6.17(c): I-V characteristics for 10-fold stacks with 20*nm *thick inner Nb layers; [sample: winfin10.5/3L], (400×10*μm²*), junction with finline antenna*

As shown in *(b)* small spread in critical currents in the stack lead to a current locking behavior[6.8]. This effect is also present for small external fields. The measured total *10*-junction gap voltage is *24*mV which is lower than the expected *10×2.7*mV. Here the *20*nm thin intermediate electrodes cause a decrease in the energy gap of niobium down to *2.4*mV for the individual junctions. This effect had already been observed in former experiments[6.9]. To measure the flux-flow behavior, we applied an external magnetic field. For samples with a finline antenna, we used the ground electrode as control line instead of a solenoid. Typical results are shown in *Fig.6.18*.

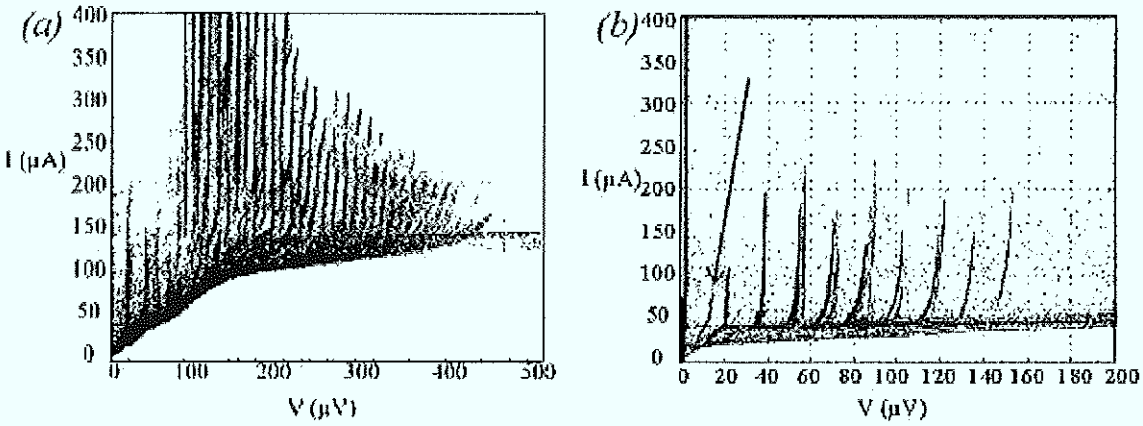


*Fig.6.18: I-V(H) characteristics for long 10-fold stacks with H-sweep*
*(a) [sample: winfin10.4/2.2], (350×20*μm²*), (b) [sample: winfin10.4/2.1], (10×10*μm²*)*

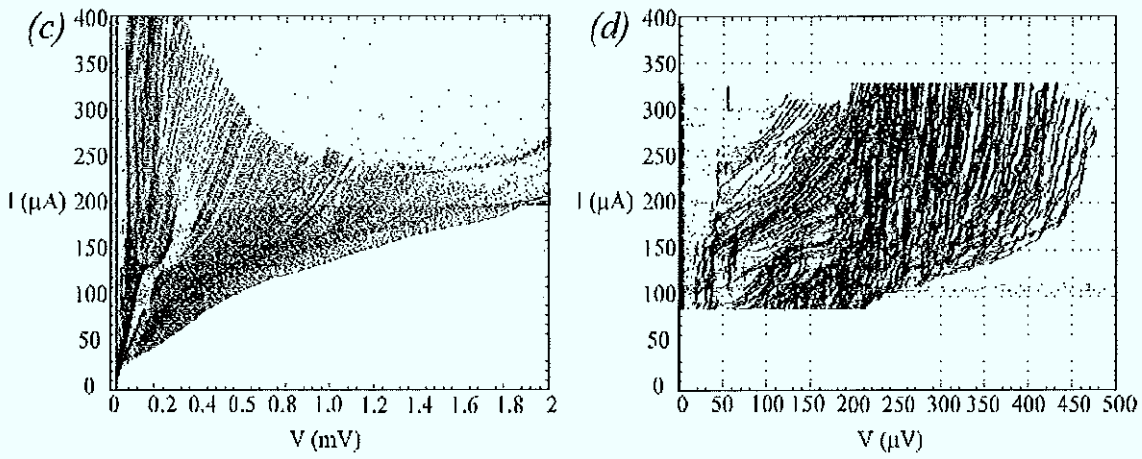


*Fig.6.18: I-V(H) characteristics for long 10-fold stacks with H-sweep*
*(c) [sample: winfin10.4/1L], (200×10μm²), (b) [sample: winfin10.4/3R], (400×10μm²)*

Flux-flow behavior is observed up to the voltages of about *1.6*mV. Clear Fiske-like resonances ($V_{FS} \cong 19.5\mu V$) have been measured for the window type junction stacks *(a)* and *(b)*. For high magnetic field values a single resonant step at *17*μV appears. The origin of this state is not clear. The finline geometry samples do not show Fiske-like steps (*Fig.6.18(c)* and *(d)*). We can only conclude that it is difficult to interpret the experimental data since the model does not include a dependence on the sample geometry. For a new mask layout the junction length is reduced to *80*μm. For this shorter length and lower critical current density an evidence for a stable *in-phase* state for all inner junctions was found in numerical simulations[6,10]. In *Fig.6.19* a snapshot of this state is shown with the dots indicating fluxon centers.

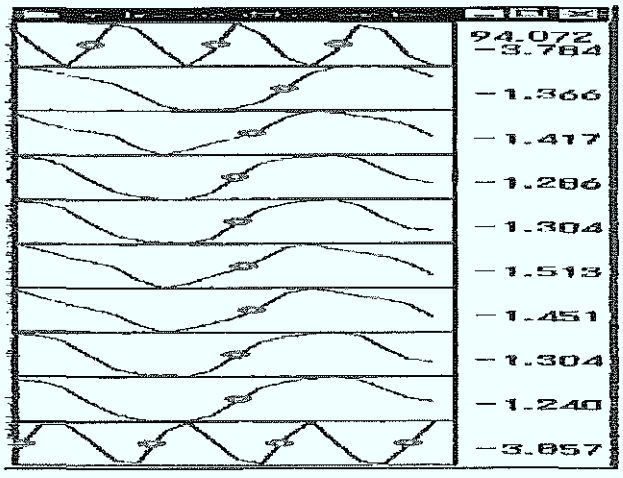


*Fig.6.19: Snapshot of the dynamic state from the real time simulation*

The voltages of individual junctions and the sum voltage across the whole stack are shown in *Fig.6.20.*

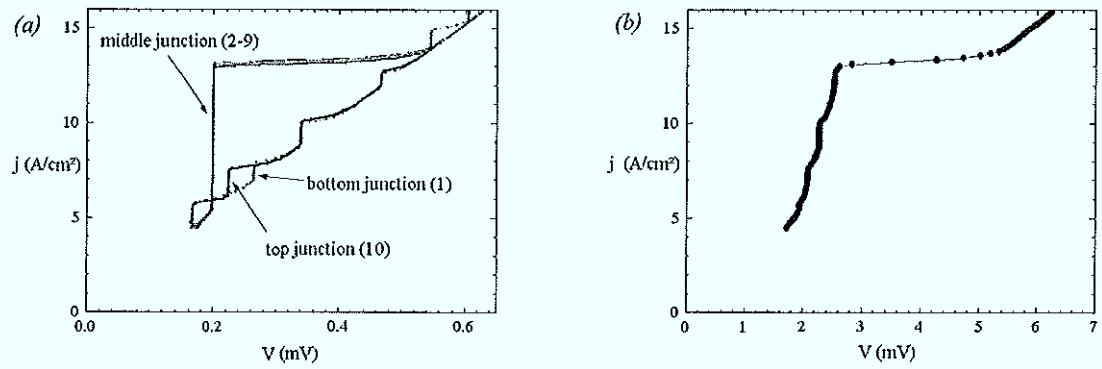


*Fig.6.20: Numerical simulation for a 10-fold stack*[6.10], $Nb_{middle}$=*20*nm, $j_c$=*20*A/cm², *80*μm *long stack*
*(a) individual voltage, and (b) total voltage*

The first preparation run for *10*-fold stacks with the *80*μm long junction layout showed an exceptionally large parameter spread. The reasons were sputtering and lithographic problems during the preparation procedure. Examples of the *I-V* curves of these stacks are shown in *Fig.6.21.* The critical currents differ by up to *50%* and more.

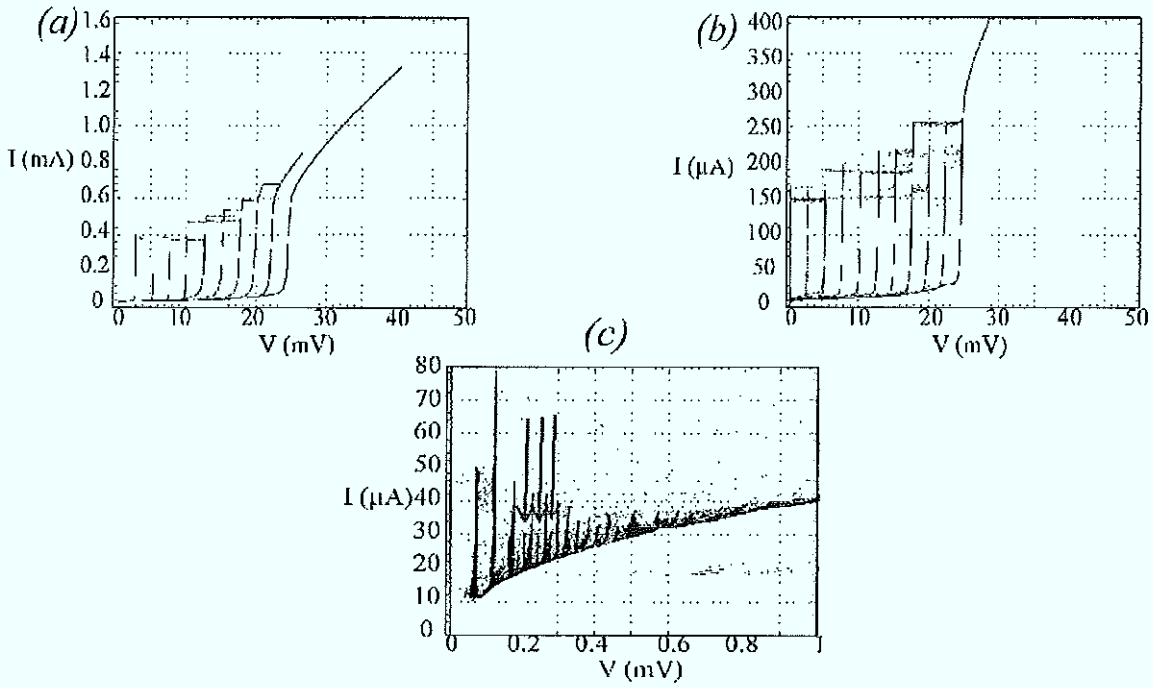


*Fig.6.21: I-V characteristics for 10-fold stacks with 20*nm *middle electrode*
*(a)[sample: finchip3.10.3/2R], (80×5*μm²*), (b)[finchip3.10.7/4L], (80×10*μm²*),*
*(c) Fiske steps [sample: finchip3.10.3/2R]*

The preparation procedure was improved by changing the photoresist etching mask treatment and the etching parameters. *Fig.6.21(b)* shows that the improvement was still not sufficient to achieve small spread. The different preparation attempts are described in detail in **chapter 3.2.** There are two possibilities to apply the external field. The first one is to use the Nb bottom layer as control line. A current along this control line generates magnetic field in the plane of the junction. In *Fig.6.21(c)* the Fiske steps for a *10*-fold stack are shown. Again additional resonant steps occur (see arrows). Their origin is hard to explain due to the large spread in junction parameters. The most likely reason is that they are related to the influence of the thick top Nb electrode on the junctions. For larger fields the contribution of the individual resonances from the bottom junction is increasing. The later argumentation assumes a homogeneous external field for all junctions in the stack, which is unlikely. A test with applying an external magnetic field by a coil did not show any resonant voltage steps. The maximum field of the coil were too low to produce a significant effect on the stack. Increasing of the current in the coil was limited by heating of the contact wires.

## 6.7. Stacking limits in Nb-Al technology

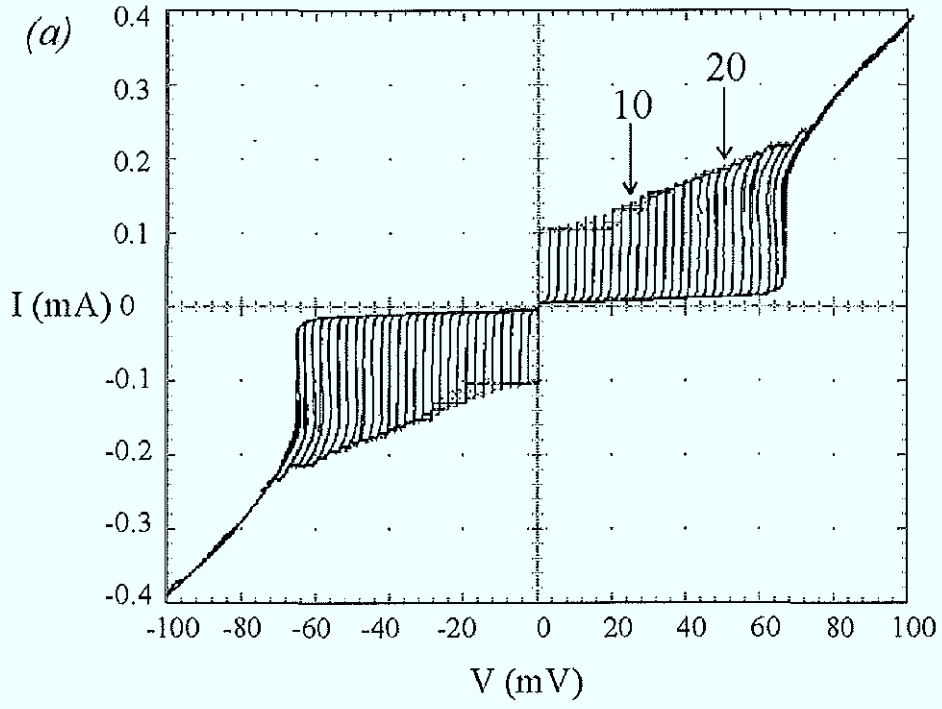


*Fig.6.22(a): I-V characteristics of 28-fold stacks with 20*nm *intermediate Nb thickness [sample: winfin 30.1/2.1], (20×20*μm²*)*

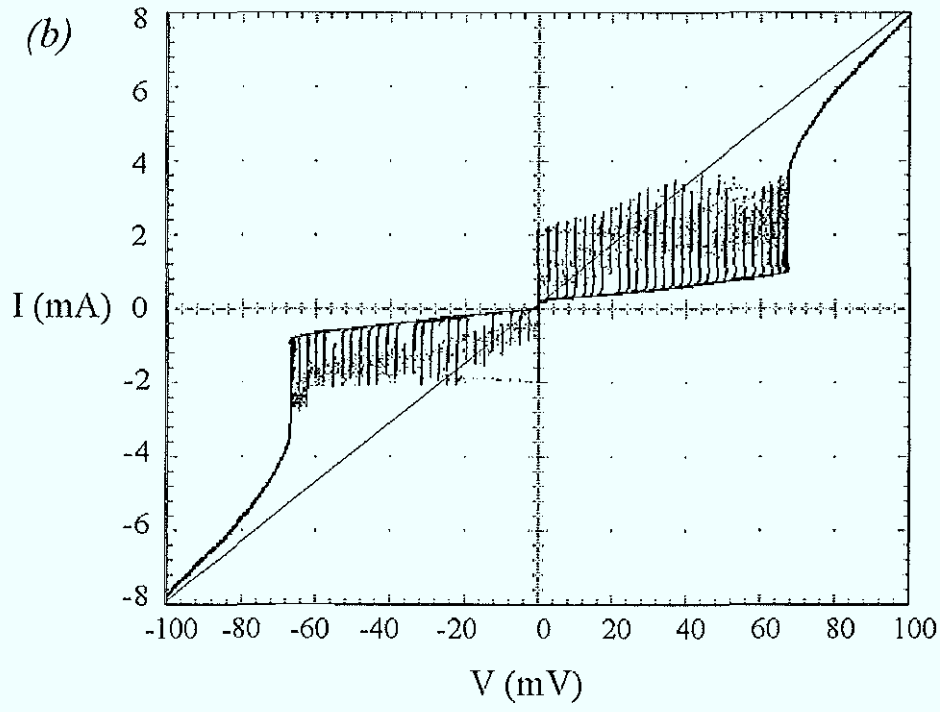


*Fig.6.22(b): I-V characteristics of 28-fold stacks with 20*nm *intermediate Nb thickness [sample: winfin 30.1/2.5], (350×20*μm²*)*

The results presented above demonstrate the preparation of multi-layer Josephson junctions with up to *10* barriers. For some preparation runs I achieved a critical current spread of less than *5%* in *10*-fold stacks. The intermediate Nb electrode thickness was varied between *20*nm and *110*nm.

In order to test the limits of stacking, I fabricated stacks of *28* working barriers. The measured *I-V* characteristics clearly display *28* different gap features as shown in *Fig.6.22*. Here the coupling is again determined by *20*nm thick intermediate Nb electrodes and the critical current density is around *50*A/cm². For such a large number of stacked junctions the spread is still in the range of *50*%. Each gap feature displays a slightly higher critical current value than the lower one. We believe that all barriers have nearly equal critical current density, and the origin of the measured spread in $I_c$ is due to different junction area in different layers. This can be a consequence of the relatively simple preparation process.

As described in **chapter 3**, the etching procedure is the most critical step in the process. The photoresist mask changes its dimension due to the large number of etching steps. Although long cooling breaks help to keep the sample temperature low and to avoid burning effects, the photoresist flanks are also etched during each process step. Therefore, the primal mask

dimensions are decreased step by step. Both photolithography steps, positive and negative, show this property.

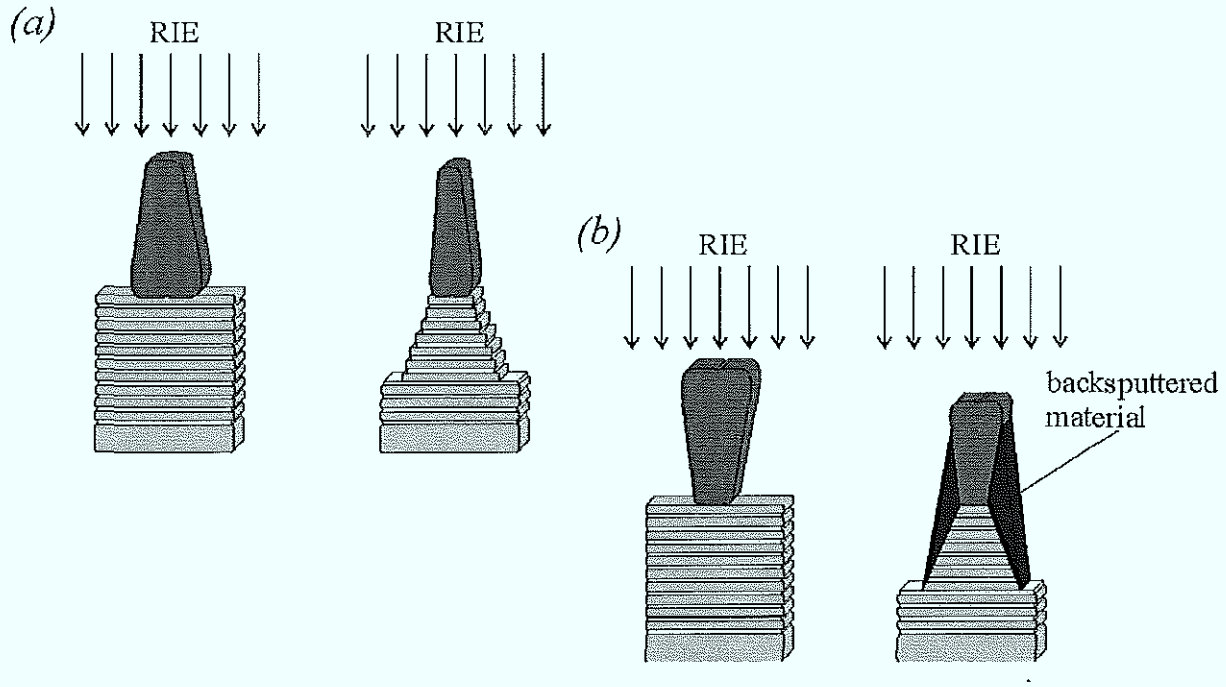


*Fig.6.23: Photoresist mask dimension change during a multilayer etching: (a) with positive photolithography; (b) with negative photolithography.*

**Positive photolithography:** For a junction width of *5*µm at the beginning we end up with *3*µm photoresist mask at the end. Thus, the top junctions are etched down to *3*µm which results in the different critical currents between the layers.

**Negative photolithography:** Here the problem is different. Due to the overhanging flanks of the etching masks more and more material is backsputtered at the flanks. While decreasing the photoresist mask's dimensions by etching, this backsputtered material enlarges the etch mask area. Again, the resulting effect leads to different junction sizes from the top to bottom of the stack. Both processes are schematically shown in *Fig.6.23*.

To solve this problem I tried different methods. The simplest and most efficient is the bakeing of a positive photoresist mask. After development, the sample is placed on the hot plate and baked in *5*minute steps of *10*°C temperature difference from *90*°C up to a maximum temperature of *120*°C. The same procedure can be used for a negative photoresist mask. The slow temperature increase is necessary to avoid a flow of the resist flanks.

Another approach is the use of a multilayer etching mask. In our case this is not trivial, because the same mask has to be used for a following lift-off process with SiO. Unfortunately, this insulating method can not be replaced by a spin-on process due to the needed prebacking

at temperatures above *180*°C. At higher temperatures the barrier is damaged[6,11]. The tried solution is a trilayer etching mask, consisting of AZ 5214E photoresist backed at *115*°C for *30*minutes, *100*nm sputtered aluminum, and a second photoresist mask. The top resist mask is defined by photolithography. Than the aluminum layer is etched by **I**on **B**eam **E**tching (IBE) under rotation with an angle of *15*°. The Ar-ion energy is defined by *500*V acceleration voltage and the intensity by *88*mA beam current. The second resist mask is than etched by RIE with an oxygen plasma and a rf power of *300*Watt. The multilayer etching can be started in-situ inside the RIE machine. This process is still not optimized, which shows the etching result in *Fig.6.24*. Rests of the underlayer photoresist cause an inhomogeneous multilayer etching.

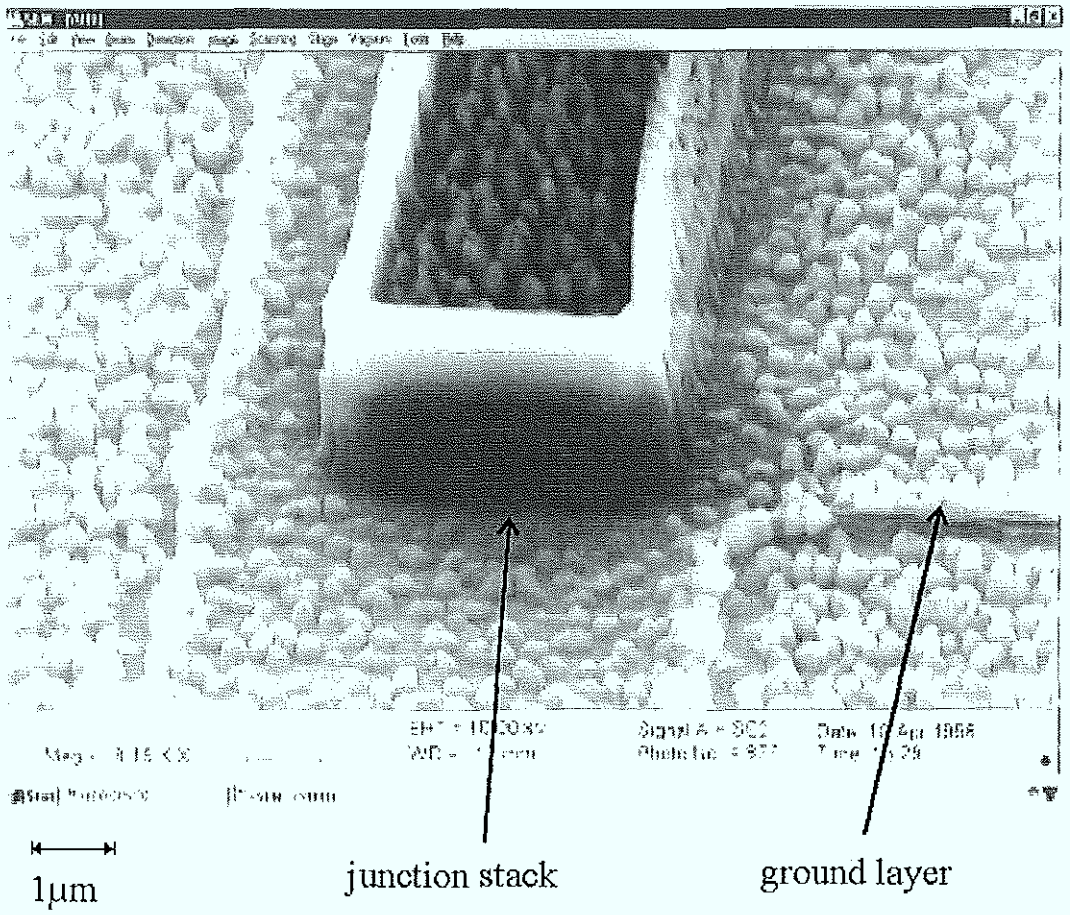


*Fig.6.24: Image of the etched surface with the trilayer etching mask.*
*This SEM picture was made by Y. Koval at the University of Erlangen-Nürnberg*

### 6.8. $I_c$(H) patterns

Remembering the discussion in **chapter 5.3**, the $I_c(H)$ dependence in a stacked system depends on the static and dynamic states of the individual junctions. We will distinguish here the cases of small ($L<\lambda_J$) and long ($L>\lambda_J$) Josephson junctions

#### 6.8.1 Small junction stacks

Bulaevskii et al.[6.12] developed the theory for small naturally stacked junctions that predicts Fraunhofer behavior of the critical current versus magnetic field across the junctions. The field is applied in plane of the layers and the resulting pattern is described by

$$I_c(H) = \frac{I_c(0)\sin\left(\pi sLH/\Phi_0\right)}{\pi sLH/\Phi_0}, \qquad \{6.6\}$$

with $I_c(0)$ being the critical current of the system without external field. $L$ stands for the junction size perpendicular to the field and $s$ is the spacing between the superconducting layers. The first minimum is expected for a flux density equal to one flux quantum per layer

$$H_{c_1} = \Phi_0/sL\,. \qquad \{6.7\}$$

An important assumption of this theory is the infinite number of stacked junctions. Therefore, it neglects completely the influence of outer junctions with different Nb layer thickness. In *Fig.6.25* patterns for small junction stacks with different junction number are shown.

The measured values for the first minimum $H_{c1}$ depend on the number of stacked junctions. We have to distinguish between strong coupling ($Nb_{middle}$=*20*nm) and medium coupling ($Nb_{middle}$=*90*nm). We focus on the results with *10*-fold and *28*-fold stacks and compare them to a single small junction. The field $H_{c1}$ for the *10*-fold stack is about *20%* smaller in comparison to that of the single junction. Also, the side maxima distance is decreased significantly. In contrast to this tendency, the *28*-fold stack shows nearly the same $H_{c1}$ value as the single junction. On the other hand, the side minima are found to have larger distances. Unfortunately we did not obtain systematic experimental data for different number of layers and, therefore, fully consistent interpretation of these measurements is difficult.

Patterns at different gap voltages for *10*-fold (*Fig.6.26(a)*) and *28*-fold (*Fig.6.26(b)*) stacks show very complicate features. Significant is the largest field sensitivity of the $I_c(V=0)$ branch.

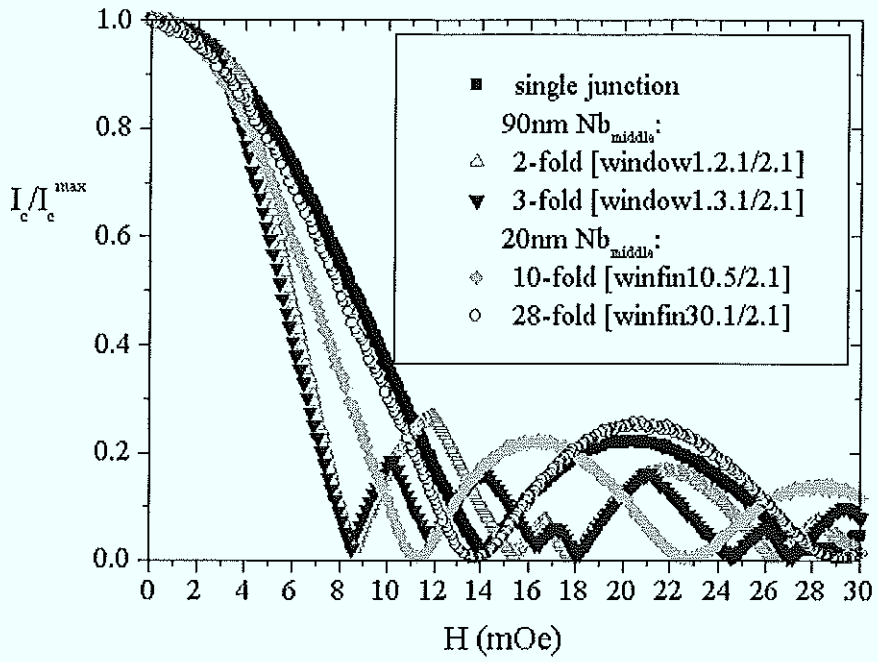


*Fig.6.25: Ic(H) for small stacks with different number of junctions; (20×20μm²)*

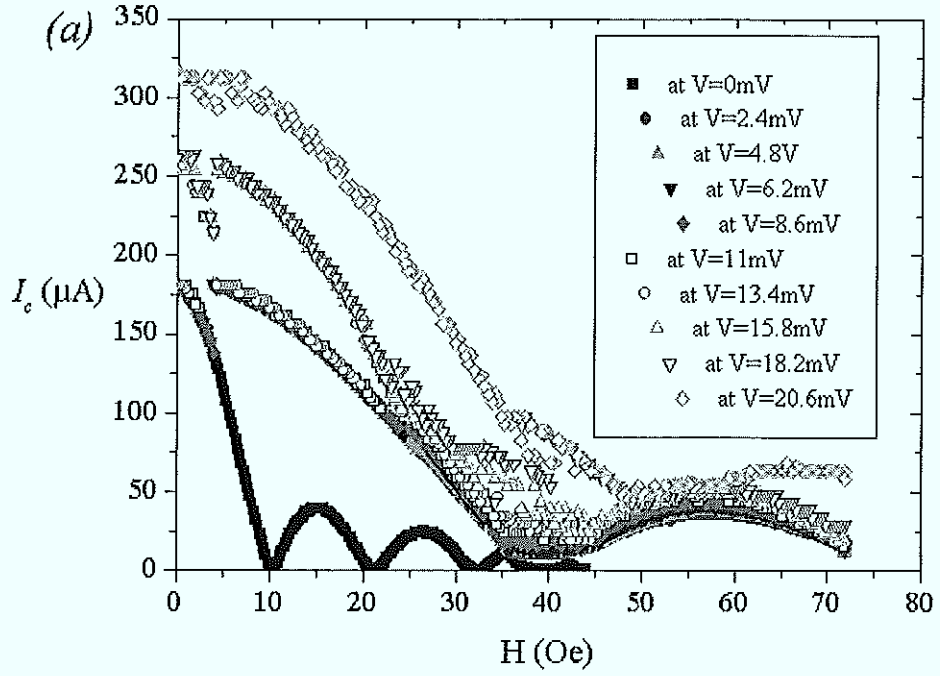


*Fig.6.26(a): Ic(H) measured at different gap voltages for a 10-fold stack; [sample: winfin10.5/2.1], (20×20μm²)*

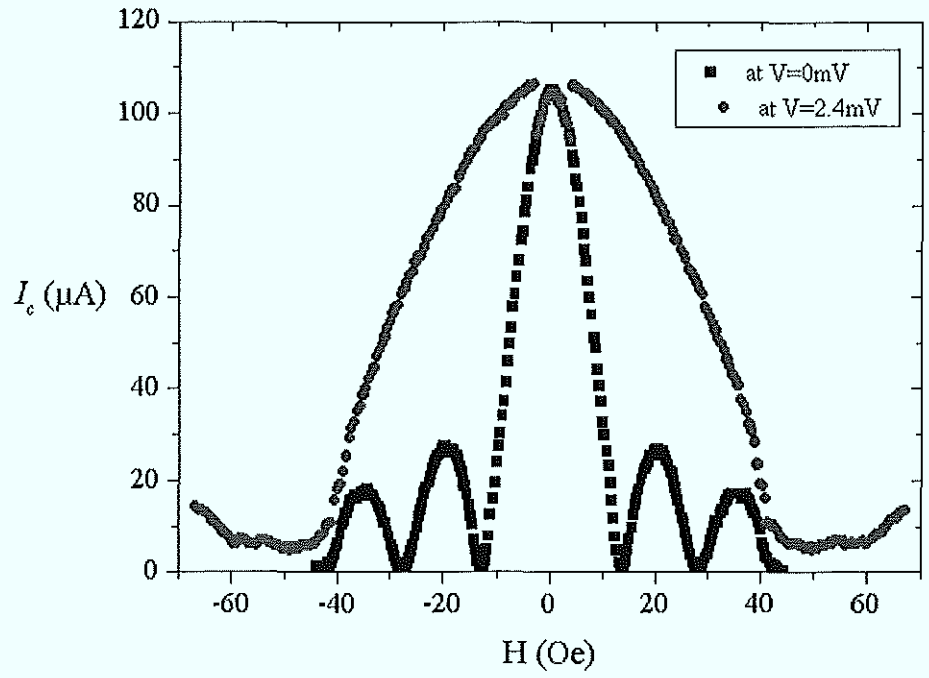


*Fig.6.26(b): Ic(H) at V=0 and at V=2.4*mV *for a 28-fold stack; [sample: winfin30.1/2.1], (20×20*μm²*)*

All samples show large difference between $I_c$ at $V=0$ and the maximum current measured at any gap voltage. The explanation here is similar to that of the *2*-fold stacks in **chapter 5.3**. At any gap voltage at least one junction has to be in the dynamic (phase whirling) state. For zero voltage measurements this is not the case and the displayed pattern characterizes the superconducting state of the whole stack. Due to the thicker top and bottom electrodes this pattern is most probably defined by one of the outer junctions. The patterns measured at different gaps are related to the inner junctions. The predicted oscillating behavior is observed for these "gap patterns" in the available field range. All $H_{c1}$ values of gaps from *2* to *6* are approximately equal. At gap number 7 and 8 the pattern changes again. This can be interpreted as follows: With increasing the number of junctions in th edynamic state, the last junctions which remain superconducting are surrounded by whirling junctions and, thus, "feel" only the nearest *20*nm Nb layers as their superconducting electrodes. At the last gap we measure the field dependence of just one junction with all the others in the whirling state. A clear tendency towards similar behavior of the critical current value at $V=2.4$mV is seen also for the *28*-fold stack (*Fig.6.26(b)*).

### 6.8.2. Long junction stacks

In the case of long Josephson junction stacks the critical current is determined by the penetration of Josephson vortices. The expected behavior of *Ic(H)* is size independent and given as[6.13,14]

$$\frac{I_c(0)-I_c(H)}{I_c(0)} \approx \sqrt{\frac{H}{H_0}}, \qquad \{6.8\}$$

with a characteristic field

$$H_0 = \frac{\Phi_0}{\pi^2 d^2} \qquad \{6.9\}$$

of the layered structure. This equation predicts a non-oscillating decay of the critical current with applied field in the case of our junctions ($H_0$=52T). The prediction made by equation {6.8} is compared with experimental results. Writing it in the form

$$I_c(H) \propto 1-\sqrt{\frac{H_{ext}}{H_0}}, \qquad \{6.10\}$$

we present it together with experimental results for a 10-fold stack in *Fig.6.28*.

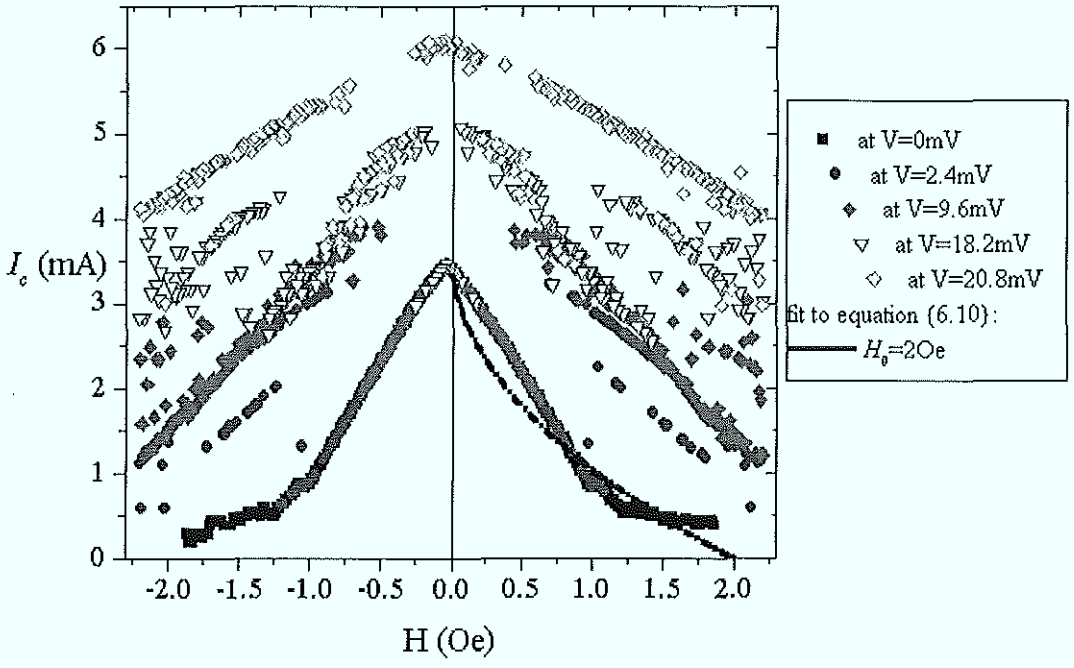


*Fig.6.27: Ic(H) for a long 10-fold stack; [sample: winfin10.5/2.2], (350×20μm²)*

Due to the arguments above, a fit to the theory is also tried using the measured maximum current at the first gap voltage. For the calculated value of $H_0$ we do not find any consensus.

As is shown in *Fig.6.27* we can not reach a good approximation with $H_0 = 2$Oe. The fit is very poor, so we have to conclude that there is a discrepancy between the applied model and the measured data.

Other data were taken from the *7*-fold stacks with an intermediate electrode thickness of *78*nm (*Fig.6.28*). As explained above we found it very difficult to avoid trapping of magnetic flux when reaching the critical current at *H=0*. For this reason measurements were performed in the current range below *2.5*mA. We observed a complicated fine structure on the curve that does not appear for small junction stacks. These irregular oscillations are rather deterministic and reproducible for different sweep directions.

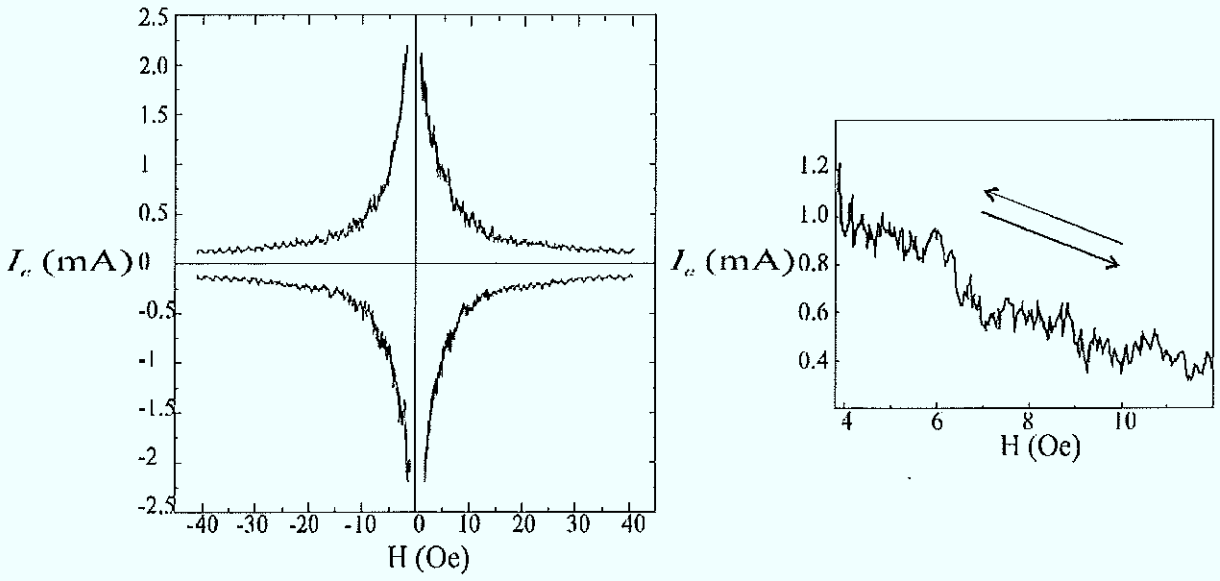


*Fig.6.28: Ic(H) for a 7-fold stack with 78*nm *intermediate electrode; [sample: window01.7.1/2.3], (350×20*μm²*)*

### 6.9. Millimeter-band measurements

For millimeter-band measurements we used the finline layout to couple the emitted radiation via a wave guide to an external *80-120*GHz superheterodyne receiver.

The emitted power can be estimated roughly by a reference measurement using the black body radiation at room temperature (*300*K) and at *77*K. It is important to distinguish between coherently emitting junctions (at ZFSs, FSs, or flux flow steps) and possible other broad band regimes of radiation like the **D**isplaced **L**inear **S**lope[2.44].

### 6.9.1. Radiation emission

As first multilayer sample I measured a *9*-fold stack with an intermediate electrode thickness of *90*nm. A slow sweep of the bias current was used to search for emitted radiation at different receiver frequencies. The result is shown in *Fig.6.29*. External field was applied using the control line with a control current of *9.2*mA.

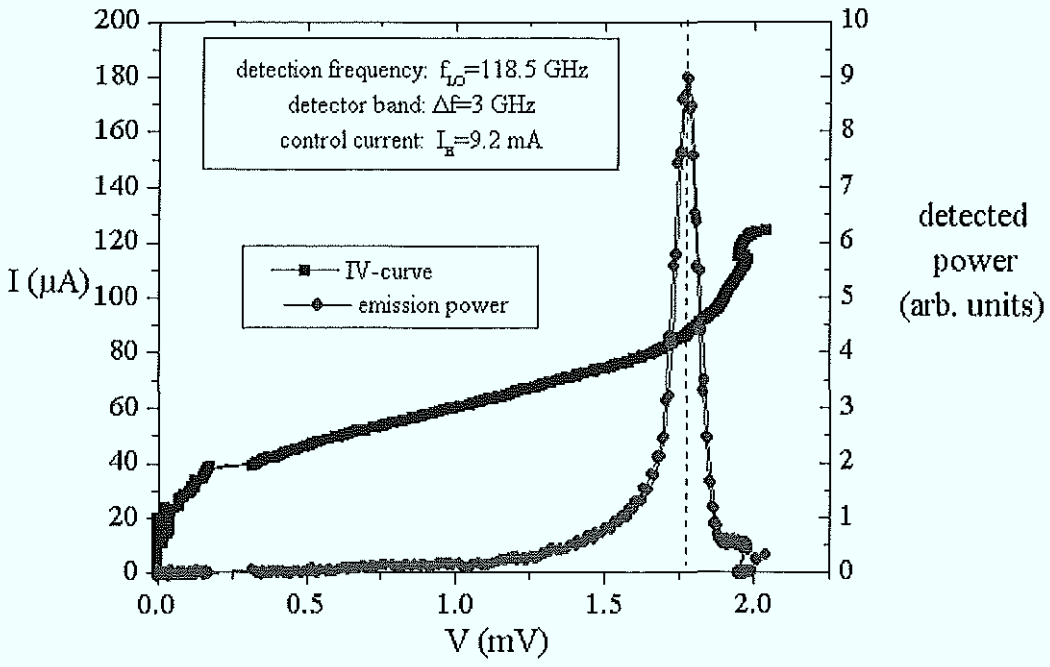


*Fig.6.29: 118 GHz radiation emission of a 9-fold stack; [sample: winfin9.1/2R]*

For interpretation of these data, we refer to the numerical calculations for the *7*-fold stack which had similar parameters. These stacks are operating at the lowest characteristic velocity, which means *out of phase* oscillations for all inner junctions. The outer junctions contain a higher number of fluxons due to their thicker Nb electrodes. Since the voltage of around *1.7*mV is considerably larger than the single-junction Josephson frequency $f_{LO} \times \Phi_0 \approx 0.24$mV, the measured radiation emission is possibly the $7^{th}$ harmonic of $\omega_p$, with a complex overlap of the *out of phase* oscillations in the stack. A comparison of the emitted power with a single junction showed lower emission power for the *9*-fold stack !

In search for a stable *in-phase* radiation mode I studied stacks with lower critical current density and stronger coupling. *10*-fold stacks with a critical current density of $<50$A/cm² and an intermediate niobium electrode thickness of *20*nm were investigated. Due to the missing stable states at higher voltages, it was only possible to bias at Fiske-like resonances in the

voltage range of several hundred μV's. *Fig.6.30* shows the obtained results for the finline samples with a junction length of *400*μm.

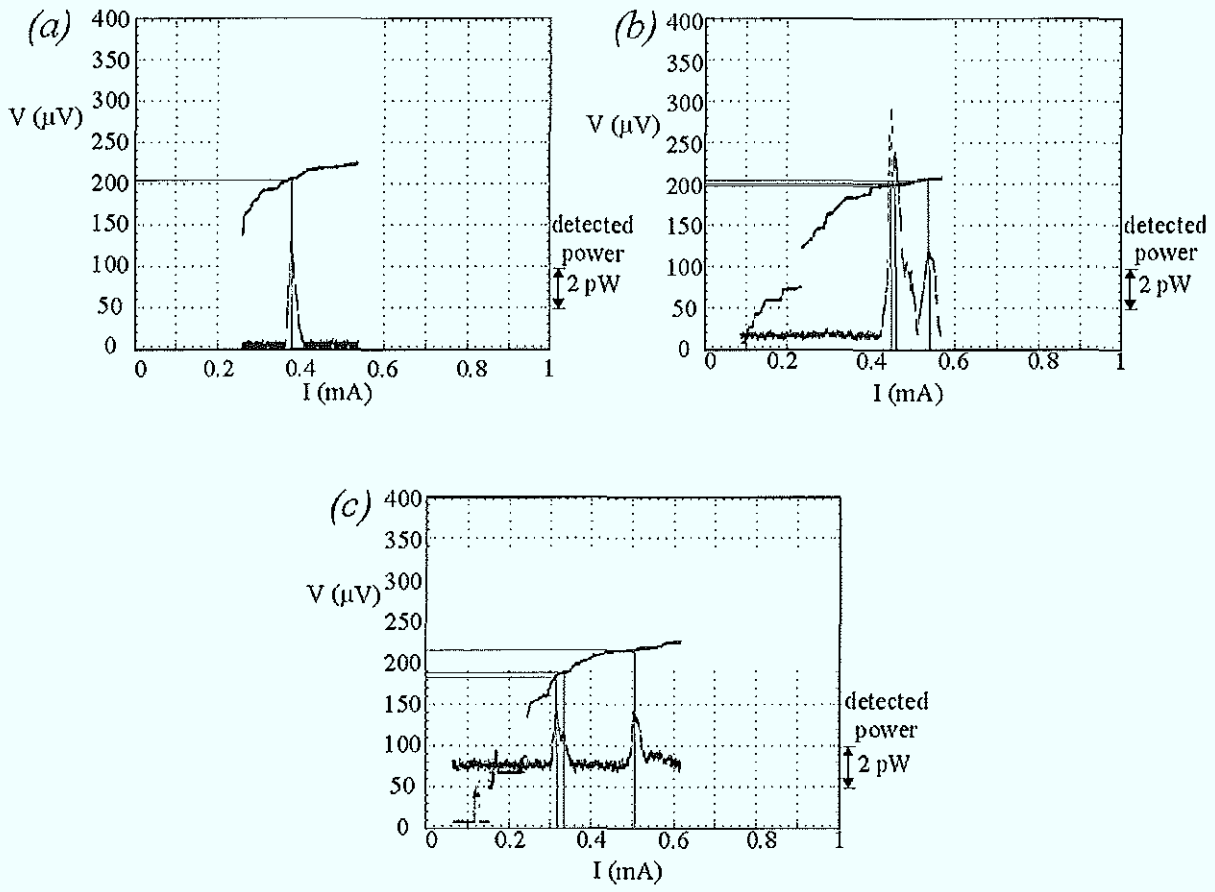


*Fig.6.30: Radiation emission of 10-fold stacks; [sample winfin10.4/3R], (400×10*μm²*)*

*(a) receiver frequency: 91*GHz, $I_H$ *: 8.45*mA,

*(b)* $I_H$ *: 8.06*mA

*(c) receiver frequency: 100*GHz, $I_H$ *: 8.46*mA

Again, the detected power is always lower than that of the single junction. With a fixed receiver frequency of *91*GHz (*Fig.6.30(a),(b)*) the magnetic field value was changed. The radiation peak at *202*μV splits in two peaks at *198*μV and *200*μV. In addition, an emission peak at *208*mV is measured. For higher receiver frequency of *100*GHz the distance between these two emission peaks is increasing (*Fig.6.30(c)*) and the position of the measured emission peaks are *182*μV, *187*μV and *212*μV. These emission peaks are always close to the Josephson voltage of a single junction. In summary, our attempts to observe the *in phase* oscillations in stacks were not successful. Due to the large spread in parameters for the new finline layout with *80*μm long junctions I did not perform any further radiation measurements.

### 6.9.2. Coupling to external radiation

With the same high frequency setup we irradiated stacks by an external millimeter-band signal. This type of operation is used in Josephson voltage standard[1.5; 6.15]. With high power and homogeneous irradiation it should be possible to lock the stacked system in different stable modes. First experiments with two-fold stacks[6.15,16] showed rather inhomogeneous power distribution in stacked junctions. Some of our results of locking to the external signal are shown for a *10*-fold stack in *Fig.6.31*.

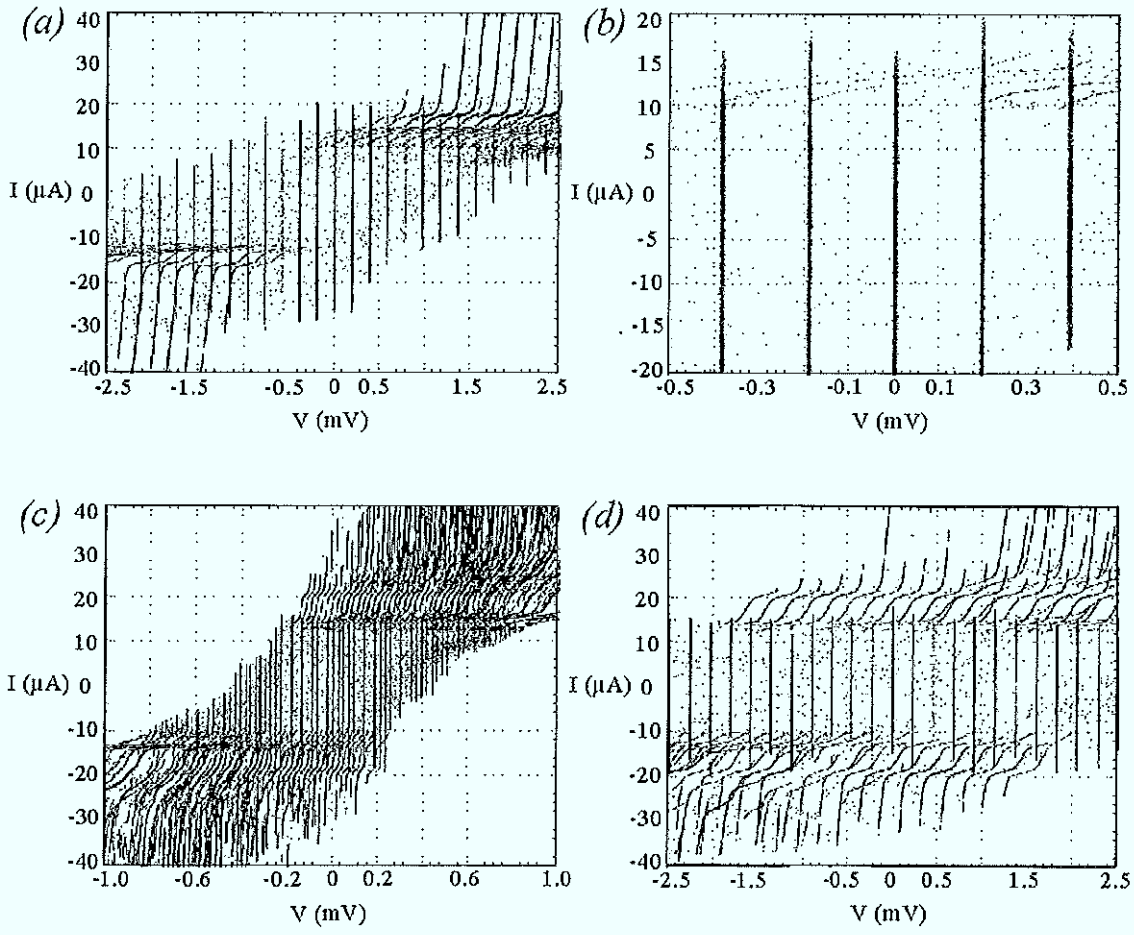


*Fig.6.31: External irradiation on a 10-fold stack; [sample: finchip3.10.11/2R], (80×10μm²)*
*(a),(b) external signal 96*GHz, *0*dBm
*(c),(d) external signal 113*GHz, *0*dBm

The measured voltage spacing between Shapiro steps is equal to the fundamental Josephson voltage for one junction. For the locked state of *N* stacked junctions the spacing is expected to be *N* times larger in comparison to a single junction response. This behavior was not observed in our measurements. The experiments indicate rather independent junction dynamics in stacks.

# 7. Special projects

I had an opportunity to contribute in several interesting side projects that are described briefly here. Sub-micrometer wide junctions were prepared and characterized in close collaboration with Dr. Yu. Koval (Institute for Microelectronic Technology, Russian Academy of Science, Chernogolovka, Russia). X-band coupling circuits were prepared and characterized in the Vigoni-DAAD project together with Prof. M. Cirillo (University of Rome, "Tor Vergata", Rome, Italy).

## 7.1 Sub-micrometer wide junctions

In this sub-project we wanted to investigate the properties of long Josephson junctions with a very small junction width, comparable with the London penetration depth $\lambda_L$ *(~100*nm*)*. For these samples one expects strong nonlocal effects that influence significantly the dynamics of the system. The preparation procedure had attempted to decrease the junction width down to *0.2*μm. The preparation scheme is shown in *Fig.7.1*.

The main structures of the base and top electrodes are defined by standard photolithography. A trilayer is sputtered on the substrate surface. The top Nb layer thickness varied between *60*nm and *100*nm, what is needed for subsequent procedures. By trilayer RIE etching we define the ground layer. Than the first boarder of the narrow long junction is defined by opening a small window in a PMMA resist using e-beam lithography. The freed trilayer inside this window is etched and the PMMA is resolved in acetone. For the insulation of this future junction boarder we use a cross-linked PMMA. The cross-linking process is carried out twice to increase the thickness of the insulator. This process creates an overlap of the insulator on the trilayer, which is a possible source of significant influences on the properties. It is possible to remove this overlap by **I**on **B**eam **E**tching (IBE) under 80° with argon. During this step, the top Nb is etched by several nanometers and, therefore, we choose a thicker top Nb film for the trilayer. The top Nb layer is defined by etching again. In a last step the e-beam lithography opens another window on the top electrode, which defines the second border of the junction.

Repeating the top layer etching offers the opportunity of stepwise narrowing of the same junction. A sequence of *I-V* curves with different width for the same junction is shown in *Fig.7.2*. The change in critical current and resistance is an indication for the change in the junction area.

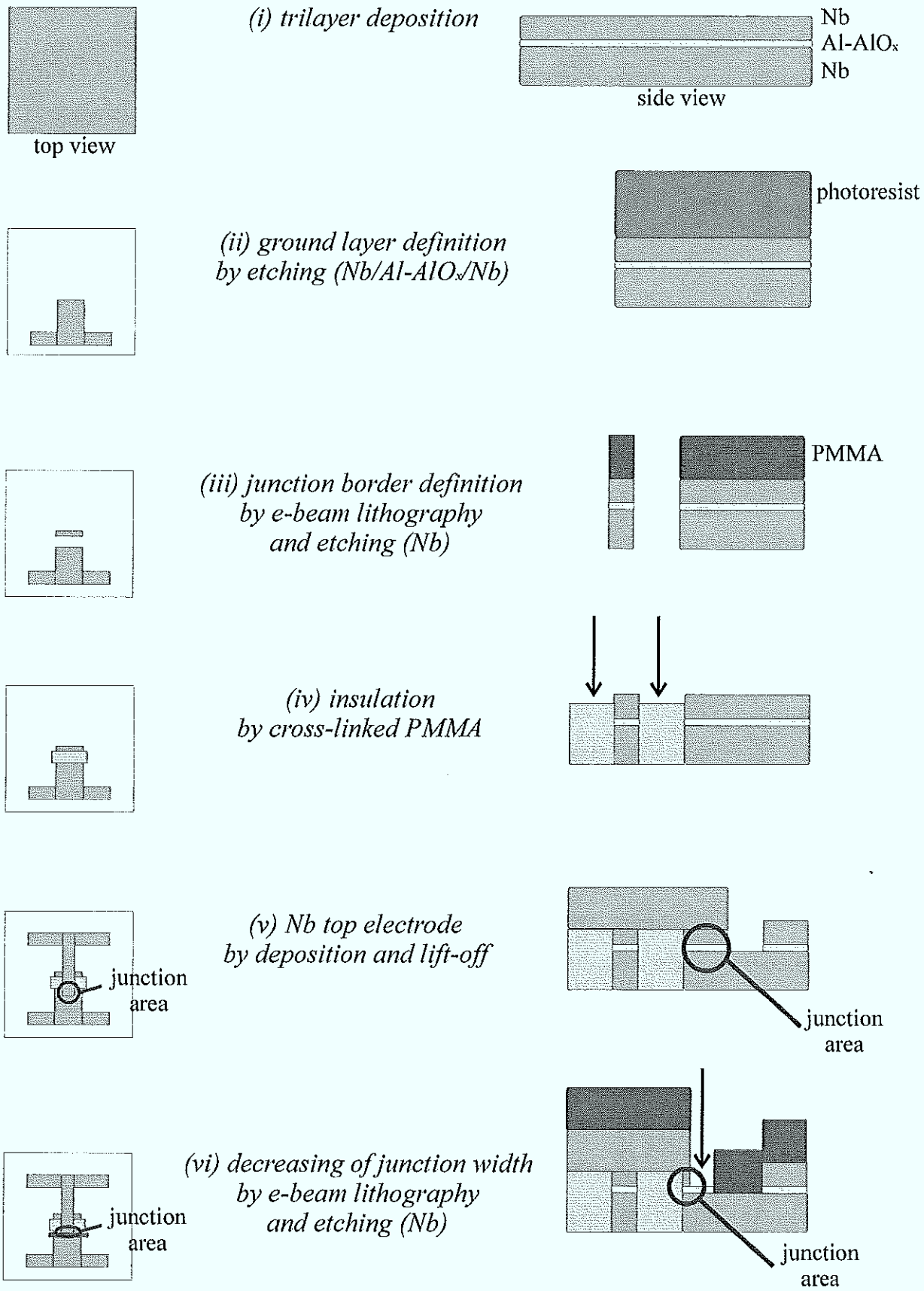


*Fig.7.1: Preparation procedure for sub-μm wide junctions*

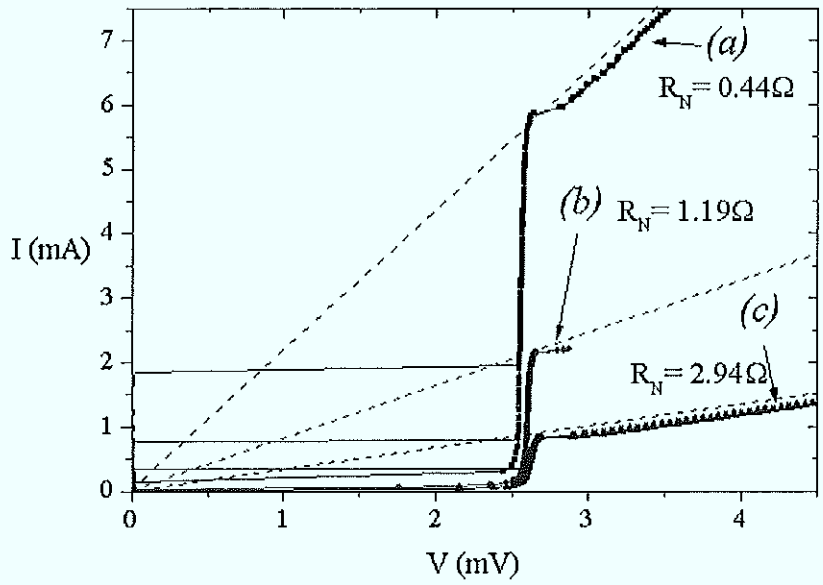


*Fig.7.2: I-V characteristics of the long Josephson junction of 200 μm length while reducing its width to (a) 4.2*μm, *(b) 1.5*μm , *and (c) 0.6*μm

The first fabricated samples did not show zero field steps. Comparing these results with letest measurements, we can conclude that this is caused by the ground electrode dimensions. Due to the preparation procedure, the ground electrode is much longer than the junction itself, and its presence possibly suppresses the reflection for fluxons as antifluxons at the junction edges. By an additional etching step the ground electrode can be shortened as shown in *Fig.7.3*.

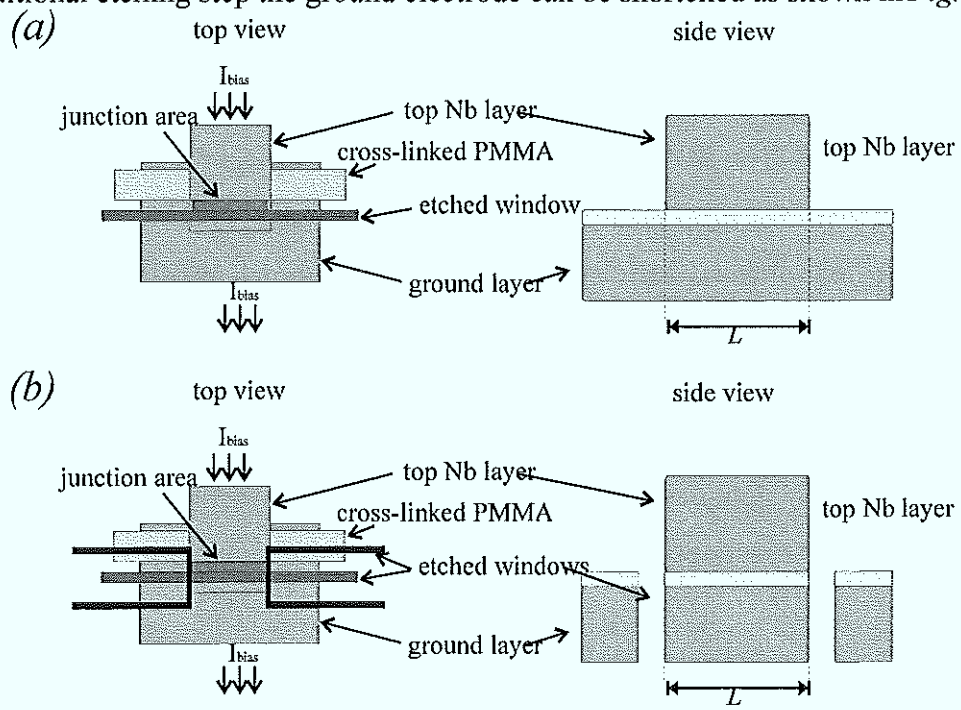


*Fig.7.3: (a) Junction with longer ground electrode, (b) shortened ground electrode*

To open the etching widows we use e-beam lithography, that serves to define exact borders. The etched borders are oxidized by a oxygen plasma in the RIE machine. This oxidation procedure was found out to be very important to improve the quality of the samples, possibly because it removes micro shorts or contamination at the edges of the junction.

We observed several new phenomena with these samples. First systematic measurements show the scaling of the Fiske step voltage spacing with the junction width *W*. An increase of Fiske step spacing with decreasing the junction width characterizes higher frequencies of the cavity resonances for narrower junctions as shown in *Fig.7.4*.

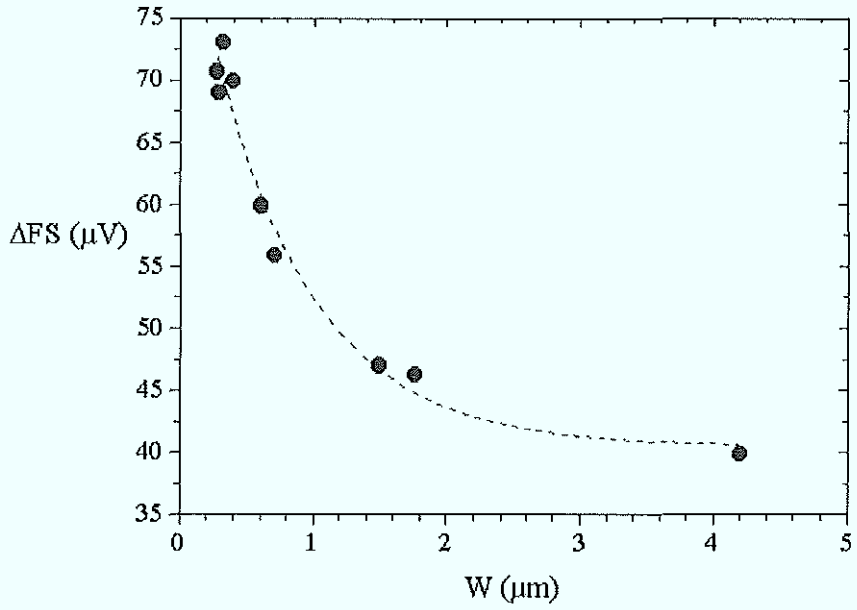


*Fig.7.4: Fiske step voltage spacing dependence on the junction width W, L=200* μm

For latest series of samples that displayed zero field steps we also measured an increased spacing in comparison to standard wide junctions. The absence of any kind of idle part for the narrow samples should even compensate partly the effect of idle windows around wide junctions. As was shown in former work[2.49,50; 7.1], the idlepart influence increases the fluxon velocity, measured as higher asymptotic voltage for ZFSs. Experimental results of ZFSs for a standard window-type junction and for a sub-micrometer wide junction are shown in *Fig.7.5*.

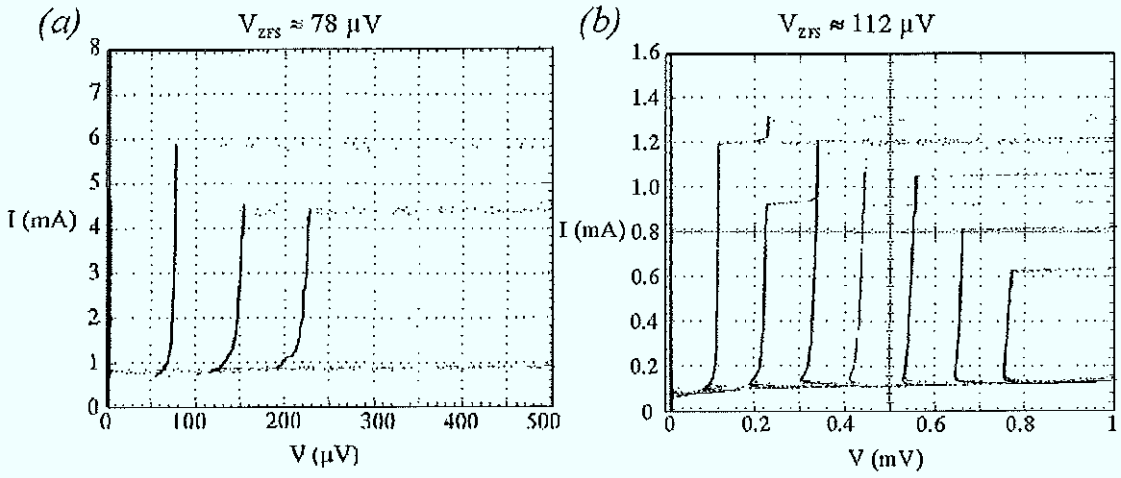


*Fig.7.5: Zero Field Steps for 200 μm long Josephson junctions*
*(a) window-type junction (W=10 μm, idle: 10μm), [sample: window01.1.7/1.3];*
*(b) narrow junction (W=2 μm), [sample: yury31]*

Another observed phenomenon is related to the modulation of the critical current by an external magnetic field. The first critical field $H_{c1}$, which characterizes the cut-off of the $I_c(H)$ pattern and the fluxon penetration, scales with the junction width. Most data show a decrease of $H_{c1}$ with decreasing $W$. At the same time, the period for mimima of higher order in the pattern decreases for narrower junctions. An example of experimental results for this shown in *Fig.7.6*

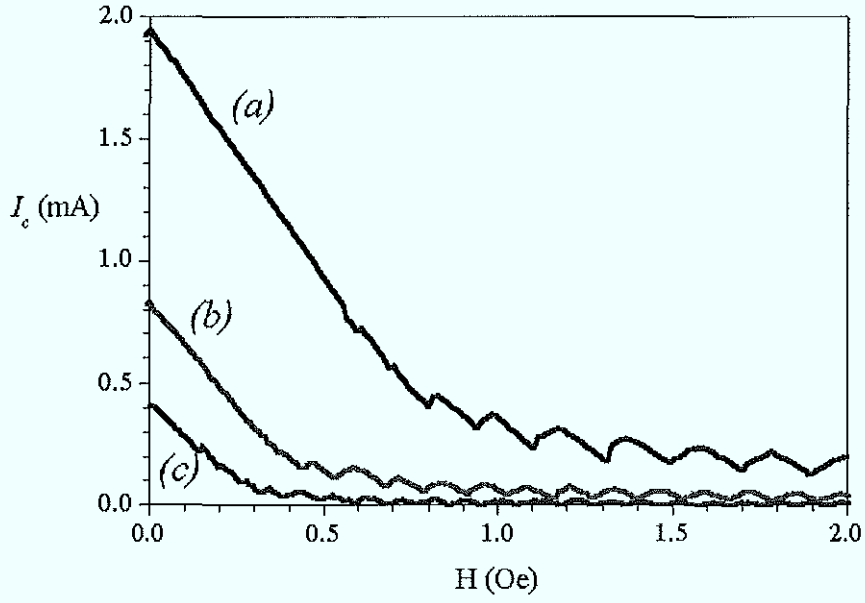


*Fig.7.6: $I_c(H)$ and side minima period for different junction width*
*(a) width: 4.2 μm (b) width: 1.5 μm , and (c) width: 0.6 μm*

In his theoretical approach M. Fistul[7.2] suggested a model which explains the scaling tendency in experimental data. Fistul proposes a correction of the $\phi_x \leftrightarrow H(x,y)$ relation. In general, the finite width of the junction can be taken into account in a corrected relation that can be written in the form

$$\frac{\partial \phi(x,y)}{\partial x}\alpha(y) = \frac{H_y(x,y)d}{\Phi_0} \quad \text{, and} \quad \frac{\partial \phi(x,y)}{\partial y}\alpha(y) = \frac{H_x(x,y)d}{\Phi_0} \; . \qquad \{7.1\}$$

Here the magnetic field is given by $H$ and the function $\alpha(y)$ is equal to one for large distances to the junction borders. Near the junction boarders $\alpha(y)$ increases, which characterizes an increase of the internal magnetic field near the boarders. In the one-dimensional sine-Gordon equation this function $\alpha(y)$ enters in the way

$$\frac{\partial^2 \phi}{\partial x^2} + \frac{\partial^2 \phi}{\partial y^2} - \frac{1}{\bar{c}^2 \alpha(y)}\frac{\partial^2 \phi}{\partial t^2} - \frac{1}{\lambda_J^2 \alpha(y)}\sin\phi = 0 \; . \qquad \{7.2\}$$

The influence of the function $\alpha(y)$ can be discussed without solving this equation analytically. For a homogeneous function the Fiske step spacing will depend on $\alpha(y)$ as

$$V_{Fs} \propto \sqrt{\langle \alpha(y) \rangle} \; . \qquad \{7.3\}$$

Here $\langle \alpha(y) \rangle$ gives the average value along the width of the junction. The previous cogitation showed, that $\alpha(y)>1$ and therefore the spacing is expected to increase. On the other hand the Josephson penetration depth will change also in the way

$$\lambda_J(w) = \lambda_J(\infty)\sqrt{\langle \alpha(y) \rangle} \; , \qquad \{7.4\}$$

which means increasing values, too. In addition, the boundary conditions have to include an increased Meissner current

$$\frac{\partial \phi(0,y)}{\partial x} = \frac{\partial \phi(L,y)}{\partial x} = \frac{H_{ext} d}{\Phi_0}\alpha(y) \; . \qquad \{7.5\}$$

Now it is possible to distinguish the case of infinite width and finite width and to determine a mapping for the parameters.

| **finite width:** | **infinite width:** |
|---|---|
| $H_{ext}\langle \alpha(y) \rangle$ | $H_{ext}$ |
| $\lambda_J \sqrt{\langle \alpha(y) \rangle}$ | $\lambda_J$ |
| $V_{Fs}\sqrt{\langle \alpha(y) \rangle}$ | $V_{FS}$ |

Without calculating the function $\alpha(y)$, we can check this model by measurements of the scaling of the experimental data. The predicted relation is

$$H_{c1}(W) \propto \left(\frac{1}{V_{FS}(W)}\right)^3 \propto (\Delta H(W))^{1/2} . \qquad \{7.6\}$$

*Fig.7.7* shows the experimental data and the two fitting curves according to {7.6}. Inspite of the large spread, the available data make it possible to positively conclude about the scaling {7.6}.

Nevertheless these results have been received with samples that have a specific geometry, which can be interpreted as idle part. They have a thin insulator (cross-linked PMMA) and an overlap structure of the latter on the junction area. Former investigations[2,49,50] show that the idle part leads to an increase of the Fiske step spacing. Latest preparation runs have shown the possibility to produce symmetric junctions without idle part and thicker insulator on the junction side. It is possible that more definite conclusions can be made by comparing the similar data for latest preparation runs with scaling {7.6}.

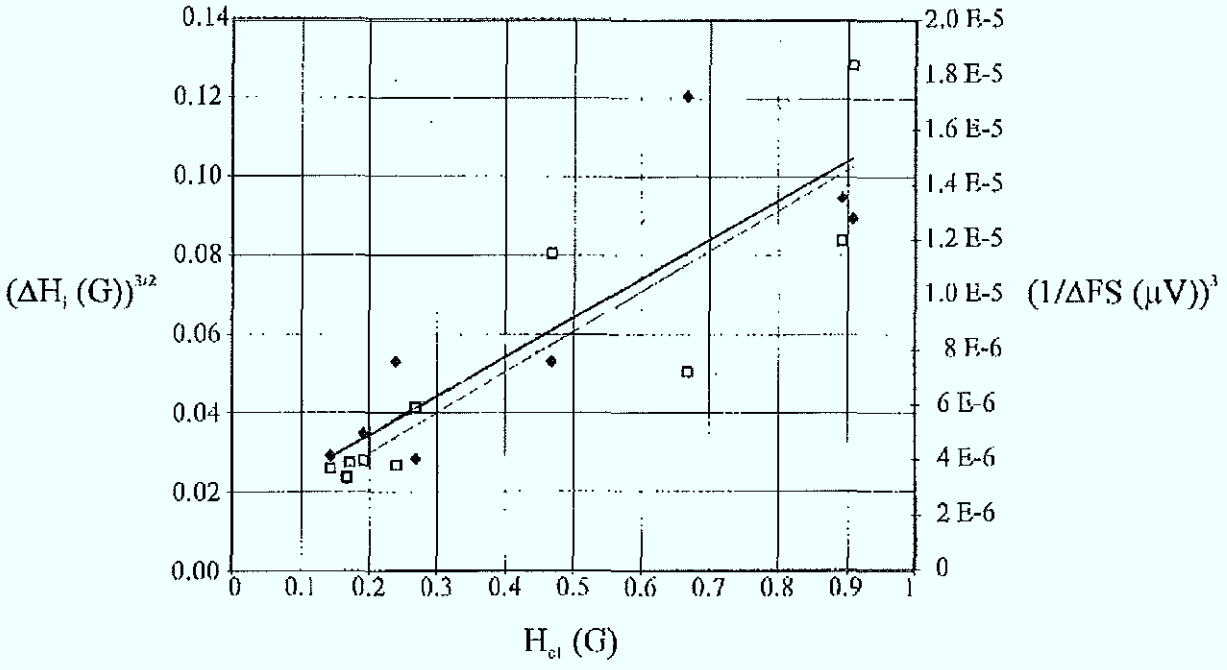


*Fig.7.7: Proportionality plot between $H_{c1}$ (x-axis), $(\Delta FS)^{-3}$ (right axis), and $(\Delta H_i)^{3/2}$ (left axis)*

The critical current modulation was also measured at various temperatures down to *300*mK. Above *4.2*K the period of side maxima is increasing. Below *4.2*K the measured values are nearly constant. The experimental data are shown in *Fig.7.8*. We should note that the abrupt increase of $\Delta H_i$ from the low temperature data (below *3*K) to high temperature data is not understood and requires additional measurements.

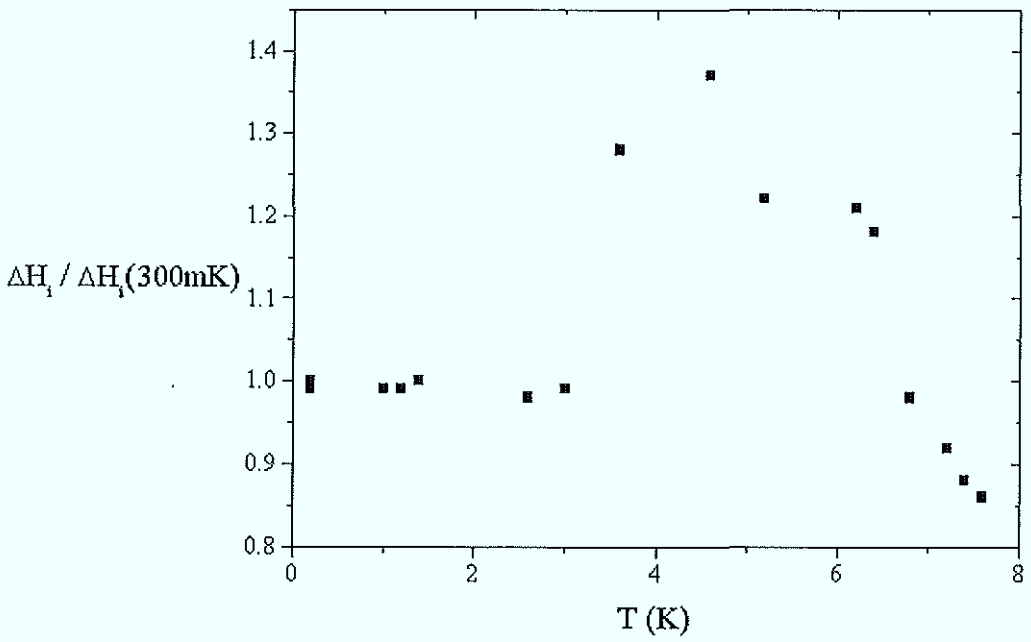


*Fig.7.8: $\Delta H_i$ for different temperatures; all data are normalized to the value at 300 mK*

For increasing temperature the effective Josephson penetration length $\lambda_J$ increases, which changes the effective junction length.

Due to the limited number of experimental data and still lacking complete theoretical model for narrow junctions, here I confined myself to the above presented phenomenological description. Additional experiments should be done with new samples.

### 7.2 Junctions with X-band coupling circuit

During the Vigoni-DAAD project we tested X-band (range *6-18*GHz) coupling circuits with long Josephson junctions. The junction is embedded in a coplanar wave guide and the used layout is shown in *Fig.7.9*. Besides the central junction, each chip contains several interferometers with *2,3, and 4* junctions, one small (*10×10*μm²), and a long (*500×10*μm²) test junction, placed on the sides of the central coplanar system.

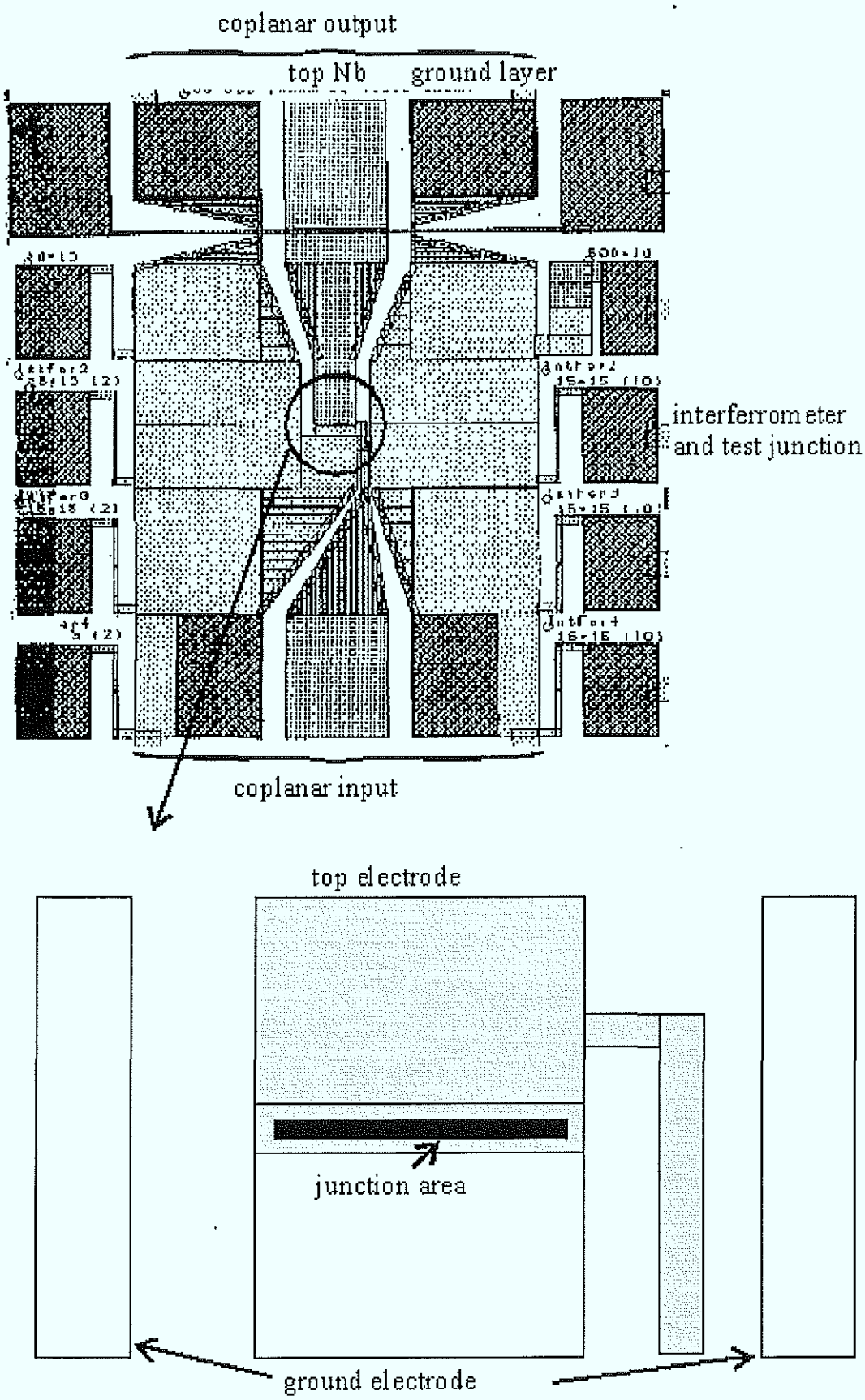


*Fig.7.9: Layout for a long Josephson junction in a coplanar wave guide*

*(Design by M. Cirillo and N. Thyssen)*

The rf-coupled junctions were single long junctions ($500 \times 10 \mu m^2$) and one-dimensional arrays of small junctions ($10 \times 10 \mu m^2$). In future, it can also serve for stacked junction preparations, because I used the standard single junction process. Just one additional step is included. Before placing the top Nb electrode, the trilayer is etched on the contact pads area, to obtain a direct top niobium contact to the ground niobium layer. A second layout was developed to prepare long shunted Josephson junctions. Therefore the preparation procedure includes the sputtering and lift-off for the Pd-Au shunt, which is done before placing the top Nb electrode. A first preparation run showed the functioning of the process, although the shunt resistance differed from the calculated values due to contamination of the target.

The samples were characterized in Rome, where experiments with external receivers and generators in the frequency range of *6 to 18*GHz are possible. In *Fig.7.10(a)* the *I-V* characteristic of the first ZFS for a *500*μm long junction is shown. The circuit has been coupled to an external generator and the voltage range of locking to its rf signal is measured. Two bias points are shown, and the locking region is up to *50*nV (*Fig.7.10(b)*). This is an evidence for a very efficient coupling of the junction to the external signal. Also with these junctions the Josephson radiation emitted in the X-band has been measured.

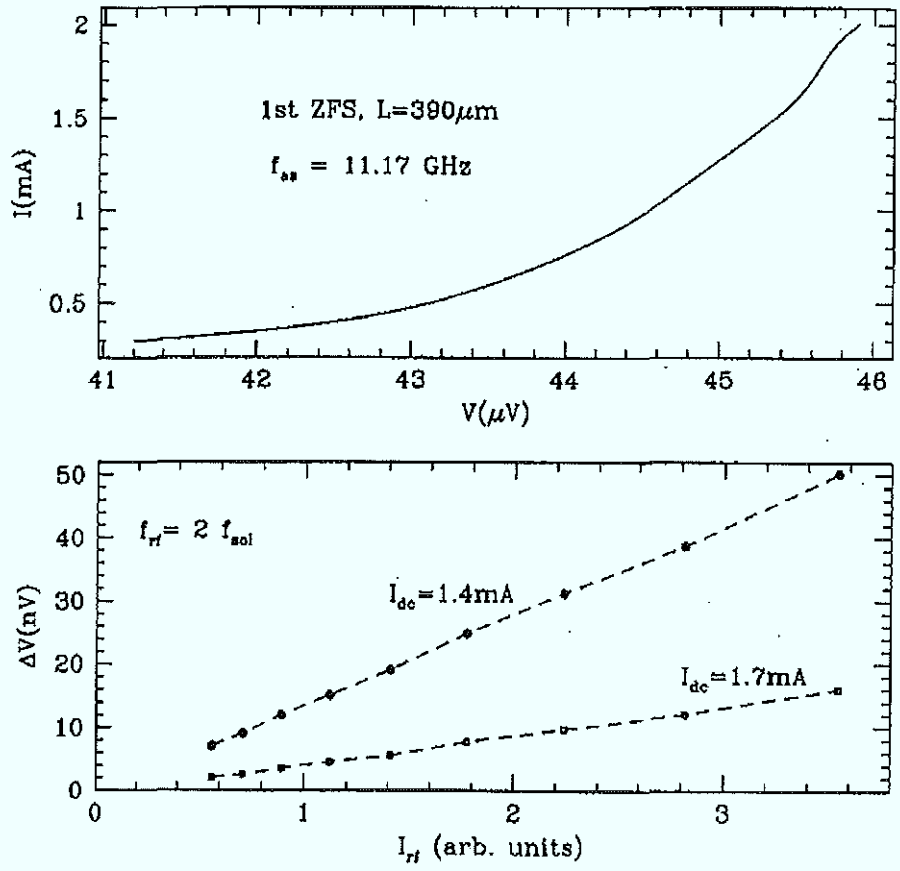


*Fig.7.10: (a) First ZFS, and (b) voltage response for the locking to an external signal at two bias points*

The theory[7,3,4] predicts a different response of the junction to different harmonics of the Josephson frequency, depending on a uniform coupling and a coupling localized at the junction borders. In *Fig.7.11* the frequency (voltage) interval for possible locking to the external frequency is shown in dependence of the irradiated signal power. *Fig.7.11(a)* shows the results for an external frequency equal to the fundamental oscillation frequency $f_{fo}$ of the junction. In *Fig.7.11(b)* the same phenomena is shown for an external frequency $f_{ext} = 3 \times f_{fo}$. The results for the second harmonic ($f_{ext} = 2 \times f_{fo}$) are shown in *Fig.7.11(c)*. The dependence on the second harmonic is much weaker in comparison with the first harmonic. This result characterizes a coupling across the edges of the junction. For applications, this possibility of efficient coupling to external signals is very interesting and the properly shunted junctions should bring a larger area of tunability.

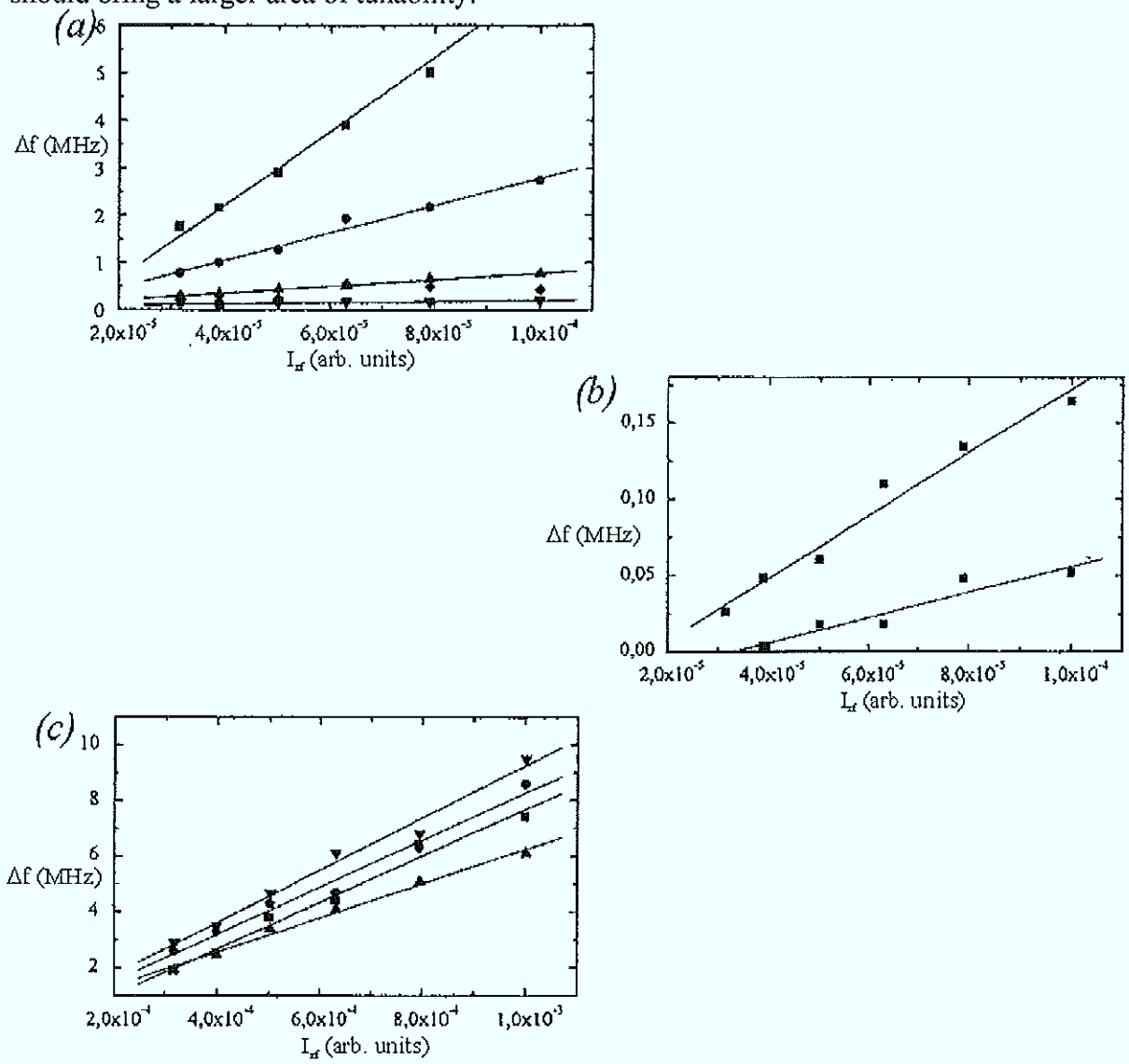


*Fig.7.11: Locking range for different external frequency*

*(a) $f_{ext}$: 1st harmonic, (b) $f_{ext}$: 3rd harmonic , and (c) $f_{ext}$: 2nd harmonic*

# 8. Conclusions

This thesis presents the first investigations of $Nb/(Al\text{-}AlO_x/Nb)_N$ multi-layer Josephson tunnel junctions. The finally achieved possibility to produce up to *10* stacked junctions with a parameter spread of less than *5%* is the state of the art in this area. A preparation of *28*-fold stacks shows future potential of the developed techniques. Several contributions in the field of fluxon dynamics had been possible during this thesis work.

In the case of single-barrier annular junctions, experimental studies of fluxon pinning and trapping by an external magnetic field showed an impressive consensus with recently developed theoretical models. The analog between the fluxon and a particle in a washboard potential is clearly demonstrated.

Experimental studies on the possibility of separating the internal and external coupling mechanisms for window type two-fold stacks were finally not conclusive. The started work was not continued due to the main priority of multi-layer junction investigations. It is rather evident that the internal coupling mechanism dominates over the external one, but quantitative measurements require further investigations. We hope that the presented results can motivate additional systematic work on the topic of the coupling to investigate the coupling mechanisms for Josephson stacks.

Experimental investigations were carried out on two-fold stacks with and without electrical contact to the middle (inner) niobium electrode. The static properties were studied by numerical simulations and experiment. Using the coupled sine-Gordon equations, a prediction of neighboring junctions in dependence of different critical currents was done at non zero fields. Our experimental $I_c(H)$ pattern showed very similar dependencies, biasing both junctions in series. This biasing leads to current locking at zero voltage and the critical current is not equal to that of a single junction due to the inductive coupling. The observed phenomenon is in agreement with independent analytical results of Goldobin and Ustinov[5.17]. They showed that a whirling state of one junction cancels any influence of its outer electrode on the properties of the second junction. This second junction behaves identically to a single junction with a thin electrode (middle electrode of the stack). We used the contact to the middle electrode to define the voltage states of the single junctions in the stack. Due to the thick outer electrodes the bottom and the top junction show a different field

dependence. We state here that this behavior might be a serious problem for achieving a homogeneous magnetic field distribution in a stack.

The evidence for Cherenkov radiation of fluxons in two fold stacks was observed on samples prepared during this thesis work. Spatial homogeneity of 2 stacked rings was rather crucial for successful observation of this effect[5.18].

Our detailed comparison of experimental results on *7*-fold stacks (medium coupling) with numerical simulations showed very impressive quantitative agreement. We conclude finally that multi-stacked Josephson tunnel junctions can be well described by the coupled sine-Gordon model[6.4]. The resonances in *I-V* curves can be interpreted as sum voltage of the *out-of-phase* states of all inner junctions plus larger voltage contributions from the bottom and top junctions. Due to the thicker bottom and top electrode the outer junctions reach another flux-flow state. First radiation emission measurements confirm the *out-of-phase* motion by their small radiation power. We tried to check experimentally the model prediction for stronger coupling. The intermediate Nb electrode thickness has been successfully decreased down to *20*nm. The developed preparation procedure was modified to achieve small parameter spread in *10*-fold stacks. Unfortunately, in the latest samples using the new lay out, the parameter spread increased and the required sample quality was not reached up to now. This is the reason why our experimental study of strongly coupled *10*-fold stacks is not conclusive at this stage. We believe that final conclusions can be made after further optimization of the preparation procedure.

We showed a stacking technology which is capable to produce multi-junction stacks with up to 28 tunnel barriers. Increasing the number of barriers in Nb/Al-$AlO_x$ stacks is not a problem for the multilayer deposition system. The most crucial part of technology is the etching procedure: we have to accept a larger parameter spread for a large number of junctions. The use of photoresist as etching mask is not satisfactory for more than *10* stacked junctions. The possible solution is a metallic or a multi-layer etching mask that would guarantee a planar dimension conservation during all the process. The tests with other etching systems like ion beam etching (IBE) showed a reasonable etching rate, but no efficient control of the etching stop. The IBE process damages the junction borders, as was shown by single junction preparations with resulting bad *I-V* curves. We think the solution for the problem can be alternative insulation. Spinned organic insulators with low backing temperatures (*<180*°C)

would be by far more advantageous. In my point of view, the technology for stacked Nb-Al junctions is presently limited by these points. Stacks with *50* junctions are already possible, but the spread in critical currents increases with increasing $N$.

We also successfully used the combination of conventional trilayer technology and e-beam lithography to prepare sub-μm wide long Josephson junctions. First samples showed a strong scaling of the Fiske steps with the width of the junction. For narrow junctions the voltage spacing increases. In addition, the first critical field $H_{c1}$ decreases and the side minima period $\Delta H_i$ increases for wider junctions. Our experimental results are in agreement with the model proposed by M. Fistul.

I hope that my contribution in this field of research motivates future systematic work on multi-layer Josephson tunnel junctions.

# 9. Zusammenfassung

In der vorliegenden Arbeit wird die technische Realisierung und Charakterisierung von gestapelten Nb/Al-$AlO_x$/Nb Josephson-Tunnelkontakten mit hoher Barrierenanzahl dokumentiert. Es handelt sich hierbei um magnetisch gekoppelte **S**upraleiter-**I**solator-**S**upraleiter Tunnelkontakte, die theoretisch mit dem Model gekoppelter sinus-Gordon Gleichungen beschrieben werden[1.22]. Ein Gleichungssystem für $N$ Tunnelkontakte sieht wie folgt aus

$$-\frac{\hbar}{2e\mu_0}\frac{\partial^2}{\partial x^2}\begin{pmatrix}\phi_{1,0}\\ \phi_{2,1}\\ \vdots\\ \phi_{i,i-1}\\ \vdots\\ \phi_{N,N-1}\end{pmatrix}=\begin{pmatrix} d'_{1,0} & s_1 & 0 & & & \cdots & 0\\ s_1 & d'_{2,1} & s_2 & \ddots & & & \vdots\\ 0 & & \ddots & & & & \\ & 0 & s_{i-1} & d'_{i,i-1} & s_i & 0 & \\ & & & & \ddots & & 0\\ \vdots & & & \ddots & & & s_{N-1}\\ 0 & \cdots & & & 0 & s_{N-1} & d'_{N,N-1}\end{pmatrix}\begin{pmatrix} j^z_{1,0}\\ j^z_{2,1}\\ \vdots\\ j^z_{i,i-1}\\ \vdots\\ j^z_{N-1,N-2}\\ j^z_{N,N-1}\end{pmatrix}.$$

Dieses Gleichungssystem stellt die Beziehung der einzelnen Phasendifferenzen $\phi_{i,i-1}$ an den Tunnelkontakten in Abhängigkeit der Kopplungskonstanten $s_i$, der magnetischen Dicke $d'_{i,i-1}$ und der jeweiligen Stromdichte $j^z_{i,i-1}$ dar. Die benötigten Randbedingungen sind für eine ringförmige Geometrie periodisch, während für lineare Systeme das externe Magnetfeld die Randbedingungen entscheidend beeinflußt. Die Untersuchungen beinhalten Ergebnisse mit hoch qualitativen Einzelkontakten und vertikalen Stapeln mit maximal *28* Josephson-Elementen.

---

Unter Verwendung von ringförmigen Tunnelkontakten konnte die Dynamik einzelner Josephson-Flußquanten untersucht werden. Dabei wurde durch dieses System das Verhalten eines relativistischen Teilchens in einem periodischen Potential experimentell dargestellt. Das externe Magnetfeld bewirkte ein cosinusförmiges Potential für Solitonen im ringförmigen Tunnelkontakt. Ein Vergleich zwischen den experimentellen Ergebnissen und dem theoretischen Modell weist beeindruckende Übereinstimmung auf[2.57].

---

Durch die Untersuchungen an Stapel mit zwei Josephson Elementen, mit und ohne elektrischen Kontakt zur mittleren Elektrode, konnte der Einfluß der Kopplung beider Kontakte auf die Magnetfeldabhängigkeit jedes einzelnen Josephson-Tunnelkontaktes nachgewiesen werden. Durch den Übergang vom statischen ($V=0$) in den dynamischen ($V\neq 0$) Zustand von einem Tunnelkontakt, wird die geänderte Magnetfeldabhängigkeit des anderen

erklärt durch eine verdünnte supraleitende Elektrode. Als Konsequenz ergibt sich für gestapelte Systeme eine starke Abhängigkeit des Systems vom Spannungszustand benachbarter Josephson Elemente.

---

Mit Hilfe eines dimensionsvariierten aktiven und Fluß fokussierenden Fensters um einen langen Tunnelkontakt wurde versucht interne und externe Kopplungsmechanismen experimentell zu trennen. Dazu wird die äußere Kopplung durch die Fenstergröße verändert, während die interne Kopplung konstant gehalten wurde. Die Resultate zeigten keine signifikante Änderung der gemessenen Kopplungsstärke im untersuchten Bereich. Das Testen anderer Parameterkonditionen zeigte ebenfalls keine klareren Ergebnisse. Die innere Kopplung ist somit um einige Größenordnungen stärker anzunehmen als die äußere Kopplung.

---

Durch das Einfangen eines einzelnen Josephson-Flußquantes in einem Ringkontaktstapel aus *2* Elementen konnte die Existenzbedingung für Cherenkov-Strahlung erfüllt werden. Ein Nachweis wurde experimentell erbracht über zusätzlich auftretende Resonanzstufen als Feinstruktur auf der Solitonenstufe im Strom-Spannungs Diagramm. Die experimentellen Daten stimmen mit den theoretischen Modellrechnungen sehr gut überein.

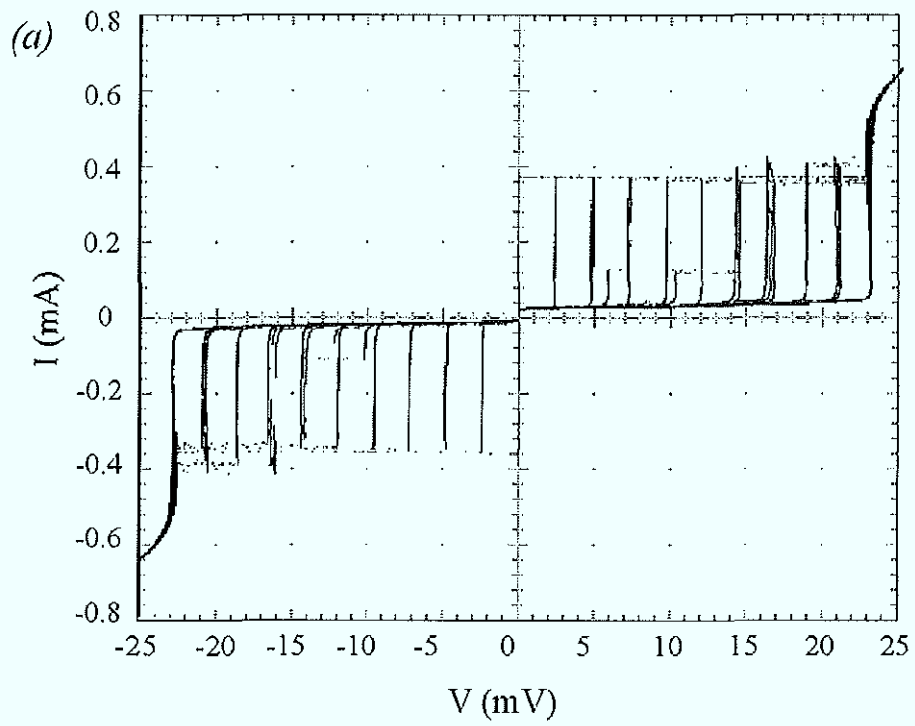


*Fig.9.1(a): Strom-Spannungs Kennlinien schmaler Josephson Tunnelkontaktstapel (20×20μm²) 10-er Stapel mit einer Parameter-Streuung von ca. 5% [Probe: winfin10s4/2.1]*

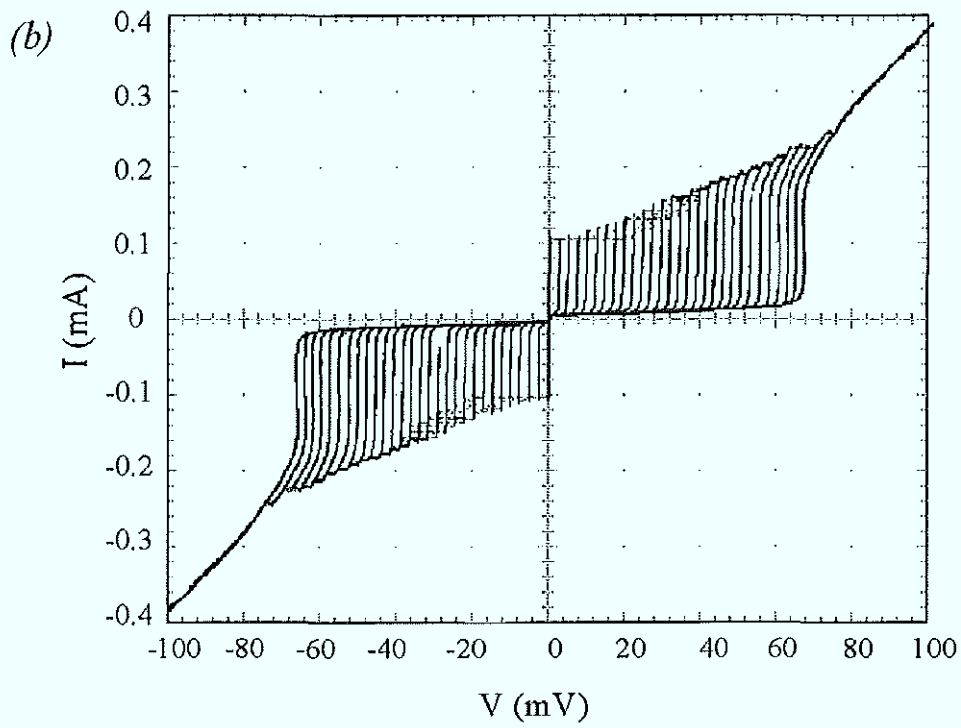


*Fig.9.1(b): Strom-Spannungs Kennlinien schmaler Josephson Tunnelkontaktstapel (20×20μm²) 28-er Stapel [Probe: winfin 30s1/2.1]*

Technologisch gelang weltweit erstmalig die Herstellung gestapelter Elemente mit hoher Barrierenanzahl und minimierter Parameterstreuung mit bis zu *10* Elementen (*Fig.9.1(a)*). Eine ungenügende Formtreue der verwendeten Lackmasken beim Ätzprozeß bedingte diese Grenze. Die Herstellung von *28* funktionsfähigen gestapelten Elementen zeigte aber das Potential der entwickelten Verfahren, auch wenn die Problematik der Dimensionsänderung während des Ätzprozesses noch nicht ganz gelöst wurde (*Fig.9.1(b)*). Die kritischen Herstellungsschritte wie Deposition und Ätzen wurden im Verlauf der Arbeit vollautomatisiert.

Beim gestapelten System treten zusätzliche Resonanzstufen bei höheren Spannungen auf, die durch numerische Simulationen mit obigem Modell interpretiert werden konnten. Es handelt sich um die Summe einer *außer-Phase* Bewegung von Josephson-Flußquanten in den inneren Kontakten und den Spannungsbeiträgen der beiden äußeren Kontakte des Stapels, welche eine größere Flußquantenanzahl aufweisen. Die Übereinstimmung der numerisch ermittelten Daten mit den experimentellen Ergebnissen ist ausgezeichnet.

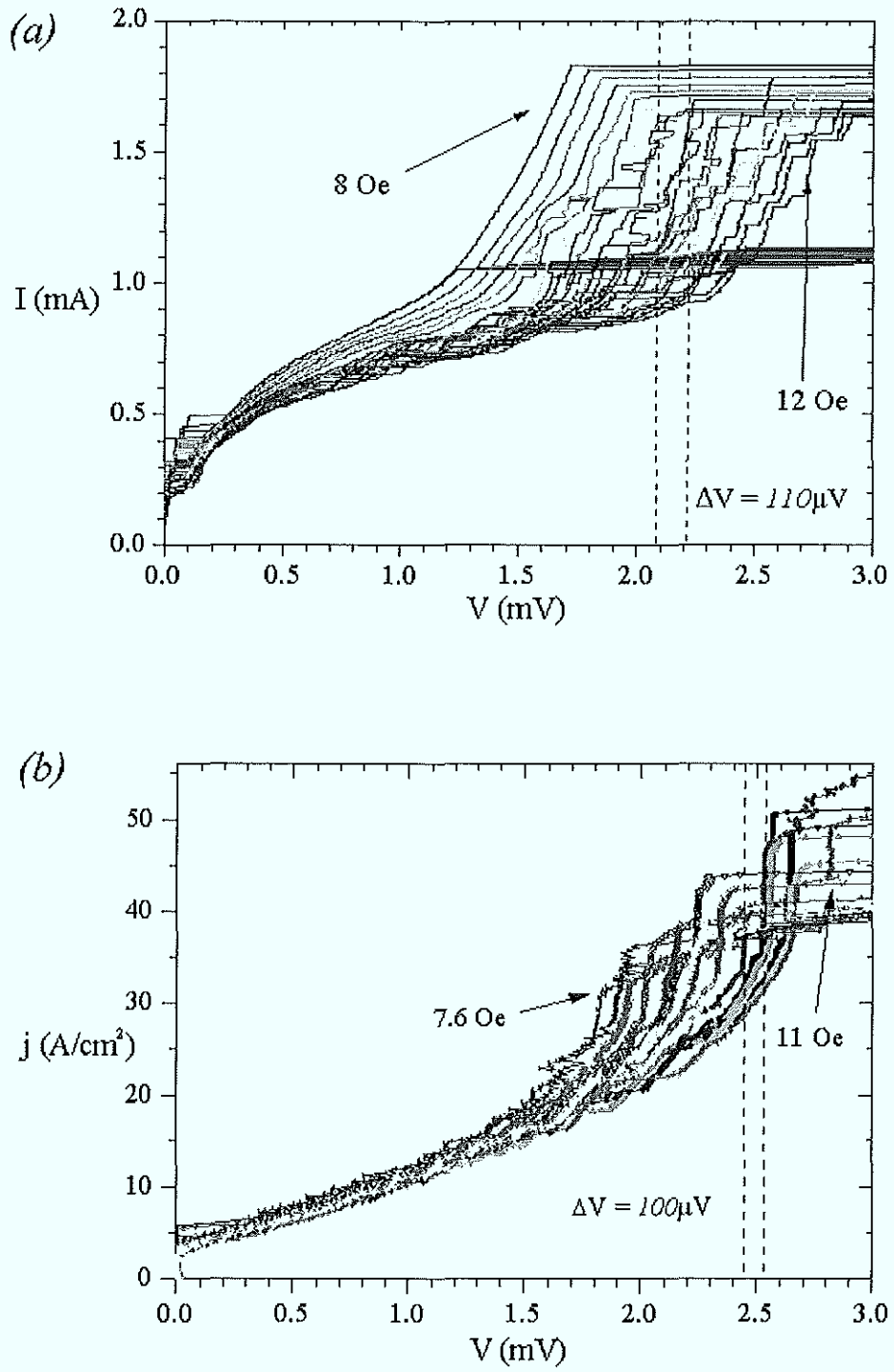


*Fig.9.2: Resonanzstufen eines 7-er Tunnelkontaktstapels unter dem Einfluß eines externen Magnetfeldes; (a) Experiment [Probe: window1.7.1/2.2] (350×20μm²), (b) numerische Simulation*

Mit dem Modell konnten wir unter Verwendung anderer Parametervorgaben eine Vorhersage machen über stabile *in-Phase* Moden der Solitonendynamik in allen inneren Tunnelkontakten eines *10*-er Stapels. Hierzu wurde die Zwischenschichtdicke auf *20*nm minimiert und die

kritische Stromdichte auf ca. *20*A/cm² erniedrigt. Erste Proben mit geänderten Layout zeigten noch nicht die erwarteten Eigenschaften, was mit zu großer Parameterstreuung durch Herstellungsmängel aufgrund verschobener Prozeßparameter erklärt werden kann.

---

Diese Arbeit zeigt die technologische Realisierbarkeit (bis zu *28* Tunnelkontakte) und ihre Grenzen (bis zu *10* Tunnelkontakte mit einer Streuung von weniger als *5*%) von Josephson-Tunnelkontaktstapeln mit hoher Barrierenanzahl und minimierter Parameterstreuung. Durch den Vergleich mit numerischen Simulationsrechnungen konnten die erhaltenen Meßergebnisse reproduziert und gedeutet werden. Auch wenn erste Strahlungsemissionsmessungen (*Fig.9.3*) an *9*-er Stapeln nicht auf eine *in-Phase* Mode zurückzuführen sind, können die Modellvorhersagen als Grundstein für weiterführende Untersuchungen gesehen werden.

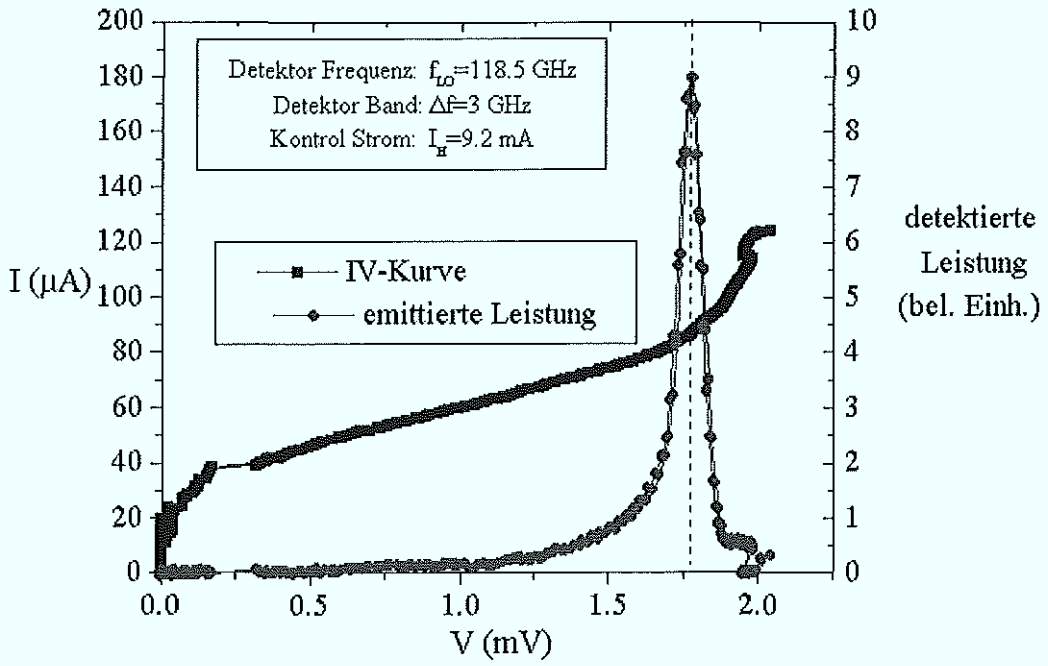


*Fig.9.3: Strahlungsemissionsmessung eines 9-er Stapels*

---

Im Verlaufe dieser Arbeit gelang es außerdem sub-micrometer schmale Tunnelkontakte herzustellen. Für Breiten im Bereich der magnetischen Eindringtiefe $\lambda_L$=*100*nm werden nichtlokale Effekte erwartet, die den Quantencharakter des Systems in experimentellen Daten widerspiegeln. Erste Proben mit Breiten bis zu *200*μm wurden systematisch vermessen, und es zeigte sich eine Vergrößerung der Fiske-Stufenabstände ($\Delta V_{FS}$) für verringerte Kontaktbreiten. Außerdem nahmen die im Fraunhofer Pattern gemessenen Werte für das erste

kritische Magnetfeld ($H_{c1}$) und die Abstände der Seitenminima ($\Delta H_i$) ab. Diese Effekte konnten mit Hilfe eines Modellansatzes von M.V. Fistul erklärt werden. Ein Vergleich der vorhergesagten Abhängigkeiten $H_{c1}(W) \propto \left(\frac{1}{\Delta V_{FS}(W)}\right)^3 \propto (\Delta H_i)^{3/2}$ mit den experimentellen Daten zeigte eine gute Übereinstimmung. Zur besseren Interpretation wurden Tests zur Optimierung der Herstellung und weiteren Minimierung der Kontaktbreite mit Erfolg abgeschlossen.

## 10. References


(1.1) H. Rogalla, and D.H.A. Blank, Applied Superconductivity 1997, Proceedings of EUCAS 1997, the third European Conference on Applied Superconductivity, held in The Netherlands, 30 June - 3 July 1997, *Institute of Physics Conference Series Number* **158**, *Institute of Physics Publishing, Bristol and Philadelphia* (1997)

(1.2) A. Barone, and G. Paterno: „Physics and Applications of the Josephson Effect", *John Wiley & Sons*, New York (1982)

(1.3) K.K. Likharev: „Dynamics of Josephson Junctions and Circuits", *Gordon and Breach Science Publishers* (1986)

(1.4) H. Kohlstedt, *Doktorarbeit Universität Kassel, IRAM Grenoble*, (1989) in German

(1.5) F. Müller, R. Pöpel, J. Kohlmann, J. Niemeyer, W. Weimann, L. Grimm, F-W Dünnschede, and P. Gutmann, *IEEE Trans. on Instrum. and Meas.* **46**, 229 (1997)

(1.6) C.A. Hamilton, C.J. Burroughs, and S.P. Benz, *IEEE Trans. on Appl. Supercond.* **7**, (1997)

(1.7) H. Yoshida, Y. Murayama, and T. Endo, *IEEE Trans. on Instrum. and Meas.* **46**, 72 (1997)

(1.8) K.K. Likharev, V.K. Semenov, *IEEE Trans. Appl. Supercond.* **1**, 3 (1991)

(1.9) T. Kato, and M. Imada, *J. Phys. Soc. Jpn.* **65 (9)**, 2963 (1996)

(1.10) J. Mannhart, and H. Hilgenkamp, *Inst. Phys. Conf. Ser. No* **158**, 1 (1997)

(1.11) A. Davidson, B. Dueholm, B. Kryger, and N.F. Pedersen, *Phys. Rev. Lett.* **55**, 2059 (1985)

(1.12) W. Buckel: „Supraleitung", *VCH Verlagsgesellschaft mbH* (1990)

(1.13) T. Van Duzer, and C.W. Turner: „Principles of Superconductive Devices and Circuits", *Edward Arnold Verlag* (1981)

(1.14) J. Mygind, V.P. Koshelets, A.V. Shchukin, S.V. Shitov, and I.L. Lapitskaya, *IEEE Trans. on Appl. Supercond.* **5**, 3057 (1995)

(1.15) T. Nagatsuma, K. Enpuku, F. Irie, and K. Yoshida, *J. Appl. Phys.* **54 (6)**, 3302 (1983)

(1.16) T. Nagatsuma, K. Enpuku, K. Yoshida, and F. Irie, *J. Appl. Phys.* **56 (6)**, 3284 (1984)

(1.17) T. Nagatsuma, K. Enpuku, K. Yoshida, and F. Irie, *J. Appl. Phys.* **58 (1)**, 441 (1985)

(1.18) S.V. Shitov, A.V. Ustinov, N. Iosad, and H. Kohlstedt, *J. Appl. Phys.* **80**, 7134 (1996)

(1.19) P.A.A. Booij, and S.P. Benz, *Proceedings of ISEC95* , 513 (1995)

(1.20) R. Kleiner, F. Steinmeyer, G. Kunkel, and P. Müller, *Phys. Rev. Lett.* **68**, 2394 (1992)

(1.21) R. Kleiner, and P. Müller, *Phys. Rev. B* **49**, 1327 (1994)

(1.22) S. Sakai, P. Bodin, and N.F. Pedersen, *J. Appl. Phys.* **73**, 2411(1993)

---

(2.1) H. Kamerlingh Onnes, *Leiden Comm.* **122b**, 124 (1911)

(2.2) W. Meissner, and R. Ochsenfeld, *Naturwiss.* **21**, 787 (1933)

(2.3) B.D. Josephson, *Phys. Lett.* **1**, 251 (1962)

(2.4) J.R. Anderson, and J.M. Rowell, *Phys. Rev. Lett.* **10**, 30 (1963)

(2.5) J.B. Bednorz, and K.A. Müller, *Z. Phys.* **B64**, 186 (1986)

(2.6) F. London, and H. London, *Proc. Roy. Soc.* **A149**, 71 (1935)

(2.7) V.L. Ginzburg, and L.D. Landau, *Zh. Eksp. Teor. Fiz.* **20**, 1064 (1950)

(2.8) A.A. Abrikosov, *Zh. Eksp. Teor. Fiz* **32**, 1442 (1957) ; *Sov. Phys. JETP* **5**, 1174 (1957)

(2.9) J. Bardeen; *Physics Today*, 41, July (1973)
(2.10) L.N. Cooper; *Physics Today*, 31, July (1973)
(2.11) J.R. Schrieffer; *Physics Today*, 23, July (1973)
(2.12) R.P. Feynman, R.B. Leighton,and M. Sands, *Lecture in Physics*, vol. **3**. *Addison-Wesley* (1965)
(2.13) A.I. Larkin, and Yu.N. Ovchinnikov, *Zh. Eksp. Teor. Fiz.* **51**, 1535 (1966); *Sov. Phys. JETPL* **24**, 1035 (1967)
(2.14) I.K. Yanson, V.M. Svistunov, and I.M. Dmitrenko, *Zh. Eksp. Teor. Fiz.* **48**, 976 (1965); *Sov. Phys. JETP* **21**, 650 (1965)
(2.15) A.A. Golubov, and M.Yu. Kupriyanov, *J. Low Temp. Phys* **70**, 83 (1988)
(2.16) A.A. Golubov, E.P. Houwman, J.G. Gijsbertsen, V.M. Krasnov, J. Flokstra, J.B. le Grand, and P.A.J. de Korte, *Phys. Rev. B* **49**, 1073 (1995)
(2.17) D.E. Mc Cumber, *J. Appl. Phys.* **39**, 3113 (1968)
(2.18) C.P. Poole Jr., H.A. Farach, and R.J. Creswick, *Superconductivity, Academic Press* (1995)
(2.19) J.C. Swihart, *J. Appl. Phys.* **32**, 461 (1961)
(2.20) S. Pagano, N.F. Pedersen, S. Sakai, and A. Davidson, *Proc. Appl. Sup. Conf., Baltimore* (1986)
(2.21) S. Pagano, *Nonlinear Dynamics in Long Josephson Junction*, PhD thesis, The Technical University of Denmark, The Danish Center for Applied Mathematics and Mechanics (1987)
(2.22) A. Davidson, N.F. Pedersen, and S. Pagano, *Appl. Phys. Lett.***48 (19)**, 1306 (1986)
(2.23) M. Cirillo, R.D. Parmentier, and B. Savo, *Physica 3D* **18**, 565 (1981)
(2.24) N.J. Zabusky, and M.D. Kruskal, *Phys. Rev. Lett.* **15**, 240 (1965)
(2.25) I.O. Kulik, *Sov. Phys. JETP* **24**, 1307 (1967)
(2.26) A. Laub, T. Doderer, S.G. Lachenmann, R.P. Huebener, and V.A. Oboznov, *Phys. Rev. Lett.* **75 (7)**, 1372 (1995)
(2.27) D.W. McLaughlin, and A.C. Scott; *Phys. Rev.* **A 18**, 1652 (1978)
(2.28) D.W. McLaughlin, and A.C. Scott; *Appl. Phys. Lett.* **30**, 545 (1977)
(2.29) G. Costabile, R.D. Parmentier, B. Savo, D.W. McLaughlin, and A.C. Scott; *Appl. Phys. Lett.* **32**, 587 (1978)
(2.30) K. Takana; *Solid State Commun.* **29**, 443 (1979)
(2.31) I.O. Kulik; *JETP Lett.* **2**, 84 (1965)
(2.32) T.A. Fulton, and R.C. Dynes; *Solid State Commun.* **12**, 277 (1973)
(2.33) B. Dueholm, E. Joergensen, O.A. Levring, J. Mygind, N.F. Pedersen, and M.R. Samuelsen; *Physica B* **108**, 1303 (1981)
(2.34) K. Yoshida, in *SQUID85, H. D. Hahlbohm, H. Lübbig, eds., Walter de Gruyter, Berlin*, 471 (1985)
(2.35) N.F. Pedersen, *Advances in Superconductivity,* Plenum Press, New York (1982)
(2.36) O.H. Olsen, N.F. Pedersen, M.R. Samuelsen, H. Svensmark, and D. Welner; *Phys. Rev. B* **33**, 186 (1986)
(2.37) P.S. Lohmdahl, O.H. Soerensen, and P.L. Christiansen; *Phys Rev. B* **25**, 5737 (1982)
(2.38) R. Monaco, and A.V. Ustinov, *J. Appl. Phys.* **79**, 327 (1996)
(2.39) B. Dueholm, O.A. Levring, J. Mygind, N.F. Pedersen, O.H. Soerensen, and M. Cirillo; *Phys. Rev. Lett.* **46**, 1299 (1981)
(2.40) R.D. Parmentier, in: *The New Superconducting Electronics,* H. Weinstock, R.W. Ralston, eds. (Kluwer, Dordrecht, 1993), p. 221
(2.41) M.D. Fiske, *Rev. Mod. Phys.* **36**, 221 (1964)
(2.42) S. Pace, and U. Gambardella, *J. Low Temp. Phys* .**62**, 197 (1986)

(2.43) M. Cirillo, U. Gambardella, and S. Pace, *Phys. Scripta* **38**, 600 (1988)
(2.44) A.V. Ustinov, H. Kohlstedt, and P. Henne, *Phys. Rev. Lett.* **77**, 3617 (1996)
(2.45) (see 1.15-1.17) ; T. Nagatsuma, K. Enpuku, K. Yoshida, and F. Irie, *J. Appl. Phys* **63**, 1130 (1988)
(2.46) V.P. Koshelets, A.V. Shchukin, S.V. Shitov and L.V. Filippenko, *IEEE Trans. Appl: Supercond.* **3**, 2524 (1993)
(2.47) Y.M. Zhang, D. Winkler, and T. Claeson, *Appl. Phys. Lett* **62**, 3195 (1993)
(2.48) V.V. Schmidt, The Physics of superconductors, P. Müller, A.V. Ustinov (Eds.), *Springer, Berlin* (1997)
(2.49) N. Thyssen, *Diplomarbeit RWTH Aachen, ISI-Forschungszentrum Jülich*, (1995)
(2.50) N. Thyssen, A.V. Ustinov, H. Kohlstedt, S. Pagano, J.G. Caputo, and N. Flytzanis, *IEEE Trans. Appl. Supercond.* **5** , 2965 (1995)
(2.51) N. Grønbech-Jensen, P. S. Lomdahl, and M. R. Samuelsen, *Phys. Lett. A* **154**, 14 (1991)
(2.52) N. Martucciello, and R. Monaco, *Phys.Rev. B* **53**, 3471 (1996)
(2.53) A.V. Ustinov, B.A. Malomed, and N. Thyssen, *Phys. Lett. A* **233**, 239 (1997)
(2.54) N. Grønbech-Jensen, P.S. Lomdahl, and M.R. Samuelsen, *Phys. Rev. B* **43**, 12799 (1991)
(2.55) W.C. Stewart, *Appl. Phys. Lett.* **12**, 277 (1968)
(2.56) A.V. Ustinov, and N. Thyssen, *J. Low Temp. Phys.* **106 (3/4)**, 147 (1997)
(2.57) A.V. Ustinov, B.A. Malomed, and N. Thyssen, *Physics Letters A* **233**, 239 (1997)
(2.58) A. Davidson, B. Dueholm, B. Kryger, and N.F. Pedersen, *Phys.Rev. Lett.* ***55***, 2059 (1985)
(2.59) G.S. Mkrtchyan, and V.V. Schmidt, *Solid St. Commun.* **30**, 791 (1979)
(2.60) A.V. Ustinov, *Pisńa Zh. Eksp. Teor. Fiz* . **63**, 178 (1996)
(2.61) N. Martucciello, J. Mygind, V.P. Koshelets, A.V. Shchukin, L.V. Filippenko, and R. Monaco, *Phys. Rev. B* **57 (9)**, 5444 (1998)
(2.62) T. Doderer, *Int. J. Mod. Phys. B* **11**, 1979 (1997)
(2.63) A.V. Ustinov, T. Doderer, R.P. Huebener, N.F. Pedersen, B. Mayer, and V.A. Oboznov, . *Phys. Rev. Lett.* **69**, 1815 (1992)
(2.64) B. Mayer, T. Doderer, R.P. Huebener, and A.V. Ustinov, *Phys. Rev. B* **44**,. 12463 (1991)
(2.65) S.G. Lachenmann, T. Doderer, R.P. Huebener, D. Quenter, J. Niemeyer, and R. Pöpel, *Phys. Rev. B* **48**, 3295 (1993)
(2.66) S.G. Lachenmann, G. Filarella, A.V. Ustinov, T. Doderer, N. Kirchmann, D. Quenter, R.P. Huebener, J. Niemeyer, and R. Pöpel, *J. Appl. Phys.* **77**, 2598 (1995)
(2.67) D. Quenter, A.V. Ustinov, S.G. Lachenmann, T. Doderer, R.P. Huebener, F. Müller, J. Niemeyer, R. Pöpel, and T. Weimann, *Phys. Rev. B* **51**, 6542 (1995)
(2.68) S. Keil, T. Doderer, I.V. Vernik, A. Laub, H. Pressler, R.P. Huebener, N. Thyssen, A.V. Ustinov, and H. Kohlstedt, *Phys. Rev. B* **54**, 14948 (1996)
(2.69) S.G. Lachenmann, G. Filatrella, T. Doderer, J.C. Fernandez, and R.P. Huebener, *Phys. Rev. B* **48**, 16623 (1993)
(2.70) I.V. Vernik, S. Keil, N. Thyssen, T. Doderer, A.V. Ustinov, H. Kohlstedt, and R.P. Huebener, *J. Appl. Phys.* **81 (3)**, 1335 (1997)

---

(3.1) H. Kohlstedt, G. Hallmanns, I.P. Nevirkovets, D. Guggi, and C. Heiden; *IEEE Trans. Appl. Supercond.* **3**, 2197 (1993)

(3.2) H.A. Huggins, and M. Gurvitch; *J. Appl. Phys.* **57**, 2103 (1985)
(3.3) H. Kohlstedt, K.H. Gundlach, and A. Schneider, *IEEE Trans. on Magnetics* **27 (No.2)**, 3149 (1991)
(3.4) M. Yuda, K. Kuroda, and J. Nakano; *Jpn. J. Appl. Phys.* **26** (3), L166 (1986)
(3.5) H. Kohlstedt, F. König, P. Henne, N. Thyssen, and P. Caputo; *J. Appl. Phys.* **80** (9), 5512 (1996)
(3.6) J. Krug, and H. Spohn, in *Solids far from Equilibrium*, edited by C. Godreche (Cambridge University Press, Cambridge, 1991)
(3.7) A. Zangwill, in *Microstructural Evolution of Thin Films*, edited by H.A. Aterwater, and C.V. Thompson (Academic , New York, 1995)
(3.8) R. Bloch, L. Brügemann, and W. Press, *J. Phys. D* **22**, 1136 (1986)
(3.9) C. Thompson, G. Palasantzas, Y.P. feng, S.K. Sinha, and J. Krim, *Phys. Rev. B.* **49**, 4902 (1994)
(3.10) V. Lacquaniti, S. Maggi, and E. Monticone, *J. Vac. Sci. Technol. B* **12**, 1734 (1994)
(3.11) K. Tsukada, J. Kawai, G. Uehara, and H. Kado, *IEEE Trans. Appl. Supercond.* **AS-3**, 2944 (1993)
(3.12) L. Nevot, and P. Croce, *Rev. Phys. Appl.* **15**, 761 (1980)
(3.13) T. Imamura, and S. Hasuo, *Appl. Phys. Lett.***58**, 645 (1991)

---

(4.1) M.B. Mineev, G.S. Mkrtchjan, and V.V. Schmidt, *J. Low Temp. Phys.* **45**, 497 (1981)
(4.2) Yu.S. Kivshar, and B.A. Malomed, *Phys. Rev B* **37**, 9325 (1988)
(4.3) N. Grønbech-Jensen, M.R. Samuelsen, P.S. Lomdahl, and J.A. Blackburn, *Phys. Rev B* **42**, 3976 (1990)
(4.4) N. Grønbech-Jensen, O.H. Olsen, and M.R. Samuelsen, *Phys. Lett. A* **179 A**, 27 (1993)

---

(5.1) A.V. Ustinov, H. Kohlstedt, *Phys. Rev. B* **54 (9)**, 6111 (1996)
(5.2) R. Kleiner, *Phys. Rev. B* **50 (10)**, 6919 (1994)
(5.3) S. Sakai, A.V. Ustinov, H. Kohlstedt, A. Petraglia, and N.F. Pedersen, *Phys. Rev. B* **50 (17)**, 12905 (1994)
(5.4) N. Grønbech-Jensen. D. Cai, and M.R. Samuelsen, *Phys. Rev. B* **48**, 16160 (1993)
(5.5) S.N. Song, P.R. Auvil, M. Ulmer, and J.B. Ketterson, *Phys. Rev. B* **52**, R6018 (1996)
(5.6) A. Petraglia, A.V. Ustinov, N.F. Pedersen and S. Sakai, , *J. Appl. Phys.* 77, 1171 (1995)
(5.7) A. Wallraff, E. Goldobin, and A.V. Ustinov, *J. Appl. Phys.* **80**, 6523 (1996)
(5.8) E. Goldobin, A. Wallraff, B.A. Malomed, and A.V. Ustinov, *Phys. Lett. A* **224**, 191 (1997)
(5.9) R.D. Parmentier, P. Barbara, G. Costabile, A. D'Anna, B.A. Malomed, and C. Soriano, *Phys. Rev. B* **55**, 15165 (1997)
(5.10) R. Monaco, A. Polcari, and L. Capogna, , *J. Appl. Phys* **78**, 3278 (1995)
(5.11) G. Carapella, G. Costabile, A. Petraglia, N.F. Pedersen, and J. Mygind, *Appl. Phys Lett.* **69**, 1300 (1996)
(5.12) N. Grønbech-Jensen, and M.R. Samuelsen, *Phys. Rev. Lett.* **74 (1)**, 170 (1994)
(5.13) N. Matucciello, and R. Monaco, *Phys. Rev. B* **53**, 3471 (1996)
(5.14) E. Goldobin, A.V. Ustinov, and H. Kohlstedt, *Appl. Phys. Lett.*, (1998)

(5.15) E. Goldobin, A.V. Ustinov, *submitted to Phys. Rev. B*, (1998)
(5.16) E. Goldobin, A. Wallraff, N. Thyssen, and A.V. Ustinov, *Phys. Rev. B* (1998)
(5.17) R.G. Mints, and I.B. Snapiro, *Phys. Rev. B* **52**, 9691 (1995)
(5.18) V.V. Kurin, and A.V. Yulin, *Phys. Rev. B* **55**, 11659 (1997)
(5.19) G. Hechtfischer, R. Kleiner, A.V. Ustinov, and P. Müller, *Phys. Rev. Lett.* **79**, 1365 (1997)

---

(6.1) A.V. Ustinov, H. Kohlstedt, M. Cirillo, N.F. Pedersen, G. Hallmanns, and C. Heiden, *Phys. Rev. B* **48**, 10614 (1993)
(6.2) I.P. Nevirkovitz, H. Kohlstedt, G. Hallmanns, and C. Heiden, *Supercond. Sci. Technol.* **6**, 146 (1993)
(6.3) R. Kleiner, P. Müller, H. Kohlstedt, N.F. Pedersen, and S. Sakai, *Phys. Rev. B* **50**, 3949 (1994)
(6.4) R. Kleiner, F. Steinmeyer, G. Kunkel, and P. Müller, *Phys. Rev. Lett.* **68**, 2394 (1992)
(6.5) Numerical subroutine library IMSL: Visual Numerics, Inc.
(6.6) In: *"Handbook of Mathematical Functions"*, Eds. Abramowitz ang Stegun, 884 (Dover, New York, 1997)
(6.7) S. Sakai, A.V. Ustinov, N.Thyssen, and H. Kohlstedt, *accepted for publication in Phys. Rev. B*, (May 1998)
(6.7a) A.V. Ustinov, and S. Sakai, *to appear in Appl. Phys. Lett.*, (July 27, 1998)
(6.8) E. Goldobin, and A.V. Ustinov, *to be published in Phys. Rev. B*, (1998)
(6.9) H. Kohlstedt, *private communication*
(6.10) A.V. Ustinov, *unpublished* (1998)
(6.11) A.M. Klushin, *private communication*
(6.12) L.N. Bulaevskii, J.R. Clem, and L.I. Glazman, *Phys. Rev. B* **46**, 350 (1992)
(6.13) M.V. Fistul, and G.F. Giuliani, *Physica (Amsterdam)* **230 C**, 9 (1994)
(6.14) Yu.I. Latyshev, J.E. Nevelskaya, and P. Monceau, *Phys. Rev. Lett.* 77 **(5)**, 932 (1996)
(6.15) S. Schornstein, *Diplomarbeit RWTH Aachen, ISI-Forschungszentrum Jülich*, (1996)
(6.16) P. Henne, *Diplomarbeit RWTH Aachen, ISI-Forschungszentrum Jülich*, (1995)

---

(7.1) J.G. Caputo, N. Flytzanis, and M. Devoret, *Phys. Rev. B* **50**, 6471 (1994)
(7.2) M.V. Fistul, *private communication*
(7.3) M. Cirillo et al., *Phys. Rev.B* **52**, 506 (1995)
(7.4) N. Grønbech-Jensen, *Phys. Rev. B* **47**, 5504 (1993)

# 11. Appendix

## 11.1. Measurement and preparation instruments and devices

The following facilities and devices had been used during this work:

- clean room (classification 100)
- spinner for photoresist (Convac 1001S)
- MA6 contact mask aligner (Süss)
- mask cleaning (APT915)
- hot plates (20-250°C)
- chromium-mask preparation by e-beam writer
- stepper mask writer machine in Rome (M. Cirillo)
- e-beam writer (SEM 525M)
- Z400S manual sputtering system (Leybold Heraeus)
- PLS 160 automatic sputtering systems (PST) consisting of:
  - 1 PLS 160 vacuum system (Pfeiffer)
  - 3 A300 series magnetron sputter sources with 3 inch targets (AJA)
  - 2 model 860 deposition controller (Telemark)
  - 1 model 279 crucible indexer (Telemark)
  - 1 DX 500 magnetron drive (Advanced Energy Industries, Inc)
  - 1 RFX 600 generator withATX tuner (Advanced Energy Industries, Inc)
  - 1 4 channel mass flow controler with high accuracy pressure transducer (MKS)
- Univex 300 and L540 thermal evaporation (Leybold Heraeus)
- cluster tool RIE/ECR automatic etching systems (Oxford Instruments)
- IBE (Oxford Instruments)
- microscopes (e.g. Leica Polyvar MET)
- oxidation oven (Tempress)
- 300-M oxygen-plasma etcher (Technics Plasma GmbH)
- Dektak 3030

- dc measurement place at 4.2K consisting of:
  - 100/ helium dewar (Helikit)
  - customer made current sources, preamplifiers
  - measurement sticks with three four channel contact lines
  - personal computer 4-86DX
  - measurement program: Gold Exi (by E. Goldobin)
  - Tektronik TDS 420 four channel digitizing oscilloscope
  - Tektronix 2254A 100Mhz Oscilloscope
  - 80-120GHz receiver/generator by Stanyuk (Nizhni Novgorod)

- Heliox $2^{VL}$ $He_3$ cryostat (Oxford Instruments)

### 11.2. Sample parameters and statistics

1.) window junction:
*name:* ***window x.y.z***
***x:*** *layout number*
***y:*** *number of stacked junctions*
***z:*** *preparation run*

| *name:* | *chips:* | $j_c$*(A/cm²)* | *film thickness (nm) Nb/Al-$AlO_x$/Nb or Nb-Nb...Nb (Al=5nm)* | *remark:* |
|---|---|---|---|---|
| window1.1.1 | 1-4 | 380 | 110/7/330 | chips 2+3 S.Pagano,Italy |
| window1.1.2 | 1-4 | 380 | 110/7/330 | chip 2 broken in Tübingen |
| window1.1.4 | 1,4 | 380 | 110/7/330 | chip 4 S. Pagano Italy |
| window1.1.5 | 2,4 | 380 | 110/7/330 | |
| window1.1.6 | 4 | 380 | 110/7/330 | |
| window1.1.7 | 1-4 | 380 | 110/7/330 | |
| window1.1.8 | 1-4 | 400 | 120/5/330 | |
| window1.1.9 | 1-4 | 400 | 120/5/230 | first sample on PLS 160 |
| | | | | |
| window1.2.1 | 1-4 | 350 | 210-90...390 | dummy junction ($AlO_x$) |
| window1.2.2 | 1-3 | 350 | 210-90...390 | dummy junction |
| window1.2.3 | 1-4 | 400 | 210-100...400 | dummy junction |
| window1.2.4 | 2-4 | 400 | 210-120...400 | dummy junction |
| window1.3.1 | 1-4 | 400 | 210-90...400 | dummy junction |
| window1.3.2 | 1-4 | 500 | 210-100...400 | dummy junction |
| window1.7.1 | 1-4 | 380 | 200-78...600 | dummy junction |
| window1.15.1 | 1-4 | 400 | 210-90...600 | defect |

2.) winfin junction: (manual combination of two mask sets: window and finchip2)
*name:* ***winfin y.z***
***y:*** *number of stacked junctions*
***z:*** *preparation run*

| *name:* | *chips: window-finline* | $j_c$*(A/cm²)* | *film thickness (nm) Nb/Al-$AlO_x$/Nb or Nb-Nb...Nb (Al=5nm)* | *remark:* |
|---|---|---|---|---|
| winfin1.5 | 2,4-1,3 | 300 | 110/7/330 | |
| winfin1.6 | 2,4-1,3 | 250 | 110/7/330 | |
| winfin1.7 | 2,4-1,3 | 400 | 110/7/330 | |
| winfin1.8 | 2,4-1,3 | 100 | 110/7/330 | |
| | | | | |
| winfin9.0 | 2,4-1,3 | 70 | 210-80...600 | |
| winfin9.2 | 2,4-1,3 | 50 | 210-90...600 | unstable |
| winfin9.3 | 2,4-1,3 | 50 | 210-90...600 | unstable |
| winfin10.1 | 2,4-1,3 | 400 | 150-20...220 | dummy junction |
| winfin10.2 | 2,4-1,3 | 450 | 180-20...400 | dummy Al (not oxidized) |
| winfin10.3 | 2,4-1,3 | 100 | 180-20...380 | dummy Al layer |
| winfin10.4 | 2,4-1,3 | 550 | 180-20...380 | dummy junction |

| | | | | |
|---|---|---|---|---|
| winfin10.5 | 2,4-1,3 | 600 | 180-20...530 | dummy junction |
| winfin10.6 | | | | defect |
| winfin10.7 | | | | defect |
| winfin30.1 | 2,4 | 100 | 230-20...570 | dummy junction, 28 O.K. |

3.) finchip junction:
*name:* ***finchip x.y.z***
***x:*** *layout number*
***y:*** *number of stacked junctions*
***z:*** *preparation run*

| *name:* | *chips:* | $j_c$*(A/cm²)* | *film thickness (nm) Nb/Al-AlO$_x$/Nb or Nb-Nb...Nb (Al=5nm)* | *remark:* |
|---|---|---|---|---|
| finchip3.1.2 | 1-12 | 200 | 160-20...400 | single junction on dummy |
| finchip3.10.1 | 1-12 | 150 | 180-20...620 | spread, dummy junction |
| finchip3.10.2 | 1-12 | 150 | 160-40...600 | spread, dummy junction |
| finchip3.10.3 | 1-12 | 150 | 140-20...620 | spread, dumma junction |
| finchip3.10.5 | 1-12 | 500 | 160-40...640 | spread, dummy Al layer |
| finchip3.10.7 | 1-12 | 170 | 150-30...420 | spread, dummy Al layer |

4.) annstac junction:
*name:* ***annstac x.y.z***
***x:*** *layout number*
***y:*** *number of stacked junctions*
***z:*** *preparation run*

| *name:* | *chips:* | $j_c$*(A/cm²)* | *film thickness (nm) Nb/Al-AlO$_x$/Nb or Nb-Nb...Nb (Al=5nm)* | *remark:* |
|---|---|---|---|---|
| annstac1.1.1 | 1-9 | 350 | 120/8/200 | (thesis A. Wallraff) |
| annstac1.1.7 | 1-9 | 350 | 120/10/200 | gap 2mV |
| annstac1.1.8 | 1-9 | 190 | 120/8/200 | gap 2.4mV, in Erlangen |
| annstac1.1.9 | 1-9 | 250 | 120/5/200 | large sub gap current |
| annstac1.1.12 | 1-9 | 250 | 120/7/200 | flux trapping possible |
| annstac1.1.17 | 1-9 | 300 | 120/7/200 | |
| annstac1.2.1 | 1-9 | 350 | 120-90-300 | (Goldobin and Wallraff) |
| annstac1.5.1 | 1-9 | 200 | 120-90...350 | in Erlangen |
| annstac1.5.2 | 1-9 | 150 | 120-20...400 | in Erlangen |
| annstac1.10.1 | 1-9 | 100 | 120-20...450 | Erlangen |

5.) vigoni junction:
*name:* ***vigoni x.z.a/b***
***x:*** *layout number*
***z:*** *preparation run*
***a:*** *long junction in center position, with and without break*
***b:*** *1-dim. array in center position*

| *name:* | *chips:* | $j_c$*(A/cm²)* | *film thickness (nm) Nb/Al-AlO$_x$/Nb* | *remark:* |
|---|---|---|---|---|
| vigoni1.1a | 1-9 | 350 | 120/5/230 | M. Cirillo, Rome |
| vigoni1.2b | 1-9 | 350 | 120/7/230 | working chips in Rome |
| vigoni1.3a | 1-9 | 350 | 120/7/230 | Erlangen |
| vigoni1.4b | 1-9 | 350 | 120/7/230 | shorts, defect |
| vigoni1.5a | 1-9 | 350 | 120/7/230 | M. Cirillo, Rome |
| vigoni1.6b | 1-9 | 350 | 120/7/230 | M. Cirillo, Rome |
| vigoni2.1a | 1-9 | 350 | 120/7/230 | wrong shunt resistance |

6.) yury junction:
*name:* ***yury z***
***z:*** *preparation run*

| *name:* | $j_c$*(A/cm²)* | *remark:* |
|---|---|---|
| yury 1-17 | 350 | missing documentation, samples with 0.2µm width |
| yury 20-24 | 350 | few junctions working, shorts at the junction border |
| yury 30-34 | 350 | junction width down to 1µm, cutted base electrode, ZFS |
| yury 40-44 | 350 | large sub-gap currents by contamination ($O_2$ plasma improved) |

**Small Statistics**

During this work **130 preparation runs were started.**

From the **92 completed runs** we got **85 working wafers.**

This is an useable **output of around 92%.**

In addition we made around **50 testing processes** for film and junction preparation.

Several samples that were prepared had been used in **5 different research groups** for investigations.

## 11.3. Abbreviations and notation definitions

| | |
|---|---|
| x, y, z : | spatial coordinates |
| t : | time coordinate |
| L : | length of the Josephson junction (*5-450*μm) |
| W : | width of the Josephson junction (*5-20*μm) |
| D : | annular junction diameter (*88-174*μm) |
| $b_i$ : | superconductor thickness (*20-200*nm) |
| d : | barrier thickness (*2*nm) |
| d': | magnetic thickness (≈*200*nm) |
| $\lambda_L$ : | London penetration depth (≈*100*nm for Nb) |
| $\lambda_J$ : | Josephson penetration depth (≈*20-30*μm for the presented samples) |
| $\Psi(r,t)$ | wave function |
| N(r,t) | density of Cooper pairs |
| $\varphi(r,t)$ | common phase of the Cooper pairs |
| $\phi$ | phase difference of two superconductors at a weak link |
| $I_c/j_c$ | critical current/current density of a tunnel junction |
| H/E | magnetic / electrical field |
| $R_N$ | normal resistance of a tunnel junction |
| $\Delta$ | binding energy of Cooper pairs (gap-energy) |
| $\xi$ | coherence length |
| C | capacitance |
| G | conductance |
| T | temperature |
| $\Phi_0$ | flux quantum |
| $\omega_p$ | plasma frequency |
| $\omega_c$ | characteristic frequency |
| $\bar{c}$ | Swihart velocity (several percentage of light velocity in Nb-Al junctions) |
| $\alpha,\beta$ | damping coefficients |
| u | fluxon velocity |
| S | coupling parameter (about *0.5* for intermediate Nb thickness of *90*nm) |
| $N_f$ | number of fluxons |
| *N* | number of stacked junctions |
| ZFS | Zero Field Step |
| FS | Fiske Step |
| FF | flux-flow |
| DLS | displaced linear slope |
| FFO | flux flow oscillator |
| RIE | reactive ion etching |
| IBE | ion beam etching |
| SNAP | selective niobium anodization process |

| | | |
|---|---|---|
| index: | $A_{xx}$ | second x-derivative of A |
| | $FF_i$ | flux-flow regime starting from the gap i-1 |
| | $b_i$ | thickness of the superconducting layer i |

## 11.4. Publication list:


1.) N. Thyssen, A.V. Ustinov, H. Kohlstedt, S. Pagano, J.G. Caputo, and N. Flytzanis, *IEEE Trans. Appl. Supercond.* **5** , (1995) , 2965
„Experimental Study of Fluxon Resonances in Window-Type Long Josephson Junctions"

2.) N. Thyssen, A.V. Ustinov, H. Kohlstedt, J.G. Caputo, S. Pagano, and N. Flytzanis, *Proceedings of the International Conference on Nonlinear Superconducting Devices and High-Tc Materials* , (1994) , 107
„Fluxon Resonances in Window-Type Long Josephson Junctions: Experiment and Numerical Simulations"

3.) N Thyssen und A.V. Ustinov, *Jahresbericht 1994, Institut für Schicht und Ionentechnik, Forschungszentrum Jülich GmbH*, (1994)
„Experimentelle Untersuchung der Josephson-Flußquantendynamik in langen Josephson Tunnelkontakten mit elektromagnetischem Fenster"

4.) N. Thyssen, A.V. Ustinov, and H. Kohlstedt, *J. Low Temp. Phys.* **106** , (1997) , 201
„Flux Flow and Resonant Modes in Multi-Junction Josephson Stacks"

5.) N. Thyssen, H. Kohlstedt, and A.V. Ustinov, *IEEE Trans. Appl. Supercond.* **7** , (1997) , 2901
„Experimental Study of Flux Flow and Resonant Modes in Multi-Junction Josephson Stacks"

6.) N. Thyssen, H. Kohlstedt, S. Sakai, and A.V. Ustinov, *Applied Superconductivity 1997*, 158, Vol.1, (1997), 499
„Josephson Flux Flow in Multi Junction Stacks: Experiment and Simulation"

7.) N. Thyssen, H. Kohlstedt, A.V. Ustinov, *Physica C* 293, (1997) , 264
„Low-$T_c$ tunnel junction stacks as models for intrinsic Josephson effect in high-$T_c$ materials"

8.) N. Thyssen, R. Monaco, A. Pedraglia, G. Costabile, H. Kohlstedt, and A.V. Ustinov, *submitted to Phys. Rev. B.*, May (1998)
„Magnetic Field Distribution in Single and Two-fold Stacks of Long Josephson Junctions"

9.) I.V. Vernik, S. Keil, A.V. Ustinov, N. Thyssen, T. Doderer, H. Kohlstedt, and R.P. Huebener, *Czechoslovak Journal of Physics.* **46**, (1996) , 649
„Trapped fluxons in annular Josephson junctions in the external magnetic field"

10.) H. Kohlstedt, F. Koenig, P. Henne, N. Thyssen, and P. Caputo, *J. Appl. Phys.* **80**, No. 9 (1996), 5512
„The role of surface roughness in the fabrication of stacked Nb/Al-$AlO_x$/Nb tunnel junctions"

11.) S. Keil, T. Doderer, I.V. Vernik, A. Laub, H. Preßler, R.P. Huebener, N. Thyssen, A.V. Ustinov, and H. Kohlstedt, *Phys. Rev. B* **54**, (1996) , 14948
„Magnetic flux quanta in annular Josephson junctions in a barrier-parallel dc magnetic field"

12.) A.V. Ustinov, and N. Thyssen, *J. Low Temp. Phys.* **106**, (1997) , 193
„Experimental Study of Fluxon Dynamics in a Potential Well"

13.) I.V. Vernik, S. Keil, N. Thyssen, T. Doderer, A.V. Ustinov, H. Kohlstedt, and R.P. Huebener, *J. Appl. Phys.* **81**, (1997), 1335
„Fluxon Pinning in annular Josephson junctions by an external magnetic field"

14.) A.V. Ustinov, B.A. Malomed, and N. Thyssen, *Phys. Lett. A* **233**, (1997), 239
„Soliton trapping in a periodic potential: experiment"

15.) E. Goldobin, A. Wallraff, N. Thyssen, and A.V. Ustinov, *Phys. Rev. B* **57**, (1998), 130
„Cherenkov radiation in coupled long Josephson junctions"

16.) A.V. Ustinov, S. Shitov, N. Iosad, E. Goldobin, N. Thyssen, and H. Kohlstedt, *Proc. of the IV Terahertz Electronics Workshop*, Erlangen (1996)
„Stacked Josephson Junction Oscillators"

17.) A. Wallraff, V.V. Kurin, D. Bolkhovsky, N. Thyssen, A.V. Ustinov, *Applied Superconductivity 1997* **158**, Vol.1, (1997), 531
„Effective length of annular long Josephson junctions with finite width: theory and experiment"

18.) S. Sakai, A.V. Ustinov, N. Thyssen, and H. Kohlstedt, *Journal of Applied Physics*, (1998)
„Dynamics of Multi-Junction Stacked Flux-Flow Oscillators: Comparison between Theory and Experiment"

19.) M. Cirillo, V. Merlo, D. Winkler, and N. Thyssen, *to appear in IEEE Trans. Appl. Supercond.*, (1999)
„Subharmonic Locking in Josephson Junctions"

## 11.5. Acknowledgments

I would like to express my deep gratitude to my supervisors Prof. Dr. Alexey V. Ustinov and Dr. Hermann Kohlstedt for sharing their vast knowledge with me and their invaluable steady support and critical contribution throughout this work.
I am thankful to the director of the Institute for Thin Film and Ion Technology (ISI), Prof. A.I. Braginski, for the opportunity to conduct this work in his institute, for his critical interest and the acceptance to act as second referee. Thanks also to Prof. H. Lüth for his temporary readiness to take over the position as first referee in the beginning of this work and to Dr. S. Sakai for several discussions and strong collaboration during the theoretical analysis.
My permanence at the University of Salerno for two month has been made possible by the cooperation and precious assistance of Prof. G. Costabile, Dr. R. Monaco and Dr. A. Petraglia. I wish to thank also Prof. M. Cirillo for the concerted time in Rome during the Vigoni project.
I thank Dr. G. Hechtfischer and Dr. R. Kleiner for discussions and for providing us with their original graphics program code for animated presentation of the phase dynamics, and Prof. P. Müller and colleagues for hospitality during my stay in Erlangen.
I acknowledge the discussions and collaboration with the ISI group members, Dr. Cornelia Horstmann, Dr. Stephan Beuven, Dr. Marian Darula, Dr. Alexander Klushin, Dipl. Phys. Maxim Levitchev, Dipl. Phys. Rolf Schmitz, Dr. Boris Chesca and Dr. Edward Goldobin. Thanks to Dr. Yury Koval for the introduction in e-beam lithography and to Dr. S. Shitov and Prof. V. Koshelets for the opportunity to participate in the integrated receiver project.
For the steady technical support I am thankful to Bernd Hermanns, F. Schroeteler, A. Steffen and F. Ringelmann. Mona Nonn is acknowledged for the excellent preparation of all photo masks. Vicarious for their teams I thank Mr. Schwan of the mechanical workshop, Mr. Otto and Mr. Schmidt of the electronic workshop.
In organisatoric and administrative questions the help from Irene Schumacher, Nicole Fuchs, P.-H. Müller and B. Neuhof is acknowledged. Thanks to Frau Barthels for the preparation of all photos.
Finally I would like to express my deep gratitude to my parents, for the assistance during all the time of my studies. I thank my wife for inexhaustible patience, the steady support and motivation and help in correcting this manuscript.

This work was partly supported by the BMBF contract number 13N6945/3. My time in Rome was financially supported by the Vigoni-DAAD project 314-vigoni dr. Two occasional research contracts with INFM (Istituto Nazionale per la Fisica della Materia) are gratefully acknowledged in connection with my stays in Salerno and Rome, too.
The collaboration with S. Sakai was partly supported financially by the Science and Technology Agency (Japan). During a visits from A.V. Ustinov in Japan we acknowledge the financial support from AIST. Connected to the collaboration with B.A. Malomed we have to thank a partly support by the German-Israeli Foundation (G.I.F.) by the research grant G-0464-247.07/95

# Flux Flow and Resonant Modes in Multi-Junction Josephson Stacks

**N. Thyssen, A. V. Ustinov, and H. Kohlstedt**

*Institute of Thin Film and Ion Technology, Research Center (KFA)*
*D-52425 Jülich, Germany*

*Magnetic field dependent current-voltage characteristics of stacked $Nb/(Al\text{-}AlO_x/Nb)_n$ long Josephson junctions are investigated experimentally. The thickness of their common superconducting electrodes provides the magnetic coupling between the junctions. For stacks of $n = 7$ Josephson junctions the current-voltage characteristics display collective flux-flow behaviour of Josephson vortices. In the interior layers Josephson vortices move simultaneously under the influence of the bias current. The flux-flow behaviour is modulated by a complicated structure of cavity-like resonances which show broad range of characteristic frequencies. The measurements can be qualitatively explained by the Kleiner model for the resonances in stacks. Mutual locking of junctions in the stack is indicated by pronounced cavity resonances with large voltage spacing.*

*PACS numbers: 74.50.+r, 85.25.Cp, 74.80.Dm, 85.40.Hp*

## 1. INTRODUCTION

Stacked Josephson tunnel junctions are interesting from various aspects. After the first observation of the intrinsic Josephson effect in layered high-$T_c$ superconductors in $Bi_2Sr_2CaCu_2O_8$,[1] stacks made using low-$T_c$ technology served to model the high-$T_c$ properties.[2] Besides that, long Josephson junctions operated in the flux-flow mode have already been successfully used as local oscillators in integrated submillimeter-wave receivers.[3] Mutually phase-locked oscillators can be used in order to increase the output power and to decrease the linewidth. Vertical stacking of Josephson junctions appears as one possible novel realization of such elements. In comparison with planar

oscillator arrays, the mutual inductive coupling in stacks can be by several orders of magnitude stronger and can be controlled by the thickness of the intermediate superconducting layers. Previous studies of two fold stacks[4] have already shown promising phase locking behaviour. For coherent functioning of such a multi-layer device a spread in critical current densities $j_c$ between the junctions of less than 5% is mostly required. So far this demand was considered as the main preparation problem of stacked arrays. Even in the case of well-reproducible and reliable single-barrier Nb/Al-$AlO_x$/Nb technology results typically show a larger spread in junction parameters.

We report on the experimental study of the flux-flow dynamics of 7−fold stacked junctions. Due to a modification of the preparation procedure, we are now able to produce Josephson junction stacks with a difference in critical currents of less than 4 %.[5] We observe high-voltage resonances that give a clear indication for the theoretically predicted Kleiner modes.[6]

## 2. SAMPLE PREPARATION

We used Nb/Al-$AlO_x$/Nb Josephson junctions of overlap geometry prepared using the modified SNAP technology.[7] In Fig. 1(a), as an example, we show a current-voltage $I - V$ characteristic of a conventionally made Nb/(Al-$AlO_x$/Nb)$_3$ three fold stack.[8] Here the same oxidation parameters were used for all tunnel barriers. Two junctions of the stack show the critical current spread of less than 2 %, whereas the third one has the critical current by about 40 % higher. While all intermediate Nb layers had a thickness of 30nm, the base Nb electrode in this sample was 110nm, as shown in the inset on Fig. 1(a). All other conventionally fabricated samples with various number of layers have shown one junction with significantly higher critical current than the others. In this conventional process the oxidation parameters for all junctions are equal and all Al layers have the thickness of 5 nm.

We found that the thickness of underlying Nb plays an important role for the formation of the barrier and is responsible for the higher critical current for the thicker Nb layer. By theory of kinetic roughning it is known, that the surface roughness increases with film thickness.[9,10] Measurements of x-ray specular reflectivity were used to determine the Nb surface roughness. By now this technique is well established and permits to measure surface roughness with a resolution of about 0.1 nm.[11,12] We found the roughness of the $SiO_2$ wafer surface to be less than 0.3nm. Niobium films 70nm and 210nm layer thick had the roughness of 0.9nm and 1.8nm, respectively. For a tunnel junction with a 210 nm base electrode, an Al-$AlO_x$ tunnel barrier of 5 nm, and a 70 nm thick Nb top electrode we found a surface roughness of 0.9nm.

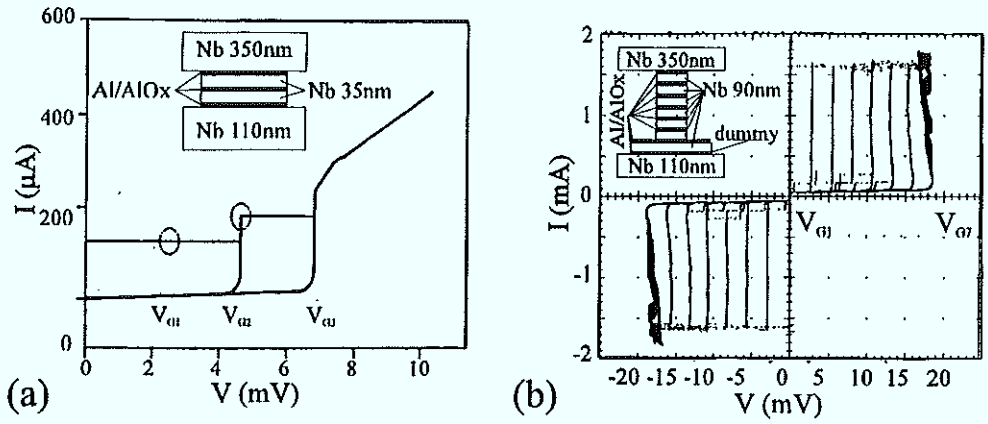


Fig. 1. (a) $I-V$ characteristic and schematic cross-sectional view of a three fold stack without underlayers. (b) $I-V$ characteristic and the cross-section of a seven-fold stack with additional dummy underlayers.

This suggests that the 70 nm thick top Nb film is grown on a well-planarized surface. Therefore, the roughness of the top Nb film is independent of Nb underlayers if there is an Al-$AlO_x$ barrier placed in between. These results clearly confirm the planarization effect of Al-$AlO_x$ on Nb studied earlier by HRTEM.[13] Thus, in order to obtain minimum spread in parameters, the thermal oxidation for each tunnel barrier has to be adjusted to the thickness of the last Nb layer.

Another solution which allows to obtain small parameter spread in stacked Nb/$AlO_x$ junctions is the use of an Al or Al-$AlO_x$ dummy layer in the base electrode.[5] This dummy junction serves to compensate the roughness of the base Nb layer. The area of this dummy junction has to be much larger than the work junction area. This can be achieved by stopping the dry etching process before the dummy layer is reached. The critical current of the dummy layer is much larger than that of the other tunnel barriers and it does not influence the measurements. As shown in Fig. 1(b), using this process the difference in critical currents is reduced to less than 4 %. We used the base Nb electrode of 110 nm, a dummy junction was formed by thermal oxidation of a 5 nm thick Al film and all following seven junctions consised of 90 nm intermediate Nb layers with barriers similar to the dummy junction. A typical value of $j_c$ was about 360 A/cm$^2$, which corresponds to the single-layer Josephson penetration depth $\lambda_J \approx 20\mu$m. Six different junction sizes were produced on the same wafer. Long Josephson junctions had the dimensions of 200 × 20, 350 × 20, 200 × 10 and 450 × 10 $\mu$m$^2$. In addition, small junctions of 10 × 10 and 20 × 20 $\mu$m$^2$ were produced. Here we report data for $n = 7$ stacked junctions. Measurements were performed at 4.2 K. $I-V$ curves were collected using a digital storage oscilloscope.

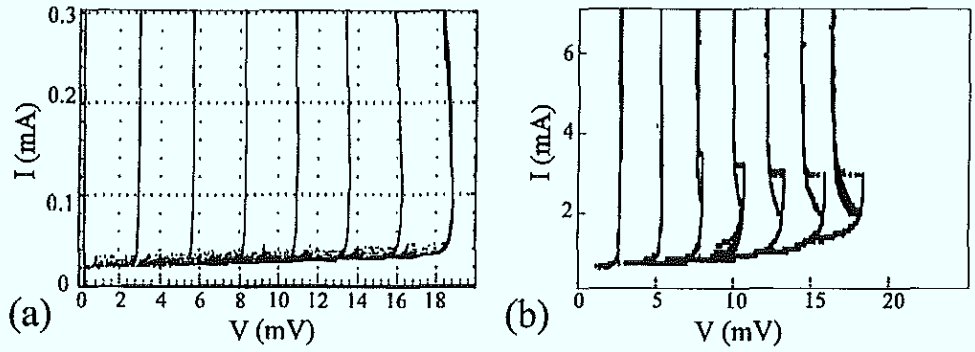


Fig. 2. I-V characteristics of (a)10 × 10 $\mu m^2$, and (b) 200 × 10 $\mu m^2$.

## 3. GAP STRUCTURE

Measurements of the $I - V$ curves clearly indicate a significant change in the individual junction gap structure as compared with the single-barrier junctions. Fig. 2 shows the data for two junctions of different size made on one wafer. The tendency of the gap supression with increasing current becomes more clear for larger junction areas. We believe that this is due to the thermal decoupling of the middle Nb layers from the surrounding. A high rate of the quasiparticle injection produce a heating effect in the superconducting layers. This effect can not be easily avoided due to the low thermal conductivity of the insulating surrounding of the stack.

## 4. COLLECTIVE FLUX FLOW

Measurements of $I - V$ curves were made at the range of external magnetic field $H$ from 0 to 40 Oe. With increasing H, flux flow branches appear starting from $V = 0$ and from various gap voltage branches. An example of $I - V$ curves stored during continuous $H-$sweep is shown in Fig. 3. By measuring the rate of the flux-flow voltage $V_{ff}$ dependence on $H$ we were able to determine the number of junctions participating in the flux-flow state. The number of participating junctions was different for the flux-flow modes in voltage regions between the different gap voltages $V_m = mV_g$ and $V_{m+1} = (m + 1)V_g$, where $V_g \approx 2.5$mV and $m = 0, 1, ..., 6$. The flux-flow mode observed between $V_m$ and $V_{m+1}$ may account for maximum $(n - m)$ junctions participating in the flux-flow state, since $m$ junctions there are already switched to the gap voltage $V_g$. The dependence of $V_{ff}$ on $H$ for different $m$ was measured. Comparing $dV_{ff}/dH$ for different $m$ we found at maximum 5 junctions operating in the flux-flow state. This number is smaller than the number of stacked junctions $n = 7$, and we argue that it is due to the screening effect of current leads . The lowest and the highest junc-

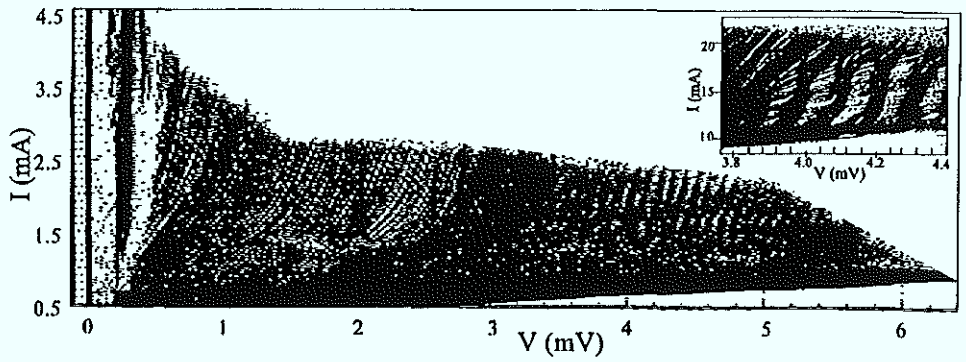


Fig. 3. Flux flow behaviour measured with continuous sweep of magnetic field $H$.

tion each have one thick superconducting electrode. These bulk electrodes significantly influence the flux penetration in this system. We suppose that the top and bottom junctions do not participate in the flux-flow behavior.

The flux-flow state of five junctions is shown in Fig. 3. The stored $I-V$ curves can be divided in three areas of different behavior. From 0 to 0.4 mV resonances appear. The characteristic voltage spacing of these resonances is comparable with that of Fiske steps for same area single Josephson junction $\Delta V_{Fs} = 43\ \mu V$.[14] However, the measured resonances show a very complicated structure that can be explained by the interference of different resonant modes. From 0.4 mV to 3.5 mV we observe a very smooth flux-flow step that is continuously tunable by $H$ and does not show any resonances. For voltages above 3.5 mV clear resonant steps appear with voltage spacing of about 110 $\mu$V. These resonances have too large voltage spacing to be explained by the Fiske resonances of individual junctions. We compared their voltages with the theoretical model by Kleiner.[6] According to the Kleiner's model, stacked junctions form a two-dimensional resonator in the cross-sectional plane perpendicular to the tunnel barriers. Resonant voltage steps are classified by the resonance number $n_x$ in layer plane and the vertical resonance number $n_z$. The corresponding mode velocities are given by the following formula:[6,15]

$$V_{n_x,n_z} = \Phi_0 \frac{n_x}{2L} \frac{1}{\sqrt{\varepsilon\mu_0}} \sqrt{\frac{d}{d_1 + 2cos\frac{n_z\pi}{n+1}}}, \qquad (1)$$

where $L$ is the length of the junction in the direction perpendicular to magnetic field, $d$ is the tunnel barrier thickness, $\epsilon$ is its dielectric constant, $d_1$ is the magnetic thickness of the intermediate Nb layer, $s = \lambda_L/\sinh(t/\lambda_L)$ with $t$ being the thickness of the intermediate Nb layer. Taking into account that there are five active junctions in our stack, the measured voltage spacing of 110 $\mu$V fits reasonably well to the resonance $n_z = 2$ ($\approx$ 130 $\mu$V) or $n_z = 3$

($\approx$ 90 $\mu$V) in $z$-direction and with $n_x$ lying approximately between 35 and 45. Thus, the reported dc measurements are consistent with the Kleiner model of the stacked junction system.

## 5. CONCLUSION

We have shown a possibility to produce vertically stacked Josephson junctions with a minimized spread in critical currents. This effort allowed us to investigate seven-fold stacks with nearly equal junctions. Flux flow measurements have shown the coherent operation of five junctions. New resonant modes characterised by large voltage spacing are observed and attributed to the Kleiner modes. Radiation measurements from such multilayer stacks are being prepared.

## REFERENCES


1. R. Kleiner, F. Steinmeyer, G. Kunkel, and P. Müller, *Phys. Rev. Lett.*, **68**, 2394 (1992)
2. R. Kleiner, P. Müller, H. Kohlstedt, N. F. Pedersen, and S. Sakai, *Phys. Rev. B*, **50**, 3942 (1994)
3. V. P. Koshelets, A. V. Shuchukin, S. V. Shitov, and L. V. Filippenko, *IEEE Trans. Appl. Supercond.*, **3**, 2524 (1993)
4. A. V. Ustinov, H. Kohlstedt, and C. Heiden, *IEEE Trans. Appl. Supercond.*, **5**, 2743 (1995)
5. H. Kohlstedt, F. König, P. Henne, N. Thyssen, and P. Caputo (to be published)
6. R. Kleiner, *Phys. Rev. B*, **50**, 6919 (1994)
7. H. A. Huggins and M. Gurvitch, *J. Appl. Phys.*, **57**, 2103 (1985), and refs. therein
8. H. Kohlstedt, G. Hallmanns, I. P. Nevirkovets, D. Guggi, and C. Heiden, *IEEE Trans. Appl. Supercond.*, **3**, 2197 (1993)
9. J. Krug, and H. Spohn, "Kinetic Roughening of Growing Surfaces" in "Solids far from Equilibrium", Ed. C. Godreche, Cambridge University Press (1991)
10. A. Zangwill: "Theory of Growth-Induced Surface Roughness" in "Microstructural Evolution of Thin Films", Ed. H. A. Atwater and C. V. Thompson, Academic Press, New York (1995)
11. R. Bloch, L. Brügemann, and W. Press, *J. Phys. D*, **22**, 1136 (1989)
12. C. Thompson, G. Palasantzas, Y. P. Feng, S. K. Sinha, and J. Krim, *Phys. Rev. B*, **49**, 4902 (1994)
13. T. Imamura, and S. Hasuo, *Appl. Phys. Lett.*, **58**, 645 (1991)
14. N. Thyssen, A. V. Ustinov, H. Kohlstedt, S. Pagano, J. G. Caputo, and N. Flytzanis,*IEEE Trans. Appl. Supercond.*, **5**, 2965 (1995)
15. S. Sakai, A. V. Ustinov, H. Kohlstedt, A. Petraglia, and N. F. Pedersen, *Phys. Rev. B*, **50**, 12905 (1994)

# Experimental Study of Flux Flow and Resonant Modes in Multi-Junction Josephson Stacks

N. Thyssen, H. Kohlstedt, and A. V. Ustinov
Institute of Thin Film and Ion Technology, Research Center (KFA), D-52425 Jülich, Germany

*Abstract* — **Magnetic field dependence of current-voltage characteristics of 7-layer stacked Nb/Al-$AlO_x$/Nb long Josephson junctions are investigated experimentally. The magnetic coupling between the junctions is provided by their common superconducting electrodes of the thickness smaller than the London penetration depth. The current-voltage characteristics clearly display collective flux-flow behavior of Josephson vortices (fluxons) which simultaneously move in up to 5 layers of the stack under the influence of the bias current. The flux-flow behavior is modulated by a complicated structure of cavity-like resonances which show a broad range of characteristic frequencies. Our observations can be qualitatively explained as the interplay between the Fiske modes and the two-dimensional resonances in these stacks. For the intermediate magnetic field range, we find pronounced resonant modes with large voltage spacing which indicates mutually coherent operating junctions.**

## I. Introduction

Stacked Josephson tunnel junctions are interesting from various aspects. Long Josephson junctions operated in the flux-flow mode have already been successfully used as local oscillators in integrated submillimeter-wave receivers [1]. Mutually phase-locked oscillators increase the output power and decrease the linewidth. Vertical stacking of Josephson junctions appears as one possible novel realization of such elements. In comparison with planar oscillator arrays, the mutual inductive coupling in stacks can be by several orders of magnitude stronger and can be controlled by the thickness of the intermediate superconducting layers. Previous studies of two fold stacks [2] have already shown promising phase locking behaviour. In addition, stacks made with low-$T_c$ technology serve to model the properties in layered high-$T_c$ superconductors [3], and in particular to understand the intrinsic Josephson effect [4].

For coherent functioning of a multi-layer Josephson device a spread in critical current densities $j_c$ between the junctions of less than 5 % is usually required. So far this demand was considered to be the main preparation problem of stacked arrays. Even in the case of well-reproducible and reliable single-barrier Nb/Al-$AlO_x$/Nb technology results typically show a larger spread in junction parameters. Due to a modification of the preparation procedure, we are able to produce Josephson junction stacks with a difference in critical currents of less than 4 % [5]. We report on the experimental study of the flux-flow dynamics of 7−fold stacked junctions with up to five coupled working junctions. High-voltage steps are observed on the current-voltage characteristics ($I-V$ curves). These steps give a clear indication for two-dimensional resonances, theoretically predicted by Kleiner [6], which we call in the following the Kleiner modes.

Manuscript received August 25, 1996.

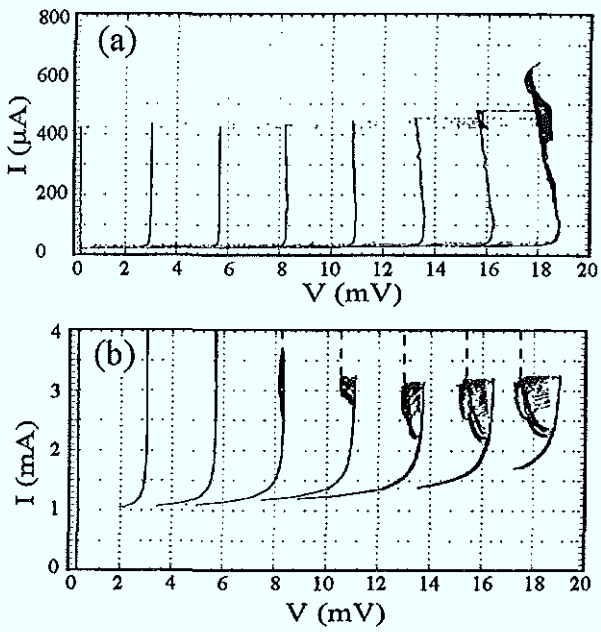


Fig. 1. I-V characteristics of 7-fold stacks: (a)10 × 10 $\mu m^2$, (b) 200 × 10 $\mu m^2$.

## II. Sample fabrication

Using the modified SNAP technology [7] we prepared Nb/Al-$AlO_x$/Nb Josephson junctions of overlap geometry. Usually fabricated samples with various numbers of layers show one junction with significantly higher critical current than the others. In the conventional process the oxidation parameters for all junctions are equal and all Al

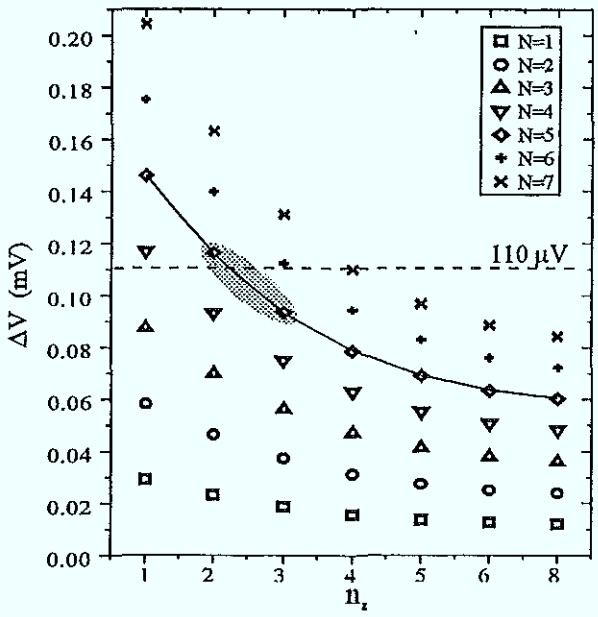


Fig. 4. Voltage spacing between the Kleiner modes according to Eq.(2). Various points correspond to different number $N$ of junctions operating coherently. $N$ values are shown on the plot.

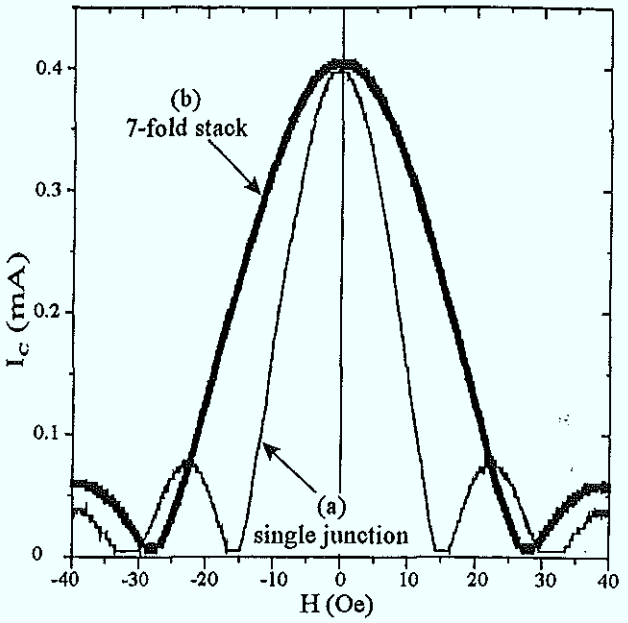


Fig. 5. $I_c(H)$ measurements: (a)$10 \times 10\ \mu m^2$ single junction, (b) $10 \times 10\ \mu m^2$ 7-fold stack.

flow behaviour: the flux-flow voltage increases with increasing $H$. By measuring the flux-flow voltage $V_{ff}$ dependence on $H$ we were able to determine the number of junctions participating in the flux-flow state. The number of participating junctions $N$ was different for the flux-flow modes in voltage regions between the various gap voltages, $V_m = mV_g$ and $V_{m+1} = (m+1)V_g$, where $V_g \approx 2.75$mV and $m = 0, 1, ..., 6$. The flux-flow mode observed between $V_m$ and $V_{m+1}$ may account for maximum $(n-m)$ junctions participating in the flux-flow state, since $m$ junctions are already switched to the gap voltage $V_g$. Here $n$ is the number of stacked junctions. The dependence of $V_{ff}(H)$ for different $m$ was measured. Comparing $dV_{ff}/dH$ for different $m$ we found at maximum 5 junctions operating in the flux-flow state. This number is smaller than the number of stacked junctions $n = 7$, and we argue that it is due to the screening effect of current leads. The lowest and the highest junction each have one thick superconducting electrode. These bulk electrodes should significantly influence the magnetic field penetration in the stack. We suppose that the top and bottom junctions do not participate in the flux-flow behavior.

The flux-flow state of five junctions is shown in Fig. 3. The stored $I - V$ curves can be divided in three areas of different behavior. From 0 to 0.4 mV resonances appear. The characteristic voltage spacing of these resonances is comparable with that of Fiske steps for single Josephson junction $\Delta V_{Fs} = 43\ \mu$V of the same area [13]. However, the measured resonances show a very complicated structure that can be explained by the interference of different resonant modes. From 0.4 mV to 1.6 mV we observe a very smooth flux-flow step that is continuously tunable by $H$ and does not show any resonances. We note that in this range the $I - V$ curve looks similar to the so-called displaced linear branch (DLS) of a single-barrier long Josephson junction. It has been demonstrated recently [14] that DLS is a signature of very complicated and even chaotic fluxon dynamics in the junction. For voltages above 1.6 mV clear resonant steps appear with voltage spacing of about 110 $\mu$V. These resonances have too large voltage spacing to be explained by the Fiske resonances of individual junctions. We compared their voltages with the theoretical model by Kleiner [6]. According to the Kleiner's model, stacked junctions form a two-dimensional resonator in the cross-sectional plane perpendicular to the tunnel barriers. Resonant voltage steps are classified by the resonance number $n_x$ in layer plane and the vertical resonance number $n_z$. The corresponding voltages in the coherent flux-flow state of $N$ junctions are given by the following formula: [6],[15]

$$V_{n_x,n_z} = \Phi_0 \frac{n_x}{2L} \frac{N}{\sqrt{\varepsilon\mu_0}} \sqrt{\frac{d}{d_1 + 2s\cos\frac{n_z\pi}{n+1}}}, \qquad (1)$$

where $L$ is the length of the junction in the direction perpendicular to magnetic field, $d$ is the tunnel barrier thickness, $\varepsilon$ is its dielectric constant, $d_1$ is the magnetic thickness of the intermediate Nb layer, $s = -\lambda_L/\sinh(t/\lambda_L)$ with $t$ being the thickness of the intermediate Nb layer. Here we assume that the number of junctions participating in the flux-flow state is $N \leq n$.

Fig. 4 shows the voltage spacings between the expected Kleiner resonances:

$$\Delta V = V_{n_x,n_z} - V_{n_x-1,n_z}. \qquad (2)$$

The dashed line shows the voltage spacing between the experimentaly found cavity-like modes of Fig. 3. One can

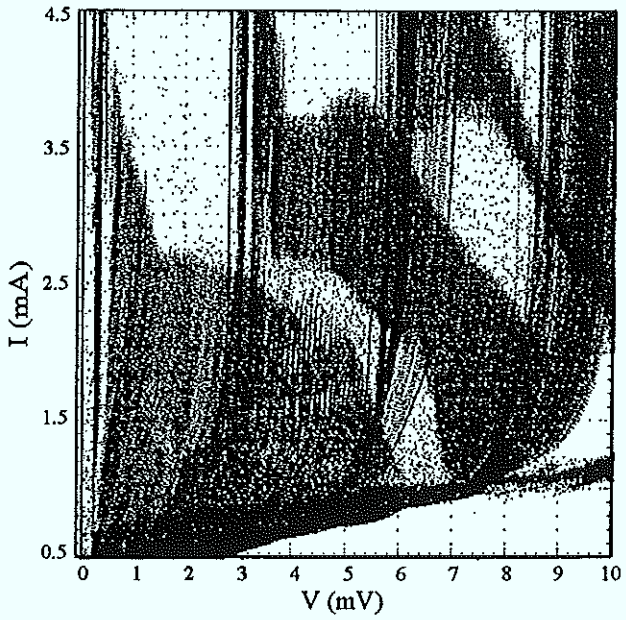


Fig. 2. Flux-flow behaviour measured at continuous sweep of magnetic field $H$ for $450 \times 10\,\mu m^2$ stack.

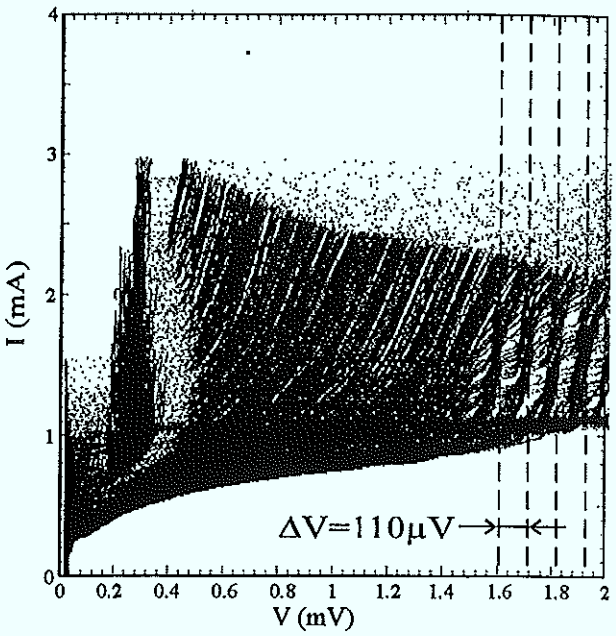


Fig. 3. Coherent resonances of five coupled junctions for $350 \times 20 \mu m^2$ stack.

layers have a thickness of 5 nm. Nb layers are nevertheless different because the ground Nb electrode is typically much thicker than the intermediate Nb layers.

The thickness of underlying Nb plays an important role for the formation of the barrier and is responsible for the higher critical current for the thicker Nb layer. By the theory of kinetic roughning, it is known that the surface roughness increases with film thickness [8],[9]. Measurements of x-ray specular reflectivity were used to determine the Nb surface roughness [10],[11]. We found the roughness of the top Nb film to be independent of Nb underlayers if there is an Al-$AlO_x$ barrier placed in between. These results clearly confirm the planarization effect of Al-$AlO_x$ on Nb studied earlier by HRTEM [12]. Thus, in order to obtain minimum spread in parameters, the thermal oxidation for each tunnel barrier has to be adjusted to the thickness of the last Nb layer.

Another solution which makes it possible to obtain small parameter spread in stacked Nb/$AlO_x$ junctions is the use of an Al or Al-$AlO_x$ dummy layer in the base electrode [5]. This dummy junction serves to compensate the roughness of the thicker base Nb layer. The critical current of the dummy layer is much larger than that of the other tunnel barriers and it does not influence the measurements. Using this process the difference in critical currents is reduced to less than 4 %. We used the base Nb electrode of 110 nm, a dummy junction was formed by thermal oxidation of a 5 nm thick Al film and all following seven junctions consisted of 90 nm intermediate Nb layers with barriers similar to the dummy junction. A typical value of $j_c$ was about $360 A/cm^2$, which corresponds to the single-layer Josephson penetration depth $\lambda_J \approx 20\mu m$. Six different junction sizes were produced on the same wafer. Long Josephson junctions had the dimensions of $200 \times 20$, $350 \times 20$, $200 \times 10$ and $450 \times 10\,\mu m^2$. In addition, small junctions of $10 \times 10$ and $20 \times 20\,\mu m^2$ were produced. Here we report data for $n = 7$ stacked junction wafer. Measurements were performed at 4.2 K. $I - V$ curves were collected using a digital storage oscilloscope.

## III. Gap structure

Measurements of the $I - V$ curves clearly indicate a significant change in the individual junction gap voltages as compared with single-barrier junctions. Fig. 1 shows the data for two junctions of different size made on one wafer. The tendency of the gap suppression with increasing current becomes more clear for larger junction areas. We believe that this is due to the thermal decoupling of the middle Nb layers from the surrounding. A high rate of the quasiparticle injection produces a heating effect in the superconducting layers. This effect can not be easily avoided due to the low thermal conductivity of the insulating surrounding of the stacks.

## IV. Flux-flow characteristics

Measurements of $I - V$ curves were made at the range of external magnetic field $H$ from 0 to 40 Oe. An example of $I - V$ curves stored during continuous $H$–sweep is shown in Fig. 2. With increasing $H$, flux-flow branches appear starting from $V = 0$ and from various gap voltage branches. In Fig. 2 the individual junction gap branches are seen at the voltages of about $V_1 \approx 2.7$ mV, $V_2 \approx 5.5$ mV, $V_3 \approx 8.2$ mV, and so on. At the gap branch for $H = 0$ some junctions (one or more) are switched to their gap voltage while the others remain at zero voltage state. With increasing the magnetic field the latter junctions show flux-

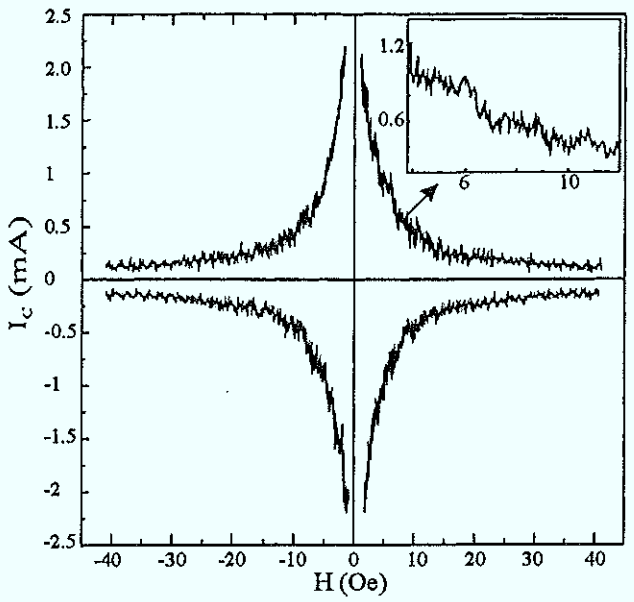


Fig. 6. $I_c(H)$ measurements for a $350 \times 20\,\mu m^2$ 7-fold stack.

see, that taking into account $N = 5$ active junctions in our stack, the measured voltage spacing of 110 $\mu$V fits reasonably well to the resonance $n_z = 2$ ($\Delta V \approx 117\,\mu$V) or $n_z = 3$ ($\Delta V \approx 94\,\mu$V) in $z$-direction. From Fig. 3 one can see that $n_x$ for the observed resonances is taking the values between 15 and 20. Thus, the reported dc measurements are consistent with the Kleiner model of the stacked junction system.

## V. $I_c(H)$ DEPENDENCE

In Fig. 5 we show the comparison of $I_c(H)$ dependences for a small area stack with a single-barrier junction. The dimensions of both samples are equal and also the critical currents are close to each other. In the stacks, the minima of the Fraunhofer pattern are clearly shifted to higher fields, as expected due to thin intermediate superconducting electrodes. Measurements for a long junction stack are shown in Fig. 6. For long stacks we found it very difficult to avoid trapping of magnetic flux when reaching the critical current at $H = 0$. For this reason measurements were performed in the current range below 2.5 mA. We observed a complicated fine structure on the curve that does not appear for a single junction. Comparison of experimental data with theory for large-area stacks [16] is in progress. The inset in Fig. 6 shows a blown up region of $I_c(H)$. We found that noise-like oscillations on the main $I_c(H)$ curve are rather deterministic and reproducible for different sweep directions.

## VI. CONCLUSION

A new method for the preparation of vertically stacked Josephson junctions with a minimized spread in critical currents is introduced. This effort allowed us to investigate seven-fold stacks with nearly equal junctions. A coherent operation of up to five junctions was observed in the samples. New resonant modes characterised by large voltage spacing are observed and attributed to the Kleiner modes. Radiation measurements are prepared to verify this behaviour. A clear change in the $I_c(H)$ dependence is observed for stacks with increasing their planar dimensions.

## REFERENCES

[1] V. P. Koshelets, A. V. Shuchukin, S. V. Shitov, and L. V. Filippenko, *IEEE Trans. Appl. Supercond.*, **3**, 2524 (1993)
[2] A. V. Ustinov, H. Kohlstedt, and C. Heiden, *IEEE Trans. Appl. Supercond.*, **5**, 2743 (1995)
[3] R. Kleiner, P. Müller, H. Kohlstedt, N. F. Pedersen, and S. Sakai, *Phys. Rev. B*, **50**, 3942 (1994)
[4] R. Kleiner, F. Steinmeyer, G. Kunkel, and P. Müller, *Phys. Rev. Lett.*, **68**, 2394 (1992)
[5] H. Kohlstedt, F. König, P. Henne, N. Thyssen, and P. Caputo, "The role of surface roughness in the fabrication of stacked Nb/Al-AlO$_x$/Nb tunnel junctions",(to be published)
[6] R. Kleiner, *Phys. Rev. B*, **50**, 6919 (1994)
[7] H. A. Huggins and M. Gurvitch, *J. Appl. Phys.*, **57**, 2103 (1985), and refs. therein
[8] J. Krug, and H. Spohn, "Kinetic Roughening of Growing Surfaces" in "Solids far from Equilibrium", Ed. C. Godreche, Cambridge University Press (1991)
[9] A. Zangwill: "Theory of Growth-Induced Surface Roughness" in "Microstructural Evolution of Thin Films", Ed. H. A. Atwater and C. V. Thompson, Academic Press, New York (1995)
[10] R. Bloch, L. Brügemann, and W. Press, *J. Phys. D*, **22**, 1136 (1989)
[11] C. Thompson, G. Palasantzas, Y. P. Feng, S. K. Sinha, and J. Krim, *Phys. Rev. B*, **49**, 4902 (1994)
[12] T. Imamura, and S. Hasuo, *Appl. Phys. Lett.*, **58**, 645 (1991)
[13] N. Thyssen, A. V. Ustinov, H. Kohlstedt, S. Pagano, J. G. Caputo, and N. Flytzanis,*IEEE Trans. Appl. Supercond.*, **5**, 2965 (1995)
[14] A. V. Ustinov, H. Kohlstedt, and P. Henne, *Phys. Rev. Lett.*, **77**, 3617 (1996)
[15] S. Sakai, A. V. Ustinov, H. Kohlstedt, A. Petraglia, and N. F. Pedersen, *Phys. Rev. B*, **50**, 12905 (1994)
[16] M. V. Fistul, G. F. Giuliani, *Physica C*, **230**, 9 (1994)

# Experimental Study of Flux Flow and Resonant Modes in Multi-Junction Josephson Stacks

N. Thyssen, H. Kohlstedt, and A. V. Ustinov
Institute of Thin Film and Ion Technology, Research Center (KFA), D-52425 Jülich, Germany

*Abstract* — **Magnetic field dependence of current-voltage characteristics of 7-layer stacked Nb/Al-$AlO_x$/Nb long Josephson junctions are investigated experimentally. The magnetic coupling between the junctions is provided by their common superconducting electrodes of the thickness smaller than the London penetration depth. The current-voltage characteristics clearly display collective flux-flow behavior of Josephson vortices (fluxons) which simultaneously move in up to 5 layers of the stack under the influence of the bias current. The flux-flow behavior is modulated by a complicated structure of cavity-like resonances which show a broad range of characteristic frequencies. Our observations can be qualitatively explained as the interplay between the Fiske modes and the two-dimensional resonances in these stacks. For the intermediate magnetic field range, we find pronounced resonant modes with large voltage spacing which indicates mutually coherent operating junctions.**

## I. Introduction

Stacked Josephson tunnel junctions are interesting from various aspects. Long Josephson junctions operated in the flux-flow mode have already been successfully used as local oscillators in integrated submillimeter-wave receivers [1]. Mutually phase-locked oscillators increase the output power and decrease the linewidth. Vertical stacking of Josephson junctions appears as one possible novel realization of such elements. In comparison with planar oscillator arrays, the mutual inductive coupling in stacks can be by several orders of magnitude stronger and can be controlled by the thickness of the intermediate superconducting layers. Previous studies of two fold stacks [2] have already shown promising phase locking behaviour. In addition, stacks made with low-$T_c$ technology serve to model the properties in layered high-$T_c$ superconductors [3], and in particular to understand the intrinsic Josephson effect [4].

For coherent functioning of a multi-layer Josephson device a spread in critical current densities $j_c$ between the junctions of less than 5 % is usually required. So far this demand was considered to be the main preparation problem of stacked arrays. Even in the case of well-reproducible and reliable single-barrier Nb/Al-$AlO_x$/Nb technology results typically show a larger spread in junction parameters. Due to a modification of the preparation procedure, we are able to produce Josephson junction stacks with a difference in critical currents of less than 4 % [5]. We report on the experimental study of the flux-flow dynamics of 7−fold stacked junctions with up to five coupled working junctions. High-voltage steps are observed on the current-voltage characteristics ($I-V$ curves). These steps give a clear indication for two-dimensional resonances, theoretically predicted by Kleiner [6], which we call in the following the Kleiner modes.

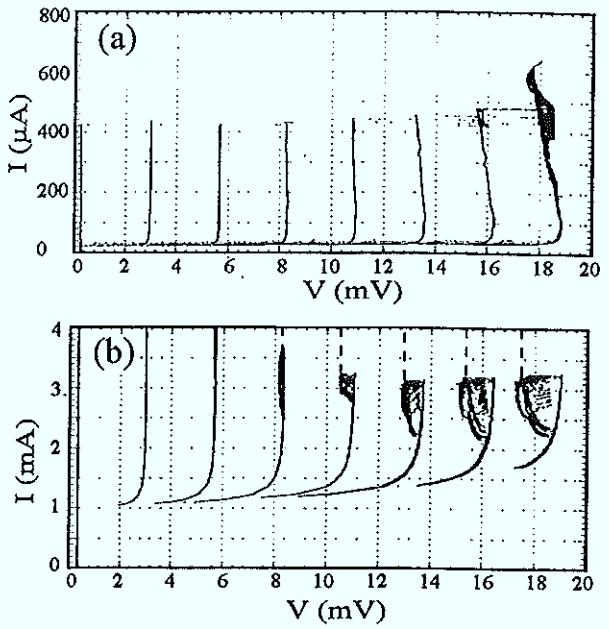


Fig. 1. I-V characteristics of 7-fold stacks: (a)10 × 10 $\mu m^2$, (b) 200 × 10 $\mu m^2$.

## II. Sample fabrication

Using the modified SNAP technology [7] we prepared Nb/Al-$AlO_x$/Nb Josephson junctions of overlap geometry. Usually fabricated samples with various numbers of layers show one junction with significantly higher critical current than the others. In the conventional process the oxidation parameters for all junctions are equal and all Al

Manuscript received August 25, 1996.

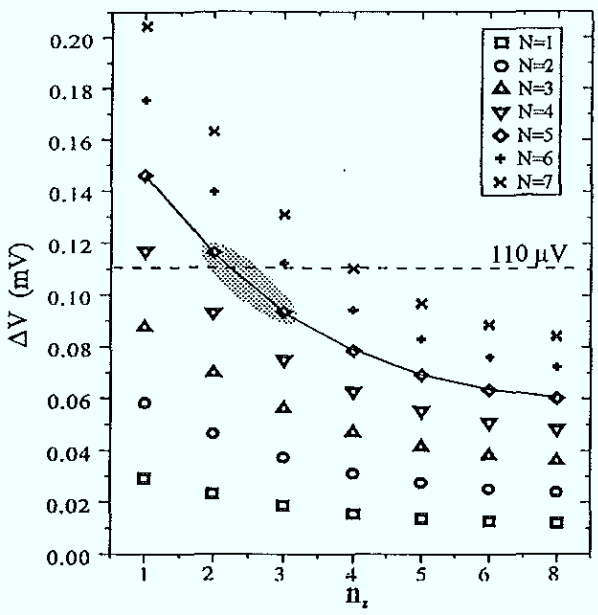


Fig. 4. Voltage spacing between the Kleiner modes according to Eq.(2). Various points correspond to different number $N$ of junctions operating coherently. $N$ values are shown on the plot.

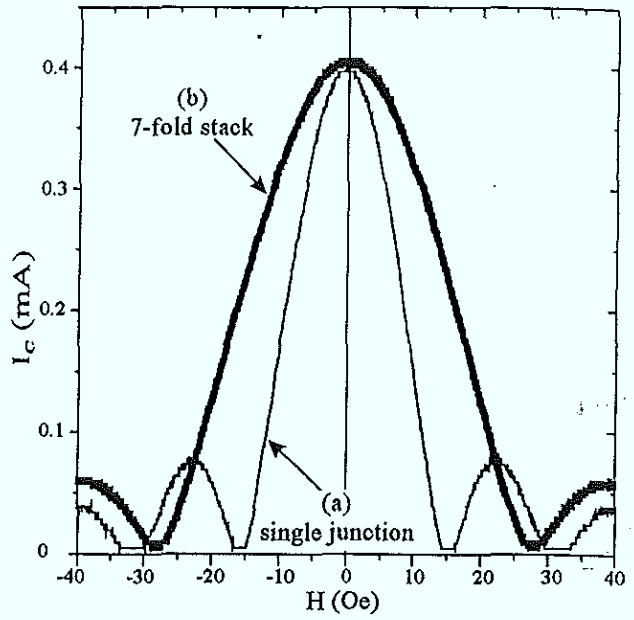


Fig. 5. $I_c(H)$ measurements: (a)$10 \times 10\ \mu m^2$ single junction, (b) $10 \times 10\ \mu m^2$ 7-fold stack.

flow behaviour: the flux-flow voltage increases with increasing $H$. By measuring the flux-flow voltage $V_{ff}$ dependence on $H$ we were able to determine the number of junctions participating in the flux-flow state. The number of participating junctions $N$ was different for the flux-flow modes in voltage regions between the various gap voltages, $V_m = mV_g$ and $V_{m+1} = (m+1)V_g$, where $V_g \approx 2.75$mV and $m = 0, 1, ..., 6$. The flux-flow mode observed between $V_m$ and $V_{m+1}$ may account for maximum $(n-m)$ junctions participating in the flux-flow state, since $m$ junctions are already switched to the gap voltage $V_g$. Here $n$ is the number of stacked junctions. The dependence of $V_{ff}(H)$ for different $m$ was measured. Comparing $dV_{ff}/dH$ for different $m$ we found at maximum 5 junctions operating in the flux-flow state. This number is smaller than the number of stacked junctions $n = 7$, and we argue that it is due to the screening effect of current leads. The lowest and the highest junction each have one thick superconducting electrode. These bulk electrodes should significantly influence the magnetic field penetration in the stack. We suppose that the top and bottom junctions do not participate in the flux-flow behavior.

The flux-flow state of five junctions is shown in Fig. 3. The stored $I-V$ curves can be divided in three areas of different behavior. From 0 to 0.4 mV resonances appear. The characteristic voltage spacing of these resonances is comparable with that of Fiske steps for single Josephson junction $\triangle V_{Fs} = 43\ \mu$V of the same area [13]. However, the measured resonances show a very complicated structure that can be explained by the interference of different resonant modes. From 0.4 mV to 1.6 mV we observe a very smooth flux-flow step that is continuously tunable by $H$ and does not show any resonances. We note that in this range the $I-V$ curve looks similar to the so-called displaced linear branch (DLS) of a single-barrier long Josephson junction. It has been demonstrated recently [14] that DLS is a signature of very complicated and even chaotic fluxon dynamics in the junction. For voltages above 1.6 mV clear resonant steps appear with voltage spacing of about 110 $\mu$V. These resonances have too large voltage spacing to be explained by the Fiske resonances of individual junctions. We compared their voltages with the theoretical model by Kleiner [6]. According to the Kleiner's model, stacked junctions form a two-dimensional resonator in the cross-sectional plane perpendicular to the tunnel barriers. Resonant voltage steps are classified by the resonance number $n_x$ in layer plane and the vertical resonance number $n_z$. The corresponding voltages in the coherent flux-flow state of $N$ junctions are given by the following formula: [6],[15]

$$V_{n_x,n_z} = \Phi_0 \frac{n_x}{2L} \frac{N}{\sqrt{\varepsilon\mu_0}} \sqrt{\frac{d}{d_1 + 2s\cos\frac{n_z\pi}{n+1}}}, \qquad (1)$$

where $L$ is the length of the junction in the direction perpendicular to magnetic field, $d$ is the tunnel barrier thickness, $\varepsilon$ is its dielectric constant, $d_1$ is the magnetic thickness of the intermediate Nb layer, $s = -\lambda_L/\sinh(t/\lambda_L)$ with $t$ being the thickness of the intermediate Nb layer. Here we assume that the number of junctions participating in the flux-flow state is $N \leq n$.

Fig. 4 shows the voltage spacings between the expected Kleiner resonances:

$$\triangle V = V_{n_x,n_z} - V_{n_x-1,n_z}. \qquad (2)$$

The dashed line shows the voltage spacing between the experimentaly found cavity-like modes of Fig. 3. One can

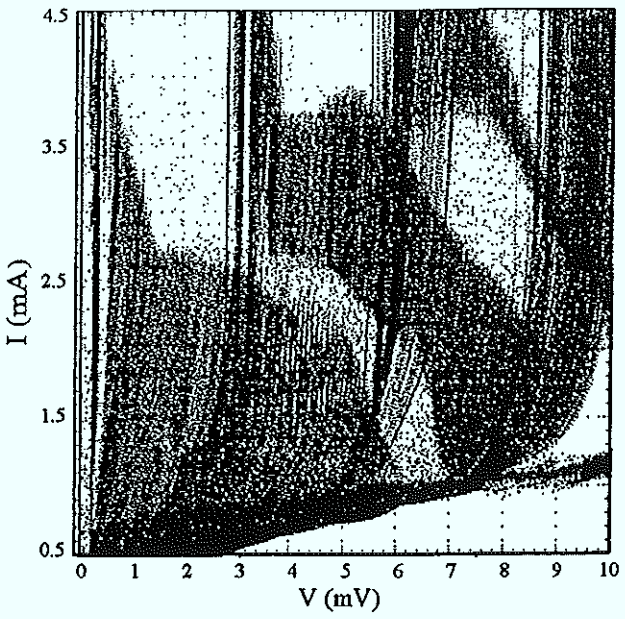


Fig. 2. Flux-flow behaviour measured at continuous sweep of magnetic field $H$ for $450 \times 10\,\mu m^2$ stack.

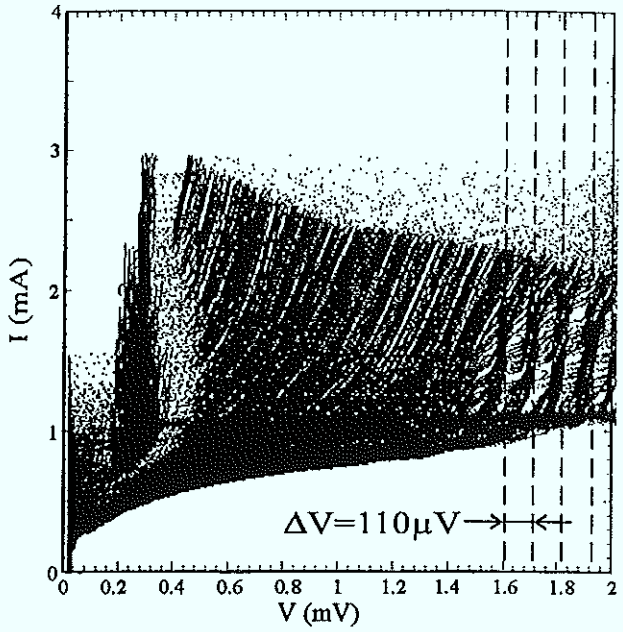


Fig. 3. Coherent resonances of five coupled junctions for $350 \times 20\,\mu m^2$ stack.

layers have a thickness of 5 nm. Nb layers are nevertheless different because the ground Nb electrode is typically much thicker than the intermediate Nb layers.

The thickness of underlying Nb plays an important role for the formation of the barrier and is responsible for the higher critical current for the thicker Nb layer. By the theory of kinetic roughning, it is known that the surface roughness increases with film thickness [8],[9]. Measurements of x-ray specular reflectivity were used to determine the Nb surface roughness [10],[11]. We found the roughness of the top Nb film to be independent of Nb underlayers if there is an Al-$AlO_x$ barrier placed in between. These results clearly confirm the planarization effect of Al-$AlO_x$ on Nb studied earlier by HRTEM [12]. Thus, in order to obtain minimum spread in parameters, the thermal oxidation for each tunnel barrier has to be adjusted to the thickness of the last Nb layer.

Another solution which makes it possible to obtain small parameter spread in stacked Nb/$AlO_x$ junctions is the use of an Al or Al-$AlO_x$ dummy layer in the base electrode [5]. This dummy junction serves to compensate the roughness of the thicker base Nb layer. The critical current of the dummy layer is much larger than that of the other tunnel barriers and it does not influence the measurements. Using this process the difference in critical currents is reduced to less than 4 %. We used the base Nb electrode of 110 nm, a dummy junction was formed by thermal oxidation of a 5 nm thick Al film and all following seven junctions consisted of 90 nm intermediate Nb layers with barriers similar to the dummy junction. A typical value of $j_c$ was about $360\,A/cm^2$, which corresponds to the single-layer Josephson penetration depth $\lambda_J \approx 20\mu m$. Six different junction sizes were produced on the same wafer. Long Josephson junctions had the dimensions of $200 \times 20$, $350 \times 20$, $200 \times 10$ and $450 \times 10\,\mu m^2$. In addition, small junctions of $10 \times 10$ and $20 \times 20\,\mu m^2$ were produced. Here we report data for $n = 7$ stacked junction wafer. Measurements were performed at 4.2 K. $I - V$ curves were collected using a digital storage oscilloscope.

## III. Gap structure

Measurements of the $I - V$ curves clearly indicate a significant change in the individual junction gap voltages as compared with single-barrier junctions. Fig. 1 shows the data for two junctions of different size made on one wafer. The tendency of the gap suppression with increasing current becomes more clear for larger junction areas. We believe that this is due to the thermal decoupling of the middle Nb layers from the surrounding. A high rate of the quasiparticle injection produces a heating effect in the superconducting layers. This effect can not be easily avoided due to the low thermal conductivity of the insulating surrounding of the stacks.

## IV. Flux-flow characteristics

Measurements of $I - V$ curves were made at the range of external magnetic field $H$ from 0 to 40 Oe. An example of $I - V$ curves stored during continuous $H$–sweep is shown in Fig. 2. With increasing $H$, flux-flow branches appear starting from $V = 0$ and from various gap voltage branches. In Fig. 2 the individual junction gap branches are seen at the voltages of about $V_1 \approx 2.7$ mV, $V_2 \approx 5.5$ mV, $V_3 \approx 8.2$ mV, and so on. At the gap branch for $H = 0$ some junctions (one or more) are switched to their gap voltage while the others remain at zero voltage state. With increasing the magnetic field the latter junctions show flux-

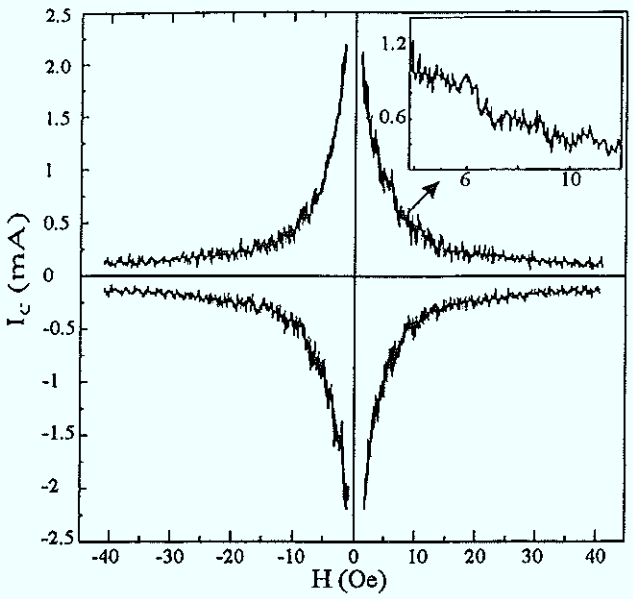


Fig. 6. $I_c(H)$ measurements for a $350 \times 20\,\mu m^2$ 7-fold stack.

see, that taking into account $N = 5$ active junctions in our stack, the measured voltage spacing of 110 $\mu$V fits reasonably well to the resonance $n_z = 2$ ($\Delta V \approx 117\,\mu V$) or $n_z = 3$ ($\Delta V \approx 94\,\mu V$) in $z$-direction. From Fig. 3 one can see that $n_x$ for the observed resonances is taking the values between 15 and 20. Thus, the reported dc measurements are consistent with the Kleiner model of the stacked junction system.

## V. $I_c(H)$ DEPENDENCE

In Fig. 5 we show the comparison of $I_c(H)$ dependences for a small area stack with a single-barrier junction. The dimensions of both samples are equal and also the critical currents are close to each other. In the stacks, the minima of the Fraunhofer pattern are clearly shifted to higher fields, as expected due to thin intermediate superconducting electrodes. Measurements for a long junction stack are shown in Fig. 6. For long stacks we found it very difficult to avoid trapping of magnetic flux when reaching the critical current at $H = 0$. For this reason measurements were performed in the current range below 2.5 mA. We observed a complicated fine structure on the curve that does not appear for a single junction. Comparison of experimental data with theory for large-area stacks [16] is in progress. The inset in Fig. 6 shows a blown up region of $I_c(H)$. We found that noise-like oscillations on the main $I_c(H)$ curve are rather deterministic and reproducible for different sweep directions.

## VI. CONCLUSION

A new method for the preparation of vertically stacked Josephson junctions with a minimized spread in critical currents is introduced. This effort allowed us to investigate seven-fold stacks with nearly equal junctions. A coherent operation of up to five junctions was observed in the samples. New resonant modes characterised by large voltage spacing are observed and attributed to the Kleiner modes. Radiation measurements are prepared to verify this behaviour. A clear change in the $I_c(H)$ dependence is observed for stacks with increasing their planar dimensions.

## REFERENCES

[1] V. P. Koshelets, A. V. Shuchukin, S. V. Shitov, and L. V. Filippenko, *IEEE Trans. Appl. Supercond.*, 3, 2524 (1993)
[2] A. V. Ustinov, H. Kohlstedt, and C. Heiden, *IEEE Trans. Appl. Supercond.*, 5, 2743 (1995)
[3] R. Kleiner, P. Müller, H. Kohlstedt, N. F. Pedersen, and S. Sakai, *Phys. Rev. B*, 50, 3942 (1994)
[4] R. Kleiner, F. Steinmeyer, G. Kunkel, and P. Müller, *Phys. Rev. Lett.*, 68, 2394 (1992)
[5] H. Kohlstedt, F. König, P. Henne, N. Thyssen, and P. Caputo, "The role of surface roughness in the fabrication of stacked Nb/Al-$AlO_x$/Nb tunnel junctions",(to be published)
[6] R. Kleiner, *Phys. Rev. B*, 50, 6919 (1994)
[7] H. A. Huggins and M. Gurvitch, *J. Appl. Phys.*, 57, 2103 (1985), and refs. therein
[8] J. Krug, and H. Spohn, "Kinetic Roughening of Growing Surfaces" in "Solids far from Equilibrium", Ed. C. Godreche, Cambridge University Press (1991)
[9] A. Zangwill: "Theory of Growth-Induced Surface Roughness" in "Microstructural Evolution of Thin Films", Ed. H. A. Atwater and C. V. Thompson, Academic Press, New York (1995)
[10] R. Bloch, L. Brügemann, and W. Press, *J. Phys. D*, 22, 1136 (1989)
[11] C. Thompson, G. Palasantzas, Y. P. Feng, S. K. Sinha, and J. Krim, *Phys. Rev. B*, 49, 4902 (1994)
[12] T. Imamura, and S. Hasuo, *Appl. Phys. Lett.*, 58, 645 (1991)
[13] N. Thyssen, A. V. Ustinov, H. Kohlstedt, S. Pagano, J. G. Caputo, and N. Flytzanis,*IEEE Trans. Appl. Supercond.*, 5, 2965 (1995)
[14] A. V. Ustinov, H. Kohlstedt, and P. Henne, *Phys. Rev. Lett.*, 77, 3617 (1996)
[15] S. Sakai, A. V. Ustinov, H. Kohlstedt, A. Petraglia, and N. F. Pedersen, *Phys. Rev. B*, 50, 12905 (1994)
[16] M. V. Fistul, G. F. Giuliani, *Physica C*, 230, 9 (1994)

# Josephson Flux Flow in Multi-Junction Stacks: Experiment and Simulation

**N. Thyssen†[1], H. Kohlstedt†, S. Sakai‡, and A. V. Ustinov⋆**

† Institut fur Schicht- und Ionentechnik, Forschungszentrum Jülich GmbH, D-52425 Jülich, Germany

‡ Electrotechnical Laboratory, 1-1-4 Umezono, Tsukuba-shi, Ibaraki 305, Japan

⋆ Physikalisches Institut III, Universität Erlangen-Nürnberg, D-91058 Erlangen, Germany

**Abstract.** Long $N-$layered Nb/Al-$AlO_x$/Nb Josephson junctions are investigated experimentally and by numerical simulations. Magnetic field dependent current-voltage characteristics show collective flux-flow behavior in the experiment. In order to interpret the observed dynamics we performed numerical analysis using a finite difference method. The displayed structure of cavity-like resonances is accounted by the characteristic frequencies calculated using the coupled sine-Gordon equation. A static $I-V$ curve obtained numerically for a 7-junction stack shows phase-locked flux-flow motion among all the 7 junctions, although the number of vortices in the top and bottom junction were found to be larger than those of the inner junctions because of the thicker top and bottom Nb-electrodes. Numerical data show good overall agreement with the experiment.

## 1. Introduction

Long Josephson junctions operated in the flux-flow mode are presently being successfully used as local oscillators in integrated submillimeter-wave receivers [1]. Mutually phase-locked oscillators increase the output power and decrease the linewidth, which improves the performance of such devices. Vertical stacking of Josephson junctions appears as natural realization of such oscillators. In comparison with planar oscillator arrays, the mutual inductive coupling in stacks can be by several orders of magnitude stronger and the impedance is higher than that of single-layer junctions. Study of two fold stacks [2] have already shown promising phase locking behavior with possible in phase and out of phase oscillations in the two junctions. First experiments with multi-layer stacks [3, 4] showed rather complex behavior which appears to be difficult to interpret without detailed numerical modeling of these systems. For the parameters of intrinsic Josephson junction stacks with identical layer thickness, such modeling together with resonant mode analysis was reported by Kleiner [5].

The theoretical model developed for stacked Josephson junctions [6] is proved to be a very useful tool for understanding the dynamics of stacks. Using this model, detailed quantitative comparison of its predictions with experimental data for 2- and 3-fold stacks was made and good agreement was found [7].

[1] E-mail: Thyssen@isitel1.isi.kfa-juelich.de

## 2. Model

Josephson junction stacks consisting of $N$ junctions ($j = 1, ..., N$) contain $N+1$ superconducting layers (numbered $i = 0, ..., N$). The system of equations which describes the Josephson phase dynamics in the stack can be written in the following form [6]:

$$\frac{\Phi_0}{2\pi\mu_0}\frac{\partial^2}{\partial x^2}\begin{pmatrix}\phi_1\\ \vdots\\ \phi_j\\ \vdots\\ \phi_N\end{pmatrix} = \begin{bmatrix} d'_1 & s^1 & 0 & 0 & 0 & 0 & 0 \\ s^1 & d'_2 & s^2 & 0 & 0 & 0 & 0 \\ 0 & \ddots & \ddots & \ddots & 0 & 0 & 0 \\ 0 & 0 & s^{i-1} & d'_j & s^i & 0 & 0 \\ 0 & 0 & 0 & \ddots & \ddots & \ddots & 0 \\ 0 & 0 & 0 & 0 & s^{N-2} & d'_N - 1 & s^{N-1} \\ 0 & 0 & 0 & 0 & 0 & s^{N-1} & d'_N \end{bmatrix} \begin{pmatrix} J_1^Z \\ \vdots \\ J_j^Z \\ \vdots \\ J_N^Z \end{pmatrix} , \qquad (1)$$

where $\phi_j$ is the superconducting phase difference on the junction number $j$ and $\Phi_0$ is the magnetic flux quantum. The coupling is determined by the parameters:

$$d'_j = d_j + \lambda^{i-1}\coth\frac{t^{i-1}}{\lambda^{i-1}} + \lambda^i \coth\frac{t^i}{\lambda^i} \qquad \text{and} \qquad s^i = \frac{-\lambda^i}{\sinh(t^i/\lambda^i)} , \qquad (2)$$

where $d_j = d_{i,i-1}$ is the tunnel barrier thickness, $t^i$ and $\lambda^i$ are the thickness of the superconducting layer number $i$ and its London penetration depth, respectively. The sum of current components across the junction is:

$$J_Z^j = \frac{\Phi_0}{2\pi}C^j\phi_{tt}^j + \frac{\Phi_0}{2\pi}\frac{1}{R^j}\phi_t^j + j_c^j\sin(\phi^j) - j^j \ . \qquad (3)$$

Here $C^j$, $R^j$, $j_c^j$ and $j^j$ are the junction capacitance, resistance, critical current and bias current densities, respectively.

Numerical simulations were made by solving the system of equations (1) numerically by finite difference method. Boundary conditions determined by external magnetic field were introduced similarly to Ref. [6].

## 3. Experiment

Details on fabrication of multilayer Nb/Al-AlO$_x$/Nb junctions and first measurements of them were reported in Refs. [3, 4]. Improved preparation procedures allowed us to reduce the difference in critical currents in a stack to less than 4 % [8].

An example of current-voltage ($I - V$) curves for 7-junction ($350 \times 20\ \mu\text{m}^2$) stack taken in the magnetic field interval from 8 Oe to 12 Oe is shown in Fig. 1(a). The inner Nb layers of the stack had the thickness about 78 nm, the lowest and the highest junction each had thicker superconducting electrodes (180 nm and 600 nm, respectively). By measuring the slope of flux-flow voltage dependence on $H$ we were able to evaluate the number of junctions participating in the flux-flow state [3] which turned to be close to the number of layers in the stack. At lower fields the $I - V$ curve is rather smooth, resembling displaced linear slope of a single long Josephson junction [9]. With increasing $H$, there appear resonant branches with characteristic voltage spacing of about 110 $\mu$V. These resonances have too large voltage spacing to be explained by the Fiske resonances of individual junctions. Since stacked junctions are measured in series, it is not possible to determine individual junction voltages in this experiment.

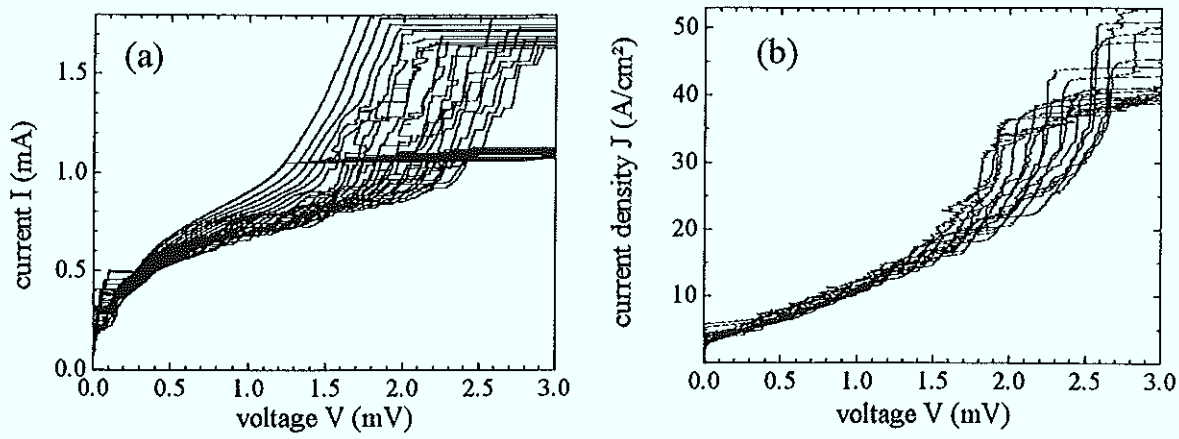


Figure 1. (a) Experimental $I-V$ characteristics of 7-fold stack; magnetic field is varied from 8 Oe to 12 Oe with 0.2 Oe increment. (b) Numerically simulated $I-V$ characteristics; magnetic field changed between 7.6 Oe and 11 Oe with increment 0.2 Oe.

## 4. Simulations

In order to interpret the observed dynamics we performed numerical simulations using the model (1) with parameters chosen according to the experiment. Fig. 1(b) shows the simulated $I-V$ curves which are in fairly good agreement with the experimental data in Fig. 1(a). The obtained characteristic voltage spacing of about 100 $\mu$V is close to the experimental one of 110 $\mu$V. Fig. 2(a) shows a clear resonant flux-flow regime for a fixed magnetic field of 10.6 Oe. The dc voltages on the individual junctions are presented at Fig. 2(b). Junctions 1 and 7 have larger voltages than junctions 2 to 6. The reason for this behavior is the much thicker top (600 nm) and bottom (180 nm) electrodes in comparison with the intermediate Nb layers (78 nm). A detailed analysis simulated at J = 45 A/cm$^2$ shows that the existing fluxon numbers ($N_i$) of junctions 1, $2-6$, and 7 are about 21, 13, and 25, respectively. By using these values of $N_i$, the appeared dc voltage $V_i$, the junction length $L$, and the equation: $V_i = \Phi_0(N_i/L)u_i$ for i = $1-7$, the evaluated fluxon velocities $u_i$ are in the range of $(4.05 \pm 0.06) \times 10^6$ m/s for all the junctions. This value is very close to the smallest characteristic electromagnetic wave velocity of $4.16 \times 10^6$ m/s calculated using Eq.(6) in Ref. [7]. Obtained voltage patterns for all junctions at a given time show that among every other junction the positions giving the voltage maxima (or minima) coincide each other, while in the neighboring junctions the oscillations are out of phase with each other. This checkered pattern is the characteristic of the smallest velocity mode as mentioned above. Thus, the flux-flow dynamics in this regime is accompanied by electromagnetic resonances that may be characterized by the lowest characteristic velocity of the 7-fold stack.

## Acknowledgments

The support of this work by the BMBF contract number 13N6945/3 and partial support by Science and Technology Agency (Japan) is gratefully acknowledged.

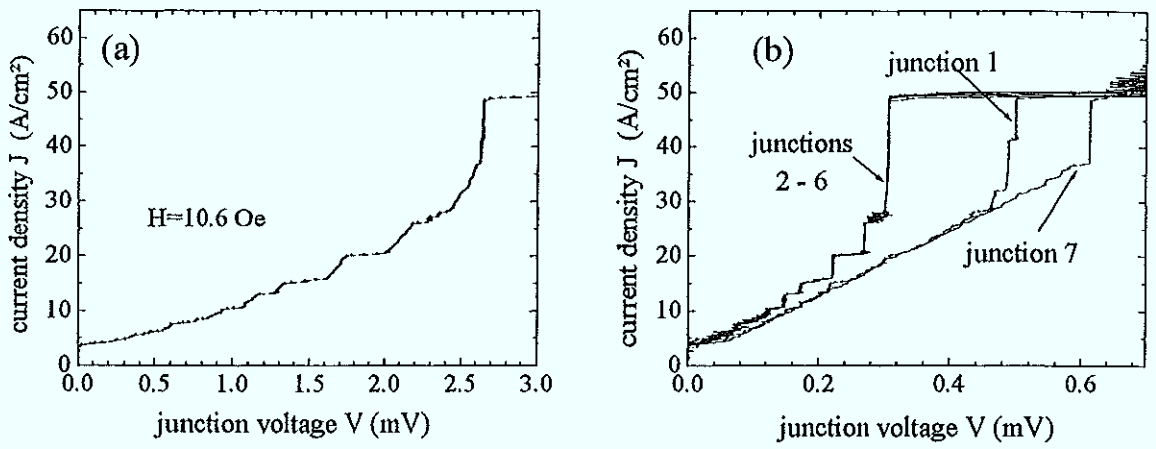


Figure 2. Simulated $I-V$ characteristics for the 7-fold stack:(a) total voltage on the stack (sum of all); (b) individual junction voltages.

## References


[1] V. P. Koshelets, A. V. Shuchukin, S. V. Shitov, and L. V. Filippenko, *IEEE Trans. Appl. Supercond.* **5**, 3057 (1995)

[2] A. V. Ustinov and H. Kohlstedt. *Phys. Rev. B* **54**, 6111 (1996)

[3] N. Thyssen, A. V. Ustinov, and H. Kohlstedt, *J. Low Temp. Phys.* **106**, 201 (1997)

[4] N. Thyssen, H. Kohlstedt, and A. V. Ustinov, To appear in *IEEE Trans. Appl. Supercond.* **7** (1997)

[5] R. Kleiner, *Phys. Rev. B* **50**, 6919 (1994)

[6] S. Sakai, P. Bodin, and N. F. Pedersen, *J. Appl. Phys.* **73**, 2411 (1993)

[7] S. Sakai, A. V. Ustinov, H. Kohlstedt, A. Petraglia, and N. F. Pedersen, *Phys. Rev. B*, **50**, 12905 (1994)

[8] H. Kohlstedt, F. König, P. Henne, N. Thyssen, and P. Caputo, *J. Appl. Phys.* **80**, 5512 (1996)

[9] A. V. Ustinov, H. Kohlstedt, and P. Henne, *Phys. Rev. Lett.* **77**, 3617 (1996)

Reprinted from

PHYSICA C

Physica C 293 (1997) 264–267

# Low-$T_c$ tunnel junction stacks as models for intrinsic Josephson effect in high-$T_c$ materials

N. Thyssen [a], H. Kohlstedt [a], A.V. Ustinov [b,*]

[a] *Institute of Thin Film and Ion Technology, Research Centre (KFA), D-52425 Jülich, Germany*
[b] *Physikalisches Institut III, Universität Erlangen-Nürnberg, Erwin-Rommel-Straße 1, D-91058 Erlangen, Germany*

ELSEVIER

ELSEVIER

Physica C 293 (1997) 264–267

PHYSICA C

# Low-$T_c$ tunnel junction stacks as models for intrinsic Josephson effect in high-$T_c$ materials

N. Thyssen [a], H. Kohlstedt [a], A.V. Ustinov [b,*]

[a] *Institute of Thin Film and Ion Technology, Research Centre (KFA), D-52425 Jülich, Germany*
[b] *Physikalisches Institut III, Universität Erlangen-Nürnberg, Erwin-Rommel-Straße 1, D-91058 Erlangen, Germany*

**Abstract**

Current–voltage ($I$–$V$) characteristics and radiation emission experiments at 80–120 GHz with 7- and 9-layer stacked Nb/Al–$AlO_x$/Nb Josephson junctions are reported. The $I$–$V$ curves measured in magnetic field applied parallel to the layers display the flux-flow behavior modulated by resonances which are consistent with two-dimensional modes predicted by Kleiner. Voltage dependence of the radiation power indicates collective fluxon motion. © 1997 Elsevier Science B.V.

Intrinsic Josephson effect discovered in BSSCO crystals [1] indicated that some of high-$T_c$ materials are essentially natural stacks of closely packed Josephson tunnel junctions. The interactions between vortices in layered superconductors and superconducting multilayers has become a subject of intensive investigations. Josephson-coupled layers exhibit properties which differ from that of isotropic superconductors. On the other side, their behavior is different from a single Josephson junction due to mutual interactions between the junctions in a stack. The magnetic coupling between the junctions is provided by their common superconducting electrodes of thickness smaller than the London penetration depth. When a magnetic field is applied parallel to the superconducting planes, Josephson vortices (fluxons) can penetrate between the planes. Screening currents of a Josephson vortex extend over several layers and provide a strong coupling between vortices allocated in different junctions.

Josephson tunnel junction stacks made with low-$T_c$ technology may serve to model the properties of naturally layered high-$T_c$ superconductors [2]. One of the most critical fabrication requirements is to achieve a small spread in critical current densities $J_c$ between the junctions. Recently we have reported [3] on a modified preparation procedure which allows to produce Nb/Al–$AlO_x$/Nb stacks with a difference in critical currents of less than 4%. In order to obtain small parameter spread in stacked Nb/$AlO_x$ junctions we use an Nb–Al or Nb–Al–$AlO_x$ dummy layer in the base electrode. This dummy junction serves to compensate the roughness of the thicker Nb base layer [3].

We report on the experimental study of the flux-flow dynamics of 7- and 9-fold stacked Nb/Al–$AlO_x$/Nb junctions. The junctions with a critical current density $J_c$ of about 400 A/cm$^2$ were formed between 90 nm thick stacked Nb layers. Measurements were performed at 4.2 K. Both dc and W-band

* Corresponding author. Tel.: +49 9 131 857 272; fax: +49 9 131 15249; e-mail: ustinov@merlin.physik.uni-erlangen.de.


*PII* S0921-4534(97)01553-0

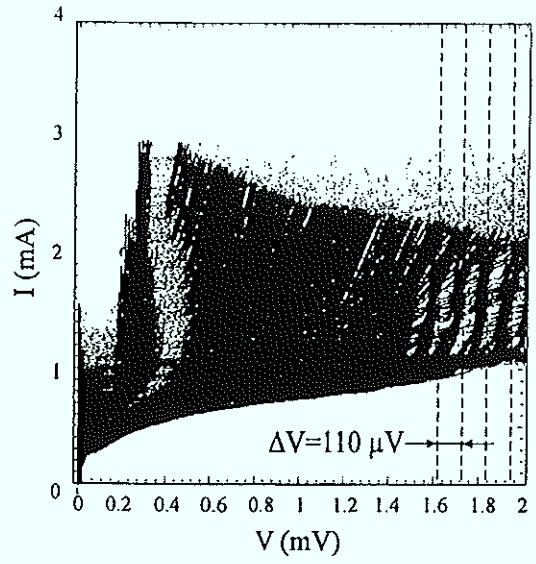


Fig. 1. $I$–$V$ curves of 7-junction stack recorded while continuously sweeping the magnetic field parallel to the layers. Dashed lines indicate characteristic resonances with voltage spacing about 110 μV.

Josephson radiation measurements are performed. High-voltage steps observed on the current–voltage characteristics ($I$–$V$ curves) indicate the existence of two-dimensional resonances theoretically predicted by Kleiner [4].

Measurements of $I$–$V$ curves were made at the range of external magnetic field $H$ from 0 to 40 Oe. An example of $I$–$V$ curves recorded in the low-voltage region during continuous $H$-sweep is shown in Fig. 1. The stack had the planar dimensions 350 × 20 $\mu m^2$ and consisted of 7 junctions. We observed a pronounced flux-flow step which was moving towards high voltages with increasing $H$. The step disappeared at the voltage of about 6 mV which is by a factor of 4 to 5 larger than the highest possible flux-flow voltage of an individual junction. Details about the gap voltages and other dc measurements are presented elsewhere [5].

From 0.4 mV to 1.6 mV in Fig. 1 we observe a very smooth flux-flow step that is continuously tunable by $H$ and does not show clear resonances. We note that in this range the $I$–$V$ curve looks similar to the so-called displaced linear branch (DLS) of a single-barrier long Josephson junction. It has been demonstrated recently [6] that DLS is a signature of very complicated, nearly chaotic fluxon dynamics in the junction. For voltages above 1.6 mV clear resonant steps appear with characteristic voltage spacing of about 110 μV. This voltage spacing is larger than that of Fiske resonances in individual junctions: the spacing of about 43 μV was measured for similar single-barrier junctions of the same planar dimensions.

We compared the voltage spacing between the branches in Fig. 1 with the theoretical model by Kleiner [4]. According to his model, stacked junctions form a two-dimensional resonator in the cross-sectional plane perpendicular to the tunnel barriers. Resonance voltages are classified by the resonance number $n_x$ in layer plane and the vertical resonance number $n_z$. The corresponding voltages in the coherent flux-flow state of $N$ junctions in $n$-fold stack are given by the following formula [4,7]:

$$V_{n_x,n_z} = \Phi_0 \frac{n_x}{2L} \frac{N}{\sqrt{\epsilon\mu_0}} \sqrt{d/\left[d_1 + 2s\cos\frac{n_z\pi}{n+1}\right]}, \quad (1)$$

where $L$ is the length of the stack in the direction perpendicular to magnetic field, $d$ is the tunnel barrier thickness, $\epsilon$ is its dielectric constant, $d_1$ is the magnetic thickness of the intermediate Nb layers, $s = -\lambda_L/\sinh(t/\lambda_L)$ with $t$ being the thickness of the intermediate Nb layer. Here we assume that the number of junctions participating in the flux-flow state is $N \leq n$.

Fig. 2 shows the voltage spacings between the expected Kleiner resonances $\Delta V = V_{n_x,n_z} - V_{n_x-1,n_z}$. The dashed line shows the voltage spacing between the experimentally measured modes of Fig. 1. One can see, that taking $N = 5$ active junctions for our stack, the measured voltage spacing of 110 μV fits reasonably well to the resonance $n_z = 2$ ($\Delta V \approx 117$ μV) or $n_z = 3$ ($\Delta V \approx 94$ μV) in $z$-direction. From Fig. 1 one can see that $n_x$ for the observed resonances takes the values between 15 and 20. Thus, our dc measurements are consistent with the Kleiner model.

Experimental data on radiation detection from a 9-fold stack are presented in Fig. 3. The sample layout is schematically shown in the inset (a). The stack is integrated in a microstripline ending with a

finline antenna [8] inserted into a slit of a waveguide. The magnetic field $H$ parallel to the stack plane is provided by a control current $I_H = 9.2$ mA through the bottom Nb electrode. Radiation with the center frequency $f = 118.5$ GHz is measured with a room temperature superheterodyne receiver. The receiver is operated as radiometer with the double-side band about 3 GHz. The radiation power from the stack is detected while recording the $I$–$V$ curve.

As in single-junction DLS measurements [6], here we observe a rather broad voltage range of radiation emission from the stack. The maximum of the radiation power is detected at about $V_p = 1.75$ mV. For our detection frequency, the Josephson voltage of an individual junction is expected to be about $V_f = 245$ μV. Thus, assuming that several junctions operate at nearly equal voltages, the total number of junctions which may contribute to the radiation peak in Fig. 3 can be estimated as $N = V_p/V_f \approx 7$. Since the radiation peak is rather broad on voltage scale, we cannot conclude that junctions here operate coherently. The radiation peak was observed to shift towards lower voltages and become even broader for receiver frequencies below 100 GHz.

Both dc and rf measurements presented above indicate that the number of junctions $N$ which contribute in the flux-flow voltage of our stacks with the total number of junctions $n = 7$ and $n = 9$ is equal to $n - 2$. One may speculate that that it is due to the screening effect of the thick top and bottom electrodes of the stack [5]. These bulk electrodes should significantly influence the magnetic field penetration in the stack. However, preliminary numerical simulations [9] indicate that the density of fluxons in the top and bottom junctions is *larger* than in the center of the stack. These two junctions should contribute into flux-flow state by a voltage larger than that of inner junctions. Thus, a detailed comparison of experimental data with numerical simulations has to be a subject of future studies.

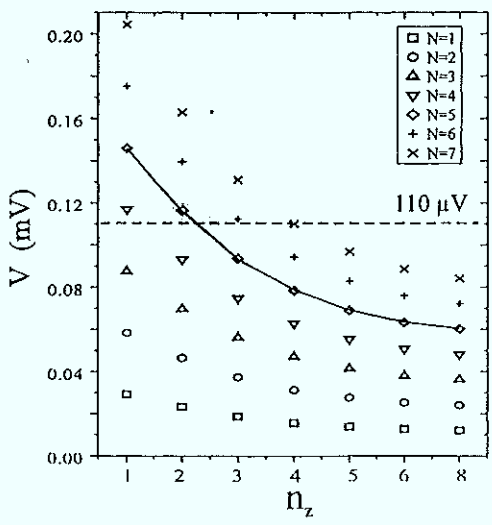


Fig. 2. Voltage spacing $\Delta V$ between the calculated Kleiner resonances. Different points correspond to different numbers $N$ of junctions operating coherently.

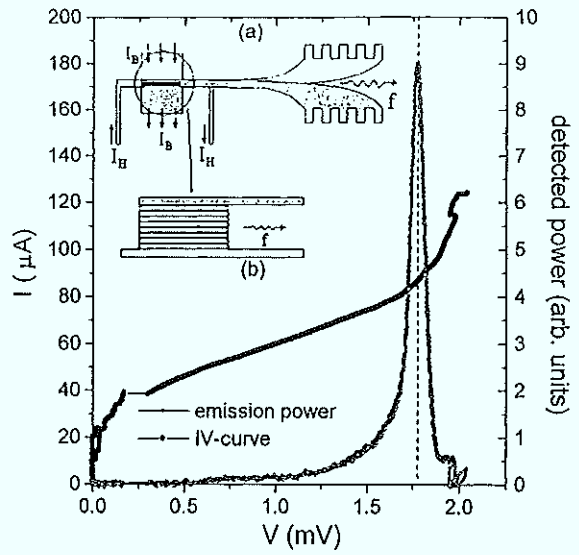


Fig. 3. Radiation power measured by a radiometer with the center frequency $f = 118.5$ GHz from 9-fold Nb/Al–$AlO_x$–Nb stack. The detected power was recorded simultaneously with $I$–$V$ curve while sweeping the current through the stack. Insert (a) shows the top view of the stack with a finline antenna. Insert (b) sketches a cross-section of the stack perpendicular to the substrate plane.

## References

[1] R. Kleiner, F. Steinmeyer, G. Kunkel, P. Müller, Phys. Rev. Lett. 68 (1992) 2394.
[2] R. Kleiner, P. Müller, H. Kohlstedt, N.F. Pedersen, S. Sakai, Phys. Rev. B 50 (1994) 3942.
[3] H. Kohlstedt, F. König, P. Henne, N. Thyssen, P. Caputo, J. Appl. Phys. 80 (1996) 5512.
[4] R. Kleiner, Phys. Rev. B 50 (1994) 6919.

[5] N. Thyssen, H. Kohlstedt, A.V. Ustinov, Presented at Appl. Supercond. Conf. 1996, to be published in: IEEE Trans. Appl. Supercond. (1997).
[6] A.V. Ustinov, H. Kohlstedt, P. Henne, Phys. Rev. Lett. 77 (1996) 3617.
[7] S. Sakai, A.V. Ustinov, H. Kohlstedt, A. Petraglia, N.F. Pedersen, Phys. Rev. B 50 (1994) 12905.
[8] A.V. Ustinov, J. Mygind, V.A. Oboznov, J. Appl. Phys. 72 (1992) 1203.
[9] S. Sakai, Unpublished work, 1996.

# Static properties of stacked Josephson junctions: comparison of experiments with the inductively coupled sine-Gordon model

N. Thyssen[1], R. Monaco[2,3], A. Petraglia[2],

G. Costabile[2], H. Kohlstedt[1], and A. V. Ustinov[4]

[1] *Institut fur Schicht- und Ionentechnik Forschungszentrum Jülich GmbH, D-52425 Jülich, Germany,*

[2] *Dipartimento di Fisica e Unità INFM, Università di Salerno, I-84081 Baronissi (Sa) Italy,*

[3] *Istituto di Cibernetica del C.N.R., I-80072 Arco Felice (Na), Italy,*

[4] *Physikalisches Institut III, Universität Erlangen-Nürnberg, D-91058 Erlangen, Germany.*

*We report on the static properties of two-fold stacks of long Josephson junctions fabricated with the Nb/Al-$AlO_x$/Nb technology. The current-voltage characteristics of these structures typically show three different values of the critical current for a constant external magnetic field. This property can be explained by the inductive coupling model. Numerical calculations based on a system of coupled sine-Gordon equations show that the effective magnetic field in one of the junctions depends on whether the other junction is in the zero voltage state or not. This leads to different critical currents for each junction. This phenomenon was observed for the annular and straight overlap junctions with various parameters.*

PACS 74.50.+r,74.60.-w

Following many years of systematic investigation of the static and dynamic properties of single Josephson junctions, now the interest in vertically stacked junctions is growing. Several aspects converge to stimulate this field of research. In fact, stacking turns out to be a promising technique for Josephson oscillators. As demonstrated by Koshelets et al. [1], long Josephson junctions can work as local oscillators in integrated submillimeter-wave receivers. For a suitable coupling of stacked Josephson junctions such devices could provide larger output power and smaller linewidth than single junctions (depending on the number of coupled junctions), since the fluxon oscillations can phase-lock, as already observed in experiment [2]. In comparison to planar arrays, the mutual inductive coupling in the stacked system can be by several orders of magnitude stronger and can be easily controlled by the thickness of the intermediate superconducting electrode. Another application that could benefit from junction stacking is the Josephson voltage standard [3]. The model that we assume to describe the static and the dynamic behavior of stacked Josephson junctions is the coupled sine-Gordon system [4]. We emphasize that also the intrinsic Josephson effect in high-$T_c$ superconductors [5] by now seems to be well described by this model, and therefore the low-$T_c$ artificial stacks can well serve as model systems for natural high-$T_c$ stacks.

In this paper we consider the effect of an external magnetic field applied in-plane to the barriers of two-fold Josephson junction stacks, a configuration which plays a crucial role for the use of stacked systems. After introducing the model and the numerical results , the sample preparation and the experiments will follow and a brief discussion will conclude the paper.

We make use of the inductive coupling model by Sakai, Bodin, and Pedersen [4], which well accounts for many dynamical phenomena observed in long stacked junctions. They wrote a set of equations (for arbritary barrier geometry and different parameters for each layer) in which the interaction between the junctions depends strongly on the spatial non-uniformity of the local magnetic field. We apply the equations to a two-fold stack with annular geometry in the presence of an external magnetic field. Grønbech-Jensen et al. suggested [6] that a uniform magnetic field acts on a ring-shaped junction as a sink-like

potential and it is accounted by a sinusoidal bias term in the perturbed sine-Gordon equation. Considering the critical current density for each barrier as the only different parameter between the junctions ($\Delta J{=}J_1/J_2$) the equations are:

$$\begin{aligned} \varphi_{tt} &= \varphi_{xx} + S\psi_{xx} - \alpha\varphi_t - \sin\varphi - \eta k^2 \sin(kx) + \gamma \\ &, \\ \psi_{tt} &= \psi_{xx} + S\varphi_{xx} - \alpha\psi_t - \tfrac{1}{\Delta J}\sin\psi - k_\eta \eta k^2 \sin(kx) + \gamma \end{aligned} \qquad (1)$$

where $\varphi$ and $\psi$ are the gauge invariant phase differences across the two barriers which have periodic boundary conditions. Length and time are normalized as usual [6] and the damping constant $\alpha$ is defined as for the single junction; $S$ is the coupling term depending on the physical and geometrical parameters of the system [4], and it can vary from 0 (no coupling) to 1 (infinite coupling); $\eta$ and $\gamma$ stand for the normalized flux coupled into the junction and the uniform bias current normalized to the maximum junction Josephson current, respectively; $k_\eta$ is the ratio between the effective external fields acting on either junction; it can be calculated from the original equations [4] and can be ascribed to the different thickness of the upper and lower electrode. The term $k$ accounts for an annular junction and it is defined as $k = 2\pi/L$, where $L$ is the circumference of the junction [6,7]. In the following, $A$ is the junction whose phase is $\varphi$ , and $B$ is the other one. Recently, it has been verified for single-barrier annular junctions [7–9] that the field-induced term ($\propto \sin(2\pi x/L)$) well accounts for their experimentally observed behavior.

In Fig. 1 we show a calculated dependence of the critical current versus the external field calculated for a stack of two long annular junctions. The parameters were chosen to be consistent with the experiments reported below. The three patterns correspond to the switching from the zero voltage state: i) lower pattern: both junctions switch together from the zero voltage state to the normal state; ii) middle pattern: critical current of junction B while junction A is in the normal state; iii) higher pattern: critical current of junction A while junction B is in the normal state.

Hence, the different states, static or dynamic, of one junction while the other is still in the zero-voltage state are responsible for the different critical current patterns. This

phenomenon, which has been also experimentally observed earlier [10,11], can be visualized considering the spatial modulation of the phase originated by the magnetic field and can be explained in the framework of the model in Eq. (1). In order to clarify this point we focus on the behavior of a single junction. Fig. 2 shows the numerically calculated space derivative of the phase in a single annular junction embedded in a small magnetic field ($\eta = 3$) for different values of the normalized bias current. The curves belong clearly to two families corresponding to a zero voltage state (the lower amplitude family) and a non-zero voltage state (the higher amplitude family). This result can be easily interpreted by observing that when the junction is in the zero voltage state it is in a Meissner-like state and a screening supercurrent prevents the field from entering the barrier completely. On the contrary, when the junction is in the whirling (normal) state, the external field can freely enter the barrier and modulate the phase. In a stack such behavior influence the equation of the other junction through the term proportional to $\varphi_{xx}$, originating a less perturbed state when the first junction is still static (lower pattern) and a more perturbed state when the first junction has switched to a dynamic state. A detailed analysis of this behavior will appear elsewhere.

To check the numerical results we prepared the samples using a modified Selective Niobium Anodizatip Process (SNAP) Nb/Al-Al$O_x$/Nb technology [12,13]. All films were DC-sputtered and the oxide barrier was defined by thermal oxidation under well controlled pressure and temperature. Standard two-fold stacks were fabricated by replacing the single trilayer sputtering with an in-situ sputtered multilayer. Before using the anodic oxidation for passivating the junctions, the upper Nb/Al-Al$O_x$/Nb films were etched by reactive ion etching (R.I.E.). Other type of samples, with a superconducting contact to the middle Nb electrode, was produced using a different process. After the first trilayer was deposited on the substrate, an additional lithographic step for defining the access to the middle electrode was introduced and only after that the second trilayer was sputtered ex-situ. This preparation procedure leads to a larger parameter spread between the stacked junctions when compared to the in-situ process. Two different geometries were prepared and investigated.

Long overlap junctions were fabricated (with and without access to the middle electrode), and annular stacks. The normalized length of these junctions varied between 5 and 12 for the overlap geometry and was 14, 20 or 28 for the annular ones. The intermediate Nb layer was 90nm thick, which results in a coupling parameter $S$ of about 0.5.

The measurements were performed at 4.2K. $I-V$ curves and $I_c-H$ patterns were recorded with a PC using a LABVIEW interface. The dc currents for the junction and the solenoid supplying the external magnetic field were provided by battery powered sources. Fig. 3 shows the $I-V$ characteristics of a two fold stack with an applied field of about 1.5 Oe. The two different critical currents $I_{C\text{base}}$ and $I_{C\text{top}}$ at the first gap voltage at about 2.6 mV are clearly distinguished. Comparing the slightly different voltages of the two branches (see inset in Fig. 3) with the measurement of the single junction characteristics, we can identify the corresponding junction $I_C$ 's. The magnetic field dependence of these three values for the stack biased in series is shown in Fig. 4. In good agreement with the numerical results, we can see three patterns with different values for the first critical field ($H_{c1}$). Tests of individual junctions using the access to the middle electrode have proved that the critical field for each junction changes depending on whether the second junction is in the zero-voltage state or in the whirling state. When the second junction is in zero-voltage state, the critical field is small. While biasing the second junction at the gap voltage, the critical field increases. This effect is also seen in numerical simulations, that predict different sensitivity to the magnetic field for a junction depending on the state of its neighbour. We carried out similar measurements on two-fold stacks having straight overlap geometry, which showed qualitatively similar but less pronounced difference in the critical currents.

To summarize, the static properties of two-fold stacked Josephson junctions were studied in numerical simulations and experiments. The numerical simulations using the coupled sine-Gordon equations predicted different critical currents at a given field value for the fields different from zero. Very similar dependencies were also measured in experiments. Biasing both junctions in series leads to the "current locking" effect [14] at zero voltage. The critical current here is not equal to the critical current of the single junction, due to

the inductive coupling between the junctions. Indeed, it can be shown analytically [14] that a whirling state of the second junction simply cancels any influence of its outer electrode on the properties of the first junction; the latter junction in this case behaves identically to a single junction with a thin electrode (middle electrode of the stack). Measuring the critical currents from the $I-V$ characteristics of the stack at the first gap, i.e. where one of the junctions is biased at the gap voltage, we are able to distinguish between the different critical currents of the junctions in the external magnetic field. These measurements do not show any anomaly in their temperature dependence.

[1] V. P. Koshelets, A. V. Shukin, S. V. Shitov, and L. V. Filippenko, *IEEE Trans. Appl. Supercond.*, **3**, 2524 (1993)

[2] A. V. Ustinov, H. Kohlstedt, and C. Heiden, *IEEE Trans. Appl. Supercond.*, **5**, 2743 (1995)

[3] A. M. Klushin, S. Schornstein, H. Kohlstedt, G. Wende, F. Thrum, H.-G. Meyer, *IEEE Trans. Appl. Supercond.*, **7**, 2423 (1997)

[4] S. Sakai, P. Bodin, and N. F. Pedersen, *J. Appl. Phys.*,**73**, 2411 (1993).

[5] R. Kleiner, P. Müller, H. Kohlstedt, N. F. Pedersen, and S. Sakai, *Phys. Rev. B*, **50**, 3942 (1994).

[6] N. Grønbech-Jensen, P.S. Lomdahl, and M.R. Samuelsen, *Phys. Lett. A*, **154**, 14 (1991).

[7] N. Martucciello and R. Monaco, *Phys. Rev. B*, **53**, 3471 (1996).

[8] S. Keil, I.V. Vernik, T. Doderer, A. Laub, H. Preßler, R.P. Huebener, N. Thyssen, A.V. Ustinov, and H. Kohlstedt, *Phys.Rev. B*, **54**, 14948 (1996).

[9] A.V. Ustinov, B.A. Malomed and N. Thyssen, *Phys. Lett. A*, **233**, 239 (1997).

[10] R. Monaco, A. Polcari, and L. Capogna, *J. Appl. Phys.* **78**, 3278-3286 (1995).

[11] E. Goldobin, A.V. Ustinov and H. Kohlstedt, *Appl. Phys. Lett.* **68**, 250 (1996).

[12] H. A. Huggins and M. Gurvitch, *J. Appl. Phys.*, **57**, 2103 (1985), and refs. therein

[13] H. Kohlstedt, F. König, P. Henne, N. Thyssen, and P. Caputo, *J. Appl. Phys.* **80**, 8621 (1996).

[14] E. Goldobin and A. V. Ustinov, submitted to Phys. Rev. B (April 1998).

## Table and Figure Captions

Fig. 1 Magnetic field dependence of the critical currents of a two-fold annular stack obtained from the numerical simulation using Eqs. (1). Parameters: $L = 12$, $\alpha = 0.05$, $S = 0.5$, $k_\eta = 1.2$, $\Delta J = 1$.

Fig. 2 Numerically calculated spatial phase derivative along anannular Josephson junction for different values of the bias $\gamma$. Parameters: $L = 12$, $\alpha = 0.05$, $\eta = 3.0$.

Fig. 3 Measured $I - V$ curve for a two fold annular stack (dimension: diameter $122\mu$m, width $10\mu$m) at $H_{ext} = 1.5$Oe; inset: individually measured junctions at $H_{ext} = 0$.

Fig. 4 Measured magnetic field dependence of the critical currents for the two-fold annular stack (see Fig. 3) biased in series.

Fig. 1

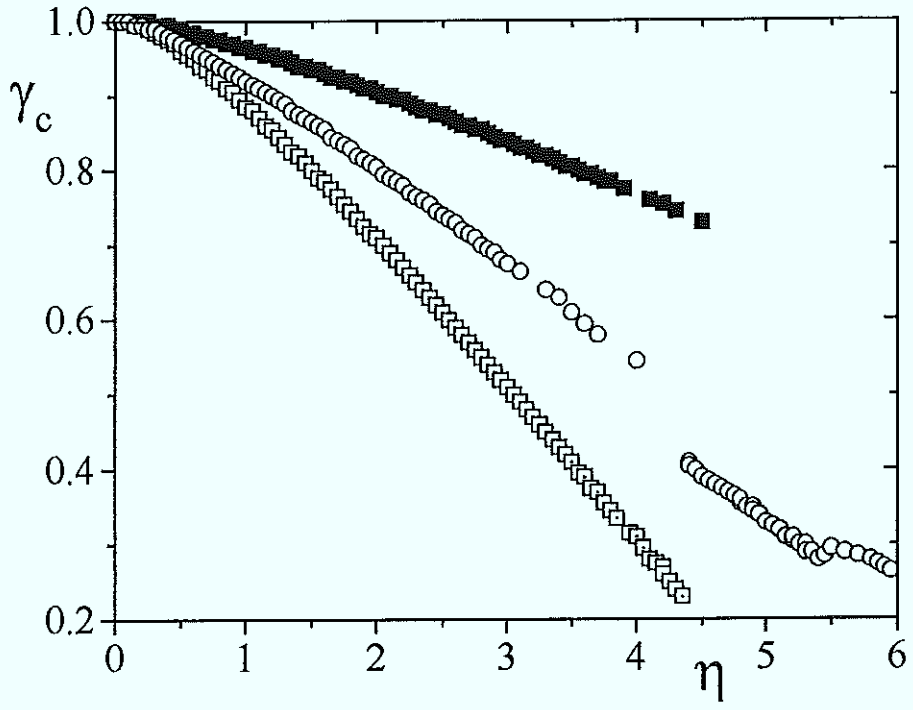
1.0
0.8
0.6
0.4
0.2
$\gamma_c$
0
1
2
3
4
5
6
$\eta$

Fig. 2

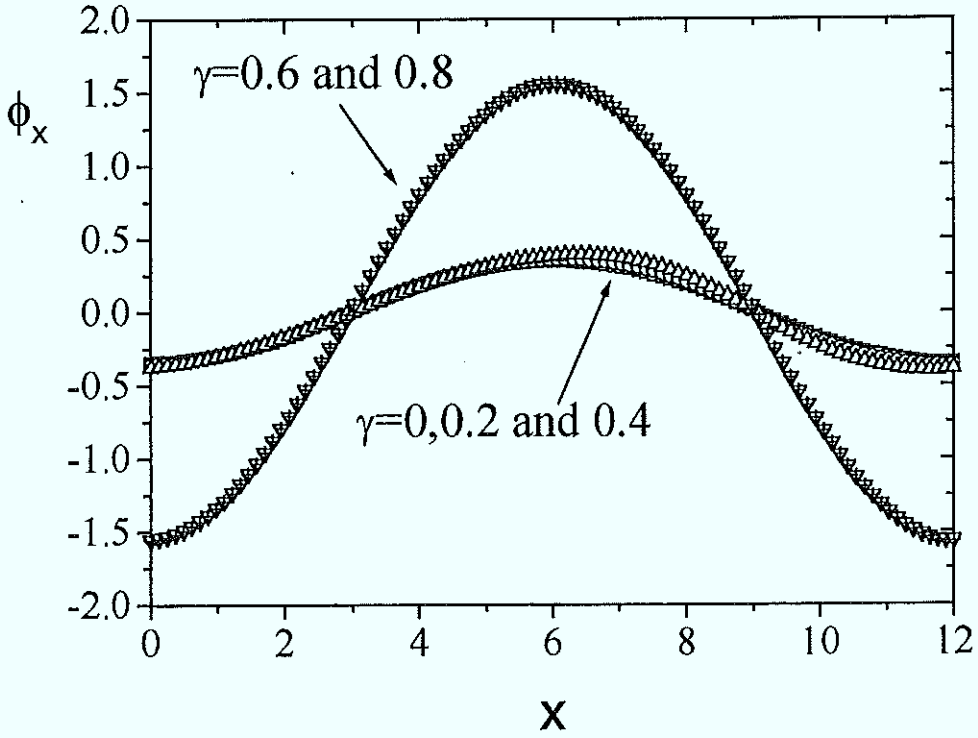
2.0
1.5
1.0
0.5
0.0
-0.5
-1.0
-1.5
-2.0
$\phi_x$
γ=0.6 and 0.8
γ=0,0.2 and 0.4
0
2
4
6
8
10
12
x

Fig. 3

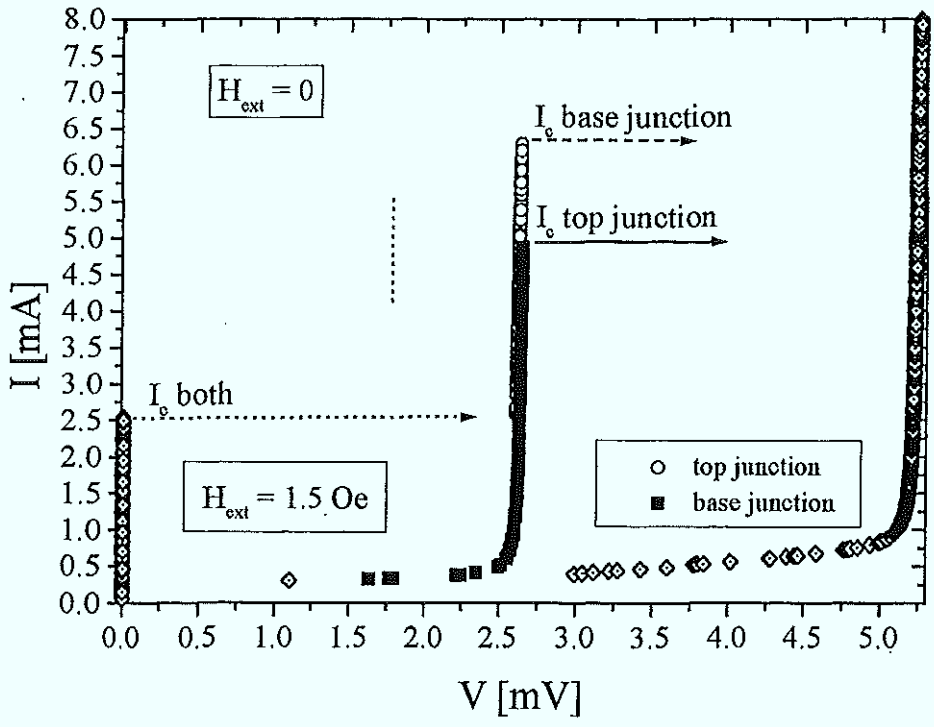
I [mA]
V [mV]
H_ext = 0
I_c base junction
I_c top junction
I_c both
H_ext = 1.5 Oe
top junction
base junction

Fig. 4

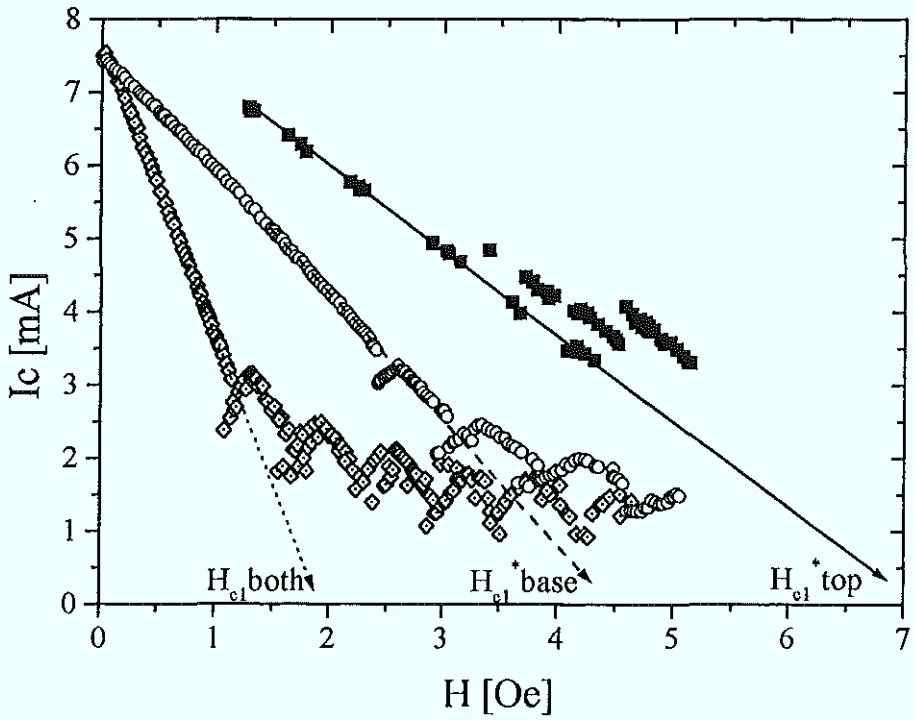
Ic [mA]
H [Oe]
H_c1 both
H_c1 * base
H_c1 * top

Forschungszentrum Jülich

Jül-3656
May 1999
ISSN 0944-2952